FACULDADE DE ENGENHARIA DA UNIVERSIDADE DO PORTO

Fatigue Strength of Friction Stir Weldbonded Single Lap Joints

Jorge Alexandre Soares dos Santos

Dissertation for the Degree of Master in Mechanical Engineering

Supervisor: Pedro M.G.P. Moreira (INEGI)

Co-Supervisors: Lucas F. M. da Silva (FEUP)
Daniel F.O. Braga (INEGI)

July, 2016

© Jorge A.S. dos Santos, 2016

Fatigue Strength of Friction Stir Weldbonded Single Lap Joints

Jorge Alexandre Soares dos Santos

Dissertation for the Degree of Master in Mechanical Engineering

July, 2016

Resumo

Preocupações de carácter económico e ambiental tem vindo a pressionar a indústria dos transportes para uma incessante busca de inovações que conduzam a reduções significativas no consumo de combustível assim como na emissão de poluentes. Uma das vias a seguir para atingir estes objetivos é o estudo de novos processos de junção de modo a permitir *designs* estruturais mais eficientes.

As ligas de alumínio são amplamente usadas na indústria aeronáutica, havendo a necessidade de promover ligações estruturais robustas. De modo a reduzir a massa das estruturas em alumínio aumentando a eficiência ambiental e económica, novas formas de ligar estes componentes sob a forma de juntas sobrepostas com um maior rácio de resistencia/massa são necessárias.

Uma vez que as ligas de alumínio apresentam uma fraca soldabilidade é necessário a utilização de métodos alternativos à soldadura "tradicional" como por exemplo a utilização da adesão estrutural ou o *Friction Stir Welding* (FSW) que permitem ultrapassar essas limitações.

No âmbito desta tese de Mestrado o *Friction Stir Weldbonding*, uma tecnologia de ligação hibrida inovadora foi estudada. Este novo método combina a adesão estrutural e a soldadura por FSW numa configuração de junta sobreposta.

O comportamento sob solicitações estáticas foram estudadas para os três tipos distintos de juntas (FSW, adesivas e hibridas), a fim de avaliar as diferenças entre elas. Uma avaliação do comportamento à fadiga foi realizado para os mesmos grupos de juntas. O efeito do aumento do comprimento de sobreposição na resistência à fadiga das juntas adesivas foi analisado. As capacidades de amortecimento das juntas são uma característica importante em termos de saúde, segurança e conforto. A capacidade de amortecimento está relacionada com o comportamento à fadiga, assim sendo esta foi avaliado de forma a fazer-se um paralelo entro amortecimento e fadiga. Outro tipo de análises foram realizadas, como por exemplo uma análise às superfícies de falha e superfícies anodizadas recorrendo à tecnologia EDS. Modelos numéricos foram também desenvolvidos de modo a prever os três primeiro modos naturais de cada tipo de junta, bem como a resistência de cada tipo de junta sob solicitações estáticas.

Constatou-se que a junta adesiva foi a que apresentou melhor desempenho, para a geometria estudada, sob solicitações estáticas e fadiga. Quanto às juntas hibridas em estudo, algumas dificuldades no processo de fabrico das mesmas resultaram numa elevada inconsistência na avaliação do comportamento à fadiga. Provou-se que o tratamento de superfície aplicado nas juntas adesivas e híbridas resultou numa estrutura porosa como desejado e que o modo de rotura na camada de adesivo foi coesiva junto à interface. A análise à capacidade de amortecimento permitiu concluir que o melhor modo de vibração para avaliar as capacidades de amortecimento deste tipo de juntas no regime livre-livre é o segundo modo. A análise numérica permitiu a obtenção de previsões precisas na determinação das frequências e modos naturais de cada tipo de junta em estudo, assim como a previsão da resistência estática das juntas simuladas.

Abstract

Environmental and efficiency concerns are pressuring vehicle manufacturers to introduce disruptive innovations to reduce CO_2 emissions and fuel consumption. Reducing structural weight is part of this effort. New manufacturing and assembly technologies are required to allow improved structural designs.

In civil aeronautical industry the main material used for the fuselage and structural parts are aluminium alloys. In order to reduce weight, leading to a better fuel and economic efficiency, there is the need to find innovative solutions to join the aluminium components in a single lap joint (SLJ) configuration with higher strength to weight ratio than riveting and fastening.

As it's well known this kind of alloy presents poor welding properties, being the adhesive bonding (AB) and Friction Stir Welding (FSW) interesting alternatives that overcome these limitations.

Under this Master thesis the Friction Stir Weldbonding, an hybrid joining technique that combines the the FSW and AB techniques, was studied.

Quasi-static mechanical properties were studied for three kinds of joints (FSW,AB and FS Weldbonded) in order to assess their behaviour and benchmark them. Also the fatigue behaviour was assessed for the same three joint types, being the effect of the increase in the overlap on the fatigue strength of AB joints analysed. The damping capabilities are related to the fatigue performance as well as they are an important feature in terms of health, safety and comfort that can provide to a part. So the damping ratios of each type of joint were obtained. Other analyses like the EDS were performed. Numerical models to assess the natural modes of each joint type as well as the static strength were also developed.

It was observed that the adhesive joint was the strongest joint under static and fatigue loadings for the geometry adopted, as expected. Some manufacturing problems and inconsistencies were demonstrated in the hybrid joints limiting their performance. Inconsistency limited also their study. It was proven that the surface treatment applied to the AB and hybrid joint was effective and that the failure mode is mainly cohesive near the interface. The damping analysis allowed to find that the best mode of vibration to assess the damping capabilities of the joint was mode two. The numerical analysis gave a good accuracy in determining the natural frequencies and the static strength of the joints modelled.

Acknowledgements

I would like to thank Dr. Pedro M.G.P Moreira and Daniel F.O Braga, Supervisor and Co-Supervisor from LOME (INEGI), for all the daily support and availability throughout the work developed in this Master thesis.

I would also like to extend this acknowledgement to Prof. Lucas F. M. da Silva, Co-Supervisor from FEUP, and to the ADFEUP group members.

I want also to mention Prof. Virginia Infante and João Fortunato from IST for the work developed together and opportunity to use the IST facilities.

I am grateful to the staff from LET, Prof. Miguel Figueiredo and Eng. Rui Silva, for their availability to perform the necessary experimental work and sympathy.

I would like to express my sincere gratitude to my family and close friends that helped me in many different ways, for all the support and affection throughout this five long years journey that culminate with this Master thesis.

Jorge A.S. dos Santos

"The function of education is to teach one to think intensively and to think critically.
Intelligence plus character - that is the goal of true education."

Martin Luther King, Jr.

Contents

1 Introduction **1**
- 1.1 Background and motivation . . . 1
- 1.2 Master thesis goals . . . 2
- 1.3 Research methodology . . . 2
- 1.4 Thesis overview . . . 2

2 State of the art review **4**
- 2.1 Friction Stir Welding . . . 4
  - 2.1.1 Introduction . . . 4
  - 2.1.2 FSW process overview . . . 5
  - 2.1.3 Process parameters . . . 8
    - 2.1.3.1 Tool . . . 9
    - 2.1.3.2 Machine's parameters [13] . . . 11
    - 2.1.3.3 Welding parameters . . . 13
  - 2.1.4 Joint properties . . . 14
    - 2.1.4.1 Metal flow . . . 14
    - 2.1.4.2 Temperature distribution . . . 15
    - 2.1.4.3 Microstructure . . . 17
    - 2.1.4.4 Hook defect - SLJ . . . 19
    - 2.1.4.5 Mechanical properties . . . 20
    - 2.1.4.6 Fatigue life . . . 24
  - 2.1.5 Applications . . . 26
- 2.2 Adhesive bonding . . . 28
  - 2.2.1 Introduction . . . 28
  - 2.2.2 Types of failure, types of stresses and typical joint configurations . . . 30
  - 2.2.3 Wetting . . . 32
  - 2.2.4 Surface preparation . . . 33
    - 2.2.4.1 Degreasing or cleaning treatment . . . 34
    - 2.2.4.2 Mechanical treatment . . . 35
    - 2.2.4.3 Chemical or electrochemical treatment . . . 35
  - 2.2.5 Overview of structural adhesives . . . 38
  - 2.2.6 Adhesive single lap joints [SLJ] . . . 42
    - 2.2.6.1 Rigid adherend linear elastic analyses . . . 42
    - 2.2.6.2 Volkersen's analysis . . . 43
    - 2.2.6.3 Goland and Reissner's analysis . . . 45
    - 2.2.6.4 *"Classical analyses"* limitations . . . 47
    - 2.2.6.5 Hart-Smith's analysis . . . 48
    - 2.2.6.6 Adams model . . . 48

2.2.6.7 Design features in stress distribution . . . 50
2.2.7 Fracture mechanics . . . 50
2.2.8 Mechanical properties . . . 51
2.2.9 Fatigue on adhesive SLJ . . . 52
2.3 Hybrid bonding technologies . . . 55
2.3.1 Fastened bonded joints . . . 55
2.3.1.1 Rivet-bonding . . . 55
2.3.1.2 Bolt-bonding . . . 57
2.3.2 Weld bonded joints . . . 59
2.3.2.1 Spot-weld bonded joints . . . 59
2.3.2.2 Friction stir spot weldbonding . . . 61
2.3.2.3 Laser weld-bonded joints . . . 63
2.3.3 Final comparison between hybrid joints . . . 64
2.3.4 Friction stir weldbonding . . . 64

3 Experimental Details **67**
3.1 Materials Properties . . . 67
3.1.1 Aluminium substrates . . . 67
3.1.2 Adhesive - Araldite® 420 A/B . . . 69
3.2 Specimens geometry . . . 70
3.3 Manufacturing process . . . 72
3.3.1 SL adhesive joints . . . 72
3.3.1.1 Surface treatment . . . 73
3.3.1.2 Joint assembly . . . 76
3.3.1.3 Curing cycle . . . 78
3.3.2 FSW joints . . . 79
3.3.2.1 Welding parameters . . . 80
3.3.2.2 Manufacturing steps . . . 82
3.3.3 Dummy's of bare aluminium AA 6082-T6 . . . 82
3.3.4 Hybrid joints . . . 82
3.3.4.1 Manufacturing steps . . . 83
3.4 *Quasi*-static tests . . . 85
3.4.1 Bulk tensile test . . . 85
3.4.2 FSW, Adhesive and Hybrid joints tensile static tests . . . 85
3.5 Fatigue tests . . . 86
3.6 Energy-dispersive X-ray spectroscopy (EDS) and failure surface observations . . . 88
3.7 Dynamic analysis . . . 89

4 Experimental Results **93**
4.1 Bulk tensile *quasi*-static test . . . 93
4.2 *Quasi*-static tests on SLJ . . . 95
4.2.1 20 mm overlap SLJ . . . 95
4.2.1.1 Bare AA 6082-T6 dummy (DM) . . . 95
4.2.1.2 Araldite® 420 A/B adhesive SLJ (AB-20) . . . 96
4.2.1.3 FSW single lap joint (FSW-20) . . . 98
4.2.1.4 Hybrid joint 425 kgf (Hyb-425-20) . . . 100
4.2.1.5 Hybrid joint 450 kgf (Hyb-450-20) . . . 102
4.2.1.6 Summary . . . 104
4.2.2 40 mm overlap SLJ . . . 104

4.2.2.1 Araldite® 420 A/B adhesive SLJ (AB-40) . . . 105
4.2.2.2 Hybrid joint 450 kgf (Hyb-450-40) . . . 106
4.2.2.3 Hybrid joint 450 kgf cured at 120 °C (Hyb-450-40-cure) . . . 113
4.3 Fatigue . . . 115
4.3.1 Dummy with 20 mm overlap DM-20 . . . 115
4.3.2 Adhesive joint with 20 mm overlap AB-20 . . . 116
4.3.3 FSW joint with 20 mm overlap FSW-20 . . . 121
4.3.4 Adhesive joint with 40 mm overlap AB-40 . . . 126
4.3.5 Hybrid joint with 40 mm overlap Hyb-40 . . . 129
4.3.6 Summary . . . 131
4.4 EDS surface analysis . . . 133
4.4.1 Anodization surface . . . 133
4.4.2 FSW failure surface analysis . . . 133
4.4.3 Adhesive failure surface analysis . . . 134
4.4.4 Hybrid joint failure surface analysis . . . 136
4.5 Dynamic analysis . . . 138
4.5.1 Friction stir welding SLJ with 20 mm of overlap . . . 138
4.5.2 Adhesive SLJ with 20 mm of overlap . . . 139
4.5.3 Adhesive SLJ with 40 mm of overlap . . . 140
4.5.4 Hybrid SLJ with 40 mm of overlap . . . 141
4.5.5 Summary . . . 143

5 Numerical analysis 145
5.1 *Quasi*-static tests . . . 145
5.1.1 AB-20 SLJ . . . 146
5.1.2 AB-40 SLJ . . . 147
5.1.3 FSW-20 SLJ . . . 148
5.2 Natural modes analysis . . . 148
5.2.1 AB-20 SLJ . . . 149
5.2.2 AB-40 SLJ . . . 150
5.2.3 FSW-20 SLJ . . . 151
5.2.4 Hyb-40 SLJ . . . 152
5.2.5 Summary . . . 153

6 Conclusions and Future Work 155
6.1 Conclusions . . . 155
6.2 Future Work . . . 156

List of Figures

2.1 Schematic drawing of FSW (left:butt joint; right: SLJ). [2, 4] (Edited) 6
2.2 FSW tool. [6] 6
2.3 Typical FSW joints 6
2.4 Common types of joints in FSW [8]. 7
2.5 FSW main stages of the process [11]. 10
2.6 Effect of depth on peak temperature as a function of distance from weld centerline 16
2.7 Effect of tool rotation rate on peak temperature 16
2.8 Effect of tool design on temperature distribution 16
2.9 Cross-section of SLJ weld [18]. 17
2.10 Typical microstructure of thermo-mechanically affected zone. [2] 18
2.11 Hook defect on FSW SL joints [4, 21] (Edited images) 19
2.12 Typical hardness curve across the weld of FSW 6063Al-T5 [27]. 21
2.13 Sketches of the possible lap joint configurations (A and B). [18] 22
2.14 Tensile stress distribution in an ideal tension–shear specimen. [7] 22
2.15 Shear tests results at the varying of the configuration (A or B) 22
2.16 Hooking effect and sketch of stresses generated during shear tests: (a) configuration **A** and (b) configuration **B**. [18]. 23
2.17 Fully blocked blanks in the configurations **A** and **B** [18]. 24
2.18 Concept of remote area. [30] 24
2.19 S–N curves at R = 0.1 for lap joints tested along with base material, AA 6082 butt joints.[30] 25
2.20 Number of FSW licences sold between years 1995 and 2009. [12] 26
2.21 Fanuc M-700 with C-type FSW gun developed by Honda Motor Co., Ltd. [15] . 27
2.22 Different applications of non-structural adhesives. 28
2.23 Different classifications of adhesives. 28
2.24 Example of structural adhesives on automotive industry. [40] 29
2.25 Types of failure on adhesive joints. [39] (edited) 30
2.26 Stress distribution of adhesively bonded joints in relation to riveted joints [39] (edited) 31
2.27 Types of stresses in adhesive joints. [43] (edited) 31
2.28 Example of different adhesive joints design. 32
2.29 Left: mercury on glass; right: water on glass 32
2.30 Schematic representation of static contact angles. 33
2.31 Types of surface treatment on adherends 34
2.32 Schematicly figure of the anodization process. [43] 36
2.33 Schematicly figure of the structure of anodic oxide layer on aluminium alloys. [39] 37
2.34 Comparison between electrochemical surface treatments 37
2.35 Aromatic ring representation. 40

2.36 Time–temperature–transformation diagram for thermosetting resins. [47] 40
2.37 Stresses within a single-lap joint. [50] 42
2.38 Deformations in loaded SLJ with rigid adherends [51] 43
2.39 SLJ analysed by Volkersen's method: a) elastic deformation of adherends, b) geometry and c)elemental diagram. (Edited) [51] 43
2.40 Volkersen's adhesive shear stress distribution for aluminium alloy adherends and an epoxy adhesive. [51] 44
2.41 Goland and Reissner's model. [51] 45
2.42 left: Adhesive shear stress distribution when the stress free condition at the ends of the overlap is verified; right: Goland and Reissner's adhesive shear and peel stress distributions. (Edited) [51] 47
2.43 Schematic explanation of shear plastic deformation of the adhesive. [51] 48
2.44 Simple design methodology of single lap joints based on the adherend yielding according to Adams method [51] 49
2.45 Shear stress distribution for different overlap length (L) in an adhesive SLJ. [55] . 50
2.46 Modes of bond deformation used to define adhesive bond strength. (Edited) [47] . 51
2.47 S-N curve comparing pre-treated and untreated joints tested in ambient air and 96% r.h. [57] 53
2.48 Geometry of single lap joints (dimensions in mm) used by [59] 53
2.49 Fatigue life curves of single-lap shear joints in study produced by [59] 54
2.50 Two main approaches to hybrid bonding techniques. 55
2.51 Load vs. Displacement curve for the three types of joints [63] 57
2.52 Typical Bolt-adhesive system. 58
2.53 Load displacement behaviour of the bonded, bolted and hybrid SLJ. (Edited) [32] 58
2.54 Typical spot-welding cycle and joint. (Edited) [67] 60
2.55 Left: tensile shear strength of the hybrid joints (WB2) compared to resistance spot welded (RSW); right: S-N curve for the 3 types of joints. (Edited) [68] 60
2.56 FSSW schematics. [70] 61
2.57 Load vs. Displacement curve for dissimilar FSS Wldbonded joint [71] 62
2.58 S–N curves of the dissimilar FSS Wldbonded joints [71] 62
2.59 Schematic diagram of the laser weld bonding set up. [72] 63
2.60 Tensile shear test results of the laser weldbonded joints. [74] 64
2.61 Single lap joint specimen geometry. [77] 65
2.62 Single lap joints ultimate load. [77] 66

3.1 Work program. 67
3.2 S-N curve of AA 6082-T6 w/ 0.1 R-ratio [79] 69
3.3 Araldite® 420 A/B failure mode with aluminium adherend. [59] 70
3.4 Araldite® 420 A/B cartridge. 70
3.5 Geometry of the adhesive specimen used previously by our workteam. (dimensions in mm) [75] 71
3.6 Geometry of the specimen used with an overlap of 20 mm. 71
3.7 Geometry of the specimen used with an overlap of 40 mm. 72
3.8 Geometry of the dummy's specimen used with an overlap of 20 mm. 72
3.9 Load vs Displacement curves of the first two lots 74
3.10 Adhesive failure surface of specimen B 74
3.11 Mean maximum displacement obtained in specimens AB-sc and AB, with standard deviation. 76

3.12 Mean maximum remote stress obtained in specimens AB-sc and AB, with standard deviation. . . . 76
3.13 Mould with SLJ specimens. [81] . . . 77
3.14 "Gun" and vessel used to pour and mix the adhesive. . . . 77
3.15 Adhesive SLJ specimens assembled in the mould. . . . 78
3.16 Cure cycle for Araldite® 420 A/B. . . . 79
3.17 ESAB® LEGIO^{TM} 3UL numeric control machine. . . . 79
3.18 FSW joint drawing. . . . 80
3.19 FSW clamping system used. . . . 81
3.20 Modular tool used in FSW and hybrid joints. . . . 81
3.21 "Gun" and mixer nozzle used to produce the hybrid joints. . . . 83
3.22 Hybrid joint after cutting . . . 84
3.23 Geometry of the long specimen according to EN ISO 527-2 (dimensions in mm) . 85
3.24 Clamping system used in the tensile tests. . . . 86
3.25 Example of an S-N curve with low and high cycle fatigue. [50] . . . 87
3.26 Cyclic stress spectrum and parameters used to define it. . . . 88
3.27 EDS machine used at CEMUP. . . . 89
3.28 System block diagram. [84] . . . 90
3.29 Typical set-up. [84] . . . 90
3.30 Typical FRF obtained. [84] . . . 91
3.31 Hammer used. . . . 91
3.32 Damping analysis set-up used. . . . 92

4.1 Experimental curves for the tensile bulk test of the Araldite® 420 A/B. . . . 93
4.2 UTS of Araldite® 420 A/B bulk vs. cure temperature. . . . 94
4.3 Typical Load vs. Displacement curve of the dummy specimen and failure surface. 95
4.4 Load vs. Displacement curve of the Araldite® 420 A/B adhesive w/ 20 mm of overlap SLJ specimens. . . . 96
4.5 AB vs dummy joint strength. . . . 97
4.6 Beginning of the yield of the aluminium adherend and final yielding of the adherends. 97
4.7 Failure surface of the adhesive single lap joint w/ 20 mm overlap after tensile test. 98
4.8 Load vs. Displacement curve of the FSW single lap joint specimens. . . . 98
4.9 Dummy vs AB vs FSW joint strength. . . . 99
4.10 Left: FSW failure surface ; right: side view yielding of the specimens. . . . 99
4.11 Load vs. Displacement curve of the Hybrid SLJ 425 kgf 20mm overlap specimens. 100
4.12 Representative failure surface of Hyb-425-T(1,3,4) specimens. . . . 100
4.13 Surface of failure of specimens Hyb-425-T2 . . . 101
4.14 Surface of failure of specimens Hyb-425-T5 . . . 101
4.15 Dummy vs AB vs FSW vs Hyb-425-20 joint strength. . . . 102
4.16 Failure surface of Hyb-450-20 specimen. . . . 102
4.17 Load vs. Displacement curve of the Hybrid SLJ 450 kgf 20mm overlap specimens. 103
4.18 Dummy vs AB vs FSW vs Hyb-425-20 vs Hyb-450-20 joint strength. . . . 103
4.19 Load vs. Displacement curves of the joints studied with 20mm overlap. . . . 104
4.20 Typical Load vs. Displacement curve of the AB-40 specimens. . . . 105
4.21 Failure on the AB-40 specimens. . . . 105
4.22 Load vs. Displacement curve of the Hybrid SLJ 450 kgf 40 mm overlap specimens. 106
4.23 Failure surface of the Hyb-450-40-T1 specimen. . . . 106
4.24 Failure surface of the Hyb-450-40-T2 specimen. . . . 107
4.25 EDS analysis of the failure surface on Hyb-450-40-T1 . . . 108

4.26 EDS analysis of the failure surface on Hyb-450-40-T2 109
4.27 Refrigerant liquid leak. 110
4.28 Load vs. Displacement curve of the Hybrid SLJ 450 kgf 40 mm overlap specimens produced with the refrigerant system turned off. 110
4.29 Typical failure surface of the Hybrid SLJ 450 kgf 40 mm overlap specimens produced with the refrigerant system turned off. 111
4.30 Groove at the table in the FSW machine. 112
4.31 Load vs. Displacement curve of the Hybrid SLJ 450 kgf 40 mm overlap with cure cycle of 1h at 120 °C specimens. 113
4.32 Failure surface of specimens Hyb-425-40-cure. 114
4.33 AB-40 vs Hyb-450-40 vs Hyb-450-40-cure joint strength. 114
4.34 S-N curve for the dummy specimens and bare aluminium. 116
4.35 Linear regression of the fatigue data from AB-20 specimens. 117
4.36 Normal probability plot of the residuals of $\log N$ in AB-20 specimens. 118
4.37 Plot of the residuals vs the load levels. 118
4.38 S-N curve for adhesive SLJ and bare aluminium. 119
4.39 S-N curve for adhesive SLJ and extrapolation of fit in Dummy specimen. 120
4.40 Typical failure surface of the AB-20 specimens under fatigue loads 121
4.41 Average shear stress vs number of cycles AB SLJ curve. 121
4.42 Linear regression of the fatigue data from FSW-20 specimens. 122
4.43 Normal probability plot of the residuals of $\log N$ in FSW-20 specimens. 123
4.44 Plot of the residuals vs the load levels. 123
4.45 S-N curve for FSW joint compared to the AB-20 and bare aluminium curves. . . 124
4.46 Fatigue Strength ratio FSW-20/AB-20 125
4.47 Fatigue failure surface of the FSW specimens. 126
4.48 Average shear stress vs number of cycles for FSW-20 and AB-20 curves. 126
4.49 Linear regression of the fatigue data from AB-40 specimens. 127
4.50 S-N curve for adhesive 40 mm overlap. 128
4.51 Average shear stress vs number of cycles for AB-40, FSW-20 and AB-20 curves. 129
4.52 Fatigue data for the Hybrid joint with 40 mm of overlap. 130
4.53 Failure surface of the Hyb-450-40 specimens under fatigue fatigue loads. 131
4.54 Fatigue data for the joints studied. 131
4.55 Fatigue strength for the joints studied at 10^5 cycles. 132
4.56 Anodized surface EDS analysis. 133
4.57 FSW surface analysed. 133
4.58 FSW surface analysed in EDS. 134
4.59 adhesive joint surface analysed in EDS. 135
4.60 Adhesive joint surface analysed in EDS. 136
4.61 Hybrid joint surface analysed in EDS. 136
4.62 Mode shapes for the first 3 modes for a beam under free-free boundary conditions. [39] 138
4.63 FRF and coherence function for the damping analysis in the FSW joint. 138
4.64 FRF and coherence function for the damping analysis in the AB-20 joint. 140
4.65 FRF and coherence function for the damping analysis in the AB-40 joint. 141
4.66 FRF and coherence function for the damping analysis in the Hyb-40 joint. 142
4.67 Comparison of the damping capabilities of FSW and AB SLJ. 143

5.1 Mesh used in the AB-20 specimen static FEM analysis. 146
5.2 Assembly used in FEM simulation for the FSW-20 specimen. 146

5.3 Numerical Load vs. Displacement curve of the AB-20 specimens. 147
5.4 Numerical Load vs. Displacement curve of the AB-40 specimens. 147
5.5 Failure mode obtained in FEM for AB-40. 148
5.6 Numerical Load vs. Displacement curve of the FSW-20 specimens. 148
5.7 Mesh used in the AB-20 specimen analysis. 149
5.8 Modes obtained for the AB-20 pecimen on FEM analysis. 150
5.9 Modes obtained for the AB-40 specimen on FEM analysis. 151
5.10 Mesh and partitions used in the FSW-20 specimen analysis. 151
5.11 Modes obtained for the FSW specimen on FEM analysis. 152
5.12 Joint model used in the FSW-20 specimen analysis. 153
5.13 Modes obtained for the Hyb-40 specimen on FEM analysis. 153

List of Tables

2.1 Common problems associated to traditional welding methods on aluminium alloys. [3] . . . 5
2.2 Main FSW process variables. [8] . . . 9
2.3 A selection of tools designed at TWI. [6] . . . 10
2.4 Relevant loads for the FSW process. . . . 11
2.5 FSW equipment features. [14] . . . 13
2.6 FSW hook length. [22] . . . 20
2.7 Longitudinal tensile properties of weld nugget in friction stir welded AA 7075-T651 on butt configuration[28] . . . 21
2.8 Fatigue strength of AA 6082-T6. [30] . . . 26
2.9 Inferences from types of failure [41] . . . 31
2.10 Typical thermosetting resins for adhesives. [39] . . . 38
2.11 Typical adhesives mechanical properties values . . . 51
2.12 Energy absorption of DLJ [62] . . . 56
2.13 FS Weldbonding parameters. [77] . . . 65
2.14 Single lap joints ultimate load specimens nomenclature. [77] . . . 66

3.1 Chemical composition of aluminium alloy AA 6082-T6 (*wt%*). [79] . . . 68
3.2 Mechanical and physical properties of AA 6082-T6 (*wt%*). [79] . . . 68
3.3 Araldite® 420 A/B mechanical properties . . . 69
3.4 Load vs. Displacement relevant data of the first two lots . . . 74
3.5 Changes in the Load vs. Displacement relevant data after the new anodization approach . . . 75
3.6 FSW parameters. . . . 81
3.7 Welding parameters used in hybrid joints. . . . 83

4.1 Adhesive mechanical properties obtained in the tensile bulk test (1 mm/min). . . . 94
4.2 Summary of adhesive SLJ with 20mm of overlap average mechanical properties obtained in the tensile test . . . 96
4.3 Summary of FSW SLJ with 20mm of overlap average mechanical properties obtained in the tensile test . . . 98
4.4 Summary of Hyb-425-2 SLJ with 20mm of overlap average mechanical properties obtained in the tensile test . . . 102
4.5 Summary of Hyb-450-20 SLJ average mechanical properties obtained in the tensile test . . . 104
4.6 Summary of AB-40 SLJ mechanical properties obtained in the tensile test . . . 105
4.7 Summary of Hyb-450-40 SLJ (40mm of overlap) average mechanical properties obtained in the tensile test . . . 107

4.8 Summary of Hyb-450-40 SLJ (40mm of overlap) produced with the refrigerant system turned off average mechanical properties obtained in the tensile test. . . . 111
4.9 Summary of average mechanical properties obtained in the tensile test in the 7 specimens of the joint Hyb-450-40 SLJ (40mm of overlap). 112
4.10 Summary of Hyb-450-40-cure SLJ average mechanical properties obtained in the tensile test 113
4.11 Load levels used in the fatigue tests on the dummy specimens with 20 mm of overlap and results. 116
4.12 Load levels used in the fatigue tests on the adhesive joints with 20 mm of overlap and results. 117
4.13 Load levels used in the fatigue tests on the FSW joints with 20 mm of overlap and their results. 122
4.14 Load levels used in the fatigue tests on the adhesive joints with 40 mm of overlap and their results. 127
4.15 Load levels used in the fatigue tests on the hybrid joints with 40 mm of overlap and their results. 130
4.16 Coefficients found for S-N curves 132
4.17 Average ξ values found for the FSW joint for the first three natural modes 139
4.18 Average ξ values found for the AB-20 joint for the first three natural modes. . . . 140
4.19 Average ξ values found for the AB-40 joint for the first three natural modes. . . . 141
4.20 Average ξ values found for the Hyb-40 joint for the first three natural modes. . . 142

5.1 Material properties used in the numerical analysis. 149
5.2 Natural frequencies found in FEM vs Experimental for the AB-20 specimen. . . 150
5.3 Natural frequencies found in FEM vs Experimental for the AB-40 specimen. . . 150
5.4 Natural frequencies found in FEM vs Experimental for the FSW specimen. . . . 152
5.5 Natural frequencies found in FEM vs Experimental for the Hyb-40 specimen. . . 153

Acronyms and Symbols

Acronyms

AB	Adhesive Bonding
Ab.	Absorbed
AC	Alternate current
AP	Abrasive polish
AS	Advancing side
BM	Base material
CAA	Anodic oxidation in chromic
CAE	Chromic-acid etch
CEMUP	Centro de Materiais da Universidade do Porto
CNC	Computer Numeric Control
CW	Clockwise
DC	Direct current
DIC	Digital Image Correlation
Disp.	Displacement
DLJ	Double lap joint
DOF	Degrees of Freedom
EDS	Energy-dispersive X-ray spectroscopy
ENF	End-notched flexure
FCG	Fatigue crack growth
FEA	Finite element analysis
FEM	Finite element method
FEUP	Faculdade de Engenharia da Universidade do Porto
FRF	Frequency response function
FS	Friction Stir
FSW	Friction Stir Welding
FZ	Fusion zone
GTA	Gas–tungsten arc
HAZ	Heat-affected zone
IST	Instituto Superior Técnico
LET	Laboratório de Ensaios Tecnológicos
Max.	Maximum
Min.	Minimum
PAA	Phosphoric acid anodization
PAW	Plasma arc welding
PEEQ	Effective plastic strain
PFZ	Precipitate free zone
PI	Prediction intervals

PMZ	Partially melted zone
RPM	Rotations per minute
RS	Retreating side
RSW	Resistance spot welding
SAA	Sulphuric acid anodization
SL	Single lap
SLJ	Single lap joint
Spec.	Specimen
TTT	Time-temperature-transformation
TWI	The Welding Institute
UTS	Ultimate tensile stress
YS	Yield stress

Symbols

$\tau_{AVG.}$	Average shear stress
F_Z	Axial force
θ	Contact angle
ξ	Damping ratio
R	Fatigue load ratio
T_g	Glass transition temperature
P_{max}	Maximum load
σ_{max}	Maximum stress
σ_m	Medium stress
P_{min}	Minimum load
σ_{min}	Minimum stress
M	Moment
ω_n	Natural frequency
N	Number of cycles
σ_{remote}	Remote stress
γ	Shear strain
τ	Shear stress
θ_0	Static contact angle
ε	Strain
σ	Stress
σ_m	Stress amplitude
v	Tool rotation speed
n	Tool traverse speed
M_Z	Torque
V	Transverse force
F_X	Traverse force

Chapter 1

Introduction

1.1 Background and motivation

Climate changes and environmental awareness are forcing governments to apply new regulations on pollution emission and fuel efficiency on the transportation industry. Also economic reasons lead the transportation industry to be more efficient seeking innovative solutions that can result in lower manufacturing, maintenance and running costs.

As a response to these concerns new manufacturing methods are being used in the aeronautical, automotive and railway industries among others. However, the aeronautical industry is considerably conservative and highly regulated and as such new methodologies require a long time for validation before their implementation, being the mechanical fastening still the primary joining methods employed.

Joints are usually seen as the weakest link in a mechanical structure when compared to parts being joined. So there is the need to study and benchmark the static strength as well as their fatigue resistance. Friction Stir Weldbonding is an innovative manufacturing process that tries to gather the best properties of the Friction Stir Welding joints and adhesive bonding with a lower weight and cost. It's expected that this hybridization method leads to a joint capable to perform well under static, fatigue, dynamic loading conditions and in challenging environmental conditions, providing also redundancy which the industry always aims for.

In order to benchmark the static and fatigue behaviour of the FS Weldbonded joints, these were compared to equivalent joints with the same single lap configuration using the Friction Stir Welding or the adhesive bonding to manufacture them.

Since the FS Weldbonding is an innovative process there is room to study, benchmark and improve the proposed hybridization process. This Master thesis arises from the existing research gap and is highly challenging and interesting because it requires knowledge in two different areas the welding and the adhesive bonding being this an opportunity for the author expand his understanding about this subjects.

1.2 Master thesis goals

The main objective of the present Master thesis research is to characterize and compare the fatigue behaviour of Hybrid FS Weldbonded joints with adhesive bonded and FSW joints. The static strength of the different type of joints was also a key goal. To complement the fatigue study it was found interesting to study the damping capabilities of the joints and to perform numerical analyses to predict the static strength and natural modes of each type of joints.

1.3 Research methodology

The methodology defined to achieve the main goals of the Master thesis is described in this section. The proposed plan to reach the required results for this research work consisted in various steps such as:

- Study of previous work developed in adhesive bonding, FSW and hybrid joints technologies;
- Assessing previous works on FS weldbonded joints;
- Determination of some properties of the adhesive;
- Manufacture of adhesive joints. The FSW and Hybrid were produced with the collaboration of a Master student at Instituto Superior Técnico;
- Testing the manufactured specimens under *quasi*-static conditions;
- Testing under cyclic loads (Fatigue) in order to benchmark and analyse the differences between the types of joint in study;
- Damping capabilities assessment;
- FEM simulation of the *quasi*-static strength and natural modes of the different joint types;
- Analyse and compare the results between the different joints.

1.4 Thesis overview

The structure of the thesis is divided in six different chapters, including this one, that are the following:

Chapter 2: A review of the Friction Stir Welding is presented describing the general concepts of the process, process parameters, joint and mechanical properties and fatigue life characteristics. It's also done a review in the adhesive bonding field being approached the main concepts of this technology, surface treatments, single lap joint properties, fatigue on the SLJ configuration, among

others. Finally it is presented several hybrid single lap joints technologies explaining the concepts and the static and fatigue behaviour of each kind of joint.

Chapter 3: All the experimental details are presented in this chapter. The material characterization, the specimens geometry, the manufacturing process, the *quasi*-static test procedures, fatigue test procedures, Energy-dispersive X-ray spectroscopy (EDS) and damping analysis procedures are explained.

Chapter 4: Results for static, fatigue,EDS and damping analysis are shown and discussed.

Chapter 5: The numerical simulation procedures and results are shows and are compared to the experimental ones.

Chapter 6: The conclusions obtained within this work are presented. Suggestions to improve and continue the research of the FS Weldbonded joints are mentioned.

Chapter 2

State of the art review

In Chapter 2 a state of the art review on joining techniques for aluminium alloys is done encompassing academic works and industrial application cases. Since Friction Stir Welding and Adhesive bonding are key techniques for the hybrid process to be study, they are the main focus of this chapter. Following, a sate of the art review on hybrid joints is done, including performance under quasi-static and cyclic loading conditions.

2.1 Friction Stir Welding

2.1.1 Introduction

Environmental and resource scarcity concerns have pushed policy makers to set efficiency standards and goals for future vehicles, such as the directive [1]. In response to those requirements, steel is increasingly been replaced as a structural material for other alloys that present higher specific strength like aluminium and titanium alloys. In numerous industrial fields, such as the automotive, aeronautics, aerospace, among others, the use of aluminium is increasing. The increase use of these materials require appropriate joining methods with minimum incidence of defects and improved mechanical properties.

The welding industry soon realized that there was an handicap in traditional welding technologies, such as the difficulty of producing high-strength, fatigue and fracture resistant welds in aluminium alloys like 2XXX and 7XXX series (currently known as non-weldable series) [2]. Higher strength aluminium alloys tend to suffer some defects, like hot cracking in the cooling cycle in the fusion zone and in the partially melted zone (PMZ), or the loss of strength/ductility in the heat-affected zone (HAZ) [3]. The formation of undesired porosity, which is reflected in a considerable loss of mechanical properties compared with the base material [2], is a common defect in aluminium-lithium alloys and powder metallurgy. [3]

Common problems associated to traditional welding technologies on aluminium alloys is shown in Table 2.1.

Table 2.1: Common problems associated to traditional welding methods on aluminium alloys. [3]

Typical Problems	Alloy Type	Solutions
Porosity	Al-li alloys (severe)	Surface scraping or milling Thermovacuum treatment Variable-polarity keyhole PAW
	Powder-metallurgy alloys (severe)	Thermovacuum treatment Minimize powder oxidation and hydration during atomization and consolidation
	Other types (less severe)	Clean workpiece and wire surface Variable-polarity keyhole PAW
Solidification cracking in FZ	Higher-strength alloys (2xxx,6xxx,7xxx)	Use proper filler wires and dilution In autogenous GTA welding, use arc oscillation or less susceptible alloys
Hot cracking & low ductility in PMZ	Higher-strength alloys	Use low heat input Use proper filler wires Low-frequency arc oscillation
Softening in HAZ	Work-hardened materials	Use low-heat input
	Heat-treatable alloys	Use low-heat input Postweld heat treating

The kind of limitations presented in Table 2.1 inhibited the wide use of traditional welding methods in aeronautics to replace riveted joints (despite the stress concentration factors associated with riveted joints that cause adverse effects in fatigue life of the structure).

As a way to overcome the current joining methods shortcomings (e.g, difficulties to weld some aluminium and magnesium alloys), in the early 90's, Friction Stir Welding was invented at The Welding Institute (TWI), in the United Kingdom. FSW is a solid-state joining technique which has the ability to join plates with less heat input than traditional welding allowing joining without material melting. [2]

2.1.2 FSW process overview

In a conceptual point of view this technique is simple. It consists on a non-consumable rotating tool composed of two major elements (the pin and the shoulder), that locally soften the workpiece, through heat input generated by friction (between the workpiece and the rotating tool) and plastic work. The rotating movement is complemented with a linear one that allows the tool to stir and join the surfaces. Figure 2.1 schematically presents the FSW process.

Two terms that are commonly used when discussing FSW and that are relevant to define are advancing side and retreating side. The former is the side of the joint where the material is stirred in the same direction as the tool movement while the later is the opposite side of the weld. Despite the apparent simplicity of the process the physics that govern it are highly complex. Some authors describe it as a combination of *in-situ* extrusion combined with forging [5]. One of the factors

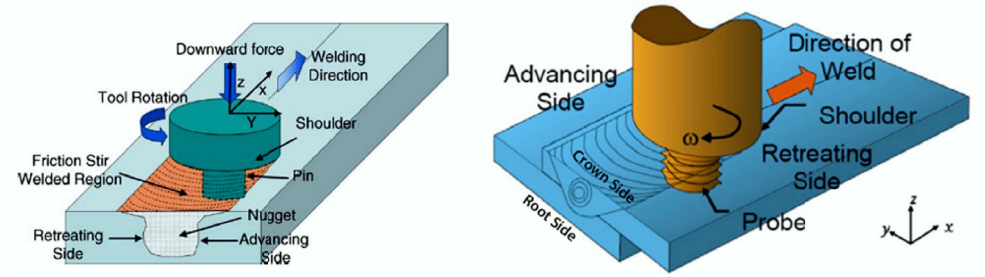

Figure 2.1: Schematic drawing of FSW (left:butt joint; right: SLJ). [2, 4] (Edited)

that influence the process is the geometry of the tool used. In fact the tool, as said before, is elementary composed by a shoulder and a pin (Figure 2.2 represents an actual FSW tool). The shoulder is responsible for the application of the vertical load that generates the heat input due to rotational friction. The linear movement has a minimal effect on heat input when compared with the rotational one. This heat input is enough to soften the material of the workpiece. Severe plastic deformation and flow of this plasticised metal occurs as the tool is translated along the welding direction [6]. There is a material flow from the front of the tool to the trailing edge where it is forged into a joint [2].

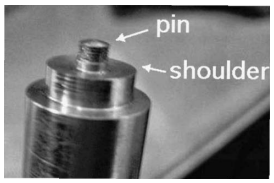

Figure 2.2: FSW tool. [6]

The tool also pushes the material in order to prevent the ascendant movement of the material acting like a "barrier".

The intense plastic deformation imposed by the tool results in an elevated temperature, that in the case of aluminium alloys goes between 400 °C and 480 °C. This leads to a generation of fine and equiaxed recrystallized grains and consequently good general mechanical properties [2].

The geometry of the tool has been studied [5, 7] in order to find its influence on weld quality. There are, nowadays, countless pin and shoulder designs to achieve the desired configuration and to join diverse materials with higher quality and efficiency.

A transverse section from a typical butt joint configuration is shown in Figure 2.3.

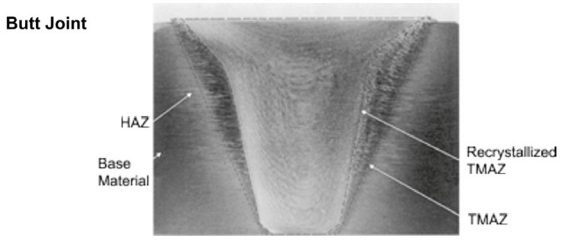

Figure 2.3: Butt joint in 25.4-mm thick 2195 aluminium-lithium plate [8]. (Edited)

In Figure 2.3 four distinct areas can be observed. The base material (BM) is the area were the material does not present any change compared to the original material despite the elevated temperature during welding. Closer to the weld is the heat-affected zone (HAZ), like the name suggests this zone is sufficiently heated during the welding process to modify it's mechanical properties and the microstructure although with no evidence of plastic deformation on it's structure [9]. The nature of this changes is recovery of cold work and coarsening of precipitates [8]. The mechanical strength, ductility, toughness and corrosion resistance of the workpiece suffer some degradation [8].

The thermomechanically affected zone (TMAZ) is the welded zone where the heat input and the external forces are enough to produce a plastic deformation of the original grain structure and a local softened material. The TMAZ includes the unrecrystallized TMAZ and the nugget zone (recrystallized TMAZ, the central area of the weld). The nugget is a fully recrystallized area and is the zone where previously the tool pin has been [9]. In aluminium alloys, the nugget zone is an important region of the weld because it can be of a significant size and can represent a region of low micro-hardness and increased corrosion susceptibility [8].

There are, at least, five common types of FSW joints: butt joint, overlap joint (Single Lap Joint - SLJ), T-joint, 90 degree joint and the oblique angle joint (Figure 2.4). The scope of this Master thesis is on SLJ type due to its large industrial application potential (similarity with employed riveted and adhesive bonded joints and generally easier tolerance management).

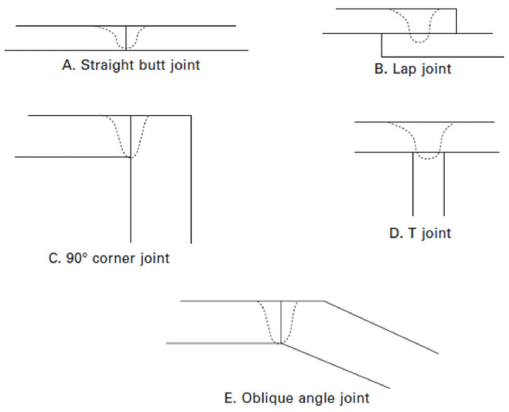

Figure 2.4: Common types of joints in FSW [8].

The FSW process requires a robust clamping system in order to counteract the vertical load and torque applied by the tool. This fact represents one of the main limitations of this process which limits its applicability and portability [10].

According to Chen *et al.* and Mahoney *et al.* [8, 9], this method exhibits several advantages over other welding technologies:

Technical benefits:

- Solid phase process;
- Allows joining of dissimilar materials;

- Improved weldability;
- Improved cosmetic appearance;
- Low welding distortion and good dimensional stability;
- Low residual stresses;
- Improved stress corrosion cracking performance;
- Improved static strength and ductility;
- Improved fatigue behaviour;
- Low risk of cold cracking;
- Weldability of dissimilar alloys and materials;
- No edge due to the filler material.

Environmental benefits:

- Lower energy consumption;
- Normally, no surface cleaning and degreasing required;
- No shielding gases required and no gases emission;
- Consumable materials savings.

Economic benefits:

- Low energy consumption;
- Lower processing time;
- Low defects ratio;
- No consumables;
- Joint weight reduction.

However, there are some drawbacks and limitations that inhibit the use of the FSW in certain applications like [8, 9]:

- The poor fatigue behaviour in configurations like Single Lap Joint;
- Requires special fixture systems;
- Reaction to the process loads;
- The beginning of the weld usually presents lower properties;
- Reduction of maximum elongation at break;
- Root flaws along the welding line;
- The end of the weld has the a material void from pin extraction (keyhole).

In several cases these drawbacks can be overcome, making FSW a method with an huge potential. In Sub-Section 2.1.3 the main control parameters in the process will be addressed.

2.1.3 Process parameters

There are several variables that influence the final FSW weld quality. It is very important to study and asses their influence in the joint mechanical properties like: static strength, fatigue

life, toughness, behaviour in corrosive environments and several others in order to maximize the performance and reproducibility. Over decades of academic research the focus was on the study of parameters effects on heat generation and dissipation, which are the main properties changer mechanism. Other areas of study include the effect of process parameters on material flow, defect formation, process forces, grain size, etc. [8]

The main variables of FSW are shown in Table 2.2.

Table 2.2: Main FSW process variables. [8]

Tool design variables	**Machine variables**	**Other variables**
Shoulder and pin materials	Welding speed	Anvil material
Shoulder diameter	Spindle speed	Anvil size
Pin diameter	Plunge force or depth	Workpiece size
Pin length	Tool tilt angle	Workpiece properties
Thread pitch		
Feature geometry		

2.1.3.1 Tool

The tool is described, by some authors, as the most influential variable of the process [2]. As mentioned previously the tool consists of a shoulder and a pin, and its two major roles are the localized heating of the workpiece and promoting the material flow. Tool design influences the heat generation, the plastic flow, the power required, and the uniformity of the welded joint [6]. The first stage of the friction stir welding process is the pin plunge in the workpiece. During this initial stage, represented in Figure 2.5 a), the heat input results primarily from the friction between pin and workpiece. The tool is plunged until the moment were the shoulder touches the piece, Figure 2.5 b). From this point until the end of the process the main responsible for the heat input is the friction between the shoulder and the workpiece. The most influential variable in heat input is the relative size of the shoulder and the pin, being the other variables neglected [9]. Beyond the heating function, the tool is also responsible for stirring and moving the softened material along the welding line to promote a joining, Figure 2.5 c). The shoulder also acts like a "barrier" against the rising material flow and provides confinement for the heated volume of base material. The last stage, Figure 2.5 d), leaves marks in the workpiece (keyhole) which size is nearly the equivalent of the volume removed in the first stage. The keyhole, whenever possible, is left in an "appendix" that is machined later. [2, 6, 8, 9]

The tool geometry, as seen before, is a key point in the process. For example, the pin length determines the maximum hight of the weld. The introduction of a threaded pin leads to a drastic reduction in the trend of formation of a void near the end of the pin, when compared with the typical cylindrical pin. The natural tendency is for the soften material to be expelled upward and out past the tool shoulder [8]. Chen [8] says that even a small loss of material past the tool shoulder results in a void because in the FSW process there is no addition of material. The inclusion of a

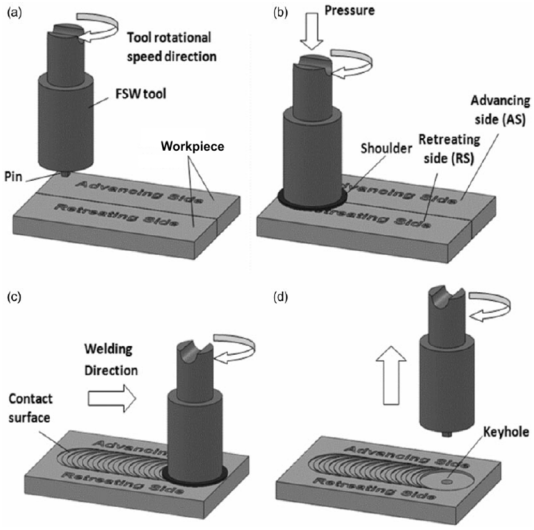

Figure 2.5: FSW main stages of the process [11].

screw in the pin results in a forced downward movement of the material avoiding the appearance of a void.

Another important property of the tool is the ratio between the swept volume during rotation and the volume of the pin itself. This ratio can be defined as the "dynamic volume to the static volume ratio" that is important to provide an adequate flowpath. The greater the ratio, the higher the workpiece material volume affected is.The greater the ratio, the better is the pin design because it can affect more workpiece material than it's own volume. The typical values for the cylindrical tools are around 1.1 : 1, but there are disruptive designs that allows ratios of 2.6/1 (the MX TrifluteTM® pin). [2]

There has been many research publications in this field, and in some of these studies, authors report that there are designs that can improve the welding speed by 100%, significantly reducing the required axial load, reducing of the upper plate thickness effect in single lap (SL) joints along with other diverse improvements when regarding the original cylindrical pin design. [9]

Table 2.3: A selection of tools designed at TWI. [6]

Tool	Cylindrical	Whorl™	MX triflute™	Flared triflute™	A-skew™	Re-stir™
Schematics				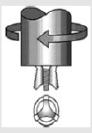		
Tool pin shape	Cylindrical with threads	Tapered with threads	Threaded, tapered with three flutes	Tri-flute with flute ends flared out	Inclined cylindrical with threads	Tapered with threads
Ratio of pin volume to cylindrical pin volume	1	0.4	0.3	0.3	1	0.4
Swept volume to pin volume ratio	1.1	1.8	2.6	2.6	Depends on pin angle	1.8
Rotary reversal	No	No	No	No	No	Yes
Application	Butt welding; fails in lap welding	Butt welding with lower welding torque	Butt welding with further lower welding torque	Lap welding with lower thinning of upper plate	Lap welding with lower thinning of upper plate	When minimum asymmetry in weld property is desired

The Table 2.3 show some of the different designs available in the market. It is possible to assess how the design features of the tool influence several parameters.

Krasnowski et al. [12] conducted a study in order to identify the influence of the tool shape and weld configuration on the microstructure and mechanical properties of AA 6082 alloy FSW joints. Three types of tool with different probe shapes and shoulder surfaces, and two weld configurations (one-sided and two-sided) were used. It's important to highlight that is the same material that will be used in the experimental work reported in this Master thesis. Some of the conclusions of Krasnowski et al. [12] were that the shape of the tool used in the FSW process influences the mechanical properties of the joints. The change of the tool shape in the welding process influences the joints hardness profile, as well as their tensile strengths. The joint configuration influences mechanical properties, with the two-sided welds performing worse than the single-sided ones (there are a larger heat input in two-sided weld). [12]

2.1.3.2 Machine's parameters [13]

In a recent work (2016), a literature review was done by Mendes et al. [13] on the machine and control systems applied in FSW. The main technical variables of the machine identified were: force, stiffness, accuracy, sensing and flexibility.

Load capability

The imposed loads during FSW process are challenging design requirements when developing new FSW machines. These loads depend greatly on the type of material and thickness of the workpieces. The most relevant loads acting on a machine during the FSW process are the axial force (F_Z), the traverse force (F_X), the side force (F_Y), and the torque (M_Z) (Table 2.4).

Table 2.4: Relevant loads for the FSW process.

Axial force (F_Z)	Axial force is one of the main process parameters. It is responsible for the friction between the FSW tool and the workpieces. Furthermore, axial force is responsible for applying forging pressure which is vital to obtain good weld formation;
Traverse force (F_X)	Traverse force is responsible for supporting material resistance to the tool movement along the joint line;
Side force (F_Y)	The side force arises due to the asymmetry of the FSW process, caused by the direction of tool rotation. The advancing side of the weld is warmer than the retreating side of the weld, consequently, the material on the advancing side is softer and less resistant. This force has the direction from the retreating side to the advancing side of the weld;
Torque (M_Z)	Torque is also responsible for friction between the FSW tool and the workpieces.

Stiffness and accuracy capability

The stiffness is a major concern when designing a FSW equipment, since it must withstands loads without undergoing plastic deformation or deflection and minimize the vibrations. If a machine does not have enough stiffness it vibrates causing the deviation of the tool from the desired welding path, strongly affecting the weld quality.

Sensing capability

The precise process control is always a requirement in an industrial machine. Nowadays it's easier the implementation in the control system of the equipment several sensors in order to allow process self-adaptation. The data provided from sensors is used as feedback to the control system. This provides a high potential for the process automation.

Flexibility capability

The number of axis (degrees of freedom - DOF) that a machine possesses establishes its flexibility and determines the type of weld path that can be performed. A one-dimensional (1D) welding path is the least complex, and requires the least machine flexibility (only two axes are required). A 2D welding path requires more flexibility, not only to move the FSW tool through the two directions but also to maintain work and travel angles. A 3D welding path is the most demanding in flexibility, and the machine must have at least five axes.

Types of machines and their control systems [13, 14]

During the early developments of FSW non-dedicated CNC machines were used to perform the welds. However, the high loads involved in FSW process require the usage of large dimension CNC machines, which can be a technical drawback. Another drawback of using this kind of machine is the absence of force sensors and data acquisition devices that could be used for process monitoring and control. Due to these limitations, custom built machines for the specific use of FSW emerged. These machines looked similar to milling machines, but with a large amount and diversity of sensors for process monitoring and control beyond the traditional position control. Nowadays efforts are being made in order to use industrial robots to perform FSW welds [15]. This would allow the manufacturing of non-traditional joint designs.

As mentioned there are three major groups of machines used in FSW:

- Conventional machine such as milling or CNC machines;
- Dedicated FSW machines;
- Industrial robots

Table 2.5 shows the features of each type of machine.

There are three main types of machine control, the position (or motion) control, the force control and the hybrid control that are the most used despite the existence of other like the temperature and torque control for example.

The position control is advantageous in very rigid and structurally sound FSW machines. These machines can withstand large process loads and prevent tool deflection. The high rigidity allows the positioning of the welding tool to be controlled very accurately during the welding process. This kind of control demands a proper support and clamping of the workpiece in order to promote rigidity and positional consistency. The workpieces must be dimensionally consistent as well. If these requirements are not achieved the position controlled machines produce welds with reduced quality.

Table 2.5: FSW equipment features. [14]

Characteristics	**Equipment**			
	Milling machine	*FSW machine*	*Parallel robot*	*Articulated robot*
Flexibility	low	low/medium	high	high
Cost	medium	high	high	low
Stiffness	high	high	high	low
Work volume	medium	medium	low	high
Setup time	low	high	medium	medium
Number of programming options	low	medium	high	high
Capacity to produce complex welds	low	medium	high	high
Control type	motion	motion/force	motion	motion

Force control has some advantages when there are circumstances like the following ones: parts dimensionally inconsistent, part position varies, or the machine is not rigid enough to sustain the loads. However the main advantage is the response capability to the changes in the workpiece due to the heat input. Several studies have shown that to successfully weld lap joints, force control must be used due to the inconsistencies in part setup at the faying surface. Force control will ensure that the parts are squeezed together properly in the welding environment. The force control, normally, controls the downward axial force. This force can be controlled by adjusting the vertical position, the traverse speed, or the rotation rate of the tool. One drawback of the force control is the tendency to become unstable, which can result in welding flaws.

An attractive alternative to force control is welding binary control. This method consists on maintaining a constant welding torque during the welding operation. This control architecture has the benefits of simplicity and lower cost.

2.1.3.3 Welding parameters

In the friction stir welding process the main welding parameters are the tool rotation speed [v - RPM], the direction could be in clockwise or counter-clockwise, and the tool traverse (linear) speed [n -mm/min]. There are other important parameters like the applied axial force, the plunge depth of the pin, etc. The rotation movement of the tool leads to a stirring and mixing of the soften material around the pin, and the translation movement of the tool moves the stirred material from the leading edge of the pin to the back of it, where the material cools and solidifies. [2] A variation of the rotation speed, like an increase, conducts to a higher temperature (more friction between the shoulder and workpiece) which results in an intensification of the stirring and mixing of the material.

However Mishra and Ma [2] affirms that coupling of tool surface with workpiece is the mechanism that govern the heat input and a monotonic increase in heating with increasing tool rotation speed is not expected as the coefficient of friction at interface changes with increasing tool rotation speed.

The high complexity of this process is demonstrated when regarding for example the fact that when increasing tool rotation the friction stir zone will decrease instead of increasing. The same occurs with the deformation zone, it will not continuously increase with ever increasing tool rotation speed. This happens because that increasing rotation speed increases processing temperature to the point where workpiece material in the direct vicinity of the joining tool significantly loses flow strength. [8]

Another important parameter is the tool angle respect to the workpiece surface. A smooth tilt of the pin towards the trailing direction guarantee that the shoulder holds the stirred material (by the pin) and move the material efficiently from the front to the back of the pin. The development of "scrolled" tool shoulder allows good quality FSW welds with 0° tool tilt. [2]

Another process parameter is the depth of pin insertion into the workpiece. This depth is associated with the pin height (tool design). There are two extreme scenarios: the excess plunging and the lack of it. When the insertion depth is too "superficial", the shoulder of tool doesn't contact the workpiece surface which restrain the efficiency of movement of the stirred material from the front to the back of the pin. The common defects associated with this issue is the appearance of inner channel or surface groove in the weld. When the insertion depth is too deep, the shoulder of tool plunges into the workpiece creating excessive flash. In this case, a significantly concave weld is produced, leading to local thinning of the welded plates. [2]

There are other parameters that can be important like the usage of heating or cooling sources.

2.1.4 Joint properties

In this Subsection a review of joint properties will be done with special focus on aluminium alloys, primarily, on the AA 6082 alloy or similar ones (6XXX series).

2.1.4.1 Metal flow

The metal flow is a complex mechanism that correlates with joints mechanical properties making it important to study. Simulation, nowadays, is a tool that allows engineers to quickly know if the path taken is the right one. Mishra *et al.* [2] compiled several conclusions that can be found about the metal flow in the literature review. The trends found in the literature are:

- There are no symmetry towards the weld center line;
- The final position of the stirred material, as expected, is a position behind the original one, only a small amount of the material is in front of the original position and this happens only in the advancing side (Figure 2.1);
- The final position of the stirred material is in a equivalent volume to the pin situated behind it;

- On a macroscopic level there is a clear interface between the advancing and the retreating side, and there are no visible signs of significant stirring between them;
- Depending of the direction of the screw in the pin, on the advancing side the material is pushed downward and on the retreating side it's the opposite or *vice-versa*;
- The material movement in friction stir welding can be divided in two processes. The first one, the material on the advancing side in front of a weld enters into a zone that rotates and advances simultaneously with the pin. There are a high deformation of the material and arc shaped features are formed behind the pin. In the second one, material on the retreating front side of the pin is extruded between the rotational zone and the parent metal and in the wake of the weld fills in between material sloughed off from the rotational zone;

Some authors point out that FSW is a process locally similar to the extrusion process.

2.1.4.2 Temperature distribution

The temperature distribution through the workpiece influences the microstructure, like the grain size or dissolution of precipitates, which affects the mechanical properties of the weld zone. In aluminium alloys, the range of the maximum temperature achieved in the workpiece is between 400 °C and 480 °C [16, 17], being always the fusion temperature of the workpiece.

Tang et al. [16] conducted a study on aluminium alloy AA 6061-T6 plates with a thickness of 6.4mm. The plates were instrumented with thermocouples at different distances from the weld center and with three different levels of depth (1.59, 3.18, 4.76 mm). The result of this experiment tries to assess the temperature distribution along the width and thickness of the aluminium plate. Figure 2.6 reveals three important points. As expected, the maximum peak temperature was recorded near the centerline and with the increase in distance to the center the temperature decreases. There is a isothermal region with a width around the 4mm. Lastly, Figure 2.6 shows that the peak temperature variation along the plate thickness is very smooth and reduced. This indicates that the temperature distribution within the stirred zone can be considered as a uniform one [16].

The same author conducted another experience [16] in order to investigate the effect of weld pressure and tool rotation speed on the temperature field on the weld zone. Figure 2.7 shows the temperature field vs. the rotation speed. It was concluded that the increasing tool rotation speed and the weld pressure resulted in an increase in the weld temperature.

Figure 2.8 shows the effect of shoulder in the temperature field. In the study were used two tools with and without pin. As mentioned in 2.1.3.1, the shoulder dominated the heat generation during FSW. The larger area of the shoulder and the higher linear velocity than the pin (because of a smaller radius) are the main responsible for the greater input.

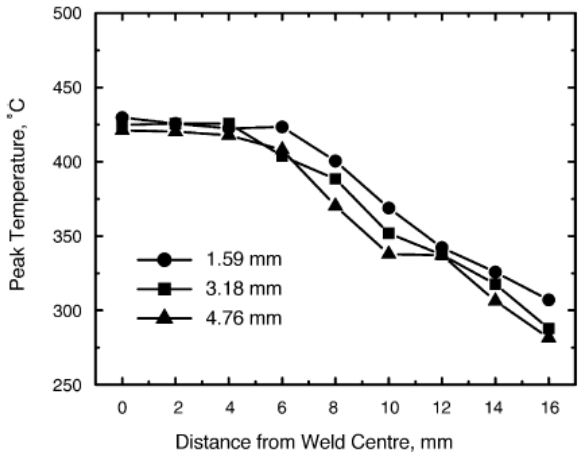

Figure 2.6: Effect of depth on peak temperature as a function of distance from weld centerline for a FSW weld made at 400 RPM and 120 mm/min traverse speed [16].

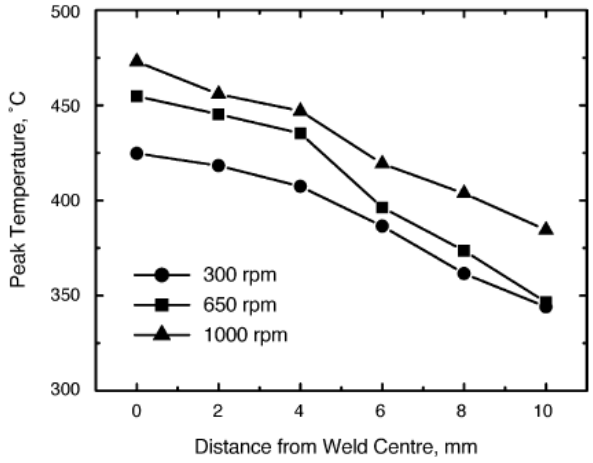

Figure 2.7: Effect of tool rotation speed on peak temperature as a function of distance from weld centerline for a 6061Al-T6 FSW weld made at 120 mm/min traverse speed [16].

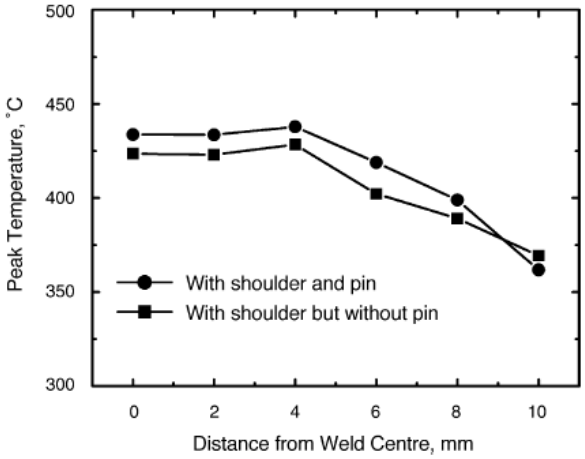

Figure 2.8: Variation of peak temperature with distance from weld centerline for a 6061Al-T6 FSW weld made with and without pin (400 RPM and 120 mm/min traverse speed) [16].

2.1.4.3 Microstructure

As seen before in 2.1.2 there are three major zones that present significantly different microstructure (the BM, HAZ, TMAZ and nugget). These differences are strongly correlated with the temperature distribution (seen in 2.1.4.2) during the process and, naturally, affect the mechanical properties of the joint. Figure 2.9 shows the typical microstructure of a SLJ weld.

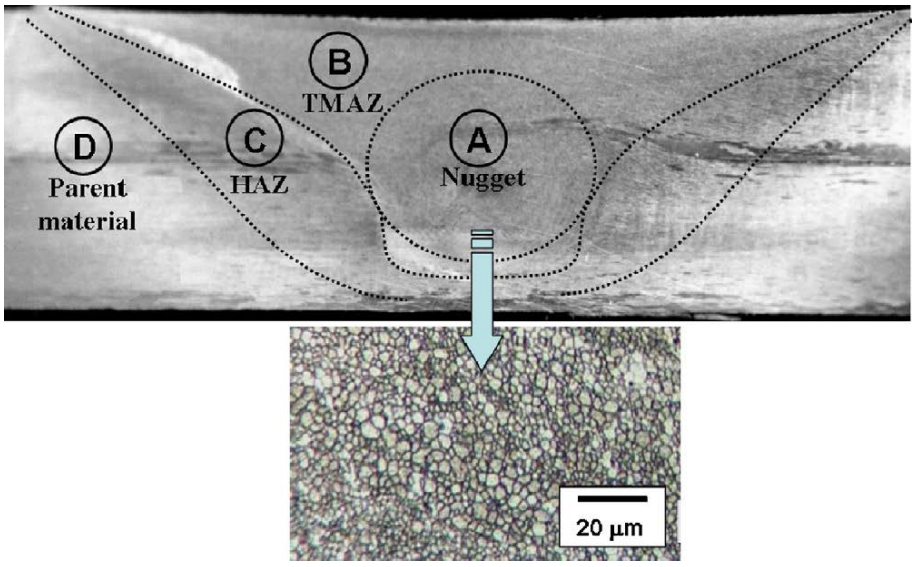

Figure 2.9: Cross-section of SLJ weld [18].

Nugget zone

In this zone (Figure 2.9 A), as mentioned in 2.1.2, occurs intense plastic deformation and frictional heating that generates a recrystallized fine-grained microstructure. Some authors concluded that the small recrystallized grains of the nugget zone contain high density of sub-boundaries, subgrains, and dislocations [2]. The interface between the nugget zone and the base material, usually, is diffuse on the retreating side of the weld and sharper on the advancing side (on right side of the Figure 2.9) [2].

Shape of nugget zone

There is a correlation between the size of the pin and the shape and size of the nugget. Normally, the nugget is slightly larger than the pin diameter, except at the bottom of the weld. Another correlation described in the literature is that as the pin diameter increases, the nugget takes a more rounded shape. [9]

Grain size, precipitate dissolution and coarsening

The typical grain size in this zone is a small one, and there are several parameters that influence that size, like the tool geometry, workpiece material, axial load, service temperature, the presence or absence of a cooling system, etc.

Some trends can be identified [2, 5, 8]:

- A decrease of $\simeq 30\%$ in the rotation/traverse speed ratio results in a decrease in the recrystallized grain size of about $\simeq 50\%$.
- An higher ratio of tool rotation speed/traverse speed results in an increase in both degree of deformation and peak temperature of thermal cycle. This increase in the degree of deformation leads to a reduction in the recrystallized grain size.
- An increase in peak temperature of the process thermal cycle results in a generation of coarse recrystallized grains and in grain growth.

The peak temperatures involved in the FSW process easily leads, in aluminium alloys, to phenomena like the coarsening of precipitates or dissolution in the aluminium matrix.

Some academics reported that, normally, the homogeneously distributed precipitates are smaller in the workpiece than in the nugget zone. However, there are fewer large precipitates in the nugget zone than in the base material. There are reports that shows a coexistence of this two phenomena at same time in FSW process. Studies on AA 6013 reported complete dissolution of the precipitates on the matrix in nugget zone [2].

Heinz and Skrotzki [19] studied an aluminium alloy AA 6013 and found that the nugget is softer than the BM.

HAZ

As said before in Sub-Section 2.1.2, the heat-affected zone (HAZ) experiences a thermal cycle that doesn't produce any visible plastic deformation. It is reported that the HAZ retains the same grain structure as the base metal. The main difference is that the thermal cycle exerts an effect on the precipitate structure. Coarsening of the precipitates occurs (an overaged condition is established) and the precipitate-free zone (PFZ) increases in size by a factor close to 5. This type of structure leads to minimum hardness values found in this zone. [19]

TMAZ

The thermo-mechanically affected zone (TMAZ) is a transition zone between the base metal and the nugget. The TMAZ is characterized by a highly deformed structure. Generally the base material grains is deformed in an upward flowing pattern around the nugget (Figure 2.10).

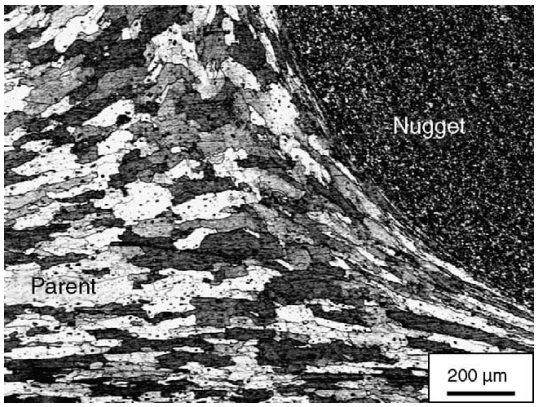

Figure 2.10: Typical microstructure of thermo-mechanically affected zone. [2]

Recrystallization is uncommon in this zone due to insufficient deformation strain. Dissolution of some precipitates occur in TMAZ due to high-temperature exposure during the process. [2, 8, 9]

2.1.4.4 Hook defect - SLJ

In single lap joint configuration, FSW produces a common defect that has negative effect on the mechanical properties. This defect appears on the advancing side of the weld [20]. The presence of a "hook" is a factor of stress concentration that reduces the fatigue life and deteriorates the strength of the joint. The "hook" defect causes a net reduction of the sheet thickness. This reduction is measured by the effective sheet thickness (EST) that can be defined as the residual thickness of the loaded sheet in correspondence to the hook or other unwelded region (there is another void in the retreating side) [4]. In other words EST is the minimum sheet thickness determined by measuring the smallest distance between any unwelded interface and the top of the top sheet [5]. The hook defect can be seen in Figure 2.11

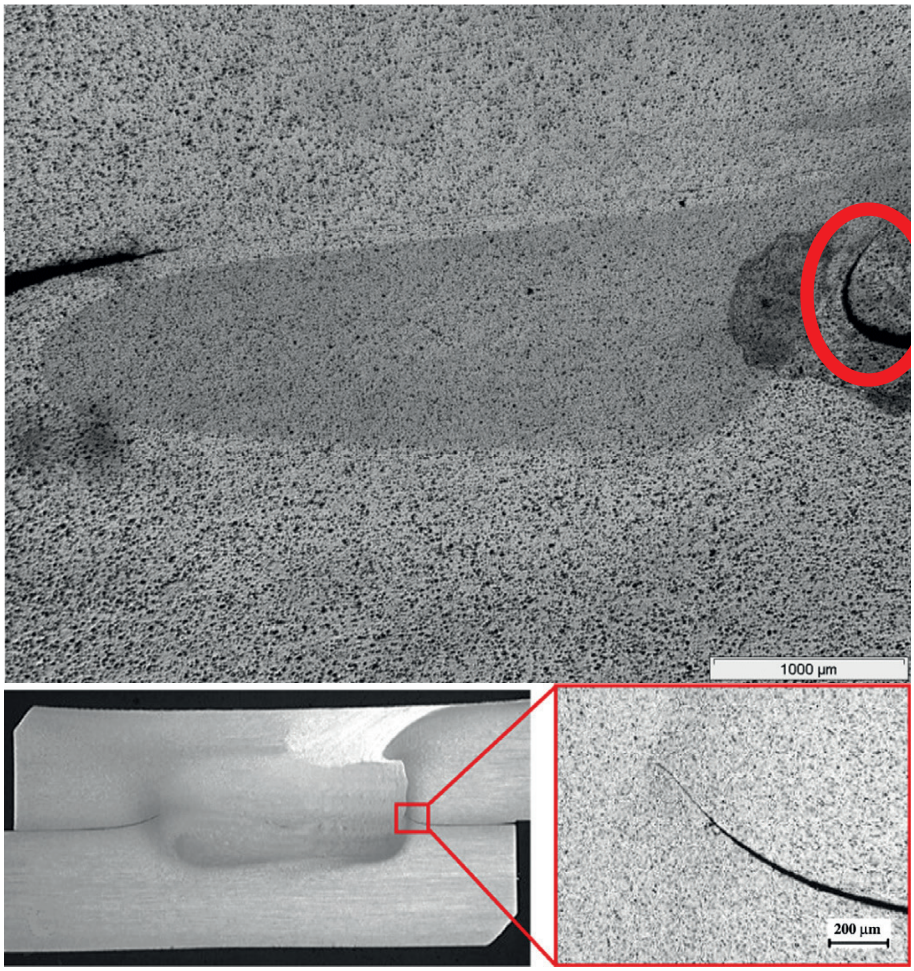

Figure 2.11: Hook defect on FSW SL joints [4, 21] (Edited images)

The hook length depends on the pin design and welding parameters. According to the measures done previously by our workteam [22], in single lap joint with plate thickness of 2 mm, and

an overlap of 60mm, from AA 6082-T6 plates and using a threaded cylindrical pin (5 mm) the hook length presented a significant scatter as seen in Table 2.6.

Table 2.6: FSW hook length. [22]

N^o of Passes [−]	**Rotation Speed** [RPM]	**Welding Speed** [mm/min]	**Pin Plunging** [mm]	**Load** [kgf]	**Hook Length** [μm]
Single	1000	200	2.8	400	1292.7
Single	1000	200	2.8	450	508.3
Double	1000	200	2.8	400/320	630.8/673.1
Double	1000	200	2.8	450/400	935.8/914.6

2.1.4.5 Mechanical properties

Residual Stresses

Residual stresses exist in most manufactured parts and are in equilibrium within a part, without any external load. The FSW process despite the lower thermal input compared with the traditional welding process, presents significant values of residual stresses. However, lower than fusion welding processes, the presence of the residual stresses is due to the rigid clamping system used [23]. The clamping system exerts an higher restraint on the welded plates, that counteracts the contraction of the heated nugget and HAZ during the cooling cycle. The residual stresses are found in longitudinal and traverse directions. The elevated levels of tensile residual stresses have a negative effect in the fatigue life of the welds. [2, 8]

Some studies about friction stir welded aluminium alloys concluded that [24–26]:

- The low residual stress, compared with fusion welding, is attributed to the lower heat input during FSW and recrystallization mechanisms that allows the accommodation of stresses;
- Longitudinal residual stresses are, generally, higher than the transverse ones and don't depend on pin diameter, tool rotation rate or traverse speed;
- The residual stress distribution across the welds are identical at the top and root side of the weld;
- The weld zone presents residual tensile stress in both directions;
- The peak longitudinal stresses increase as the traverse speed increases;
- Transverse residual stresses don't present dependence on the traverse speed;
- There is a slightly asymmetry in longitudinal residual stress profile within the nugget, being $\approx$10% higher on the advancing side;
- Maximum residual stresses were below 100 MPa as noted by several authors.

Hardness

The hardness across the weld isn't constant, as expected. On precipitation hardenable aluminium alloys, like the AA 6082-T6 studied in this Master thesis, the effect of the FSW weld is

the softening of the regions around the weld center. The softening is caused by coarsening and dissolution of strengthening precipitates during the thermal cycle of the FSW.

This differences are justified by the events that occur during the thermal cycle, like the re-crystallization mechanisms and the coarsening and dissolution of strengthening precipitates. In the literature it is reported that the hardness profile is strongly affected by precipitate distribution rather than grain size in the weld [2, 27].

Sato et al. [27] studied the loss of hardness in the AA 6063-T5 and produced the Figure 2.12 that show the hardness curve across the weld of FSW which resembles other precipitation hardenable aluminium alloy.

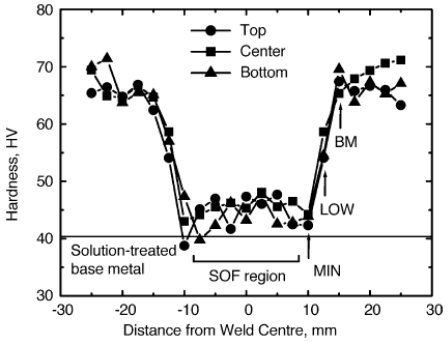

Figure 2.12: Typical hardness curve across the weld of FSW 6063Al-T5 [27].

In AA 6082-T6 the exposure to temperatures above $\approx 200\,^{\circ}C$ leads to an instability and dissolution of the strengthening precipitate β'' (Mg_5Si_6) resulting in zones with decreased hardness and mechanical properties.

Strength and ductility

In the literature there are several studies regarding FSW butt joints. This configuration presents relatively small losses in strength and ductility, as seen in Table 2.7.

Table 2.7: Longitudinal tensile properties of weld nugget in friction stir welded AA 7075-T651 on butt configuration[28]

Condition	**UTS (MPa)**	**YS (MPa)**	**Elongation (%)**
Base metal	622	571	14.5
Post-FSW	525	365	15

In FSW single lap joints this behaviour is not observed. Even the positioning of the lap joint has effects on mechanical properties. Buffa et al. [18] studied the effect of the geometrical configuration of the SLJ on mechanical properties. In single lap joints produced by FSW there are four different geometrical configurations (combination of the mutual position of the plates and of the tool rotation direction) that could be grouped in only two taking in account the plane of symmetry of the joint (Figure 2.13). In order to find which configuration performs best SL shear test was performed on the specimens produced by three different tools (T1, T2, T3) and in the two configurations A and B. [18]

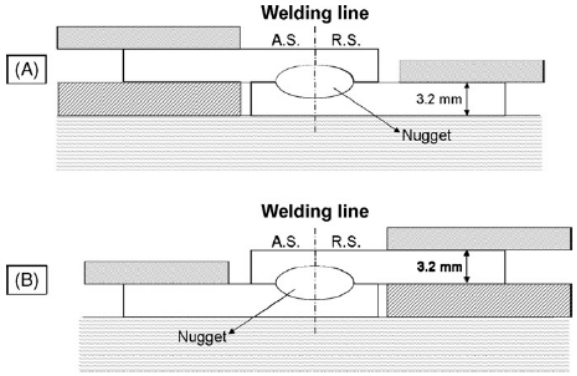

Figure 2.13: Sketches of the possible lap joint configurations (A and B). [18]

In this kind of test it's important to balance the axes offset of the lap members in order to minimize the bending effects. Generally this is overcomed with the use of little tabs (two packing pieces) with the same thickness as the sheet (Figure 2.14). In the Figure 2.14 is possible to see the theoretical stress distribution on SLJ shear test. [7]

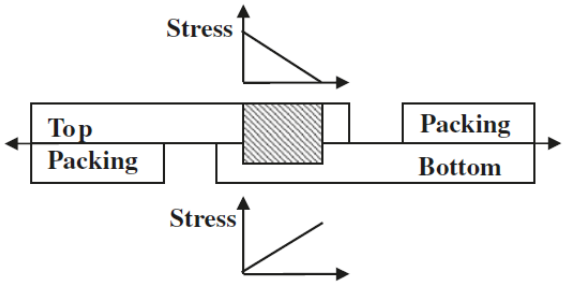

Figure 2.14: Tensile stress distribution in an ideal tension–shear specimen. [7]

The results of these joint tensile tests are presented in Figure 2.15.

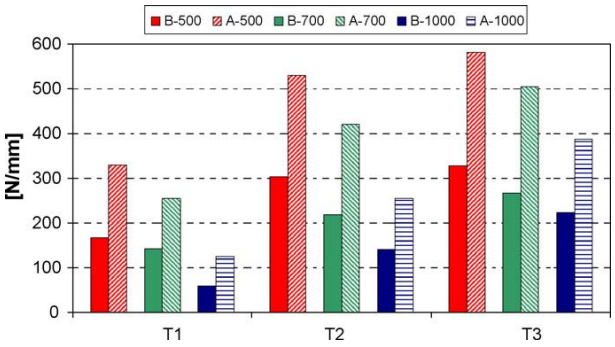

Figure 2.15: Shear tests results, expressed as maximum failure load/mm of welding, at the varying of the tool (T1, T2 and T3) and of the configuration (**A** or **B**) [18].

It's quite visible that in every case scenario studied by Buffa et al. [18] the configuration **A** presents better mechanical performances. In some cases the resistance to the shear tensile test

was $\approx$ 100% superior over the **B** configuration. In order to identify the roots of the performance difference macro analyses of the transverse section of the joints were done. Figure 2.16 shows the sections for the configurations **A** and **B**.

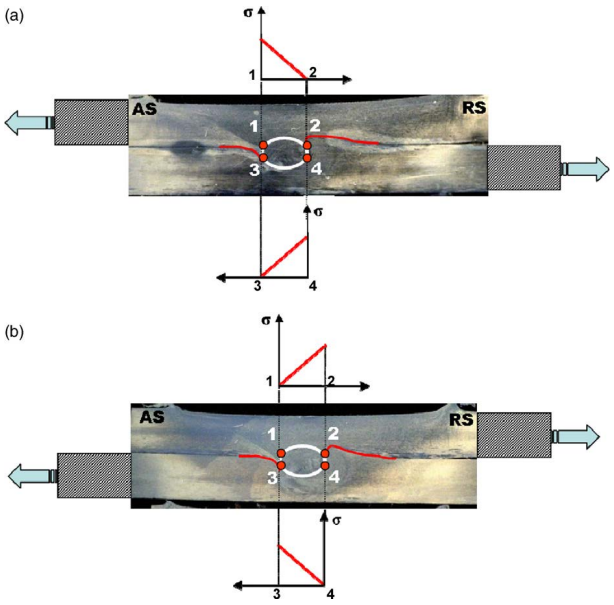

Figure 2.16: Hooking effect and sketch of stresses generated during shear tests: (a) configuration **A** and (b) configuration **B**. [18].

The two common material flows are highlighted (red lines) on Figure 2.16. The interface area between the two plates after the FSW process isn't completely horizontal which causes the appearance of the interface (separation) lines on the two sides of the joints (the hook effect). [18] The two interface lines are present in the two configurations with the same geometry. In the advancing side the hook curves downwards towards the bottom plate. In the retreating side the interface line moves upwards.

The differences in performance between the two configurations can be explained with the help of the four remarkable points indicated in Figure 2.16 and the theoretical stress distribution. The four points are contained in the border of the joined area and points 1 and 2 belong to the top sheet, the points 3 and 4 belong to the bottom sheet.

Configuration **A** has the maximum level of stress in the proximity of points 1 and 4. In fact Buffa et al. [18] said *"the reduction in thickness of the welded blanks due to the hooking effect of the interface lines occurs far away from the section of the blanks were the maximum level of stress is reached, in particular in the opposite side of the joint"*. Obviously, in configuration **B** the opposite situation occurs. The maximum shear stress level is close to points 2 and 3, where there is a lower EST due to the near hook defect. The best way to obtain the maximum properties of the SLJ is to always load the advancing side on the top sheet (configuration **A**). This is critical on single pass because in the case of double pass welding the critical side can be eliminated by switching over advancing and retreating sides in the subsequent weld run.[18, 29]

Additionally Buffa et al. [18] found that a change in the clamping system lead to better mechanical performance. The authors proposed a system where the plates to be joined are completely blocked, as seen in Figure 2.17.

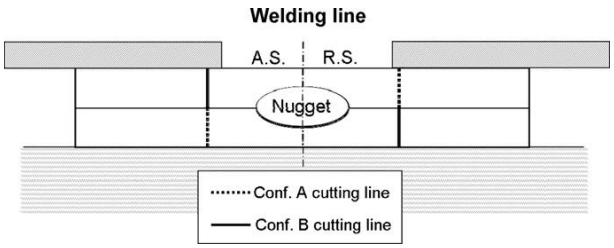

Figure 2.17: Fully blocked blanks in the configurations **A** and **B** [18].

Some authors found that on the basis of static strength, the FSW SLJ performance is comparable with resistance spot welding and riveting. The shear tensile strength of SLJ produced by FSW joints is 2.4 times greater than of single row riveted joints. [29]

Usually the stress values are presented in remote stress that can be obtained by

$$\sigma_{remote} = \frac{forcetransmitted}{remotearea}$$

The results expressed in remote stress allows the direct comparison across studies. [30]

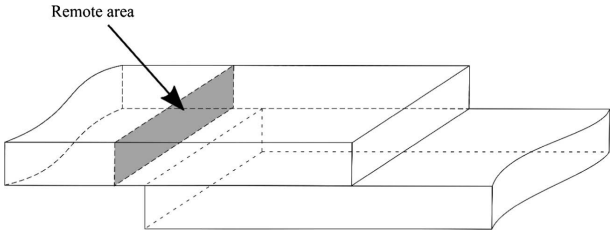

Figure 2.18: Concept of remote area. [30]

2.1.4.6 Fatigue life

The single lap joint configuration is useful in applications like aeronautical fuselages because it's easier to manage tolerances. The studies on fatigue behaviour of this kind of joint is reduced compared with studies regarding the butt joint configuration. However, there is some work done in this field [4, 20, 21, 29–33].

As seen before, the SLJ configuration has it's own particularities and, as expected, the fatigue performance is lower compared with the butt configuration.

The fatigue characterization of SLJ is a complex study as there is a combination of shear and bending on the joint. Any loads applied to the ends of the overlap results in eccentric loads in the joint area and this can lead to rotation (secondary bending). [29]

On SLJ fatigue behaviour, one of the main factors is the shape of the interface lines as they act like a stress concentration factor and in it's nature they are a crack (void). As seen before, the

EST on retreating side of the weld is, generally, reduced making it more liable to fracture. In the advancing side there is the hook defect that has a bigger impact in the fatigue life of SLJ produced by friction stir welding.

Ericsson et al. [29] had conducted a study on the fatigue behaviour of AA 6082-T6 FSW joint and concluded that:

- The joint efficiency in relation to static strength of the base metal (AA 6082-T6) was about 55%. The butt joint of the same material has an efficiency of ≈80%;
- Double pass FSW increases the joint efficiency of SLJ;
- The maximum fatigue stress at 10^5 cycles was about 20 to 30% of the static strength. In case of butt welds this value is around 90%;
- Fracture is initiated in the highly stressed area where the weld cuts through the interface between the sheets.

The values obtained by Ericsson et al. [29] are in consonance with the literature available that gives a range of efficiency that floats between 40 to 65% (for most of the cases and with single pass).

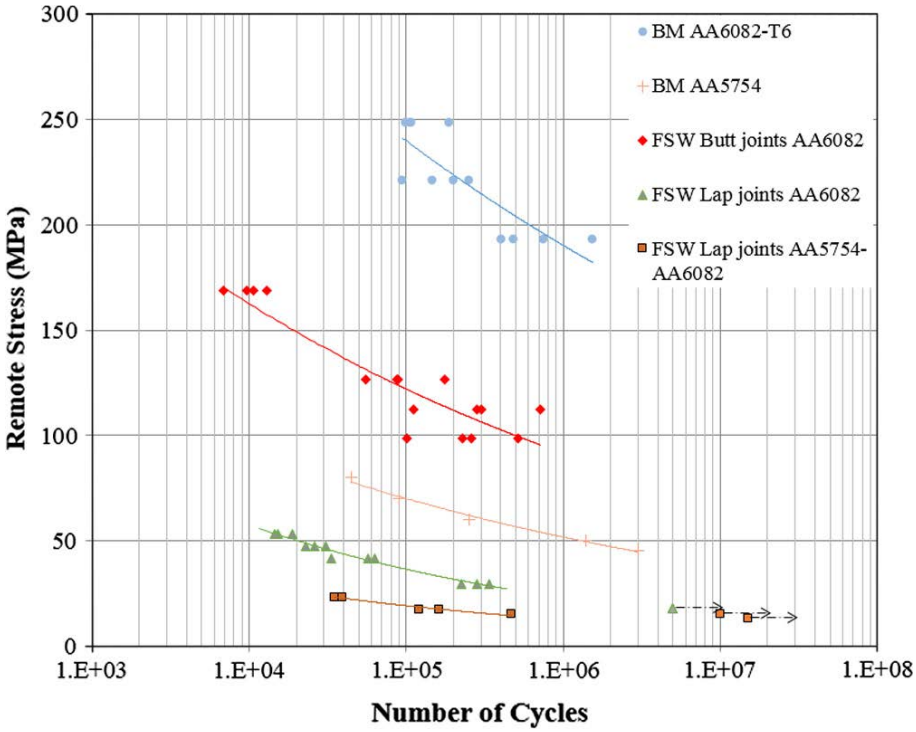

Figure 2.19: S–N curves at R = 0.1 for lap joints tested along with base material, AA 6082 butt joints.[30]

Infante et al. [30] studied SLJ produced by FSW made of AA 6082-T6 with a overlap of 60mm. Figure 2.19 shows the S-N curves for AA 6082-T6 produced by FSW on butt and SLJ configurations compared with base material. It is visible that there is a great degradation of the fatigue performance with SLJ configuration. At 2×10^6 cycles there is a reduction in the fatigue

strength compared to the base material of ≈ 88% and ≈ 78% compared to the butt configuration, as can be verified in Table 2.8.

Table 2.8: Fatigue strength of AA 6082-T6. [30]

Condition	**Fatigue strength at 2×10^6 cycles (MPa)**
BM - AA 6082-T6	177
FSW butt joint	90
FSW SLJ	20

2.1.5 Applications

Since the development of the FSW process a great future to this technology was predicted. An increasing interest in this manufacturing process trough the years can be observed when we analyse the patent licenses sold by TWI from 1995 to 2009 (Figure 2.20). Since the legal protection of the patent has expired in January 2015 it's expected an significant increase in the usage of this technology.

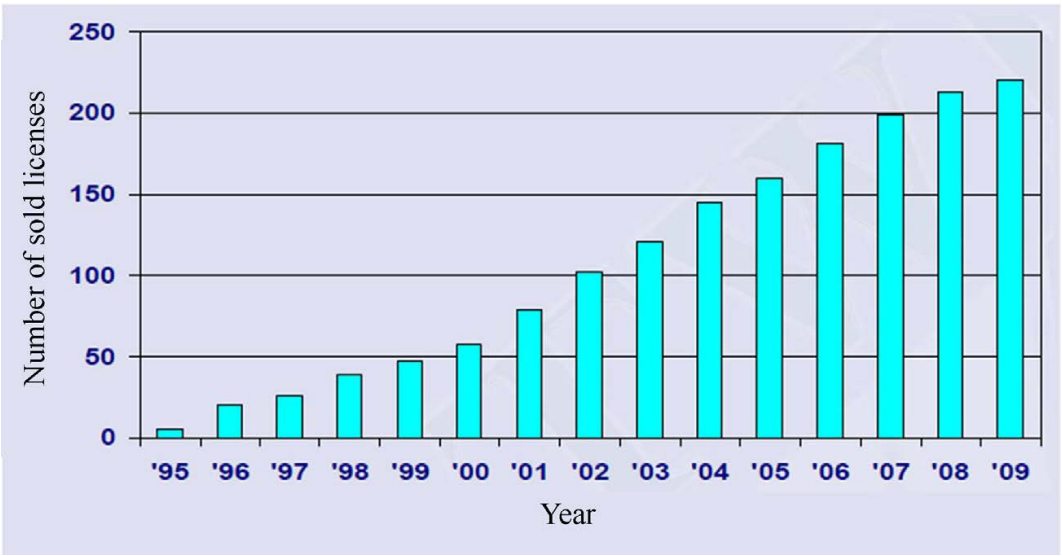

Figure 2.20: Number of FSW licences sold between years 1995 and 2009. [12]

The main industries that are currently using this joining method are the transportation industries. The key features of joining dissimilar materials and high mechanical performance of these joints is leading car manufactures to search a suitable way of applying FSW on automotive mass production.

In 2013, Honda Motor Co., Ltd gave a major step in order to spread the use o FSW in car manufacturing. They managed to use a standard off-the-shelf multi-joint robot to maneuver a FSW tool to realize welding of a complicatedly shaped sub-frame (on an Accord model) in contrast with conventional heavy duty FSW machines with limited degrees of freedom. [15] This is a major

achievement. The average axial force involved in the process is about 10 *kN*. The tool developed is shown in Figure 2.21.

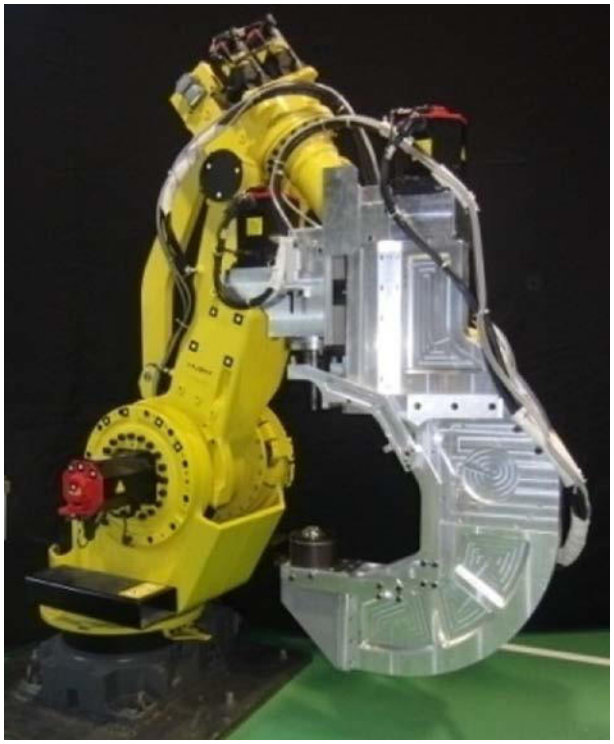

Figure 2.21: Fanuc M-700 with C-type FSW gun developed by Honda Motor Co., Ltd. [15]

The development of this tool allowed Honda to join a steel/aluminium sub-frame with a weight saving of 25% (6 kg) regarding the previous model with aluminium and steel joined through bolts. The authors reported also that the usage of the FSW allowed to change the structure of the sub-frame changing location of the mounting point for the suspension. This change resulted in an increase of rigidity of the mounting point by 20%, improving the dynamic performance of the new car. [15]

Being the sub-frame an important structural part of the car there is the need to assure zero defects that could compromise the passenger's safety. In order to assure the quality Honda Motor Co., Ltd. also developed a robotised non-destructive inspection system.

These developments made proves that FSW has an enormous growing potential in all industries that demand strong joints and dissimilar welds.

There are several other actual and potential applications for FSW technology. The aeronautical, aerospace, railway, shipbuilding, heat and piping, electrical and construction industries are making use of FSW and will continue to do so in the future. The possibility to join plastics is another advantage of the FSW that can open the door to the firm implementation of the technology. [34–37]

2.2 Adhesive bonding

2.2.1 Introduction

The use of adhesives remounts to the human past. At that time the adhesives used where natural and were not used in structural applications. This kind of adhesives are used nowadays in our daily life for example, the duck tape or post-it® present in our desks. An industrial application of non-structural adhesives is the "glued" symbols and letters on vehicles (Figure 2.22).

Figure 2.22: Different applications of non-structural adhesives.

This kind of non-structural adhesive has an enormous utility, however they are weak to bond a reinforcement panel in a vehicle. In order to sustain these loads there are adhesives known as structural adhesives. The scope of this Master thesis is in these type of adhesives.

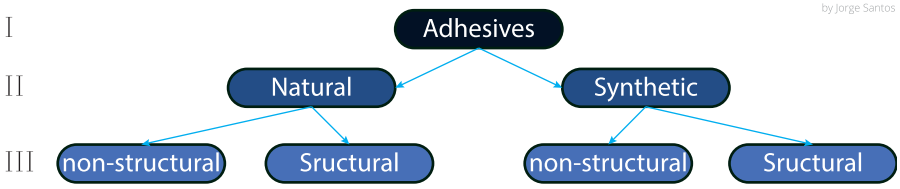

Figure 2.23: Different classifications of adhesives.

What is an adhesive? Well, there are several definitions that fit the concept of adhesive. According to A. J. Kinloch and Hall [38] an adhesive may be defined as a material that when applied to surfaces of materials can join them together and resist separation. da Silva et al. [39] defines structural adhesive like an adhesive that can resist to substantial loads and that is responsible for the strength and stiffness of the structure. In this kind of adhesive the shear strength is greater than 5 MPa depending on the nature of the adhesive. It's easy to find examples of applications for this type of adhesive. The automotive industry is one of the main users of structural adhesives and they are used to bond reinforcements and structural parts to the car body (Figure 2.24).

In order to apply an adhesive it is needed at least two substrates (or adherends) to join/bond. The role of the adhesive is to bind the substrates and that happens by adhesion phenomena [39]. Adhesion can be defined as the attraction between two substances resulting from intermolecular forces [39]. In the case of adhesive bonding the two substances in use are the adhesive and the adherend. The last one can be made of almost everything (from metal to plastic or composites, etc.), being that one of the main advantages of bonding. It's important to distinguish two concepts

Figure 2.24: Example of structural adhesives on automotive industry. [40]

that are the adhesion and the cohesion. The latter one only involves intermolecular forces inside one substance [39]. The slim zone between the adhesive and the adherend is called interphase. There is the need to distinguish this particular zone because it presents chemical and physical properties different from the bulk adhesive or adherend. The nature of the interphase is a critical factor in the determination of the mechanical properties of the adhesive bond. Another concept is the interface. It is the plane of contact between the two materials (adherend and adhesive) and it's within the interphase. [39]

There are several advantages in the use o adhesive joints such as [39, 41, 42]:

- Reducing the weight and cost (comparing to riveted joints);
- Possibility of full automation of the process resulting in lower lead times;
- Uniform stress distribution along the bonded area (Figure 2.26);
- Present higher stiffness and load transmission, compared to riveted joints;
- Minimizes or prevents galvanic corrosion between dissimilar metals;
- Joins all shapes and thicknesses;
- Seals joints;
- Joins any combination of similar or dissimilar materials (alternative to FSW);
- Can be faster and cheaper than mechanical fastening;
- Provides attractive strength-to-weight ratio;
- Damps vibration and absorbs shock;
- Higher fatigue resistance compared to welding (FSW included) and riveted joints.

However, there are some drawbacks associated with this kind of technology that makes possible the research in order to overcome the current disadvantages. Some drawbacks are listed below [39, 41]:

- It demands carefully cleaned surfaces;
- In some cases additional pre-treatments of physical an chemical nature is needed;
- Heat and pressure may be required;
- Jigs and fixtures may be needed;
- Rigid process control usually necessary;

- Useful life depends on environment;
- Low resistance to temperature and humidity conditions;
- Environmental, health, and safety considerations are necessary;
- Special training sometimes required;
- Difficult quality control without using destructive methods;
- Poor joint strength when under peeling and cleavage stresses (they concentrate the load in a small area);
- Difficulties in disassembly operations.

2.2.2 Types of failure, types of stresses and typical joint configurations

In adhesive joints there are three major types of failure, the adhesive, the cohesive failure and a combination of both (mixed).

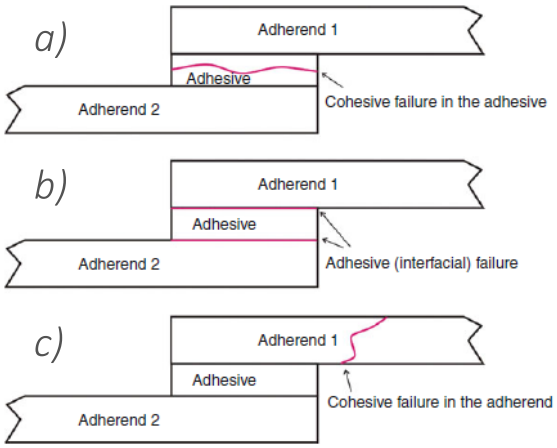

Figure 2.25: Types of failure on adhesive joints. [39] (edited)

The first one (Figure 2.25 *b)*) happens because of the lack of adhesion between the adhesive and the adherend. The wetability and wetting concepts are related to this kind of failure. It occurs in the interface of the joint. [39, 41] There are factors that could lead to an adhesive failure, like the inadequate or ineffective surface preparation. However, there are some cases that with a specific combinations of adhesive and adherent is impossible to obtain another failure besides the adhesive one. This is not, *a priori*, a red flag because if the values of strength and ductility of the joint are satisfactory there is no need to change anything. With this kind of failure we can infer that the cohesive strength is higher than the interfacial strength [41].

The cohesive failure can occur on the adhesive (Figure 2.25 *a)*) or on the adherend (Figure 2.25 *c)*). This failure is due to the reaching of the maximum strength on one of the materials. We can infer that the interfacial strength is higher than the cohesive one. In this kind of failure we are getting the maximum capabilities of the adhesive or the adherend. This type of failure is sometimes considered as a preferred one [41]. However, failure mode should not be used as a sole criterion for assess a joint. Cohesive failure doesn't necessarily guarantee if the joint is practical, economical or if it will survive the expected life [41].

Table 2.9: Inferences from types of failure [41]

Failure Type	**Inference**
Adhesive failure	Cohesive strength > interfacial strength
Cohesive failure	Interfacial strength > cohesive strength
Mixed failure	Interfacial strength ≈ cohesive strength

As said before and comparing the adhesive SLJ and a riveted joint, the adhesive allows a uniform stress distribution and minimizes the stress concentration factor (because there are no holes). This is showcased in Figure 2.26. It allows improvement in the stiffness of the structure. [39]

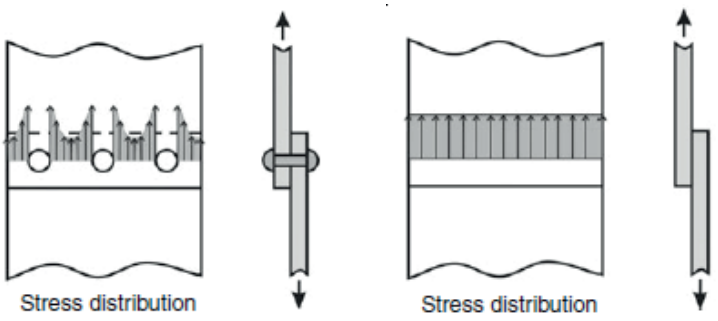

Figure 2.26: Stress distribution of adhesively bonded joints in relation to riveted joints [39] (edited)

There are multiple loading conditions that adhesive joints may undertake, the most common modes are listed below and represented in the Figure 2.27:

(a) Normal or direct stresses (it's a mode that exposes the weakness of the joint);
(b) Shear stress (preferential mode in order to maximize the joint strength);
(c) Cleavage (typically results of an offset tensile force or bending moment, undesirable);
(d) Peel stress (which appears if one or both of the substrates are flexible, undesirable).

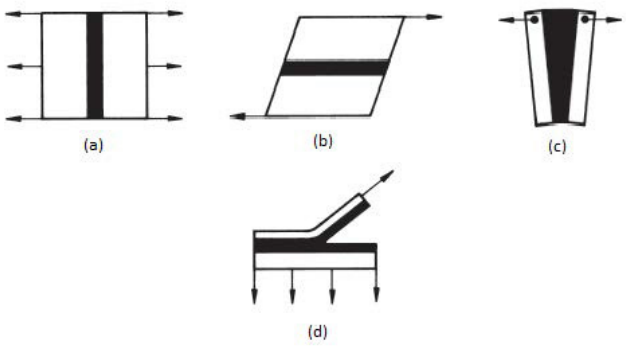

Figure 2.27: Types of stresses in adhesive joints. [43] (edited)

If possible, the joint should be designed in order to be loaded in shear mode avoiding peel and cleavage forces. However, in the majority of real applications there is a combination of several

loading conditions and the joint design is the best weapon that the engineer has. It's important to guarantee the distribution of the loads. This could be achieved by joint design features or by hybridising the joint (usage of local mechanical restraints, such as rivets, bolts, spot welds).

In terms of joint designs there are several possible configurations (Figure 2.28), however the scope of this Master thesis is the fatigue behaviour of single lap joints. In industrial applications is the most used design. The lap joint has simple and convenient geometry for evaluating adhesive joints as can be proven by its frequent use in the standard test methods. [41]

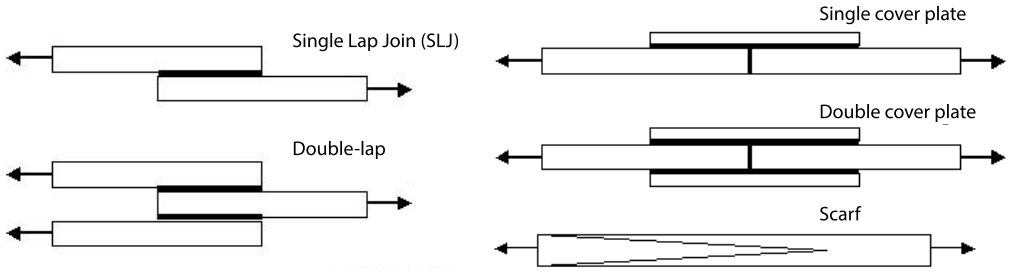

Figure 2.28: Example of different adhesive joints design.

2.2.3 Wetting

Appealing to our common sense it's easy to understand that there are differences in the behaviour of different liquids like the water or mercury. While water wets easily a glass surface, covering it all, the mercury presents a different behaviour in the latter case the liquid tucks itself up into little beads and "does not wet" the surface.

Figure 2.29: Left: mercury on glass; right: water on glass

This different behaviour is explained by the concept of contact angle, θ or in this case the "static" contact angle, θ_0 [39]. The angle θ_0 is defined by the line between the solid/liquid interface and the tangent to the liquid/air interface, as shown schematically in Figure 2.30. [39]

It is measured perpendicularly both to the solid surface and to the triple line of contact where solid, liquid, and air meet [39]. Figure 2.30 shows on left an $\theta_0 < 90^\circ$ and it's the case of a "good wetting". On the right side is represented an $\theta_0 > 90^\circ$ and this scenario is called as "poor wetting".

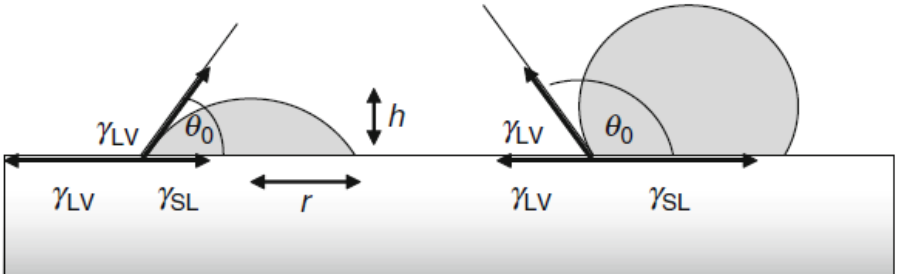

Figure 2.30: Schematic representation of low (left) and high (right) static contact angles, θ_0. Interfacial tensions are represented by arrows and termed γ_{IJ} (S = solid, L = liquid, V = vapour/surrounding fluid phase). [39]

In the extreme cases, when $\theta_0 \longrightarrow 0°$ there is a spreading of the liquid on the surface. In the other extreme when $\theta_0 \longrightarrow 180°$ there are no wetting at all. [39]

In the case of adhesives, the ability to coverage and wet solid (adherend) in contact is crucial in forming a good bond as it gives the molecules the opportunity to form adhesive interactions [39]. If the surface is rough (which is the real case), wetting tendency of an adhesive will help ensure the complete filling of the interstices. This leads to an increased true contact area and reduces stress concentrations [39].

What affects the θ_0? The nature of the material and the presence or absence of contaminations on the surface.

The mechanism that governs the wetting of a surface is the principle of minimum energy. When $\gamma_L < \gamma_S$ there is a spread of the liquid in the surface. When $\gamma_L > \gamma_S$ the opposite occurs. [43]

2.2.4 Surface preparation

As seen in Subsection 2.2.3 any kind of contamination in the surface to be bound can result in a reduction of the surface energy, this decrease the adhesion. On structural applications the surface treatment applied in any given situation depends upon the requirements and objectives of the joint, so there is no standard treatment for a specific adherend. In fact the choice of treatment is on a "fit-for-purpose" basis. [39]

There are two main purposes in the surface treatment. The first one is to promote a better adhesion between the adhesive and the adherend. The other one is to allow a better resistance to situations like the environmental ageing, corrosion, or applied loading.

A surface treatment should fulfil one or more of the following functions [39]:

- Prevent or remove any weak boundary layer on the adherend surface. A weak boundary layers could be machine oils, weak oxides or hydroxides;
- Maximize the degree of intimate molecular contact between the adhesive and the adherend. This is achieved applying a treatment that allows the creation of a high-surface free energy;
- To passivate the surface of the adherend prior to adhesive bonding. This is paramount for high-energy adherends as these are not only receptive toward the adhesive but also to all

forms of contamination. This contamination may be organic or inorganic and can influence the adherend in a number of ways, including by a reduction in its surface free energy, gross contamination, or corrosion.

There are three big types of surface treatments: the mechanical, the chemical and the degreasing treatments (Figure 2.31).

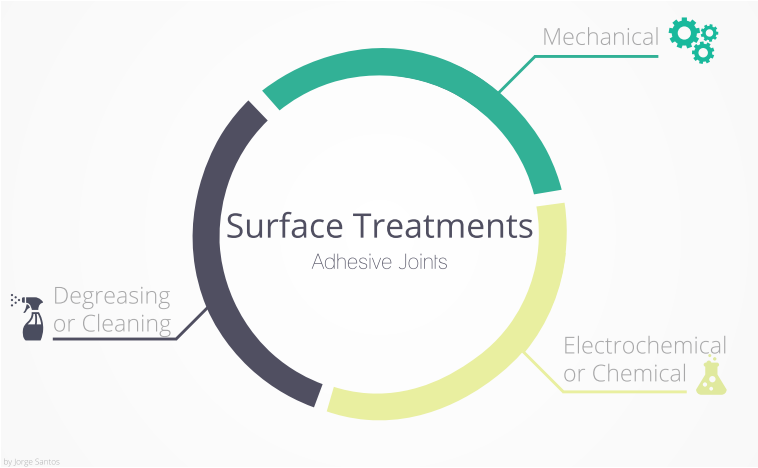

Figure 2.31: Types of surface treatment on adherends

The three major groups of surface treatments present crescent performances and in some cases are complementary.

The degreasing (or cleaning) sometimes is enough to obtain a good surface preparation. However there are occasions where it's not sufficient and a mechanical treatment like abrasion by sandpaper or the use of sandblasting machine is required, which grant better adhesion than simple cleaning. Also in the mechanical treatment the cleaning treatment is present.

When the adhesion or the resistance to environmental properties requirements are narrow, the use of chemical treatments allow better performance of the joint. In this category there are many treatments like several kinds of anodization and etchings.

As seen, the surface treatments are important to provide proper adhesion and durability to the joint. This is even more important when the adherends are made of aluminium alloys. In order to obtain a strong and stable bond between the aluminium and the adhesive it's important to remove the weak boundary layer that is naturally formed (oxide). There is the need to remove the oxide layer and replace it by a new, continuous, solid and corrosion resistant layer. [44] In order to replace that layer by another one, normally, the usage of chemical treatments is needed.

2.2.4.1 Degreasing or cleaning treatment

According to da Silva et al. [39] degreasing is the simplest possible method of achieving a clean surface and thereby increasing its surface free energy and spreading coefficient. The simplest way of degrease an adherend is to use an organic solvent and as said before this could be a single treatment our could be a stage in another type of surface treatment.

There is environmental and public health restrictions on the different types of solvents that are allowed to be used. In industrial applications, according to [39], the *"most common solvents are isopropyl alcohol, acetone, methyl ethyl ketone, perchloroethylene, trichloroethylene, or 1,1,1 trichloroethane"*.

Lately there is a trend in the usage of detergent degreasing or alkaline cleaning instead of organic solvent degreasing. There are reports of good performance achieved using aqueous-based cleaners [39].

The degreasing process could be simple like an immersion or wiping technique, or can be more complex like in the case of ultrasonic cleaning or vapour degreasing. The perfect treatment, once again, is the one that fulfils the requirements of the joint and depends on the nature of the adhesive and adherend.

2.2.4.2 Mechanical treatment

This kind of surface treatment allows the removal of the weak layer and results in a macro-rough surface. As mentioned before, mechanical treatment is combined with a simple degrease before and after the abrasion.

It's important to understand the behaviour of a liquid polymer when confronted with surface roughness or pores and there is several work done in the literature. A key conclusion of this studies is that the stresses applied to joints containing highly rough adherends present the trend of relaxing the stresses concentrated at the surfaces, transferring and distributing them more widely within the bondline, enabling more plastic energy dissipation to occur. The levels of adhesion are, consequently, higher [39]. It is reported that the presence of the surface roughness allows the stresses to dispersed into and away from the interphasial region resulting in better performance of the joint comparing with only degrease the surface [39].

2.2.4.3 Chemical or electrochemical treatment

The chemical treatments are normally aqueous-based processes. They can be applied as a spray or by immersion. Once again the degreased stage, generally, is present prior to the chemical treatment. The main type of chemical treatments used are etchants. [39]

Most of the times etch solutions are composed by strong acids (alone or multi-acid solution). However there is the possibility to use powerful alkaline solutions. The goal of performing an etching treatment is to wipe and remove any vestige of weak layer (either organic or inorganic) and leave an enhanced surface topography. In theory, and if the process was well executed, after the rinse stage, the surfaces should be of a high surface energy and atomically clean. This leads to a better adhesion. [39]

The electrochemical surface treatments are based on anodization process. This kind of process is expensive (it's difficult to anodize parts of great size), complex, long and has a negative environmental impact (especially when solutions containing chromium are used). It consists in the creation of a layer of anodic oxide.

There are several types of anodization, different solutions used, and it's reported that the most successful treatments for aluminium are the ones that uses direct current (DC) anodic oxidation in chromic (CAA), phosphoric (PAA), or sulphuric acid (SAA) electrolytes.

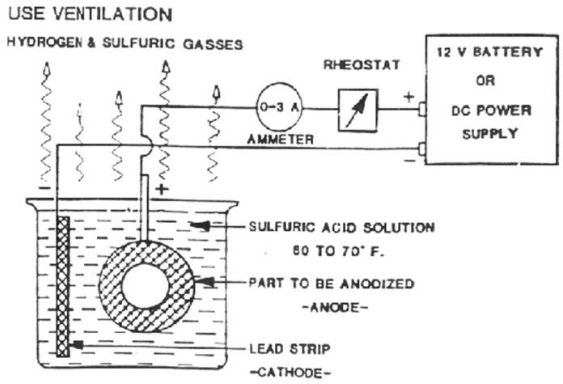

Figure 2.32: Schematicly figure of the anodization process. [43]

The principles involved in anodization process are simple. It is the chemical change caused by the passage of electrical current through and electrolyte (solution). The electrical current is transmitted to the workpiece (anode) via a cathode. The process is an exothermic reaction on an aqueous electrolyte solution and atomic oxygen is produced by electrolysis.[45] Toxic gases are also produced, depending on the electrolyte solution used. This reaction allows the creation of an oxide layer and the basic chemical equations that govern the process are:

$$2Al + 2NaOH + 2H_2O \longrightarrow 2NaALO_2 + 3H_2 \tag{2.1}$$

$$NaAlO_2 + 2NaOH \longrightarrow Al(OH)_3 + NaOH \tag{2.2}$$

The lost of evaporation of the water leads to a surface containing a layer of alumina (Al_2O_3). There is the need to use a power supply that can maintain a constant voltage. Figure 2.32 shows the typical anodization process.

On an aluminium alloy the anodic oxide formed on the surface consists of an inner, thin, compact oxide layer, called the barrier layer, and a porous outer oxide displaying a honeycomb-like hexagonal structure as seen on Figure 2.33. [39]

It is reported that production rates in a range of 1 to 5 mm/h are typical. Factors such as the alloy type, the thermal history of the metal, de-oxidizing process used, and electrolyte agitation can be very important in the formation of ordered pore arrays. [39]

The CAA, for example, is a process often used in European aerospace industry. It produces a porous surface oxide typically 2 to 3 mm thick with a pore diameter of approximately 25 to 35 nm. The PAA is preferred by Boeing Commercial Airplane Company. It allows good durability. The oxide produced has 400 to 800 nm thick incorporating 100 nm of small outwardly protruding fibrils. The phosphate content of the oxide improves stability toward water. [39]

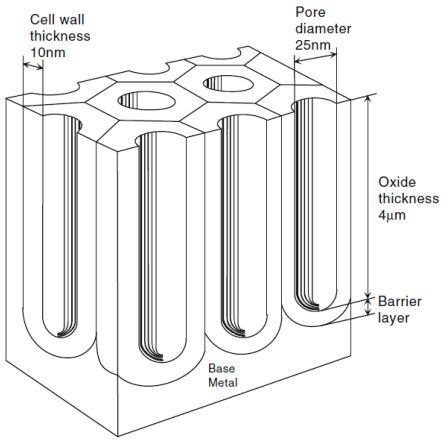

Figure 2.33: Schematicly figure of the structure of anodic oxide layer on aluminium alloys. [39]

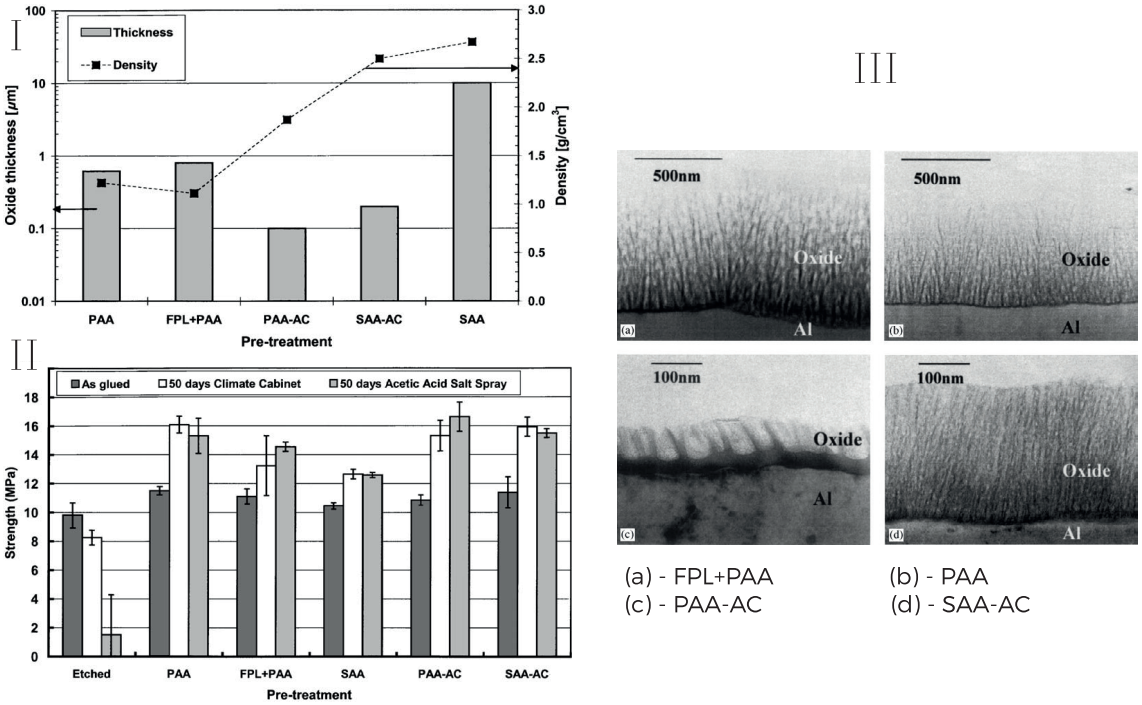

Figure 2.34: Comparison between electrochemical surface treatments: I) The thickness and density of the oxide layer obtained by PAA, hot AC anodising in phosphoric acid and sulphuric acid, and SAA; II) Tensile test for as glued AA6060-T6 single lap shear joints before and after exposure in either climate cabinet or acidified salt spray; III) TEM cross-section images of anodised oxide layers on extruded AA6060-T6. (edited images) [46]

Redford [46] conducted a study where he compared several surface treatments (on an adherend of AA 6060-T6), like the PAA and variants, SAA (sulphuric acid anodising) and etching. He obtained remarkable conclusions, such as:

- AC current causes smaller thickness of oxide, Figure 2.34 I;
- PAA presents smaller oxide thickness than SAA, Figure 2.34 I and III;

- PAA - DC, PAA - AC and SAA - AC presented similar behaviours and the best performance facing corrosion and other adverse environmental conditions, Figure 2.34 II;
- Occurred adhesive fracture of samples that were produced by AC anodization in sulphuric acid, while cohesive fracture was found for samples of PAA - AC;
- Since the AC process is quicker it is better suited to industrial applications.

This conclusions obtained by [46] are corroborated by the work done by our workteam. It was found that the application of PAA treatment resulted in a significant improvement in the mechanical behaviour of an adhesive joint (better adhesion). The improvement in the ultimate load on a SLJ configuration was $\approx 16\%$ [22].

Another way to maximize the adhesion on adhesive joints is the use of primers chemically compatible with the adhesive and adherend. The application of the primer could be done after mechanical treatments or after chemical or electrochemical process like the PAA.

2.2.5 Overview of structural adhesives

As said before a structural adhesive has to sustain high loads and demanding applications. For example, a subsonic airplane is designed to withstand a range of temperature that varies from -55 to $+80\,^{\circ}\text{C}$ [47], this represents a enormous challenge to the adhesives.

Nowadays, in order to fulfil the demanding requirements the materials used to produce structural adhesives are, mostly, thermosetting polymers. However, the majority of polymers have the potential to become an adhesive. All polymers have fundamental properties that allows adhesion. Polymeric materials has the ability to flow and then set via several reaction mechanisms in order to form a cohesively strong solid. [41] In the adhesive industry it's possible to modify the polymer's properties with additives.

The thermosetting polymers are, in the majority of the cases, the kind of polymer chosen to produce structural adhesive joints. The most commonly used groups of thermosetting adhesives are showed in Table 2.10.

Table 2.10: Typical thermosetting resins for adhesives. [39]

Type	**Advantages**	**Limitations**
Epoxy	High strength Good solvent resistance Good heat resistance Wide range of formulations Relatively low cost	Exothermic reaction Exact proportions Required Short pot life
Polyurethanes	Various cure times Tough Excellent flexibility Moderate cost	Moisture sensitive Poor heat resistance May revert with heat and moisture Short pot life

		Special mixing and dispensing equipment required
Cyanoacrylates	Rapid room-temperature cure One-component system High tensile strength Long pot life Good adhesion to metal Dispense easily from package	High cost Limited solvent resistance Poor high temperature resistance Bonds skin
Modified acrylics	Good flexibility Good peel and shear strengths No mixing required Will bond dirty(oily) surfaces Room-temperature cure Moderate cost	Low hot-temperature strength Slower cure than with cyanoacrylates Toxic Flammable Odor Limited open time Dispensing equipment required
Phenolics	Good heat resistance Good dimensional stability Inexpensive Modification of toughness by adding elastomeric resins	Brittle Possibility of pollution due to formaldehyde as curing agent

The epoxy adhesives are the most commonly used and they present the capability to cure without demanding high pressure. [47] The adhesive system based on epoxy is very versatile. In their most simple form an epoxy resin is combined to an amine in order to form a crosslink network.[47]

The majority of the structural adhesives have in their base an epoxy resin that is based on aromatic structures [47].

An aromatic ring consists on a conjugation of six carbon atoms and six hydrogen atoms connected in a spacial disposition of single and double connections that alternate each other (Figure 2.35). This kind of structure is based on the covalent bonds that provide the perfect mechanical properties for structural applications.

Epoxy resins containing aliphatic structures can be used but are rarely applied in top demanding applications alone. They are sometimes added as reactive solvents, lowering the viscosity of the resin and aiding mixing with the amine curing systems. [47]

The process that allows the solidification of the adhesive is called the cure process. Over this process the adhesive suffers several transformations. The low molecular weight resin is converted into a 3D crosslinked network. The way that the process develops itself depends on the external conditions of the cure process. Different cure process tend to result in slightly different mechanical properties.

Figure 2.35: Aromatic ring representation.

The main factors that affects the curing cycle are the chemical ingredients, pressure, time and heat. The curing process can be achieved either at elevated or room temperature.

In the beginning of the curing process the adhesive in liquid state presents low molecular weight and it's converted into more viscous resin with an higher molecular weight. This viscous resin forms a gel and that is transformed in a glassy solid.

The transformation from liquid to solid leaves behind residual stresses in the adhesive due to the formation of crosslinks that lead to shrinkage. The stresses in the matrix could cause ageing in the joint structure [47].

Curing is a complex chemical process and can be addressed in time-temperature-transformation (TTT) diagram (Figure 2.36) [47].

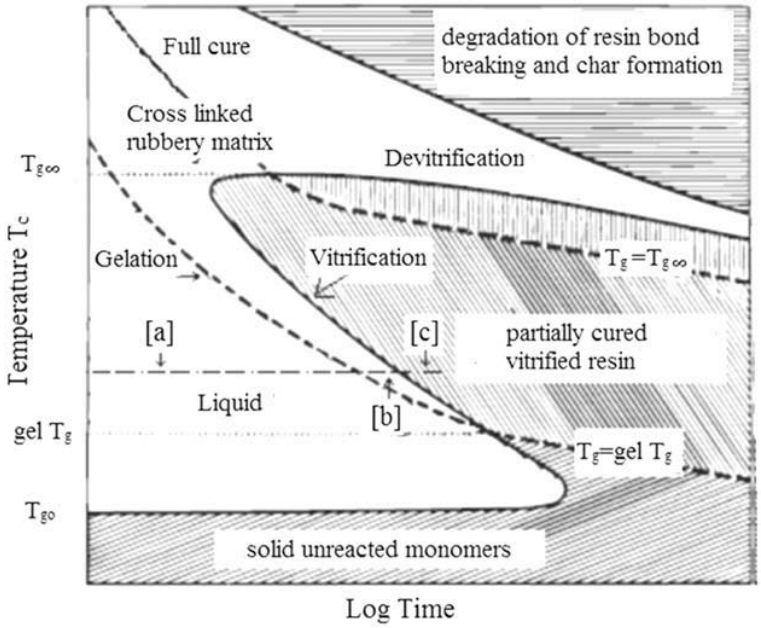

Figure 2.36: Time–temperature–transformation diagram for thermosetting resins. [47]

The TTT diagram illustrates the fundamental changes that occurs on the adhesive in the cure process. At temperatures below than T_{go} (glass–rubber transition temperature) the uncured resin is in a solid state. This property allows the thermosetting resin to be stored at low temperature which

stops the cure. Above T_{go} there are the transformation from solid to liquid and the adhesive can be qualified as a glass–rubber material, the cure process can proceed above this temperature. [47]

The curing process is characterized by two phenomena, gelation and vitrification. Once the T_c (temperature of cure) is above the T_{go} the cure occurs and the increase in T_c leads to faster cure process what reduces the processing time. In the first stage, known as gelation, occurs a dramatic increase in viscosity, while in vitrification (after gelation) there is a transformation from a liquid or rubbery state to a glassy state. Below gel T_g the adhesive has the ability of flowing. Once the gelation line is crossed this ability is suppressed and the adhesive layer is fixed. [47, 48]

Above gel T_g successive chemical reactions increase the crosslink density of the network, that leads to an increase, at low rates, in the stiffness of the adhesive. At the end of these processes is obtained a glassy structure, a fully cured thermosetting adhesive. As said before this stage is accompanied by a shrinkage. [47, 48]

The glass transition temperature T_g reaches its ultimate value when the matrix become completely cured and it is designated by $T_g = T_{g\infty}$. A simple rule of thumb is that the final T_g of the adhesive will be approximately 10 to 15 °C above the cure temperature.[47]

The most used adhesives are amorphous and the T_g is a property of the amorphous phase. The service temperature of the joint has to be below to T_g of the adhesive in order to behave as designed. The degradation of mechanical properties for temperatures in the range of T_g and above is significant, because the adhesive changes to a state softer and more flexible.

The physical and mechanical properties of the adhesive are directly dependent on the crosslinked structure created during the curing process. As said before a low cure temperature leads to a long cure time and the possibility of occurrence of partial vitrification of the adhesive before full gelation. In the other extreme, a high cure temperature for a short period of time can lead to a material degradation stage due to the high residual stress. [47]

It is a good practice to follow the manufacture guides for the cure cycle. Generally it's what happens in the industry.

There is also the possibility of performing a post-cured by exposing the adhesive to elevated temperatures after a cure cycle. It is reported that this can lead to slightly improvements in mechanical properties like the surface hardness and tensile strength However it produces a negative effect on ductility and toughness due to an increase in crosslinking. [47]

Regarding the conductivity of adhesives, they present poor heat and electrical conductibility. However both properties can be increased using fillers like powdered metals (for example silver). If the goal is to enhance only the thermal conductivity, metal oxide fillers can be used (like the beryllium or aluminium oxide). [39]

The linear thermal expansion coefficients of adhesives are generally higher than the adherends to be bonded (metals). This fact may be a problem when bonds with large areas are produced. The differences of coefficients, when there are subtle temperature changes, can lead to interfacial stresses that may damage the bond. One way to overcome this limitations is the addition of mineral fillers, that can reduce the expansion coefficient. [39]

2.2.6 Adhesive single lap joints [SLJ]

As mentioned before in Sections 2.2.1 and 2.2.2, single lap joints are one of the most used in industry. They allow better manageability of tolerance limits in large workpieces which may be an interesting feature on the transportations industries. The geometry of a SLJ leads to a complex mechanical state where a secondary bending effect is present resulting from the eccentric load that causes an extra stress allied to the shear (τ) and peel (σ) efforts. These last two are the typical stresses in the adhesive and according to Adams [49] the *peel stresses result in extension or compression of the material, known as direct strain (ε) whilst shear stresses cause a sliding deformation, known as shear strain (γ)* [49].

Figure 2.37 shows the moment when an adhesive SLJ is loaded. In the beginning of the loading (Figure 2.37 a)) the tensile forces have a line of action that is not initially parallel to the adherend sides. This eccentric loading causes a bending moment that with the increase in the load bends the adhesive and adherend (Figure 2.37 b)). Near the ends of the joint the peel and shear stresses are most severe and induce the failure in the adhesive joint. [50]

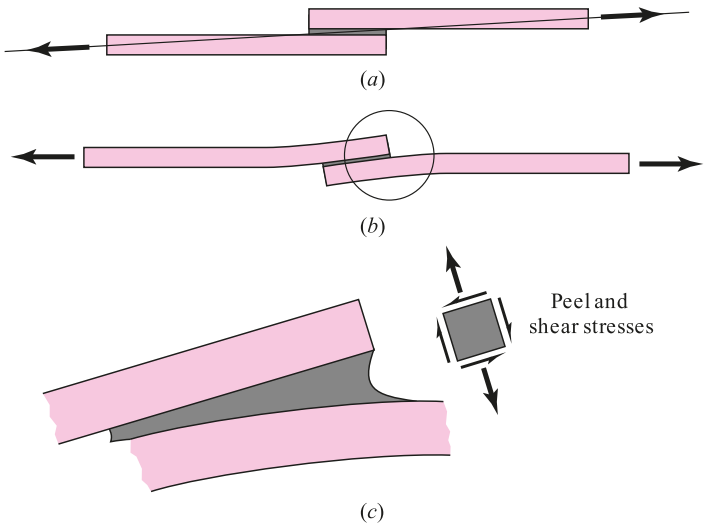

Figure 2.37: Stresses within a single-lap joint. [50]

Over the past years diverse studies were done on SLJ in order to obtain analytical models capable to describe and predict the mechanical behaviour of the joint.

An extensive literature review on existing analytical models for single lap joints was done by [51]. It was identified several approaches to the same case, some of them accounts more variables than others in order to better describe the real behaviour.

2.2.6.1 Rigid adherend linear elastic analyses

In the field of the denominated *"classical analyses"* the simplest and more expeditious approach is the method that assumes the full rigidity of the adherends and only shear deformation in

the adhesive. The adhesive shear stress (represented as τ) is considered constant over the lap joint (as seen in Figure 2.38). [51]

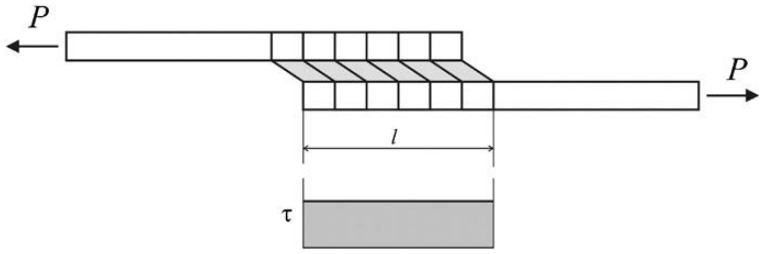

Figure 2.38: Deformations in loaded SLJ with rigid adherends [51]

The τ can be obtained by the following formula 2.3:

$$\tau = \frac{P}{bl} \tag{2.3}$$

Being P the load applied to the joint, l the overlap length and b the width. This calculation can be understood as the average shear stress across the adhesive layer. This method is unrealistic because it neglects many variables like the peel effort. [51]

2.2.6.2 Volkersen's analysis

In this method the deformation of the adherend in tension is taken into consideration (elastic behaviour). The adhesive is considered as deformable only in shear, as seen in Figure 2.39 a) and b).

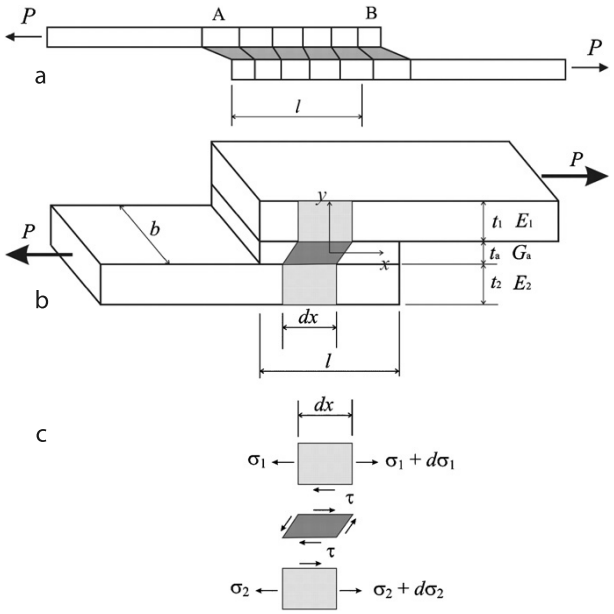

Figure 2.39: SLJ analysed by Volkersen's method: a) elastic deformation of adherends, b) geometry and c)elemental diagram. (Edited) [51]

This approach is more realistic, so the tensile stress in the upper adherend reaches the maximum value at point A (Figure 2.39 a)) and is zero at point B (the free surface). In the bottom adherend the opposite occurs leading to a non uniform stress distribution with a parabola shape where is maximum at point A and B and minimum in the middle of the joint (Figure 2.40). [51]

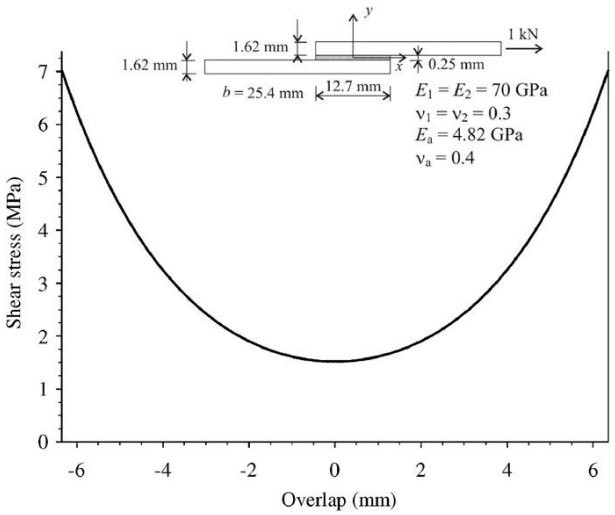

Figure 2.40: Volkersen's adhesive shear stress distribution for aluminium alloy adherends and an epoxy adhesive. [51]

The stress distribution equation is [52]:

$$\tau = \frac{P}{bl}\frac{w}{2}\frac{\cosh(wX)}{\sinh(w/2)} + \left(\frac{\psi-1}{\psi+1}\right)\frac{w}{2}\frac{\sinh(wX)}{\cosh(w/2)} \tag{2.4}$$

With P the load applied to the joint, l the overlap length and b the width and:

$$w^2 = (1+\psi)\phi$$

$$\psi = t_t/t_b$$

$$\phi = \frac{G_a l^2}{E t_t t_a}$$

$$X = \frac{x}{l}, -\frac{1}{2} \leqslant X \leqslant \frac{1}{2}$$

Being t_t the top adherend and t_b the bottom adherend thickness, E the adherend Young modulus, G_a the adhesive shear modulus, and t_a the adhesive thickness. The origin of the coordinate x is in the middle of the overlap. [52]

As can be seen by the equation 2.4 the Volkersen method does not consider the bending effect caused by the eccentric load applied conditioned by the SLJ geometry neither shear deformations.

2.2.6.3 Goland and Reissner's analysis

As mentioned previously the geometry of the SLJ allied to the eccentric load produces a bending moment (M) and a transverse force (V) applied to the ends of the joint. The first ones to consider this effects in a single lap joint were Goland and E.Reissner [53] in 1944. The method developed can be applied to an arbitrary end loaded single overlap configuration. The efforts in question in this method are the V, M and $\bar{P}$ (tensile load per unit width) which describes the reality with more accuracy than the previous methods (Figure 2.41). [52]

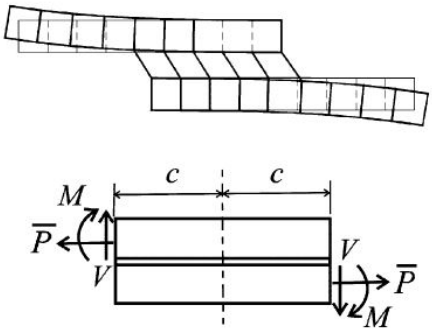

Figure 2.41: Goland and Reissner's model. [51]

The bending moment will cause a rotation in the joint. The rotation changes the direction of the line of applied load. There is a decrease in the moment, this loading cycle transforms the problem in a non-linear geometric one.[51, 53]

The M and V at the ends of the overlap can be calculated by:

$$M = k\frac{\bar{P}t}{2}$$

$$V = k'\frac{\bar{P}t}{c}$$

Where t is the adherend thickness and c is half the overlap length. If, for any reason, the rotation of the joint can be neglected the factors k and k' will be approximately equal to 1. Other wise if the rotation is greater k andk' will decrease resulting in decreasing in bending moment and the transverse load. [51]

The method of Goland and E.Reissner [53] takes into account the effect of large deflections of the adherends, however the method assumes that the adherends are integral and with a thickness of adhesive that tends to zero.[51] The expression for the bending moment factor (k) is:

$$k = \frac{\cosh(u_2 c)}{\cosh(u_2 c) + 2\sqrt{2}\sinh(u_2 c)}$$

with

$$u_2 = \sqrt{\frac{3(1-\nu^2)}{2}} \frac{1}{t} \sqrt{\frac{\bar{P}}{tE}}$$

Being E the Young's modulus and ν the Poisson's ratio of the adherend.

The bending moment factor of Goland and E.Reissner [53] is not the only one in the literature, after 1944 several authors proposed different factors like Hart-Smith that also take into account the effect of large deflections, but consider the individual deformation of the upper and lower adherends (not neglecting the adhesive layer). The mathematical expression for the factor proposed by Hart-Smith is [51]:

$$k = \left(\left(1 + \frac{t_a}{t}\right) \frac{1}{1 + \xi c + \frac{1}{6}(\xi c)^2} \right)$$

Where t_a is the adhesive thickness, D is the adherend bending stiffness and $\xi^2 = (\bar{P}/D)$.

This approach to the problem (the determination of the loads at the ends of the overlap and the calculation of the shear and peel stresses in the adhesive layer) allows the transformation from a non-linear geometric problem to a plane strain problem (loads applied to the ends). [51]

In the case of metal adherends in order to find the adhesive stresses the adhesive is considered relatively flexible and the joint flexibility is mainly due to the adhesive layer. The adherends are treated as cylindrically bent plates, being the deformations due only by longitudinal normal stress (σ_x). The bending of the adherend is transmitted through the thickness as a a peel stress. The adhesive layer thickness is considered almost null compared to the adherend thickness (constant stress adhesive layer assumption). This method is satisfactory in the range of [51]:

$$\frac{tG_a}{t_a G} < 0.1 and \frac{tE_a}{t_a E} < 0.1$$

Being G the adherend shear modulus, G_a the adhesive shear modulus and E_a the adhesive Young's modulus. Figure 2.42 shows the distributions of the adhesive shear and peel stresses given by Goland and E.Reissner. [51]

The formula that express the adhesive shear stress is [52]:

$$\tau = -\frac{1}{8}\frac{\bar{P}}{c}\left\{\frac{\beta c}{t}(1+3k)\frac{\cosh((\beta c/t)(x/c))}{\sinh(\beta c/t)} + 3(1-k)\right\} \tag{2.5}$$

$$\beta^2 = 8\frac{G_a}{E}\frac{t}{t_a}$$

$$k = \frac{\cosh(u_2 c)}{\cosh(u_2 c) + 2\sqrt{2}\sinh(u_2 c)}$$

$$u_2 = \sqrt{\frac{3(1-\nu^2)}{2}} \frac{1}{t} \sqrt{\frac{\bar{P}}{tE}}$$

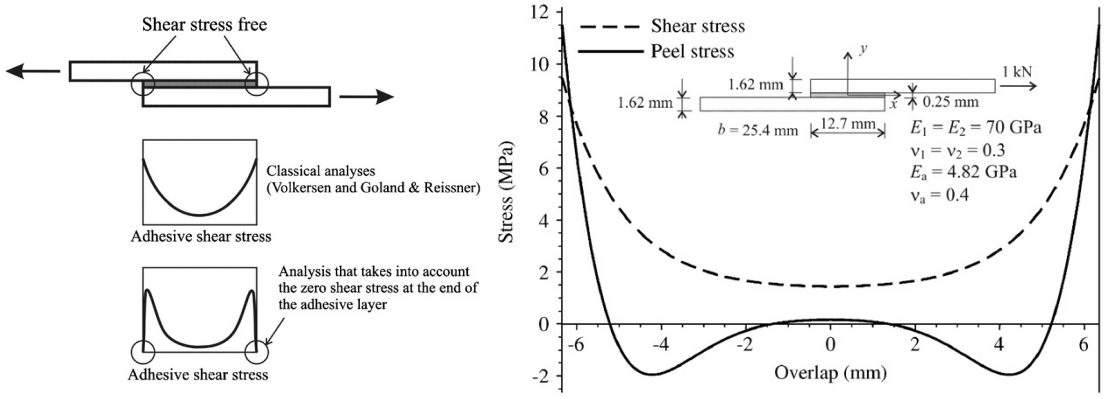

Figure 2.42: left: Adhesive shear stress distribution when the stress free condition at the ends of the overlap is verified; right: Goland and Reissner's adhesive shear and peel stress distributions. (Edited) [51]

Being $\bar{P}$ the applied tensile load per unit width, c half of the overlap length and t the adherend thickness.

For the peel stress we have [52]:

$$\sigma = \frac{1}{\Delta}\frac{t\bar{P}}{c^2}\left(R_2\lambda^2\frac{k}{2} + \lambda k'\cosh(\lambda)\cos(\lambda)\right)\cosh\left(\frac{x\lambda}{c}\right)\cos\left(\frac{x\lambda}{c}\right) + \frac{1}{\Delta}\frac{t\bar{P}}{c^2}\left(R_1\lambda^2\frac{k}{2} + \lambda k'\sinh(\lambda)\sin(\lambda)\right)\sinh\left(\frac{x\lambda}{c}\right)\sin\left(\frac{x\lambda}{c}\right)$$

Where E_a is the adhesive Young's modulus and:

$$\lambda = \gamma\frac{c}{t}$$

$$\lambda^4 = 6\frac{E_a}{E}\frac{t}{t_a}$$

$$k' = \frac{kc}{t}\sqrt{3(1-\nu^2)\frac{\bar{P}}{tE}}$$

$$\Delta = \frac{1}{2}(\sin(2\lambda) + \sinh(2\lambda))$$

$$R_1 = \cosh(\lambda)\sin(\lambda) + \sinh(\lambda)\cos(\lambda)$$

$$R_2 = \cosh(\lambda)\sin(\lambda) + \sinh(\lambda)\cos(\lambda)$$

The origin of the coordinate x is in the middle of the overlap. [52]

2.2.6.4 *"Classical analyses"* limitations

There are a number of simplifications adopted by the previous methods that leads to unsatisfactory results for some conditions. The main limitations identified are [51]:

(a) The thickness direction is considered as uniform in terms of stress distribution, this assumption may introduce errors in cases like when failure occurs close to the interface where the interface stresses are important;

(b) In some analyses the maximum shear stress occurs at the ends of the overlap, which clearly violates the stress-free condition (Figure 2.42). Analyses that ignore the stress free condition overestimate the stress at the ends of the overlap what usually gives conservative failure load predictions (bad in terms of efficiency design however it's in the side of safety).

(c) The adherends are considered as thin beams, neglecting in thickness directions the normal and shear deformations.

2.2.6.5 Hart-Smith's analysis

The previous methods are denominated *"classical analyses"* and are based on elastic behaviour neglecting the possibility of non-linear or plastic behaviour of the adhesive and/or adherend. In order to overpass this flaw in 1973 Hart-Smith presented an alternative expression for the bending moment factor, as seen in Sub-subsection 2.2.6.3.

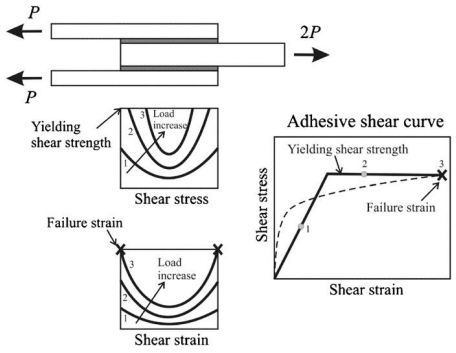

Figure 2.43: Schematic explanation of shear plastic deformation of the adhesive. [51]

Hart-Smith solution takes into consideration the plastic behaviour of the adhesive through an elasto-plastic shear stress model. The model also uses the adherend stiffness. The maximum lap joint strength is calculated using the maximum shear strain as failure criterion. [51]

However, the Hart-Smith analysis exhibits some gaps. The model neglect the large deflections in the overlap. The method is better suited for short overlaps and thin flexible adhesives. [51]

2.2.6.6 Adams model

Several applications uses adherends that are elastic and present a low yield strength (like aluminium), in this cases the Adams model is very simple and effective. The joint strength is given by the load corresponding to the total plastic deformation. This method is not well suited for brittle adhesive and elastic adherends. The best alternative is the finite element method (FEM). [52, 54]

In a SLJ the load corresponding to the total plastic deformation is calculated by [52]:

$$P_a = \tau_y bl$$

Being P_a the failure load of the adhesive joint and τ_y is the yield strength of the adhesive.

The direct tensile stress (σ_t) acting in the adherend due to the applied load P is [52]:

$$\sigma_t = \frac{P}{bt}$$

When there is bending due to a bending moment ($M = kPt/2$) the stress at the inner adherend surface (σ_s) is given by [52]:

$$\sigma_s = \frac{6M}{t^2 b}$$

The k represents the bending moment factor which reduces as the lap rotates under load. It's obvious that the total stress acting in the adherend is the sum of the direct stress and the bending stress. So, the maximum load that the adherend is capable to support that just creates adherend yield (P_s) is [52]:

$$P_s = \frac{\sigma_y bt}{(1+3k)}$$

Being σ_y the yield strength of the adherend. When in presence of low loads and short overlaps, k can be considered ≈ 1 what gives [52]:

$$P_s = \frac{\sigma_y bt}{4}$$

Other wise if the joints overlap is long compared to the adherend thickness ($l/t \geqslant 20$) the value of k tends to be zero. In this case, we have:

$$P_s = \sigma_y bt$$

The design methodology is represented graphically in Figure .

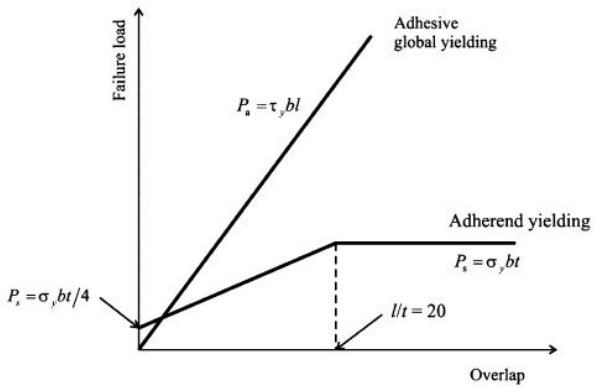

Figure 2.44: Simple design methodology of single lap joints based on the adherend yielding according to Adams method [51]

2.2.6.7 Design features in stress distribution

There are some design features that influence the stress distributions of an adhesive SLJ like the overlap length. The increase of the overlap leads to a progressive concentration of the stress at the end of the joint (edge) and a reduction of stress (unload) in the middle zone of the joint, as seen in Figure 2.45.

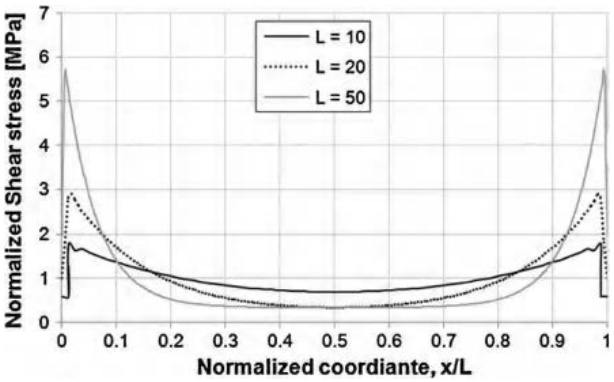

Figure 2.45: Shear stress distribution for different overlap length (L) in an adhesive SLJ. [55]

2.2.7 Fracture mechanics

Fracture mechanics is the field of mechanics that study the crack propagation and resistance to fracture in different materials. The fracture mechanics analysis consider a defect in the material like a flaw or crack. The defects are studied in order to assess their impact in the integrity of the adhesive joint trying to predict if they will cause a catastrophic failure of the system or if the joint can withstand the stresses throughout the service life.[56]

During World War I A. A. Griffith, an English aeronautical engineer, proposed the energy criterion to explain the failure of brittle materials. In his study he assumes that *the energy of a crack tip must remain finite, suggesting that an energy-based criterion on a critical stress state at which a continuum material would yield or fail is measurable. The fracture mechanics theory recognizes that a material's resistance to crack propagation is related to the energy required to separate adjoining material.* [56] This key idea can be explained in a different manner, the growth of a crack occurs, in a plate where direct stresses are applied, when the energy absorbed by the plate (due to the deformation caused by the loading) equals the critical value to form a new fracture surface. The energy supplied by the loading is known as the Energy Release Rate (G) and when it reaches or surpasses the Critical Fracture Energy (G_c), a material property which is independent of the applied loads and the geometry of the body, crack propagation takes place (propagation when: $G \geq G_c$). [39, 56]

In fracture mechanics there are three different loading modes. In Mode I (opening) the tensile properties of the adhesive are the most loaded (the load acts perpendicular to the crack plane), in Mode II (in-plane shear, shear loading perpendicular to the crack front) the shear stresses govern the fracture and the shear properties are the most requested, in Mode III (out-of-plane shear, shear

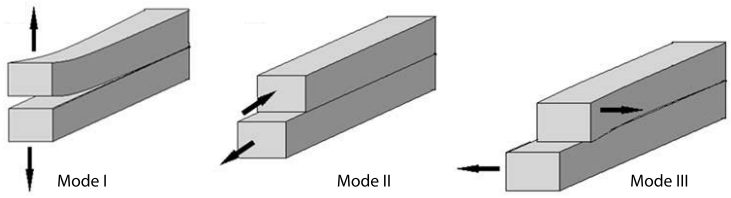

Figure 2.46: Modes of bond deformation used to define adhesive bond strength. (Edited) [47]

loading parallel to the crack front) the efforts are more complex but is dominated by the shear stresses. [47]

The Mode I fracture resistance of adhesive joints is most commonly determined by using the double cantilever beam (DCB) test. It is based on a specimen with a pre-crack loaded in Mode I that propagates trough the adhesive layer. During the test, the applied displacement and load are registered as well as the evolution of the crack length. These parameters allows the calculation of the Critical Fracture Energy (G_{Ic}) of the adhesive under mode I loading. [39, 56]

The G_{IIc} (Mode II Critical Fracture Energy) can be obtained with ENF (End-Notched Flexure) or ELS (End-Load Split) tests. The ENF is the most common method of testing in Mode II due to is simplicity. The major drawback is the difficulties to read the crack length during its growth and, under certain circumstances, the unstable crack propagation.[39, 56]

In the case of a SLJ and the majority of the adhesive joints in service the efforts that the joint is subjected are a mixture of the fundamental modes and this leads to a need in understanding the behaviour of a joint under mixed-mode conditions.

2.2.8 Mechanical properties

As mentioned in 2.2.5 the most used adhesives in structural applications are epoxies (they present high strength and temperature resistance), cyanoacrylates (poor resistance to moisture and temperature), acrylics (fast curing and high tolerance to bad adhesion), polyurethanes (good resistance to fatigue), and high temperature adhesives (phenolics and polyimides).

All of them present different mechanical properties as can be seen in Table 2.11.

Table 2.11: Typical adhesives mechanical properties values

Adhesive	Type	Shear modulus	Shear strength	Shear strain
SikaFlex 265	Polyurethane	0.7 MPa	4.5 MPa	450 %
AS1805	Silicone	0.68 MPa	1.47 MPa	330 %
RTV 106	Silicone	- MPa	1.3 MPa	400 %
DP805	Acrylic	159 MPa	8.4 MPa	180 %
Redux 326	Bismaleimide	1180 MPa	36.5 MPa	3.63 %
AV138	Epoxy	1559 MPa	30 MPa	7.8 %

The properties presented in the Table 2.11 are obtained with bulk tests. There are other properties that are relevant to assess the mechanical behaviour of an adhesive. The three different modes of fracture are useful to characterize the adhesive.

2.2.9 Fatigue on adhesive SLJ

The fatigue can be described as a phenomena of progressive damage of materials (or systems like a joint) that are under cycle variations of stress or strain. The knowledge of the behaviour of a joint under fatigue solicitations is crucial because the majority of failures in service life involve fatigue.

In order to assess the fatigue life of a joint there are two major approaches, the stress-life (S-N curves) and fatigue crack growth (FCG).

There is some work done in this field, the higher tenacity of adhesive single lap joints compared to the welding ones allows the possibility to withstand better the fatigue loadings. As mentioned before, there are some variables that influence the maximum stress and strain that an adhesive joint can take like the pre-treatment or the environmental degradation that can lead to a poorer fatigue life.

Rushforth et al. [57] conducted a study on the influence of surface pre-treatment and moisture on the fatigue performance in aluminium single lap joints. The authors used specimens with an overlap of 20 mm, a width of 25 mm and an adherend thickness of 2 mm (AA 5754) with an epoxy based adhesive. They found that the presence of a pre-treatment (silicon-based) has positive influence in the fatigue life of the joint and has also positive impact under humidity conditions. The S-N curves obtained are shown in Figure 2.47.

Abel et al. [58] also studied the effects of pre-treatment in fatigue performance on an adherend of AA 2014-T6 and an epoxy based adhesive cured at 120 °C. All adherends had a base superficial treatment that consisted on a grit-blast and a degrease. After this base treatment was studied the effect of a silane-based pre-treatment compared to chromic-acid etch (CAE). It was compared also the exposure to wet conditions. A "dry" environment of 25 ± 2 °C with a relative humidity of $55 \pm 5\%$ and a "wet" environment where the joints were fully immersed in distilled water at 28 ± 2 °C. The main conclusions that the authors found were:

- From the cyclic-fatigue tests conducted in the "dry" specimens the values of the threshold fracture energy (G_{th}) were far lower in value than the adhesive fracture energy (G_c) obtained under static-loading conditions;
- Was found a critical humidity %, somewhere between 55 to 80% r.h. (below which there is no significant effect of moisture upon the joint);
- The CAE treatment produced better fatigue behaviour.

Pereira et al. [59] conducted a study on the effect of surface pre-treatment and adherends thickness on the fatigue strength of adhesive joints. The authors adherends made of aluminium (AA6082-T6) and an high strength epoxy (Araldite® 420 A/B) as adhesive.

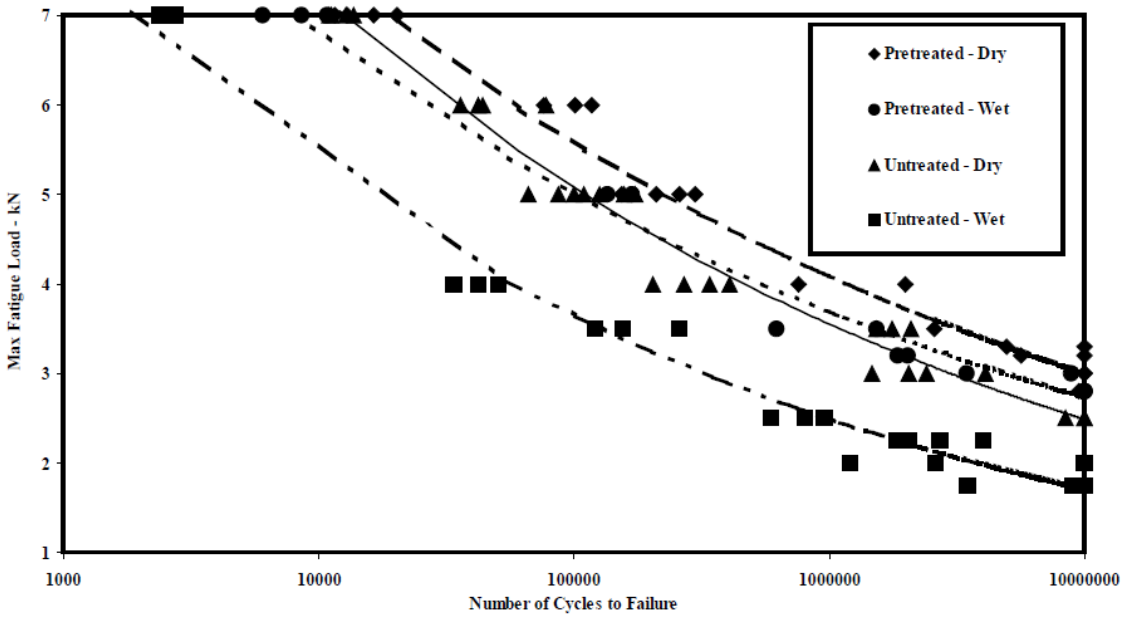

Figure 2.47: S-N curve comparing pre-treated and untreated joints tested in ambient air and 96% r.h. [57]

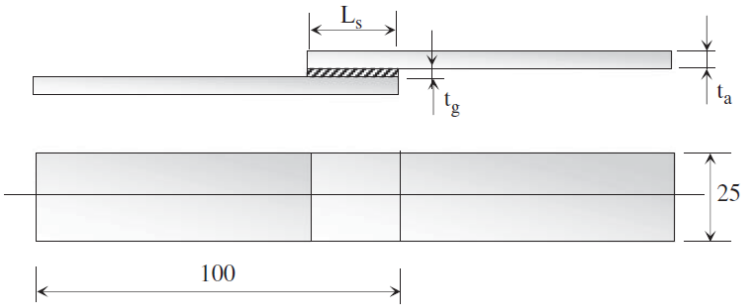

Figure 2.48: Geometry of single lap joints (dimensions in mm) used by [59]

The specimens geometry used is shown in Figure 2.48.

The thickness that was assessed were 1 and 1.5*mm*, an overlap length of 20*mm* and an adhesive thickness of 0.1*mm*. The surface treatments studied were the etch with sodium dichromate-sulphuric acid (CSA) and and abrasive polish (AP).

The main conclusions were [59]:

- The maximum fatigue strength was obtained for the CSA surface treatment. This treatment reaches a strength benefit at about 23% (for 10^5 cycles) in comparison with an abrasive polishing.
- The increase of the adherends thickness from 1 to 1.5 mm tends to decrease the fatigue strength by about 6%(for 10^5 cycles).

The S-N curves obtained can be seen in Figure 2.49.

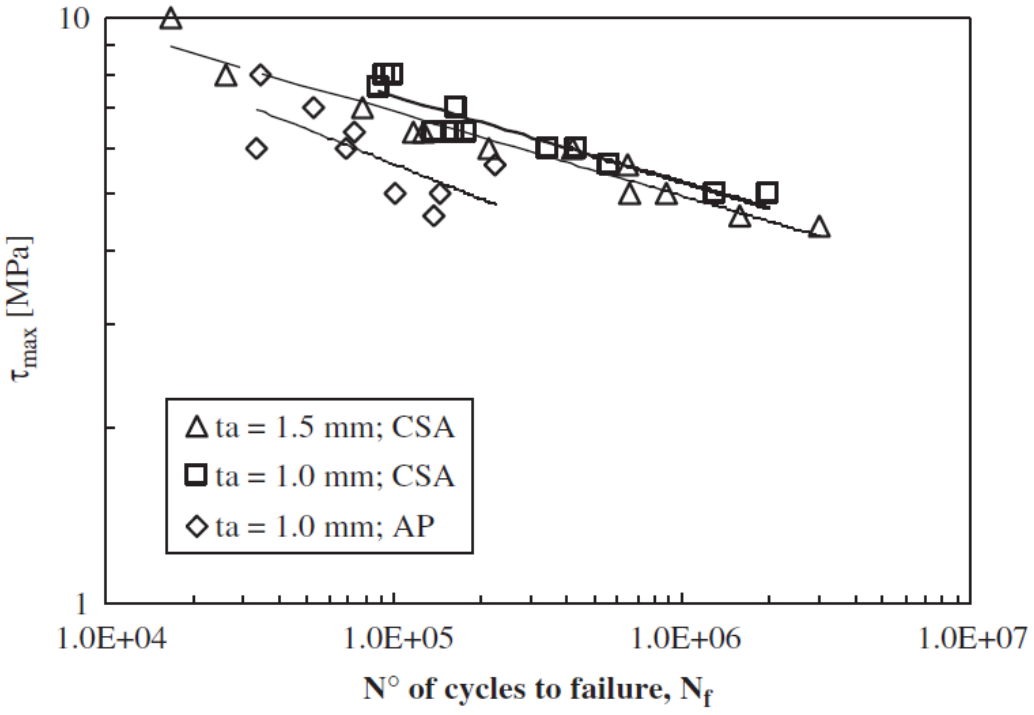

Figure 2.49: Fatigue life curves of single-lap shear joints in study produced by [59]

2.3 Hybrid bonding technologies

The hybridization process intends to gather the main advantages of the intervening processes and overcome the main limitations of adhesive joints. As seen before the maximum stresses that tend to develop near the overlap edges (due to differential straining between the adherends and load asymmetries) can lead to premature failures. Other handicaps of adhesive joints like the high sensitivity to the surface treatment, service temperature, humidity and ageing can be overcome allying it to other joining methods.

The transportation industry,due to environmental, efficiency and cost savings motivations, struggles to find lighter joining processes in order to join aluminium alloys or composites. In order to achieve these goals the industry has started to adopt different novel hybrid bonding techniques that can lead to better static and fatigue strength, stiffness and durability to the joint.

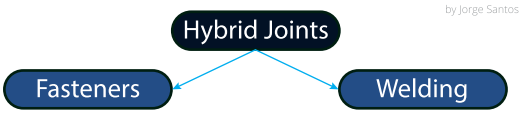

Figure 2.50: Two main approaches to hybrid bonding techniques.

There are two main approaches to the hybridization process that consist in the use of fastener connections or welding ones. The first group is the one that has currently the best implementation and acceptance in the market, mainly due to the easier maintenance operations, and we can include some techniques like the rivet-adhesive or bolt-adhesive systems. The second group has tremendous potential and the main paths of research are focus in the weld-adhesive, laser welding-adhesive and friction stir spot welding-adhesive systems. Our workteam are currently studying a novel approach to the hybridization the Friction Stir Weldbonding that will be addressed further ahead.

2.3.1 Fastened bonded joints

This kind of technique is used in the automotive industry since the early 2000's when the aluminium started to replace some steel components. For example, the BMW® 5 Series (E60 - production from 2004 to 2010) in order to overcome galvanic corrosion between steel (in the main structure) and aluminium (in exterior panels and other parts) introduced a hybrid joint that consisted in a rivet-adhesive system (rivet-bonding). [60, 61]

2.3.1.1 Rivet-bonding

This process consists in the use of rivets allied to a structural adhesive in order to obtain a joint that demands less work time (less 40% compared to arc welding), is cheaper (can be 30% cheaper than arc welding joint), is more energy efficient (reduction of electrical power consumption up to 84% compared to welding), can bond dissimilar materials and not welded alloys. [55, 60]

Concerning rivet bonded joints, there are three different manufacturing approaches that can be considered [55]:

- **Flow-in:** the rivet is placed and set, then a low viscosity adhesive infiltrates by capillarity between the adherends and cures in place. This manufacturing technique can be useful to reinforce the strength of an existing riveted joint;
- **Rivet-through cured adhesive:** it consists in the application of the rivet after the end of the adhesive curing process. It is used, mostly, to repair or increase the strength of pre-existing bonded joints;
- **Rivet-through uncured adhesive:** the adhesive is placed in the joint and after that is applied the rivets. It is the most used technique and it allows good mechanical properties (provided by the adhesive) with an easy and quick manufacturing (provided by the rivet) without any equipment for holding the parts during the adhesive curing process.

It's reported that concerning the strength, hybrid joints (adhesive + rivets) are similar to simple adhesively bonded joints (because the strength of the rivet itself is much smaller than the adhesive being the force transmitted to the adhesive). The use of rivet-bonding techniques allows to simplify the manufacturing process in comparison with the arc welding (there are no further operations to correct the effects of the high heat input) [55].

As seen in Figure 2.45 for long overlaps the stresses in the middle zone of the joint are low and the placement of a rivet in that area leads to a negligible effect of the rivet sustaining the stresses. In that cases (long overlap) the strength of the joint is, manly due to the adhesive. However for smaller overlaps the mechanical fastening contributes significantly to the load bearing and needs to be strong enough to sustain the stress otherwise the hybrid joint performs poorer than a single adhesive joint [55].

Sadowski et al. [62] studied this hybrid process and compared the capability of a joint to absorb and found that the hybrid joint compared with the adhesive joint absorbs 35% more energy in the configuration of double lap joints (DLJ).

Table 2.12: Energy absorption of DLJ [62]

Joint Type	**Energy absorption [J]**
Simple adhesive joint	122
Simple riveted joint	7
Hybrid joint	165

The Load vs. Displacement curve for the three types of joints studied in [63] are shown in Figure 2.51. The hybrid and rivet joint has 5 rivets.

It's possible to observe that there are a synergetic effect in the hybrid joint that allows the improvement of performance in tensile test.

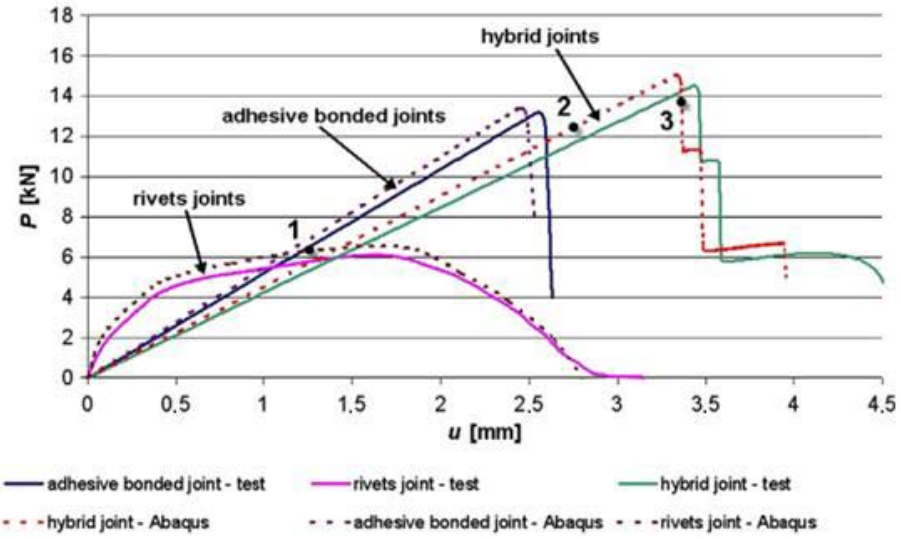

Figure 2.51: Load vs. Displacement curve for the three types of joints [63]

2.3.1.2 Bolt-bonding

In several transportation industries like automotive or nautical the bolt-bonding technique is used due to ease of manufacturing being a mean of aligning and attaching different structural parts to one another and provide fixation during adhesive cure. Another purpose to the use of this method is the possibility of it acting like a safeguard system (fail-safe-mode) to prevent defects within the adhesive layer or degradation which may lead to premature or catastrophic failure. [32, 64]

However this kind of hybridization can lead to a better mechanical performance besides the increase safety. For example hybrid joints can offer improved performance in comparison to adhesive bonded joints during crash loading where part separation is undesirable. [32]

Besides the advantages mentioned until now there are others like [64]:

- In case service temperatures reach the range of T_g of the adhesive or in emergency situations like fire the bolts may help preserving the integrity of the joint. Bolts are usually not loaded during service. However, in the event of a fire adhesives soften eventually the bolts will carry the load;
- In a bolt-adhesive hybrid joints the issue of predicting long-term performance of the bonded joint is avoided since bonding is being combined with a proven joining method.

Although there are some disadvantages pointed to this method being the major one the more time demanding and higher manufacturing cost.

The typical configuration of a bolt bonding joint is presented in Figure 2.52.

It's reported that it's possible to obtain a better fatigue life with an hybrid bolted-bonding joint (with an epoxy adhesive), comparing with an adhesive one. In that case the fatigue strength of the

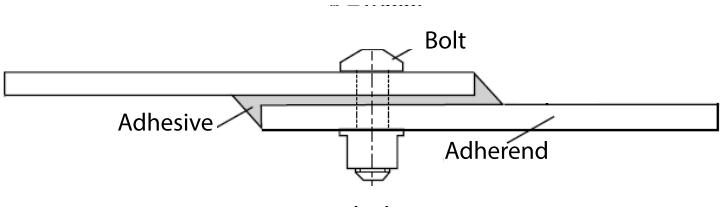

Figure 2.52: Typical Bolt-adhesive system. (Edited) [32]

joints increased with reduction in joint width to hole diameter ratio (w/d). Also the propagation rate of fatigue cracks was reduced in hybrid joints comparing with adhesive joints. [32]

Kelly [65] performed experimental and numerical studies being one of the goals test different hybrid bolt-bonding systems (different adhesives and bolts). The major conclusion that he obtained was that an hybrid joint with a stiff adhesive, the bolts have minor influence on the load transfers, however in a joint were the adhesives is ductile, the bolts play a key role on the loading transfers. The other conclusions found were [65]:

- The load transferred by the bolt increases with an increase of the thickness of the adherend and/or adhesive;
- The load transferred by the bolt decreases with an increase of pitch distance;
- The load transferred by the bolt decreases with an increase of overlap length;
- The bolts don't participate in supporting loads until the adhesive is almost failing.

Kelly [32] proved that at least in one of the configurations adopted (CFRP adherend and polyurethane adhesive with a thickness of 3.2*mm*) it's possible to obtain better *quasi-static* mechanical properties in an hybrid joint than in a single joint, as can be seen in Figure 2.53.

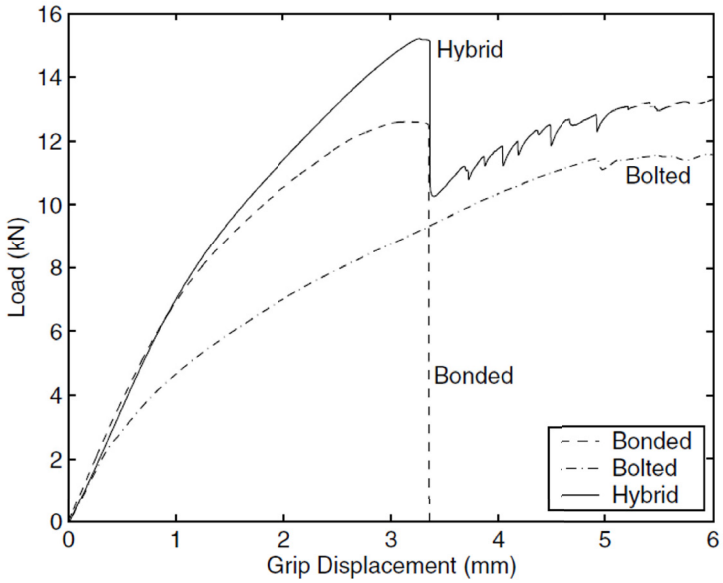

Figure 2.53: Load displacement behaviour of the bonded, bolted and hybrid SLJ. (Edited) [32]

It's possible to observe that the bolted joint demonstrated almost equal load capacity to the bonded joint. However, the stiffness of the bolted joint was lower than that of both the bonded and hybrid joints. These joints present an equal stiffness in the early stages of loading with the hybrid joint being stiffer at higher load levels. The difference in stiffness was related to the relative displacement between the adherends. The bolt participation in sustaining the loads after the deterioration of the adhesive can be seen in the final stage of the Load vs Displacement curve (Figure 2.53). The ultimate strength of the best hybrid joint studied in [32] was 25% than the best adhesive joint. [32]

In terms of fatigue behaviour is reported that the hybrid joint presents better performance than the bolted one and in some cases (distinct configurations)they perform better than a single bonded one. Kelly found that at lower loads the first stage involving fatigue of the adhesive (damage initiation) was a significant part of the joint fatigue life. The explanation of that fact can be due to the brittle nature of the epoxy adhesive. The second and third stages were extremely short with the cracks propagating through the adhesive at an high rate. [32, 65]

2.3.2 Weld bonded joints

This kind of approach to the hybrid joints has high application potential and it's use in the industrial field is been growing in the recent years. All of the hybrid processes that involve adhesives and welding present a high automation potential that can lead to a reduction in cost compared with other approaches to hybridization. Again the automotive industry is the main user of this kind of technique. The weld-bonded joints can be continuous (e.g. laser welding) or discontinuous (e.g. friction spot welding).

2.3.2.1 Spot-weld bonded joints

In order to enhance the fatigue behaviour and maintain the main advantages of the resistance spot welding (the short manufacturing time and long term resistance) the hybridization of the process can be an interesting solution. This hybrid process is simply know as weldbonding.[66]

The main stages of the process consist on the application of a paste adhesive to one adherend (sheet) and then the joint is closed (placing the other adherend on top). A spot weld is then made through the adhesive. In order to obtain electrical contact between the adherends (requisite to perform the resistance spot weld) the pressure exercised by the electrode force the displacement of the adhesive being the weld made in the normal way. [66]

The heat input of this kind of welding is very localized what leads to controlled (in area) damage in the adhesive that is limited to a small area around the weld. After the end of the weld process the cure cycle of the adhesive proceeds. If the nature of the subsequent manufacturing operations is too demanding for the joint, a cure cycle with temperature is normally applied. Otherwise it's possible to proceed the operations and leave the joint to cure at ambient temperature because the weld provides structural integrity. This feature can save manufacturing time comparing to single adhesive joint. [66]

This technology presents some advantages when compared with mechanical fasteners joint like [66]:

- Better corrosion resistance;
- Lower manufacturing costs;
- Non-existence of sealing operations;
- Better fatigue strength;
- Appropriate for automation.

The typical joint and scheme of manufacturing process is shown in Figure 2.54.

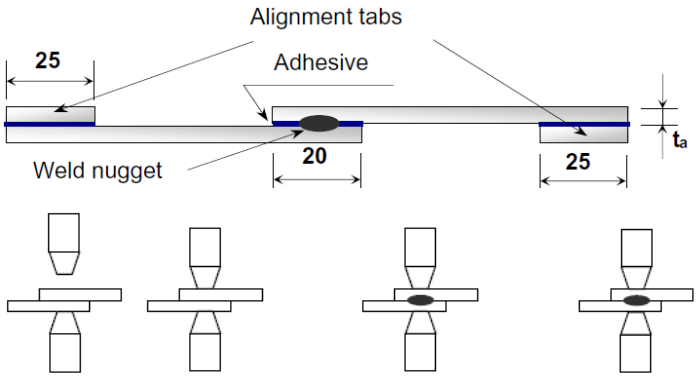

Figure 2.54: Typical spot-welding cycle and joint. (Edited) [67]

A study conducted by Gaul and Weber [68] focus on weldbonded steel single lap joints. the authors found that the tensile shear strength of the hybrid joints are greater than the only welded (Figure 2.55).

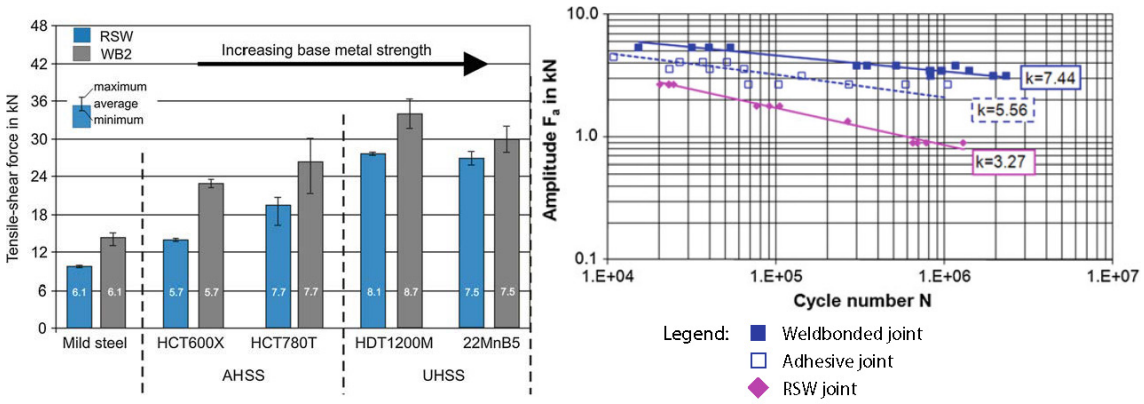

Figure 2.55: Left: tensile shear strength of the hybrid joints (WB2) compared to resistance spot welded (RSW); right: S-N curve for the 3 types of joints. (Edited) [68]

It's reported by the same authors that the absorbed energy in *quasi-static* shear load and impact shear load in the hybrid joint was higher than the absorbed energy of the RSW joint. [68]

In the same study it was found that no matter the adhesive studied the hybrid joint performed better under fatigue tests than the RSW joint (Figure 2.55).

Pereira et al. [67] studied the mechanical behaviour of single lap joint with adherend made of AA 6082-T6 and produced by weldbonding under tensile-shear and fatigue for one, three and five spot welds. The adhesive used in that work was the Araldite® 420 A/B. The main conclusions obtained in that study were:

- Was investigated which damage equation lead to more accurate fatigue life prediction and the better one was the S–W–T damage equation;
- For high loads fatigue failure occurs by the pull-out mode and for lower loads the failure mode is essentially by the sheet tearing mode;
- The fatigue strength of the weld-bonded joints is controlled by adhesive bonding;
- For higher loads the bonded and weldbonded present similar fatigue strength, for lower loads the fatigue strength is higher in the bonded joint.

There are some new trends in the field of the weldbonding using, MIG spot welding instead of RSW. The main stages of that process are the application of the adhesive, drilling through the adhesive and MIG spot welding. It is reported that this technique can lead to a weldbonded joint with a tensile shear strength about three times as large than the MIG welded joint. [69]

2.3.2.2 Friction stir spot weldbonding

Friction stir spot welding (FSSW) is a process that derives from the FSW. FSSW is also a solid state process and has the almost the same advantages and disadvantages pointed to FSW. The main difference between FSW and FSSW is that in the last one there is no transverse movement, the weld is made locally similar to a traditional spot-welding.

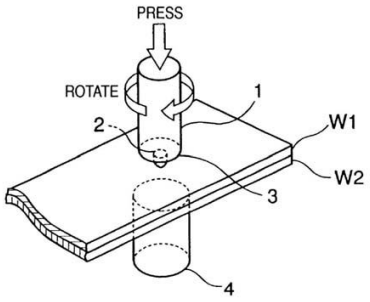

Figure 2.56: FSSW schematics. [70]

The main motivation to develop research in this field is the limitations presented in traditional spot-welding to produce joint of dissimilar materials and joints made of aluminium or magnesium alloys. This kind of alloys are being implemented in the automotive industry what leads to a demand for better process to join them. The resistance spot-welding in this kind of alloy presents some technical concerns, including weld porosity, electrode wear, high energy consumption, low production efficiency and inconsistency in failure modes [71].

Chowdhury et al. [71] conducted a benchmark the fatigue behaviour of FSS Weldbonded dissimilar joint (Al/Mg) joints. The overlap area used was $35 \times 35mm$ and the Load vs. Displacement

curve can be seen in Figure 2.57. The designation adopted (Al/Mg or Mg/Al reflects which plate is placed in the top of the joint or in bottom).

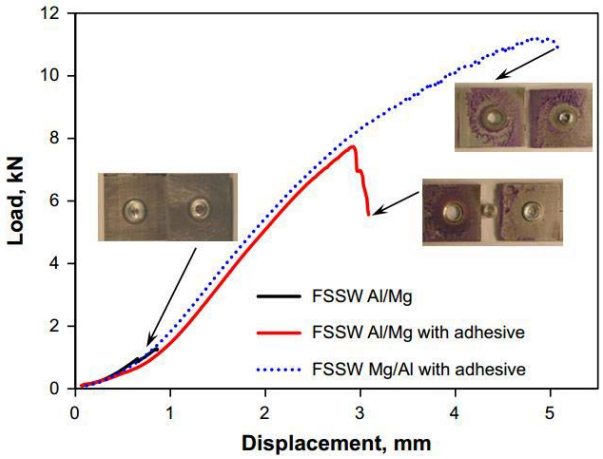

Figure 2.57: Load vs. Displacement curve for dissimilar FSS Wldbonded joint [71]

As expected the hybrid joint performs better than the welded joint. The mechanical behaviour during the tensile test is manly governed by the adhesive. The difference in behaviour between Al/Mg and Mg/Al can be explained by the presence of a brittle inter-metallic layer at the interface in the Al/Mg joint [71].

The author of the study also estimated the failure energy (area below the load vs. displacement curve) of each joint and found that for the Mg/Al the energy was $\approx$ 26.5 J, Al/Mg $\approx$ 9.5 J and the welded joint with $\approx$ 0.34 J. With these values a correlation can be made to the impact tests and it's expected that the performance of the hybrid joints to be much better than the welded one.[71]

The fatigue life was also assessed and as expected there was an huge improvement in the performance under fatigue of the hybrid joints (Figure 2.58).

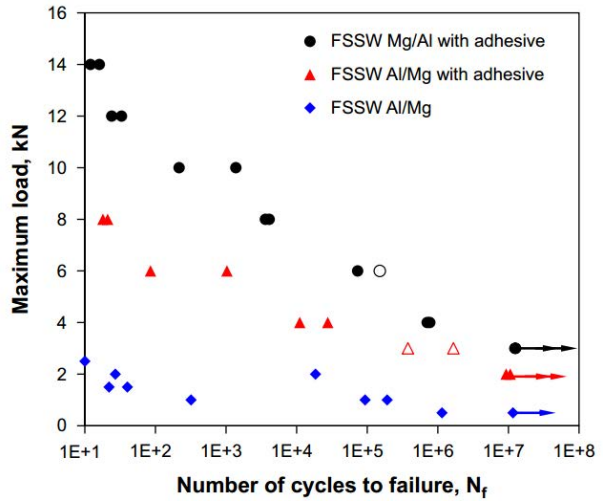

Figure 2.58: S–N curves of the dissimilar FSS Wldbonded joints [71]

The main conclusions in this study were the conclusions were that the hybrid joints compared to FSSW only joints presented a better overall mechanical performance. In terms of fatigue life two distinct failure modes were observed and was found to be dependent on the cyclic load level in the dissimilar adhesive welds. At higher load levels the failure was through nugget pull-out in both adhesive joints with a crack propagation around the nugget. At lower load levels the fatigue failure in the Al/Mg adhesive weld occurred in the bottom Mg sheet due to the stress concentration of the keyhole. [71]

2.3.2.3 Laser weld-bonded joints

Another approach to the hybridization process is the laser weld-bonded joints. This technique is used mostly to produce dissimilar joints with aluminium and magnesium alloys. It allows the minimization of the formation of the brittle inter-metallic compounds in the fusion zone, which reduce the strength of the welding joint. [72]

Figure 2.59 shows the schematic diagram of the laser weld bonding set up.

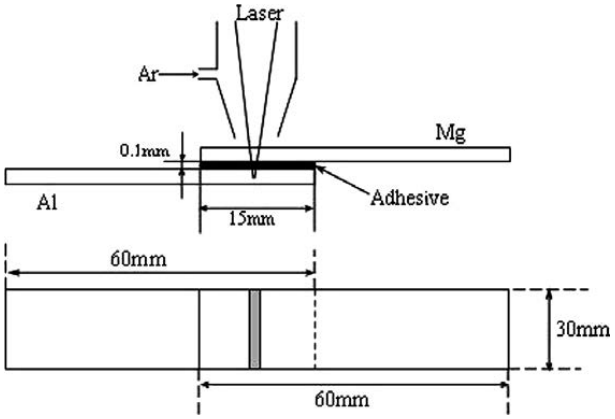

Figure 2.59: Schematic diagram of the laser weld bonding set up. [72]

The main stages of this manufacturing process are:

1. The adhesive is applied between the two adherends (sheets) to be joined;
2. The adherends are welded using a laser beam;

One of the main concerns with this method is the behaviour of the adhesive when subjected to the laser. Wang and Liu [73] conducted a study were they found that the adhesive, in the welding zone, decomposes due to the high heat input caused by the power beam laser degrading the mechanical properties to the exposure area. The parameters that influence the most this phenomena are the pulse laser beam power and adhesive thickness. [73]

In terms of mechanical behaviour the hybrid joint performed better in tensile tests than the adhesive or welded joint (Figure 2.60). The static strength of the hybrid joint is about 85% of the base material. [74]

In terms of manufacturing cost this approach is much more resource consuming than other presented in this literature review.

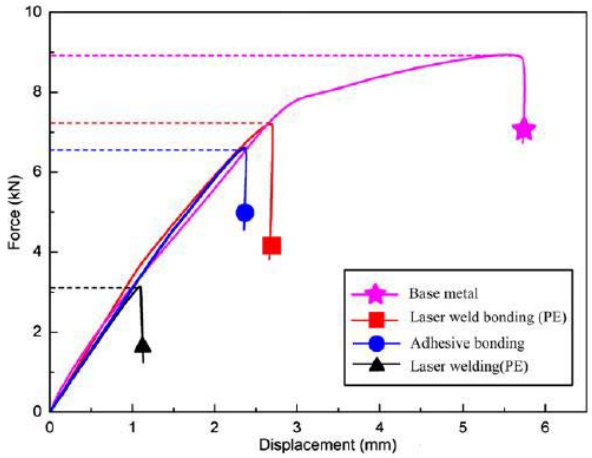

Figure 2.60: Tensile shear test results of the laser weldbonded joints. [74]

2.3.3 Final comparison between hybrid joints

Moroni et al. [60] conducted a study where benchmarked the strength of several types of hybrid joints and his work is very useful. The types studied were resistance spot-welding (RSW), clinching(C), riveting(R), self-piercing riveting (SPR) and adhesive bonding (B) and their combinations in hybrid joints.

The author found that:

- Weldbonded joints generally present an increase of strength, stiffness and energy absorption in comparison with simple spot welded joints and a strong reduction of dependence from temperature and ageing with respect to bonded joints;
- *In hybrid-fastened joints, the contribution of adhesive bonding is more evident than in weldbonded joints, with a strong improvement of the mechanical performances in general with respect to simple fastened joints. On the other hand, the temperature and ageing effect on hybrid joints is similar to that of simple bonded joints*;

The right type of hybrid joint depends on several factors like the application, service temperature, safety requirements, time of service, cost, energetic efficiency and others. The hybridization more than a trend is a need and the search for new process endows the engineer with more weapons to produce an product with the best suited process.

2.3.4 Friction stir weldbonding

The FS Weldbonding is an innovative hybrid process and the work done in this field is scarce. [22, 75–77].

The FSW process, as seen before, is relatively recent and presents several advantages like the possibility to easily join alloys, that are difficult to weld, like aluminium and magnesium, as well to join dissimilar alloys. This is one key feature on FSW that can turn the FS Weldbonding in a

major hybrid process. The use of this kind of alloys in transportation industry is growing what represents an window of opportunity to this process.

The FS Weldbonding is being studied in SLJ configuration in order to assess if the application of an adhesive layer leads to an overpass of the mechanical properties degraded by the "hook" defect present in the advancing side of the weld.

The mechanical properties under *quasi-static* of an hybrid joint composed by an adherend of AA 6082-T6, an Araldite® 420 A/B adhesive were assessed for SLJ specimens with the geometry shown in Figure 2.61.

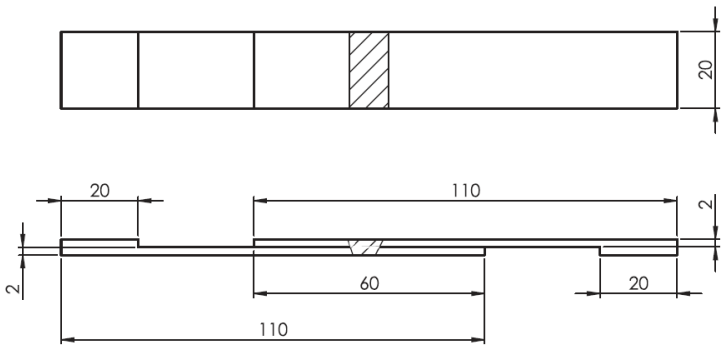

Figure 2.61: Single lap joint specimen geometry. [77]

The welding parameters that lead to the best mechanical properties are shown in Table 2.13.

Table 2.13: FS Weldbonding parameters. [77]

Parameter	**Value**
FSW control	Vertical force
Rotation direction	CW
Plunge speed	0.1 mm/s
Dwell time	5 s
Tilt angle	0°
Welding speed	200 mm/min
Rotational speed	1000 RPM
Downward force	450 kgf
Probe length	2.8 mm

The main conclusions until now were:

- Adhesive joint tensile strength is 60% higher than the highest strength of the best FSW lap joint (double pass FSW);
- The hybrid joint tensile strength matches the adhesive joint tensile strength. Although the ultimate displacement is higher in the adhesive joint (can absorb more energy);
- The hybrid joints do not result in better mechanical performance in quasi-static conditions, and at best can equal the adhesive joints performance;
- The PAA anodization process leads to better mechanical performance than the sandblast surface treatment;

- The failure mechanism of the anodized joint showed that the overlap length was over-dimensioned.

Figure 2.62 shows the SLJ tested until now by our workteam and the Table 2.14 the meaning of the specimens nomenclature.

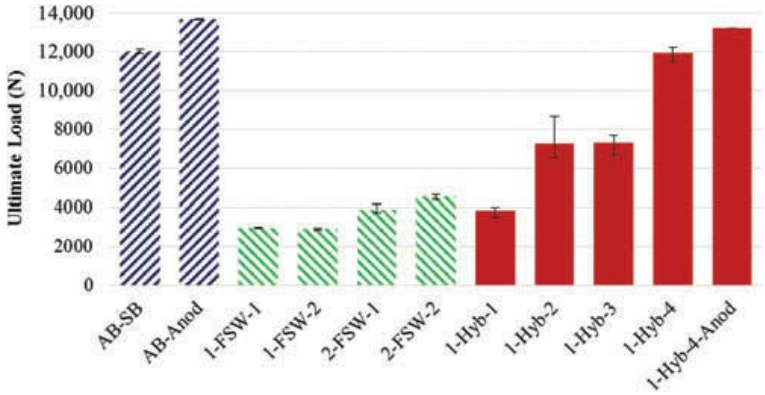

Figure 2.62: Single lap joints ultimate load. [77]

Table 2.14: Single lap joints ultimate load specimens nomenclature. [77]

Nomenclature	**Meaning**
AB-SB	Adhesive joint with sandblasted adherend
AB-Anod	Adhesive joint with anodized (PAA) adherend
1-FSW-1	FSW joint with one passage and 400 kgf
1-FSW-2	FSW joint with one passage and 450 kgf
2-FSW-1	FSW joint with two passages and 400 kgf
2-FSW-2	FSW joint with two passages and 450 kgf
1-Hyb-1	One passage, 400 kgf and channel for the adhesive
1-Hyb-2	One passage, 450 kgf and channel for the adhesive
1-Hyb-3	One passage, 400 kgf and without channel for the adhesive
1-Hyb-4	One passage, 450 kgf and without channel for the adhesive
1-Hyb-4-Anod	One passage, 450 kgf, without channel for the adhesive and PAA

Chapter 3

Experimental Details

In this Chapter 3 it will be addressed the experimental procedures and fundamental concepts in order to accurately assess and benchmark the *Quasi-static*, Fatigue and Dynamic behaviour of the different types of joints.

Figure 3.1 shows the main experimental workflow developed. The manufacturing of the three different joint types was the first step. In the case of adhesive joints an assessment on the best surface treatment was done. In order to determine the fatigue load levels to be studied *quasi-static* tests were done. A dynamic analysis, with the goal to assess the damping capabilities of the different joint types and relate with fatigue performance of these joints, was performed. An EDS analysis was also performed on the failure and anodization surfaces.

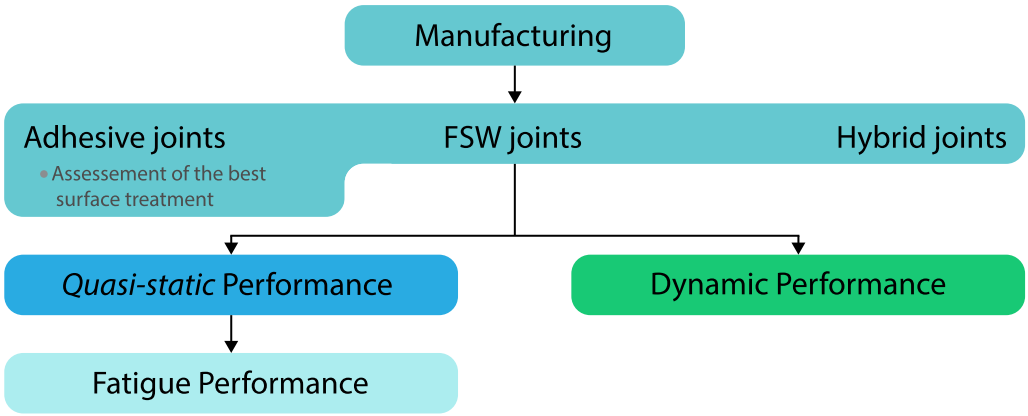

Figure 3.1: Work program.

3.1 Materials Properties

3.1.1 Aluminium substrates

For all the substrates, the material chosen was an aluminium alloy of the series 6XXX, the AA 6082-T6. This alloy containing magnesium and silicon, and is widely used in transportation and construction applications. This alloy is typically processed through forging, extruding or rolling.

The T6 condition is defined as an aluminium alloy tempered by the means of a solution heat treatment and artificially aged [78]. The chemical composition is shown in Table 3.1.

Table 3.1: Chemical composition of aluminium alloy AA 6082-T6 (*wt%*). [79]

	Al	**Cr**	**Cu**	**Fe**	**Mg**	**Mn**	**Si**	**Ti**	**Zn**	**Other**
Min.	95.2 %	0 %	0 %	0 %	0.6 %	0.4 %	0.7 %	0 %	0 %	0 %
Máx.	98.3 %	0.25 %	0.1 %	0.5 %	1.2 %	1 %	1.3 %	0.1 %	0.2 %	0.15 %

The two major alloying elements of this aluminium alloy are Manganese (Mn) and Silicon (Si). Some features associated with the use of Si are the improved castability (higher fluidity and lower shrinkage) and the improvement in the resistance to abrasive wear. Associated with the Mn there is an improvement in low cycle fatigue life and an increase of the alloy corrosion resistance. The presence of both elements strengths the alloy and improves the ductility due to the modification of Al_5FeSi intermetallic inclusions from platelet to cubic form $Al_{15}(MnFe)_3Si_2$. The resulting mechanical and physical properties are shown in Table 3.2.

Table 3.2: Mechanical and physical properties of AA 6082-T6 (*wt%*). [79]

Property	**Min.**	**Max.**	**AVG.**
Melting Point	575 °C	650 °C	612.5 °C
Density	2.67×10^3 kg/m^3	2.73×10^3 kg/m^3	2.7×10^3 kg/m^3
Hardness	95 HV	105 HV	100 HV
Young's modulus	70 GPa	74 GPa	72 GPa
Yield strength	240 MPa	290 MPa	265 MPa
Tensile Strength	280 MPa	340 MPa	310 MPa
Elongation	5 %	11 %	8 %
Shear modulus	25 GPa	27 GPa	26 GPa
Poisson's ratio	0.325	0.335	0.33
Fatigue strength at 1×10^6 **w/** 0.1 **ratio**	67.1 MPa	89.9 MPa	78.5 MPa

There is one particular property (mechanical loss coefficient) that can be useful to predict the dynamic response of the different types of joint. The mechanical loss-coefficient (a dimensionless quantity), measures the degree to which a material dissipates vibrational energy during an elastic loading cycle. The $\tan\delta$ value for this aluminium alloy is in the range of $[1 \times 10^{-4}$; 0.004]. [79]

In terms of fatigue behaviour the AA 6082-T6 presents a fatigue strength at one million cycles of 78.5 MPa that is about 25 % of the ultimate tensile stress of the material. The typical S-N curve of this alloy is shown in Figure 3.2.

The calculation of this S-N curve uses the material properties and some models like the Basquin and Coffin-Manson equations and Goodman's relation. The relations between the stress amplitude and the number of cycles to failure is given by Basquin's law for high cycle fatigue. Coffin-Manson's model relates the strain amplitude with the number of cycles to failure for low cycle fatigue. Goodman's model relates the stress amplitude with the mean stress, the corresponding zero mean stress and the ultimate tensile stress.

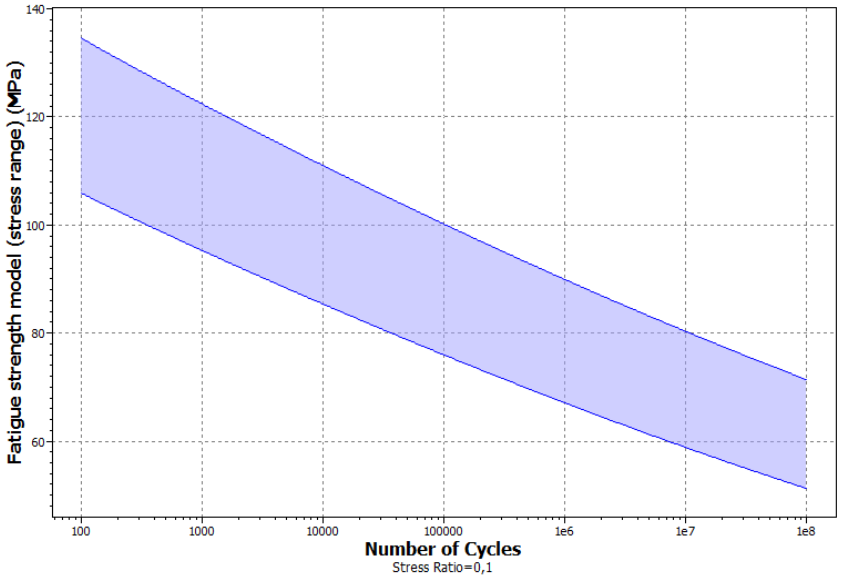

Figure 3.2: S-N curve of AA 6082-T6 w/ 0.1 R-ratio [79]

3.1.2 Adhesive - Araldite® 420 A/B

The Araldite® 420 A/B (from Huntsman, Basel, Switzerland) is an epoxy based adhesive that presents an high shear and peel strength, good toughness and resilience, fair moisture resistance and can bond several materials including metal, wood, rubber, fibreglass reinforced composites and many plastics. It is used in the transportation industry, including the aeronautical.

It can be cured at ambient temperature, however it takes between 7 to 15 days to fully cure (5 days to achieve 90% of the maximum strength). There are several cure cycles advised by the manufacturer, among them stands out a cure cycle of 1 (one) hour at 120 °C that allows the fully cure state to be obtained in a shorter time.

Our workteam, in previous work, characterized the adhesive and found the mechanical properties when cured at room temperature [22] presented in Table 3.3.

Table 3.3: Araldite® 420 A/B mechanical properties

Young's Modulus	**UTS**	**USS**	G_{Ic}	G_{IIc}	**Density**
1.85 GPa	30 MPa	35 MPa	3 N/mm	12.5 N/mm	1.05 g/cm^3

There is a peculiarity in the joints composed by this adhesive and the aluminium adherend that can be found not only on the work developed by our workteam and in the literature review as well. It was reported a consistent trend in obtaining an adhesive failure mode independently of the surface treatment used [59, 80]. The typical failure surface is shown in Figure 3.3.

The adhesive in the form of 200 ml cartridges was bought. It contains the two components of the adhesive (part A and B). This allows the mixture of the two components without the need of measurements, with the help of a mixer nozzle. This is the most similar way to the industrial

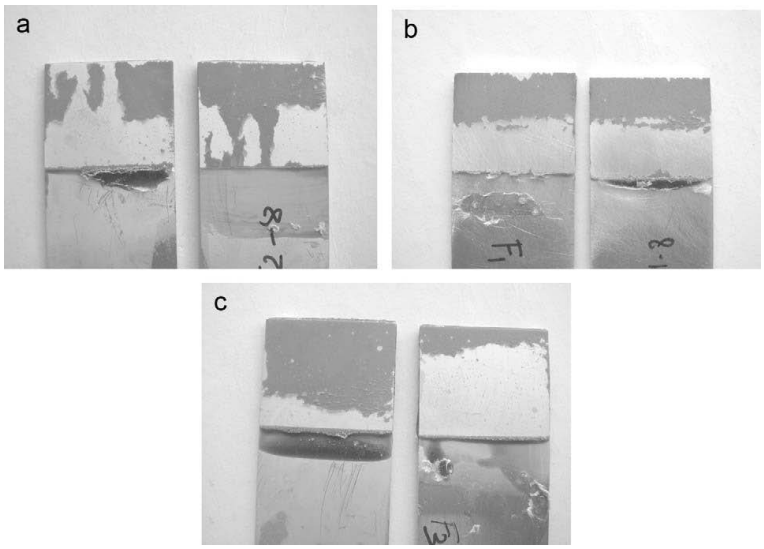

Figure 3.3: Araldite® 420 A/B failure mode with aluminium adherend. [59]

standards that demands a quick method to apply the adhesive manually or automatically (by a robotic arm).

Figure 3.4: Araldite® 420 A/B cartridge.

The CES Edupack software (material properties software) doesn't contain in its database the Araldite® 420 A/B in order to obtain the $\tan\delta$ value. However, being an epoxy based adhesive the damping capability should be similar to an epoxy resin. The $\tan\delta$ value obtained for an unfilled epoxy resin is ≈ 0.017. This is significantly greater than the values for aluminium AA 6082-T6.

3.2 Specimens geometry

The past work done by our workteam [22, 75] had specimens with a length of 160 mm a width of 20 mm and an overlap of 60 mm (Figure 3.5).

This geometry presented some problems in the assessment of the dynamic behaviour. The overlap length was very similar to the remaining specimen which caused a fatigue failure always in the adherend and not in the joint. Being the clamping length of 35 mm the free length of the specimen were of only 15 mm.

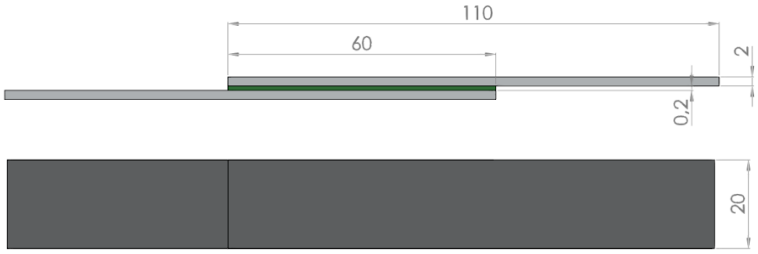

Figure 3.5: Geometry of the adhesive specimen used previously by our workteam. (dimensions in mm) [75]

In order to better assess the joints fatigue loads the free length of the specimen was changed from 50 mm to 110 mm and maintained constant thought all the work developed.

The initial plan was to study a small overlap near to the theoretical optimum for adhesive only joints. The overlap defined was enough to accommodate the FS welding and a considerable width of adhesive. The theoretical value found was near 17 mm of overlap, the overlap chosen was 20 mm in order to accommodate the shoulder of the FSW tool (16 mm of diameter). This is an extreme case of the smallest overlap possible to obtain in an hybrid FSW joint with the previous welding parameters in opposition to the work done before (overlap of 60 mm [75]).

However during the work the author and his workteam faced manufacturing difficulties that forced the production of a new group of specimens with another geometry, a new overlap length of 40 mm in the hybrid and adhesive joints. The free length of the specimen was equal to the other ones (110 mm).

For all the specimens used in *Quasi*-static, fatigue and dynamic tests the width was 25 mm and, as said before, 110 mm of free length. The specimen geometry of the FSW, adhesive and Weldbonded with 20 mm of overlap can be seen in Figure 3.6.

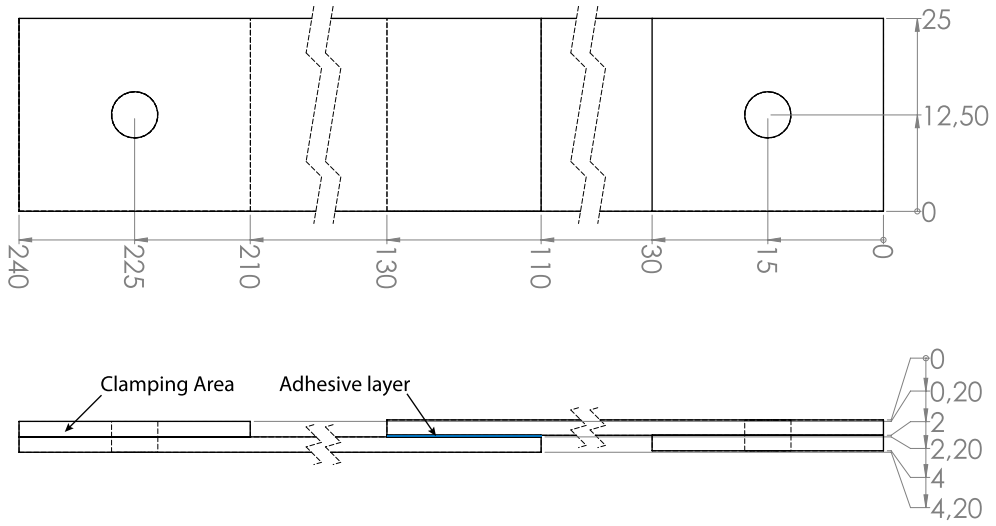

Figure 3.6: Geometry of the specimen used with an overlap of 20 mm.

The specimen with overlap of 40 mm is identical being the total length higher (260 mm vs 240 mm). The drawing can be seen in Figure 3.7.

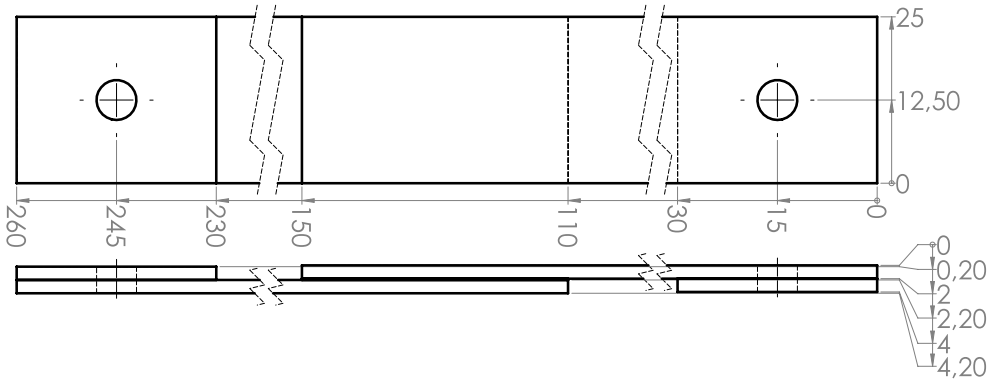

Figure 3.7: Geometry of the specimen used with an overlap of 40 mm.

In order to have a reference point on the maximum strength possible to obtain with the geometry of the joint with this adherend, dummy's specimens made of bare aluminium alloy (AA 6082-T6) were manufactured. The specimens were studied in *quasi*-static, fatigue and damping analyses. The geometry of the dummy is represented in Figure 3.8.

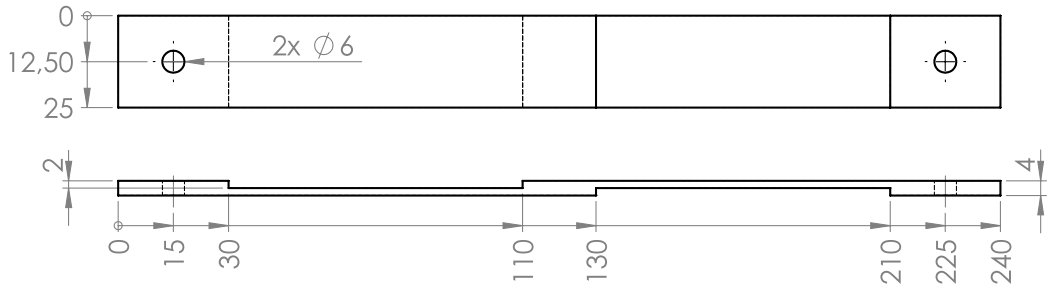

Figure 3.8: Geometry of the dummy's specimen used with an overlap of 20 mm.

3.3 Manufacturing process

The first experimental step was the manufacturing process. Joints were manufactured both at the adhesive joints manufacturing laboratory in Faculdade de Engenharia da Universidade do Porto (FEUP) and in mechanical technology laboratory in Instituto Superior Técnico (IST).

3.3.1 SL adhesive joints

The adhesive joints manufactured were all produced with the Araldite® 420 A/B. The single lap adhesive joints specimens manufactured for the tests consisted in two groups with different overlaps, 20 mm and 40 mm. The 20 mm and 40 mm specimens were tested in terms of static, fatigue and dynamic loading. However the fatigue study in the 40 mm of overlap specimens were not so extensive due to time frame limitations that will be addressed ahead.

The geometry of the specimen adopted was inspired by the ASTM D 1002 standard, being the existing differences an attempt to overcome the limitations of the previous geometry adopted in the past by our workteam. The adopted geometries are similar to those used in other researches, allowing a comparison with results from other works.

For all the adhesive joints the thickness of the adhesive layer was of 0.2 mm. This is a value within the range recommended by the manufacturer. It is also reported in the literature that for this kind of adhesive (epoxy based) the optimum adhesive layer thickness is between 0.1 and 0.2 mm, since higher thickness values lead to an increase in the secondary bending moment that consequently results in higher peeling stresses that may lead to a reduction of the joint strength.

The manufacturing process of the adhesive joints consisted on the following major steps:

- Machining the aluminium adherends;
- Surface preparation of the adherends;
- Preparation of the mold;
- Mixing and application of the adhesive and joint assembly;
- Curing under pressure.

3.3.1.1 Surface treatment

As mentioned before the surface treatment in an adhesive joint is a key step to maximize the strength of the bonding. In our workteam, in the past, it was found that the usage of an PAA anodization treatment compared to a simple sandblasting process of the adherends leaded to an increase in static strength of the joint of $\approx 14\%$ and an improvement in the maximum displacement of $\approx 145\%$. [75]

The first two lots of six specimens (maximum capacity of the mold used) of adhesive SLJ (20 mm overlap) were produced using the anodization guidelines used in the past by our workteam. The steps for the anodization process were:

1. Usage of sandpaper to abrade the bonding surface;
2. Manual acetone degreasing;
3. Adherends submerged in acetone for 5 minutes in a ultrasonic cleaner;
4. Anodization on a solution of 12 % acid phosphoric and 88 % of distilled water (% of mass) and an aluminium wire as a cathode;
5. Stoppage of the process with the submersion in tap water for 30 seconds;
6. After the anodization process the adherends were wrapped in aluminium foil until the moment that the adhesive was to be applied.

The usage of this method allied to the cure cycle adopted of 8 hours with pressure at ambient temperature and at least 7 days of cure time at the same temperature lead to a significant scatter in the ultimate strength and ultimate elongation between the 4 specimens tested.

The Load vs Displacement curves of the 4 specimens tested are shown in Figure 3.9 and the relevant results are summarized in Table 3.4.

Table 3.4: Load vs. Displacement relevant data of the first two lots

	Máx. Load	**Load scatter**	**Max. Disp.**	**Disp. scatter**	**Energy**
AB-sc-T1	14016 *N*	1.08%	2.014 mm	2.01%	17.70 *J*
AB-sc-T2	14653 *N*	3.41%	2.523 mm	22.77%	25.25 *J*
AB-sc-T3	13735 *N*	3.07%	1.883 mm	8.39%	16.13 *J*
AB-sc-T4	14273 *N*	0.74%	1.801 mm	12.37%	16.13 *J*
AVG.	14170 *N*	2.07%	2.055 mm	10.38%	18.80 *J*

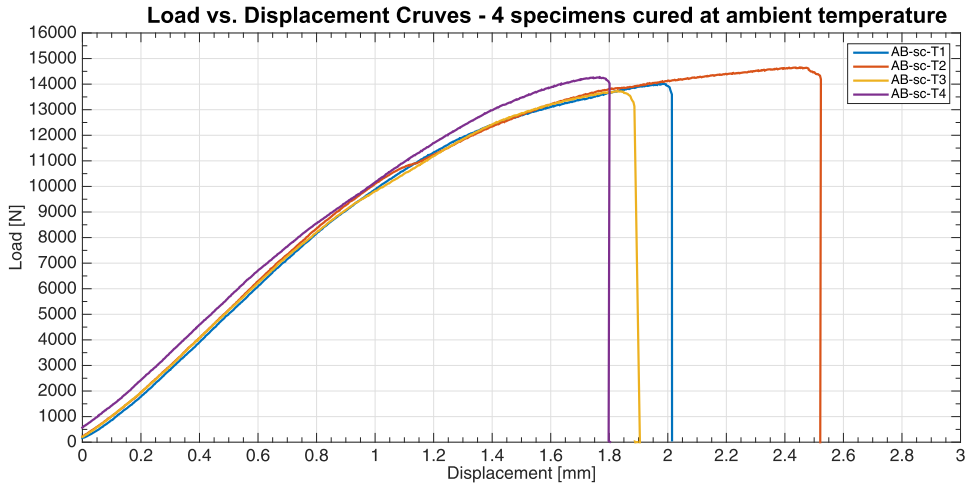

Figure 3.9: Load vs Displacement curves of the first two lots

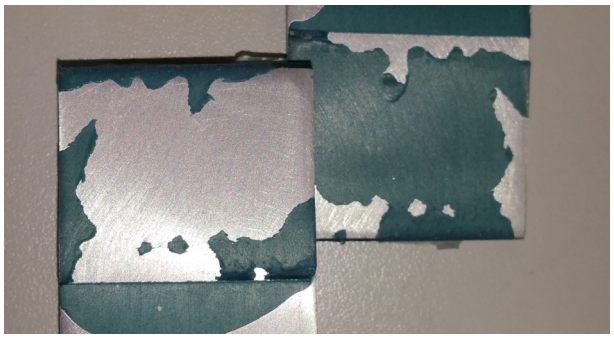

Figure 3.10: Adhesive failure surface of specimen B

As can be observed, a maximum scatter of 22.77% on the average value of maximum displacement is to high and may indicate that the process has uncontrolled variables. Another fact that sustains the possibility of doing better was the type of failure that was mainly adhesive instead of cohesive (Figure 3.10).

In an attempt to improve the failure mode and reducing the displacement scatter the author performed some changes in the anodization process according to the ASTM D 3933 as well altering the cure cycle. The new cure cycle adopted had the additional advantage of being more suitable to the time-frame limitations.

The new PAA anodization approach adopted was composed by the following steps:

1. Usage of sandpaper to abrade the bonding surface;
   1.1. Two passes in different directions with a rough sandpaper (#320 mesh);
   1.2. Three passes in different directions with a fine sandpaper (#800 mesh);
2. Degreasing;
   2.1. Manual acetone degreasing;
   2.2. Adherends submerged in acetone for 10 minutes in a ultrasonic cleaner;
3. Rinse stage with clean water for 5 minutes using an 4 litre rinse tank;
4. Anodization for 25 minutes;
   4.1. Solution of 12 % acid phosphoric and 88 % of distilled water (% of mass);
   4.2. Temperature monitoring to assure $T < 25\,^{\circ}\text{C}$;
   4.3. Bath agitation system;
   4.4. Stainless steel cathode with a larger area;
5. Rinse stage on clean water for 15 minutes with a 6 litre rinse tank;
6. Dry on clean air environment (fume hood) for at least 30 minutes until the application of the adhesive layer.

The improvements in the anodization process allied to a change in the cure cycle (120 °C for one hour) leaded to a decrease in the maximum and average displacement scatter. The failure mode obtained was mostly adhesive. The Table 3.5 shows the relative changes in the properties presented in Table 3.4 and Figure 3.11 and 3.12 . Complete information about the static test results will be addressed ahead in this report (in Chapter 3).

Table 3.5: Changes in the Load vs. Displacement relevant data after the new anodization approach

	Máx. Load	**Load scatter**	**Max Disp.**	**Disp. scatter**	**Energy**
AB-sc-T1	14016 *N*	1.08%	2.014 mm	2.01%	17.70 *J*
AB-sc-T2	14653 *N*	3.41%	2.523 mm	22.77%	25.25 *J*
AB-sc-T3	13735 *N*	3.07%	1.883 mm	8.39%	16.13 *J*
AB-sc-T4	14273 *N*	0.74%	1.801 mm	12.37%	16.13 *J*
AVG.	14170 *N*	2.07%	2.055 mm	10.38%	18.80 *J*
AB-T1	14517 *N*	0.98%	1.753 mm	5.85%	15.52 *J*
AB-T2	14682 *N*	0.15%	1.768 mm	5.03%	16.46 *J*
AB-T3	14781 *N*	0.82%	2.060 mm	10.88%	20.63 *J*
AVG.	14660 *N*	0.65%	1.862 mm	7.26%	17.54 *J*
Balance (Δ)	3%	319%	−9.42%	30.10%	−7%

The anodized surface was analysed at Centro de Materiais da Universidade do Porto (CEMUP) in order to find if the typical porous surface is achieved with the new approach. The results of this analysis will be presented in Chapter 4.4.1.

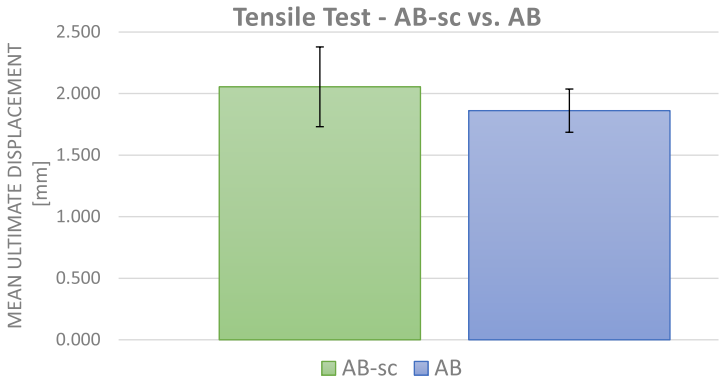

Figure 3.11: Mean maximum displacement obtained in specimens AB-sc and AB, with standard deviation.

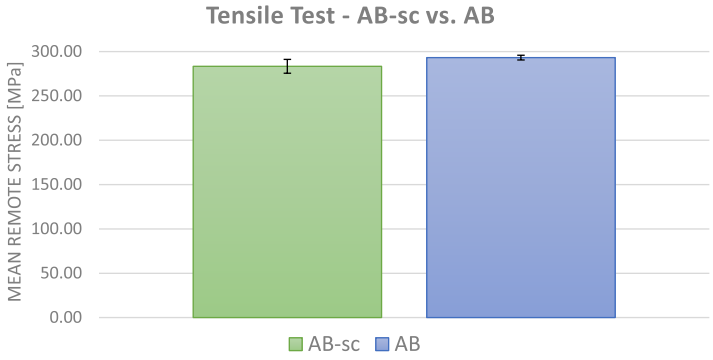

Figure 3.12: Mean maximum remote stress obtained in specimens AB-sc and AB, with standard deviation.

3.3.1.2 Joint assembly

After the surface treatment process the single lap joints were assembled. In order to easily produce SLJ with correct specimens alignment and dimensions, uniform pressure and temperature distribution, the members of the adhesive group at FEUP designed a special mould that can be seen in Figure 3.13. The mould is made of aluminium and allows the production of six specimens with 25 mm width at the same time with high quality and dimensional accuracy.

Prior to the adhesive preparation and joint assembly the mould needs to be cleaned and prepared. It's applied to the mould surface a chemical agent (release agent) Frekote® 770-NC from Loctite® that will prevent the bond of the excess of adhesive to the surface of the mould. Being this a chemical toxic agent there is the need to use the fume hood sleeve in order to perform this step safely. It's applied three coats with a brush.

The main components of the mould are the mould base and lid, the alignment pins, mould pins and the positioner blocks.

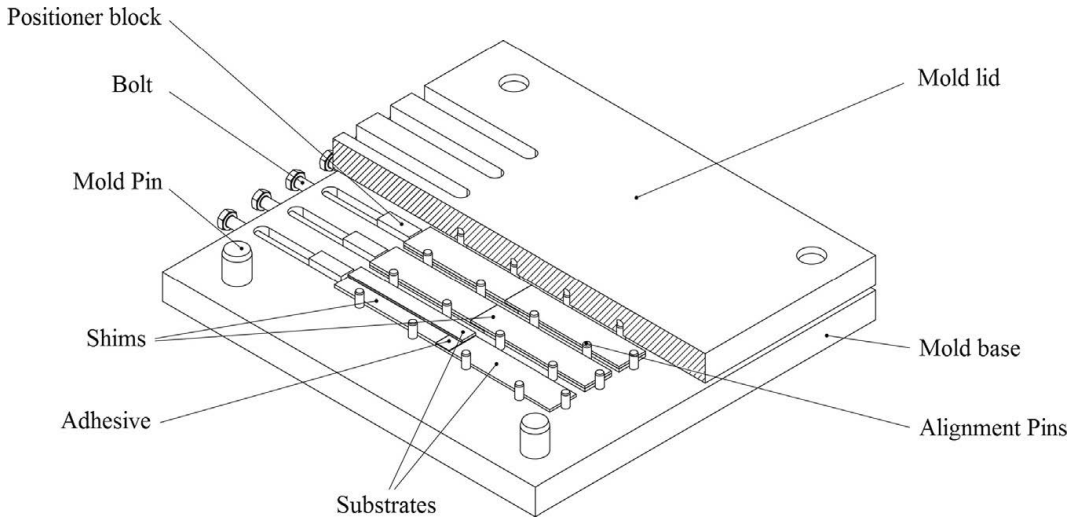

Figure 3.13: Mould with SLJ specimens. [81]

After the application of the release agent in the mould surfaces the preparation of the adhesive is performed. In order to produce the six specimens with 20 mm and 40 mm of overlap $\approx 10/20$ g of Araldite® 420 A/B adhesive is used which is poured from the cartridge to a small vessel with the help of a "gun" (Figure 3.14).

Figure 3.14: "Gun" and vessel used to pour and mix the adhesive.

The mixing of the adhesive (part A and B) was done in a centrifugal mixing machine (SpeedMixer^{TM}, FlackTek Inc, Landrum, South Carolina) for 4 minutes at a speed of 2500 RPM.

After the mixture of the adhesive the joint assembly was performed. For this step the calibration tape was important (to assure the adhesive layer thickness of 0.2 mm) and the packing shims (aluminium plates with the 25 mm width, 2 mm thickness and a length equal to the free length of the specimen) that assure the overlap length.

The joints were assembled carefully, one by one, under the fume hood sleeve to prevent any contamination due to dust or others. The application of the adhesive was done with a spatula, previously cleaned with acetone.

The first assembly step was to place one adherend (the bottom one) and one packing shim (under the shim were placed two rows of calibration tape with a thickness of 0.2 mm) in the base mould surface. Then it was placed another packing shim over the bottom adherend leaving the length of the overlap exposed. Then with the spatula the adhesive was applied. The top adherend was placed over the adhesive layer. The process was repeated for the six specimens and lastly the mould was closed. In Figure 3.13 and 3.15 is possible to observe the final result of the assembling of the joint in the mould.

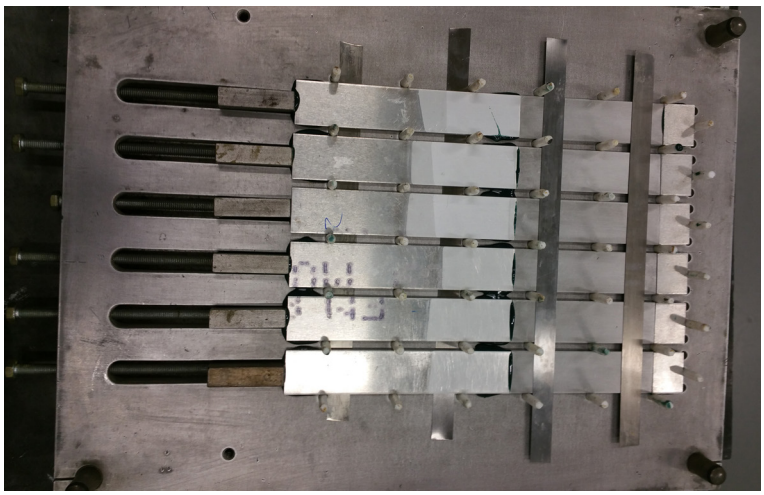

Figure 3.15: Adhesive SLJ specimens assembled in the mould.

3.3.1.3 Curing cycle

After the closure of the mould it was placed inside the hot press. There was the need to define the cycle cure and pressure to be applied.

As mentioned before, a curing cycle of 120 °C for one hour in conjunction with the changes in the anodization process lead to a better controlled process. So all the adhesive joints studied in static, fatigue and dynamic (vibration damping) were produced with this cure procedure (Figure 3.16). This is one of the cure cycles advised by the manufacturer and results in full strength immediately after the end of the cooling stage.

The pressure used in all specimens was the used before by our workteam. It was set to ≈ 11 bar and maintained constant during all the cure cycle. That pressure value is enough to avoid air entrapment and voids within the adhesive layer.

The applicability of this kind of cure cycle is not always easy to achieve in the industry, mainly for workpieces of big dimensions or that present temperature sensitive components already assembled when the joint is performed. However under this work the adhesive joint is meant to set a benchmark, this means that if this particular cure cycle allows better results it can be compared to the best configuration possible in the FSW and hybrid joints.

Once the curing process was completed, the specimens were withdrawn from the mould and separated (the adhesive between the specimens was cut) with an handsaw and any excess adhesive

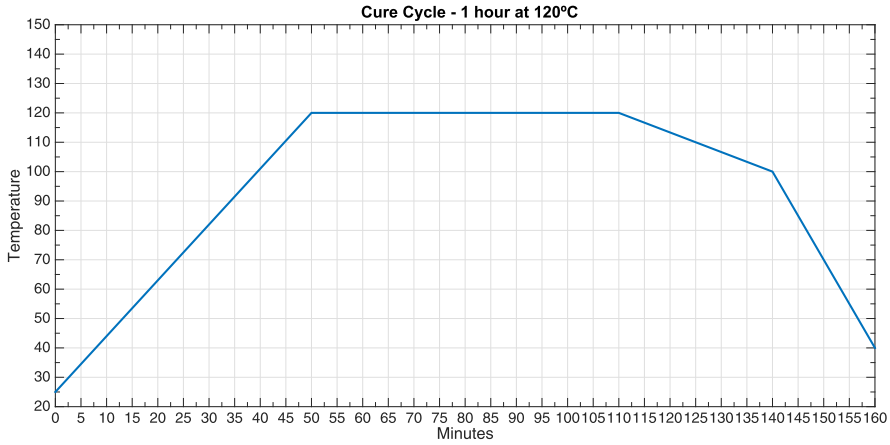

Figure 3.16: Cure cycle for Araldite® 420 A/B.

was removed using a rasp and sandpaper. After that final preparations the specimens were ready to the following tests.

3.3.2 FSW joints

The FSW single lap joints were all manufactured with the collaboration of IST (owner of the FSW machine used).

As mentioned in the Chapter 2 in the FSW process several parameters are very important like the clamping system, the alignment of the plates, and all the parameters that can be chosen in the machine.

All the FSW single lap joints produced had an overlap of 20 mm and were tested in terms of static, fatigue and dynamic solicitations.

The machine used to perform the welding was an ESAB® LEGIO^{TM} 3UL numeric control machine, being the tool used a modular one with a cylindrical threaded pin with 5 mm diameter and a 16 mm diameter shoulder (Figure 3.17).

Figure 3.17: ESAB® LEGIO^{TM} 3UL numeric control machine.

All the FSW joints studied had an overlap length of 20 mm being the welding line performed approximately in the middle of the overlap. In order to perform the welding it's necessary to have plates with bigger width than the specimens because the beginning of the weld present lower mechanical properties. It is also difficult to weld a small length. The AA 6082-T6 plates used to produce the FSW joints and the joint configuration are represented in Figure 3.18.

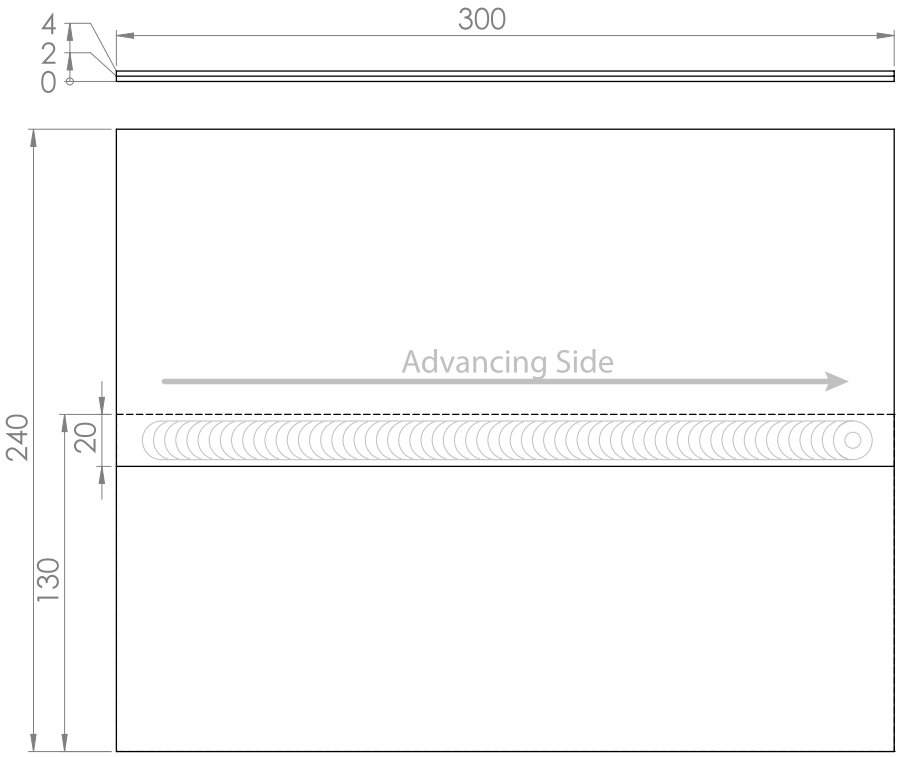

Figure 3.18: FSW joint drawing.

As mentioned in Sub-subsection 2.1.4.5, the FSW joints were manufacture with a configuration that assures that the advancing side was always loaded on the top sheet what maximizes the joint strength.

3.3.2.1 Welding parameters

The FSW joints studied had a single pass and were manufactured with the parameters that revealed best performance in past work done by our workteam [75] except the load that was fixed at 425 kgf (in previous work was studied two load levels, 400 and 450 kgf and was found that the joint strength was almost insensitive between the two levels) in order to assess if the strength stays the same or if there is a significant change.

The welding parameters used to perform the FSW welding are shown in Table 3.6.

The clamping system used built-in the substrates in order to perform the FSW welding (Figure 3.19). The x movement (red axis) is prevented by a groove present in the base. The pressure exercised by the clamping plates is the main responsible for the clamping in the y and z direction.

Table 3.6: FSW parameters.

Parameter	Value
FSW control	*Vertical force*
Rotation direction	*CW*
Plunge speed	0.1 mm/s
Dwell time	5 s
Tilt angle	0°
Welding speed	200 mm/min
Rotational speed	1000 RPM
Downward force	425 kgf
Probe length	3 mm
Should diameter	16 mm
Pin diameter	5 mm

The packing shims act like in the adhesive joints, assuring the overlap length. The alignment system assures that the welding is performed in the middle of the overlap and is parallel to the longitudinal edge of the specimen.

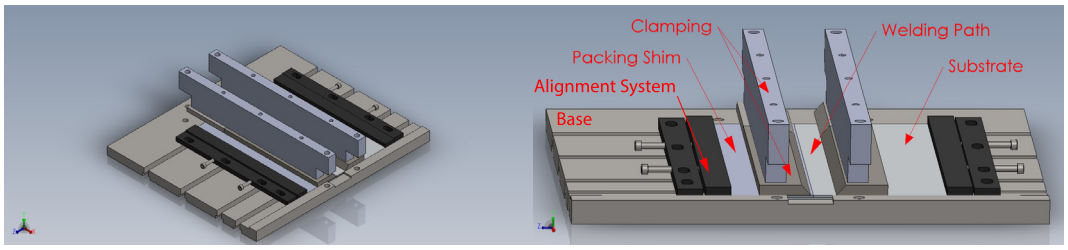

Figure 3.19: FSW clamping system used.

The tool used is modular, the shoulder and pin geometry and dimensions can be changed. The shoulder used has a flat surface with an helical path relief. The pin selected was a threaded cylinder. The tool is shown in Figure 3.20.

Figure 3.20: Modular tool used in FSW and hybrid joints.

3.3.2.2 Manufacturing steps

The manufacturing of the FSW joints was done following the subsequent steps:

1. Mounting the pin and shoulder on the modular tool;
2. Assure the correct length of the pin (3 mm);
3. Mounting the tool on the ESAB® LEGIO^{TM} 3UL numeric control machine;
4. Pressing the tool against a plastic surface with ≈ the double of the load used in the welding in order to tighten the screws;
5. Program the zero reference point of the machine;
6. Place the bottom substrate and a packing shim on the base;
7. Place the upper substrate and packing shim;
8. Alignment of the substrates with the help of the alignment system;
9. Placing of the clamping plates over the upper substrate and shim;
10. Screwing, uniformly, the alignment system and loading of clamping system;
11. Beginning of the welding process with a dwell time of 5 seconds and the parameters defined. (Table 3.6);
12. Monitoring of the process until the end;
13. Cutting the welded plates into the final geometry (specimen geometry).

3.3.3 Dummy's of bare aluminium AA 6082-T6

The dummy specimens were produced by machining a 4 mm thick AA 6082-T6 plate in order to obtain a geometry identical to the other specimens with 20 mm of overlap.

3.3.4 Hybrid joints

The manufacturing process of the FS Weldbonded joints is a combination of the two process described until now and share some common points. Like in the case of the SL adhesive joints, the hybrid ones produced, consisted in two groups with different overlaps, 20 mm and 40 mm. Due to limitations of the process (addressed in Chapter 4) the 20 mm overlap specimens were tested in terms of static and dynamic solicitations. The 40 mm of overlap specimens were tested under static, fatigue and dynamic solicitations (damping capabilities).

In order to produce the FS Weldbonded single lap joints the procedure developed previously by our workteam was adopted, except the surface treatment. The surface treatment used was the PAA anodization process with the changes implemented by the author according to the ASTM standard (described in Sub-subsection 3.3.1.1).

The manufacturing process of the adhesive joints consisted on the following major steps:

- Machining the aluminium adherends plates (similar to the plates used in the FSW process);
- Surface preparation of the adherends plates using the PAA anodization;
- Mixing and application of the adhesive and joint assembly;

- FS welding;
- Curing process.

In order to mix and apply the adhesive in the FS Weldbonded SLJ it was used a cartridge of adhesive, a "gun" and a nozzle (assures the mixing) as seen in Figure 3.21.

Figure 3.21: "Gun" and mixer nozzle used to produce the hybrid joints.

The adhesive layer was chosen to have 0.2 mm of thickness like the adhesive SL joints. However, despite the usage of the calibration tape of 0.2 mm, the thickness is not always easy to obtain due to the high loads and deformations induced by the friction stir welding process.

The welding parameters used in the hybrid joint manufacturing are shown in Table 3.7.

Table 3.7: Welding parameters used in hybrid joints.

Parameter	**Reference**	**Value**	**Reference**	**Value**
FSW control		Vertical force		Vertical force
Rotation direction		CW		CW
Plunge speed		0.1 mm/s		0.1 mm/s
Dwell time		5 s		5 s
Tilt angle		0°		0°
Welding speed	**Hyb-450**	200 mm/min	**Hyb-425**	200 mm/min
Rotational speed		1000 RPM		1000 RPM
Downward force		450 kgf		425 kgf
Probe length		3 mm		3 mm
Should diameter		16 mm		16 mm
Pin diameter		5 mm		5 mm

It's important to lay emphasis on the main difference between the two hybrid SLJ, which is in the downward force used. The two different group of specimens were tested to assess if the result obtained in the past by our workteam is valid for different overlap lengths. In previous work was proven that with an overlap of 60 mm the force that leaded to the best results in *Quasi*-static tests was the 450 kgf. This welding parameter is the only one that changes in the hybrid joints.

3.3.4.1 Manufacturing steps

The manufacturing of the Hybrid joints was done following the subsequent steps:

1. Mounting the pin and shoulder on the modular tool;
2. Assure the correct length of the pin (3 mm);
3. Mounting the tool on the ESAB® LEGIO^{TM} 3UL numeric control machine;
4. Pressing the tool against a plastic surface with ≈ the double of the load used in the welding in order to tighten the screws;
5. Program the zero reference point of the machine;
6. Place the bottom adherend and a packing shim (under the shim was placed two pieces of calibration tape of 0.2 mm) over the base;
7. Place the upper packing shim;
8. Appliance of the adhesive, with the help of the "gun" and nozzle, over the exposed overlap length;
9. Place the upper aluminium plate adherend over the adhesive;
10. Remove the excess of adhesive;
11. Alignment of the substrates with the help of the alignment system;
12. Placing of the clamping plates over the upper substrate and shim;
13. Screwing, uniformly, the alignment system and loading of clamping system;
14. Beginning of the welding process with a dwell time of 5 seconds and the parameters defined. (Table 3.6);
15. Monitoring of the process until the end;
16. Cutting the welded plates into the final geometry (specimen geometry).

The result of the manufacturing is shown in Figure 3.22. The $A8$ reference represents the beginning of the weld, the $A0$ represents the end (that has the keyhole).

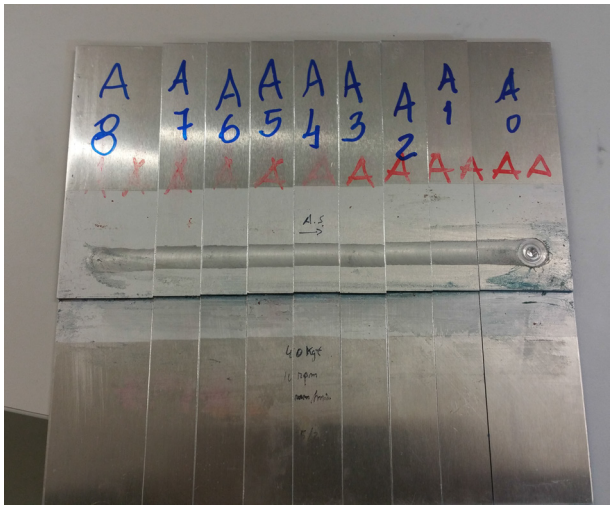

Figure 3.22: Hybrid joint after cutting

3.4 *Quasi*-static tests

The *Quasi*-static tests under constant displacement rate had the goal of characterizing the different kind of joints and to determine the performance differences between them. All kinds of joint produced were tested under this loading conditions. Also the adhesive itself was tested as a bulk specimen.

3.4.1 Bulk tensile test

For the adhesive bulk tests an universal test machine INSTRON® (Norwood, Massachusetts, USA) model 3367, equipped with a load cell with a maximum capacity of 30 kN was used.

The bulk testing allowed to determine the stress-strain curves at low strain rate (1 mm/min). This goal is achieved with the measurement of the load and the displacement during the test (an extensometer to record the displacement was used). Loads and displacements were recorded up to failure. This characterization is important to accurately determine mechanical properties of the adhesive that can be an input for the FEM simulations. The adhesive characterized was the Araldite® 420 A/B with the cure cycle adopted (one hour at 120 °C).

The specimens used were produced according to the EN ISO 527-2 standard. The long specimen defined in the standard was used. It's a common practice to use this specimen version on epoxy based adhesives. The details of the geometry are presented in Figure 3.23.

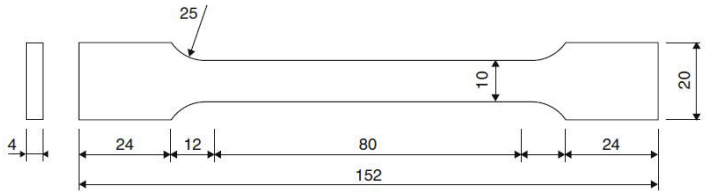

Figure 3.23: Geometry of the long specimen according to EN ISO 527-2 (dimensions in mm)

The testing procedure consists in the loading of the specimen in a longitudinal direction until failure. The strain rate of the test influences the behaviour of the adhesive, due to the high sensitivity that they present as a intrinsic characteristic. In the scope of this Master thesis only the low strain rate was accounted. It's important to refer that this kind of data obtained is not valid for example as an input for FEM analysis of high velocity impact tests.

3.4.2 FSW, Adhesive and Hybrid joints tensile static tests

All different types of specimens produced were tested under tensile *Quasi*-static loads with a displacement rate of 1 mm/min that was maintained constant during the test. This kind of test allows the assessment of the joint strength and it's useful to define the load levels of interest to study under cyclic loads (fatigue).

To perform those tests an universal test machine INSTRON® model 3367 (at IST), with maximum load capacity of 50 *kN* and a servo-hydraulic MTS® machine (at FEUP) with a maximum capacity of 250 *kN* were used.

A constant displacement rate of 1 mm/min until failure was maintained. The tests allowed to obtain the Load vs Displacement curves being possible to measure the maximum load and displacement at failure.

In order to minimize the effect of the eccentric load were used tabs with 2 mm of thickness and 25×30 mm (W×L).

The clamping system used in the servo-hydraulic machine is shown in Figure 3.24.

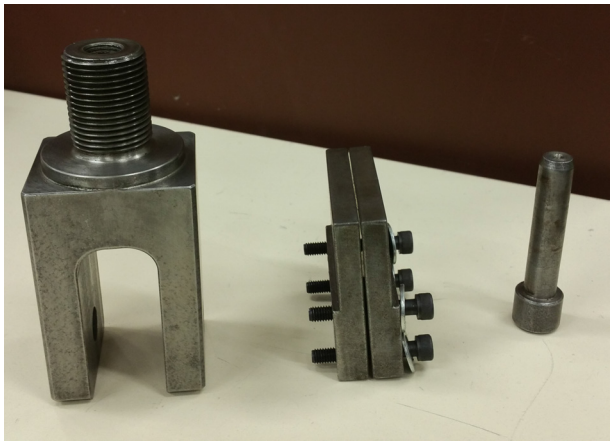

Figure 3.24: Clamping system used in the tensile tests.

3.5 Fatigue tests

It's well known that a material subjected to repeated stress cycles may fail even when the peak stress is well below the tensile strength, or even below the yielding limit. This phenomena is called fatigue failure. Despite the full mechanism of the fatigue behaviour is not completely understood there is the need to design and predict the behaviour of a structure under cyclic loads that may lead to fatigue failure. In order to attend that need there are three major fatigue life methods used in design and analysis. The stress-life method, the strain-life method, and the linear-elastic fracture mechanics method. These three different methods attempt to predict the specimen life in number of cycles to failure (N) for a specific level of loading (force, stress or strain). [50]

In Figure 3.25 is presented an example of an S-N curve with low and high cycle fatigue. Generally the distinction between two regimes of fatigue loading and behaviour is done. A life of $1 \leq N \leq 10^3$ cycles is generally classified as low-cycle fatigue, whereas high-cycle fatigue is considered to be $N > 10^3$ cycles. The main interest under the scope of this Master thesis is study the high cycle fatigue that is governed by the Basquin law.

The method used under this work is widely used to benchmark a material under fatigue loads, the stress-life method. In this method, in order to determine the strength of the materials under

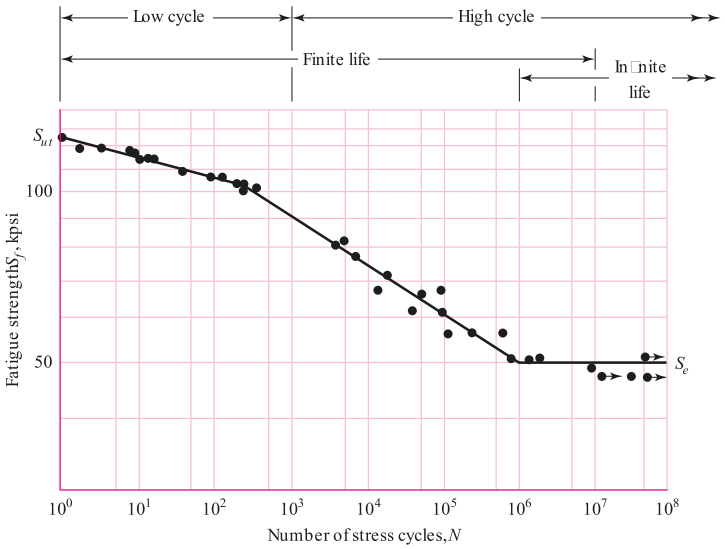

Figure 3.25: Example of an S-N curve with low and high cycle fatigue. [50]

the action of fatigue loads, specimens are subjected to repeated or varying forces of specified magnitudes while the cycles or stress reversals are counted to destruction. Several levels of loads are tested. To establish the fatigue strength of a joint there is the need to perform a considerable number of tests for each load level because of the statistical nature of fatigue. Due to time frame limitations the number of specimens tested were limited, however were the necessary to present a supported trend of the behaviour of each type of joint.

The S-N curves are the main objective of the fatigue analysis developed, and it may allow to compare and infer if the hybridization of the FSW joint leads to a better fatigue performance.

To perform the fatigue tests and obtain the S-N curves, stress/load spectrums with constant amplitude loading were defined. The load ratio (or stress ratio) represented as R, was defined as a common parameter through all the specimens independently of the nature of the joint. The value was:

$$R = \frac{P_{min}}{P_{max}} = \frac{\sigma_{min}}{\sigma_{max}} = 0.1$$

It indicates that the sinusoidal load spectrum as a minimum value that is 10% of the peak load/stress.

The loading spectrum that the joints are subjected is shown in Figure 3.26.

The maximum stress (σ_{max}) is defined as a fraction of the ultimate stress. The minimum stress (σ_{min}) is defined with the R and the σ_{max}. The medium stress/load (σ_m/P_m) can be defined as:

$$\sigma_m = \frac{\sigma_{max} + \sigma_{min}}{2}$$

and the stress/load amplitude (σ_a/P_a) as:

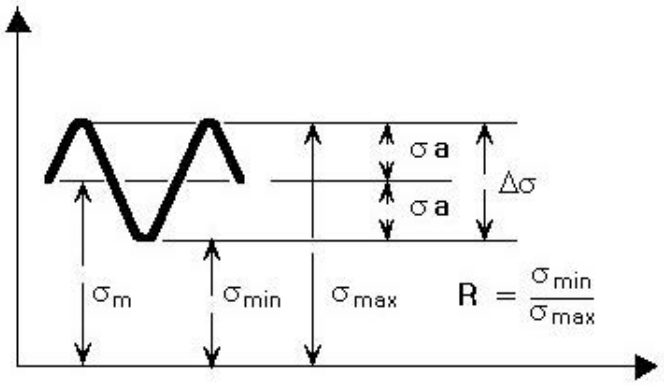

Figure 3.26: Cyclic stress spectrum and parameters used to define it.

$$\sigma_a = \frac{\sigma_{max} - \sigma_{min}}{2}$$

The infinite life criteria (stoppage criteria) was set on $N = 2 \times 10^6$.

Under this study the different levels studied were expressed in remote stress, however it's easy to obtain the results in levels of average shear stress. The advantage of the remote stress is that it's independent of the area of the overlap.

According to the Best Practice Guide on Statistical Analysis of Fatigue Data produced by the International Institute of Welding [82], there are four assumptions that need to be respected in order to obtain a valid S-N curve and they are the following:

1. There is an underlying linear relationship between logS and logN of the form:

$$\log N = \log A - m \log S$$

   This will only remain true between certain limits on S;
2. The fatigue life N for a given stress range S is log-normally distributed;
3. The standard deviation of log N does not vary with S.;
4. Each test result is statistically independent of the others.

All this assumptions were verified and are in accordance to the reality of the tests done.

3.6 Energy-dispersive X-ray spectroscopy (EDS) and failure surface observations

It was performed failure surface microscopic observations and Energy-dispersive X-ray spectroscopy (EDS) analysis in the three different types of joint studied in order to asses the chemical composition of each failure surface as well to find which failure mode was obtained. This analysis was also useful to evaluate the quality of the manufacturing process of each joint type. The failure

surfaces observed were an adhesive and FSW joint after fatigue loadings, hybrid joints after tensile tests and an anodization surface.

The goals were:

1. Find if the anodization process used produced the right porous surface;
2. Assess if the failure mode of the adhesive and hybrid joints was mixed, cohesive or adhesive;
3. Identify the source of manufacturing problems in the hybrid joints;

The EDS technology is based on the detection of characteristic X-rays emitted by an element as a result of the de-excitation of core electron holes created by an high energy electron beam. The de-excitation is read by the machine and generally the electron energy levels are different from element to element with only a few spectral peaks overlapping. The EDS technique can be used to determine the composition of a specimen as a whole as well as the composition of individual components. The X-rays that have sufficient energy to escape the material surface can be detected, resulting in a spectrum with peaks at the characteristic energies for the elements present. The measurements are expressed as a quantitative composition.

The tests were performed at CEMUP, the machine used is shown in Figure 3.27.

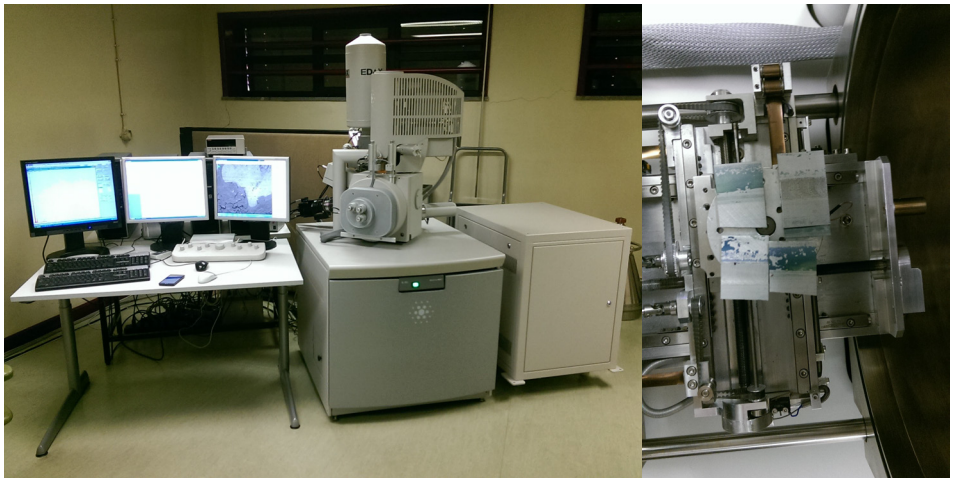

Figure 3.27: EDS machine used at CEMUP.

3.7 Dynamic analysis

The damping capabilities of the joints has implications in terms of health, safety and comfort on the structure where they are implemented. Since this kind of analysis is inexistent in the literature with this kind of joints, is useful to investigate their behaviour. In order to assess the damping capabilities of different kind of joints and benchmark them, an experimental set up was developed in order to obtain the damping ratio (ξ) for the first three natural modes with free-free boundary conditions. Frequency Response Functions (FRF) of the joints were obtained. This analysis can be useful to establish a parallel between the damping capabilities and the fatigue performance.

Damping exists in all vibratory systems and it's responsible for removing the energy of the system. The majority of the mechanical structures are inherently lightly damped. In free vibration, the loss of energy from damping in the system results in the decay of the amplitude of motion. [83]

The modal testing set up used was the frequency response function method, which measures the input excitation and output response simultaneously, as shown in the block diagram in Figure 3.28.

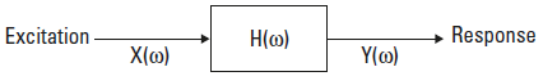

Figure 3.28: System block diagram. [84]

A load is used as an input, a technique commonly known as single-point excitation, for simple structures like the joints tested for making measurements the exciter mechanism can be as basic as an instrumented hammer. The main part of the test system is the controller which is the link between the human and the analyser. The transducers and a suitable power supply are needed to measure input force and responses. The piezoelectric types, which measure force and acceleration, are the most widely used for modal testing. Figure 3.29 shows the schematics of a typical set up for this kind of analysis.

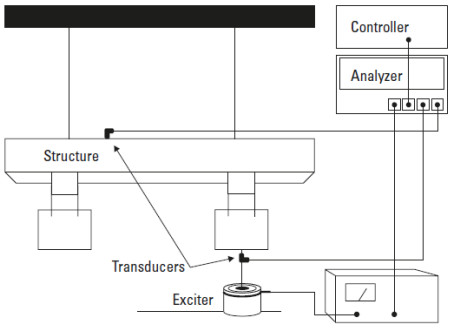

Figure 3.29: Typical set-up. [84]

The first step in setting up a structure for frequency response measurements is to consider the fixturing mechanism necessary to obtain the desired constraints (boundary conditions). Analytically, boundary conditions can be specified in a completely free or completely constrained sense. The free condition means that the structure is floating in space with no attachments to ground and exhibits rigid body behaviour at zero frequency. A typical example of this type of boundary condition is an airplane in mid air.

This type of boundary condition was chosen to study the joints. The implementation of a constrained system is more difficult to achieve in a test environment. There are several factors that influence the accuracy of the measurements like the base to which the structure is attached that tends to have some motion. Also, the attachment points will have some degree of flexibility due to the bolted connections.

In order to suspend the structure soft elastic cords were used. The typical FRF obtained in a structure with free-free boundary conditions is shown in Figure 3.30.

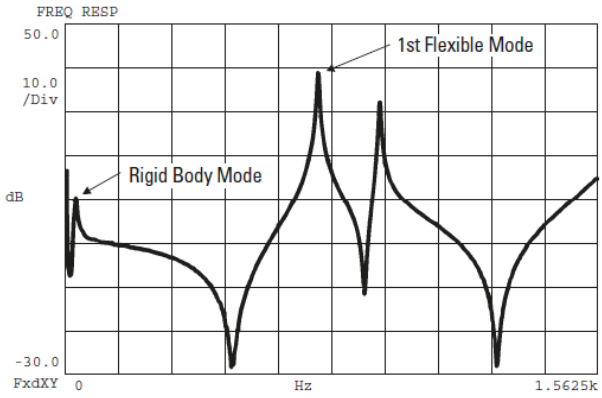

Figure 3.30: Typical FRF obtained. [84]

The excitation method chosen (instrumented hammer) dictates an impulsive type of excitation function. It is a common excitation mechanism in modal testing and it's called an impact device. The hammer used is shown in Figure 3.31.

Figure 3.31: Hammer used.

Since the force is an impulse, the amplitude level of the energy applied to the structure is a function of the mass and the velocity of the hammer (linear momentum). The specimens studied had a mass that was in the range of 33 to 44 g. The hammer used was of reduced size in order to induce a proper level of energy in the joint.

The force pulse is very short relative to the length of the time record, the portion of the signal after the pulse is signal noise and was eliminated without affecting the pulse itself with the usage of a force window. The response signal is an exponential decaying function. It decayed out after the end of the measurement like the guidelines in this kind of tests recommend.

The transducer coupled to the structure in study is responsible to measure the output. Generally an accelerometer is used, that when vibrates, an internal mass applies a force to crystal element which is proportional to the acceleration [83]. They are based in the Newton's Law. A good accelerometer needs to have linearity under the frequency range of interest. The accelerometer used had a mass of 2 g and was an unidirectional one. The effect of mass loading from the accelerometer is an important factor. When the mass of the accelerometer is a significant fraction of the

effective mass of a particular mode it influences to much the measurements. The accelerometer chosen represented 6% of the mass of the specimen which is a good value.

Tests were made in two specimens of the different kind of joints. In each specimen were done three measurements.

It was saved the frequency response function (FRF) and the coherence function that allows the assessment of the coherence between values obtained in the three measurements done by specimen.

The set-up used is shown in Figure 3.32.

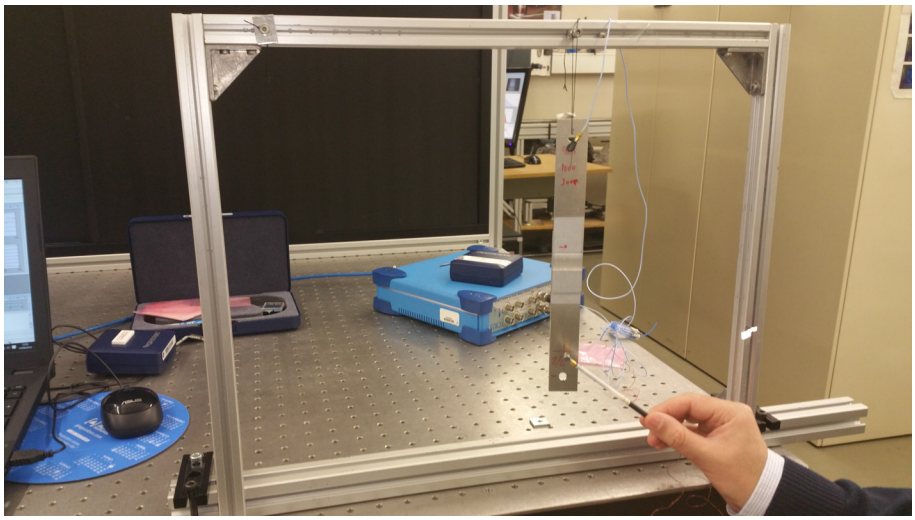

Figure 3.32: Damping analysis set-up used.

In order to reduce the statistical variance of a measurement with a random excitation function (such as random noise) and also reduce the effects of non-linearities, it is necessary to employ an averaging process. For each specimen, three measurements were done, resulting in a average FRF and a coherence function, providing statistical reliability.

The specimens studied were the FSW and adhesive joints with 20 mm of overlap, the hybrid and adhesive joint with 40 mm of overlap.

In order to obtain the ξ the half-power bandwidth method (or 3dB method) was used. This method enables the evaluation of damping from vibration tests. It assumes that the damping ratio ξ is small and that the frequency of maximum amplitude is approximately equal to the undamped natural frequency. The relation between the damping ratio to the half-power bandwidth can be expressed by:

$$\xi = \frac{\omega_b - \omega_a}{2\omega_n} \tag{3.1}$$

Where ω_a and ω_b are the half-power frequencies, they can be found 3dB bellow the ω_n. The equation 3.1 is valid for damping ratio less than 0.1 ($\xi < 10\%$). [85]

Being the damping ratio a dimensionless measure it will be used to assess the damping capabilities of each type of joint.

Chapter 4

Experimental Results

In Chapter 4, the experimental results obtained during static, fatigue, dynamic tests and EDS of the specimens are presented. The analysis and discussion of this results is also made.

4.1 Bulk tensile *quasi*-static test

This kind of test allows to obtain the Young's modulus, the ultimate tensile stress and the maximum strain of the adhesive, that can be used in FEM simulations and to understand the joint behaviour. Our workteam had already fully characterized the adhesive for another cure cycle (7 days at ambient temperature) and bulk tests for other two cures were done. The results obtained will be compared with these obtained in the past.

A representative stress vs strain curve for the result was compared to the curve obtained in the past for the cure cycle at room temperature and it's shown in Figure 4.1.

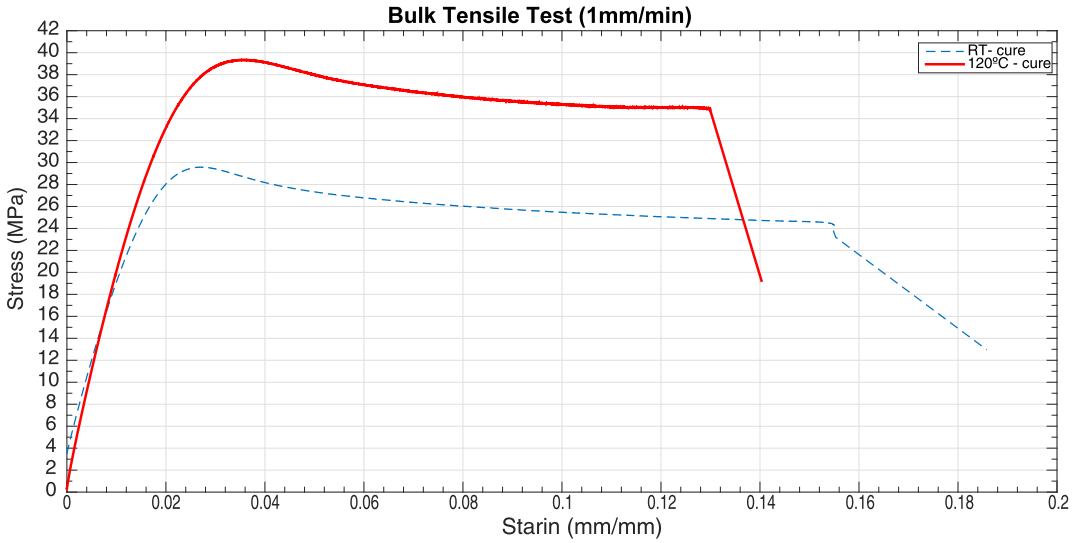

Figure 4.1: Experimental curves for the tensile bulk test of the Araldite® 420 A/B.

As expected there was a slight increase in the Young's modulus when the cure temperature was raised. The ultimate tensile stress also increased with the rise of the temperature. The maximum strain has reduced with increase of the cure temperature, being the adhesive more brittle. The effects of the cure lead to a stiffer and stronger material, however less ductile. The Table 4.1 summarizes the mechanical properties obtained in the tensile bulk test with the three specimens tested.

Table 4.1: Adhesive mechanical properties obtained in the tensile bulk test (1 mm/min).

Young's modulus	**Ultimate tensile stress**	**Maximum strain**
1869 ± 172 MPa	38.11 ± 1.09 MPa	14.47 ± 1.09 %

Using the mechanical properties obtained in the past by our workteam [22, 75] it's possible to find a trend on the UTS of the adhesive depending on the curing cycle.

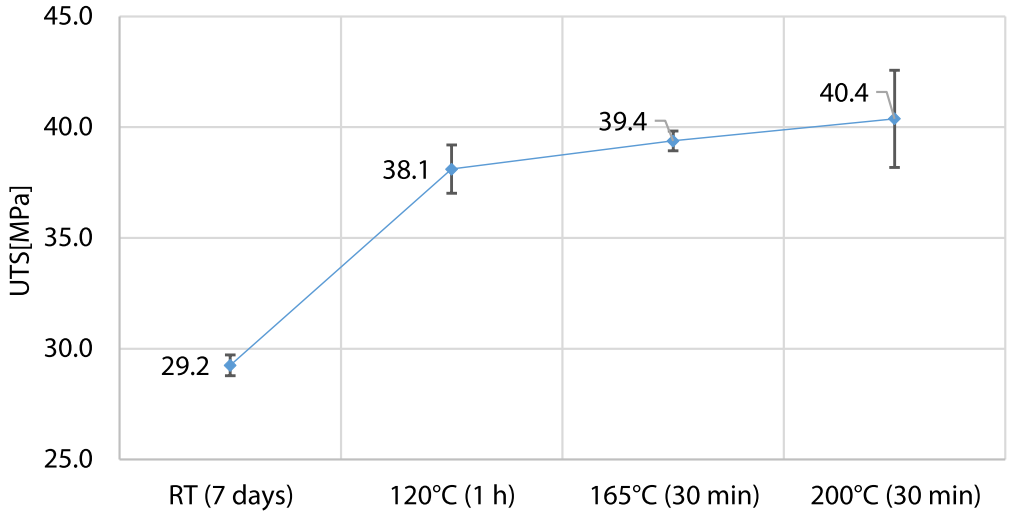

Figure 4.2: UTS of Araldite® 420 A/B bulk vs. cure temperature.

In Figure 4.2 is possible to observe that the UTS obtained with a cure at room temperature is clearly lower than the UTS obtained with curing temperatures above 120 °C. However, there is no significant difference in the UTS between the cure cycles with high temperature. The trend obtained presents a logarithmic shape where a plateau is reached. This means that the adhesive cured at room temperature will always present lower strength, however the ductility will be higher. The plateau is an interesting feature, if the application of high temperatures is allowed without constraints it's possible to reduce even more the production time without changing significantly the mechanical properties of the adhesive.

4.2 *Quasi*-static tests on SLJ

The *quasi*-static tests performed during the work were useful to assess the joint static strength, the quality of the manufacturing process and determine the load levels to the fatigue tests. All tests were done with a displacement velocity of 1 mm/min.

4.2.1 20 mm overlap SLJ

The research plan defined contemplated the static study of three different specimens (adhesive, FSW and hybrid joints), the author proposed the study of a dummy specimen too. All of them with 20 mm of overlap

4.2.1.1 Bare AA 6082-T6 dummy (DM)

The dummy specimens allowed to set a reference point on the maximum strength possible to obtain using AA 6082-T6 in this configuration.

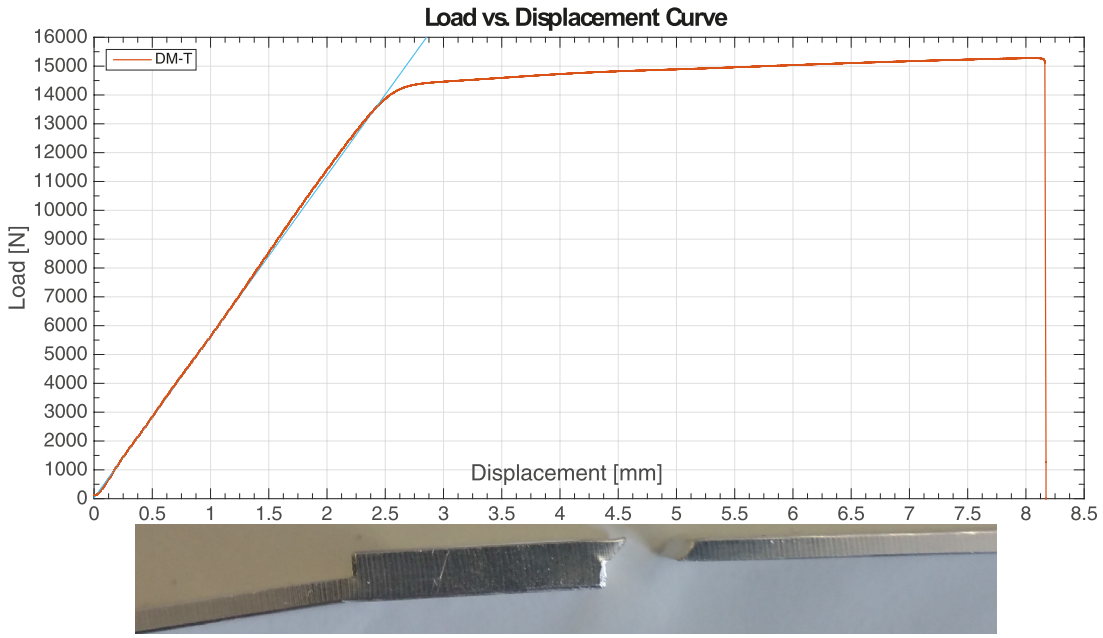

Figure 4.3: Typical Load vs. Displacement curve of the dummy specimen and failure surface.

The maximum displacement achieved by the dummy specimen was 8.31 mm and the maximum load was 15282.7 N. This load represents a σ_{remote} of 305.65 MPa (obtained with the ultimate load and the remote area $= 50$ mm^2) or a $\tau_{AVG.}$ of 30.57 MPa (calculated with the overlap area $= 25 \times 20 = 500$ mm^2). A rough calculation of the maximum strain can be obtained if we consider an $L_0 = 180$ mm, the maximum strain was $\approx 4.62\%$.

The non-linearity shown in the Figure 4.3 of the experimental curve when compared with the theoretical elastic behaviour curve occurs at the same load level (8 kN) that a visible bending of

the joint takes place (a rotation in turn of the center of the overlap similar to the Figure 2.37) due to the eccentric load path of the geometry.

As expected the failure occurred on the edge of the end of the overlap, in the side where was the load cell. Figure 4.3 shows also the fracture surface. It's possible to observe a severe yielding of the dummy specimen.

4.2.1.2 Araldite® 420 A/B adhesive SLJ (AB-20)

As mentioned before two types of adhesive joints were produced, with different cure cycles. The results obtained with the longer cure cycle were already presented in the Sub-section 3.3.1.1.

The change in the cure cycle was useful due to time-frame limitations (it's quicker to produce and be ready to the fatigue tests).

The static tests performed with this kind of joint allowed the admeasurement of the joint strength and the definition of the fatigue loads that were used.

The Load vs Displacement curve of the three specimens tested are shown in Figure 4.4.

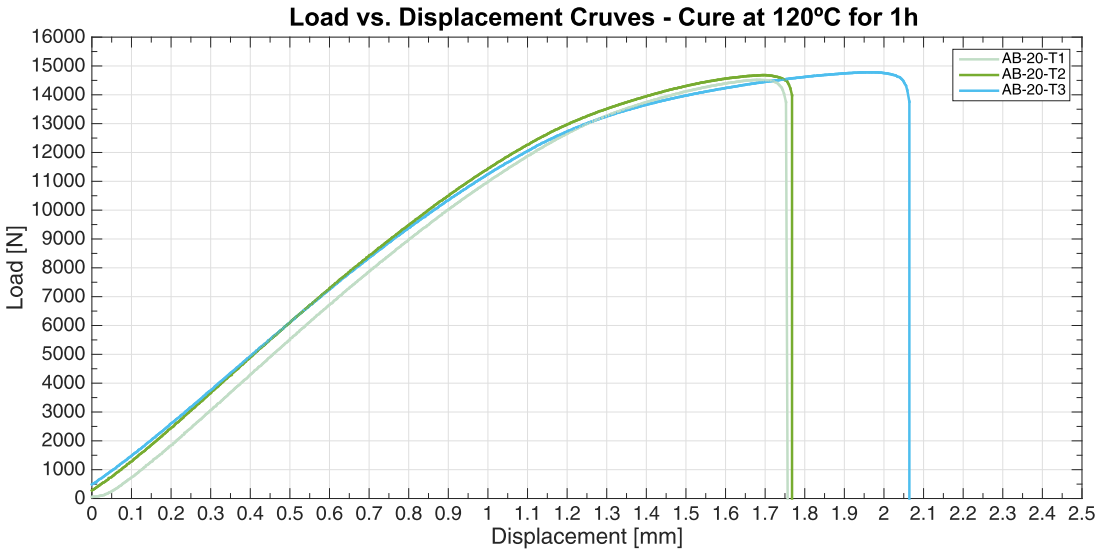

Figure 4.4: Load vs. Displacement curve of the Araldite® 420 A/B adhesive w/ 20 mm of overlap SLJ specimens.

The adhesive SLJ with 20mm of overlap revealed a good coherence in the values of maximum load and displacement. The Table 4.2 summarizes the results of the static tests.

Table 4.2: Summary of adhesive SLJ with 20mm of overlap average mechanical properties obtained in the tensile test

Max. Load	**Max.** σ_{remote}	**Max.** $\tau_{AVG.}$	**Max. Disp.**	**Energy Ab.**
14660 ± 133 N	293.20 ± 2.66 MPa	29.18 ± 0.34 MPa	1.86 ± 0.18 mm	17.54 ± 2.72 J

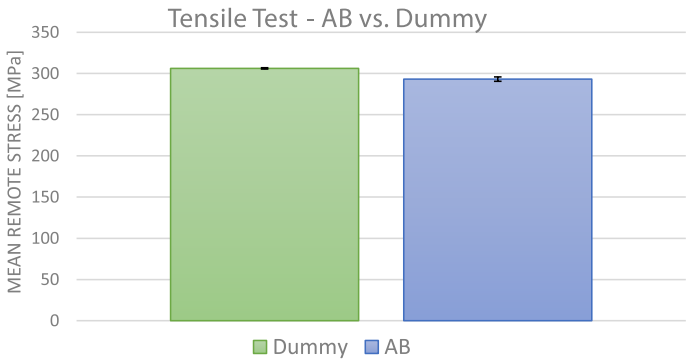

Figure 4.5: AB vs dummy joint strength.

A remarkable fact is that the AB SLJ mechanical strength efficiency, when compared with the dummy specimen, of the adhesive joint is about $\approx 96\%$. This indicates that the joint strength is near the maximum potential for this geometry (Figure 4.5).

It's interesting to observe that the load range where the joint begins to bend and yield the aluminium adherend in the adhesive joint is close to the value obtained in the dummy tensile test. In the AB SLJ the Load vs Displacement curve begins to be non linear around 8 kN (Figure 4.6). A severe yielding of the adherends is observed in this kind of joint.

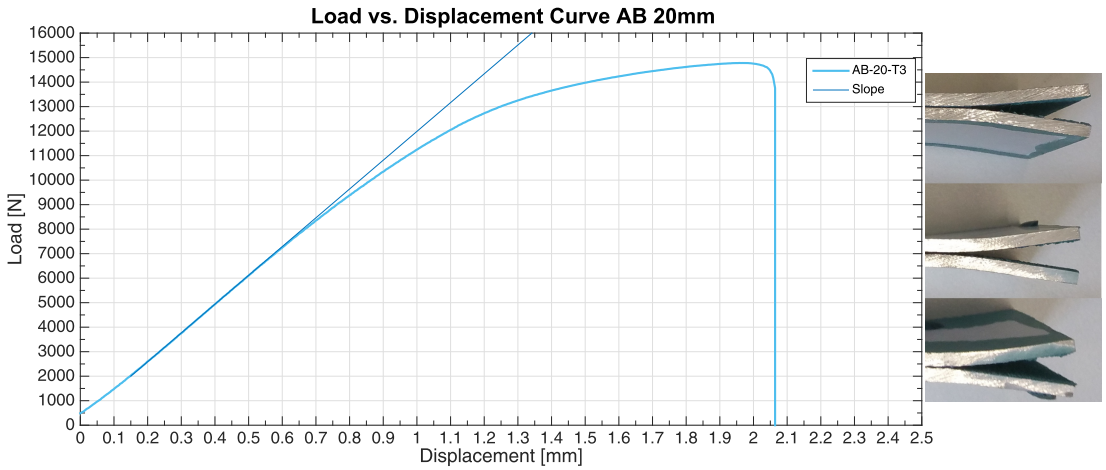

Figure 4.6: Beginning of the yield of the aluminium adherend and final yielding of the adherends.

The energy absorbed (fracture energy) during the tensile tests can be an indicator to the performance expected under fatigue. The value obtained was interesting and indicates a good fatigue performance. This estimative was done calculating the area underneath the Load vs Displacement curve.

The failure mode observed was mixed (neither fully adhesive or fully cohesive, with areas where the failure was really close to the interface however its possible to identify a thin layer of adhesive) and it's shown in Figure 4.7. It seems to be a progress in the right path with this system of adhesive and adherend due to the reports in the literature review pointing to an adhesive failure mode, as mentioned earlier.

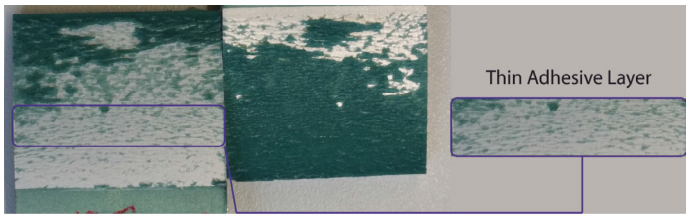

Figure 4.7: Failure surface of the adhesive single lap joint w/ 20 mm overlap after tensile test.

4.2.1.3 FSW single lap joint (FSW-20)

The welding parameters used in the FSW specimens were the same that in previous work presented the best mechanical behaviour for a single pass welding (Table 3.6).

The Load vs Displacement curves obtained are shown in the Figure 4.8.

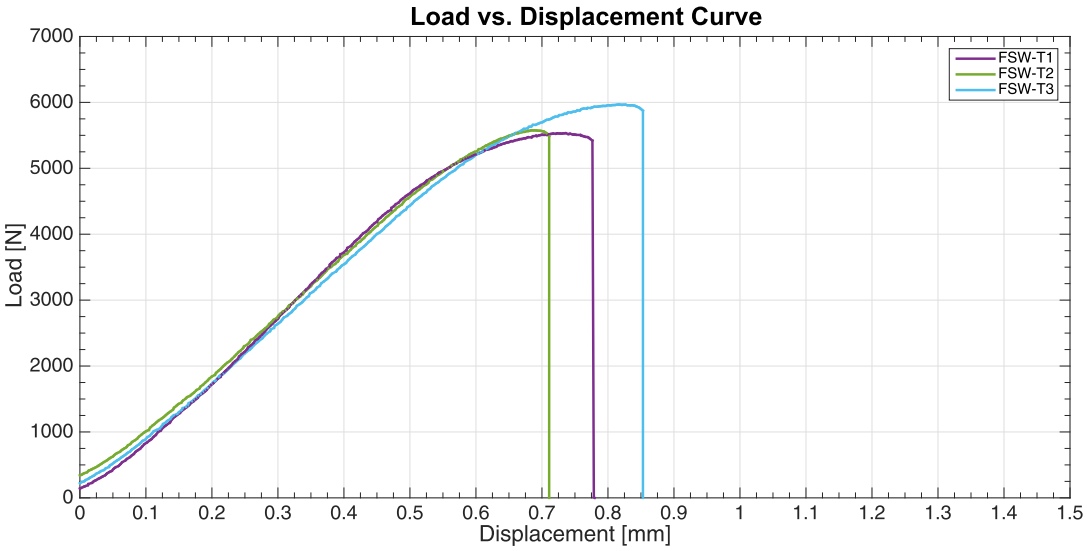

Figure 4.8: Load vs. Displacement curve of the FSW single lap joint specimens.

Table 4.3 summarizes the results obtained in tensile tests.

Table 4.3: Summary of FSW SLJ with 20mm of overlap average mechanical properties obtained in the tensile test

Max. Load	**Max.** σ_{remote}	**Max.** $\tau_{AVG.}$	**Max. Disp.**	**Energy Ab.**
5692 ± 240 N	114.31 ± 3.86 MPa	11.72 ± 0.40 MPa	0.78 ± 0.07 mm	2.65 ± 0.38 J

FSW joint performed worst, as expected, than the adhesive joints (Figure 4.9). Being the static strength only 39% when compared to adhesive SLJ (61% reduction). The yielding of the aluminium alloy substrates in the tensile tests were very low (due to the lower loads supported, Figure 4.10).

The effective width welded is lower than the overlap of 20 mm and this justifies the big difference in the strength of the joint (smaller solicited area). Also the presence of the "hook" defect and

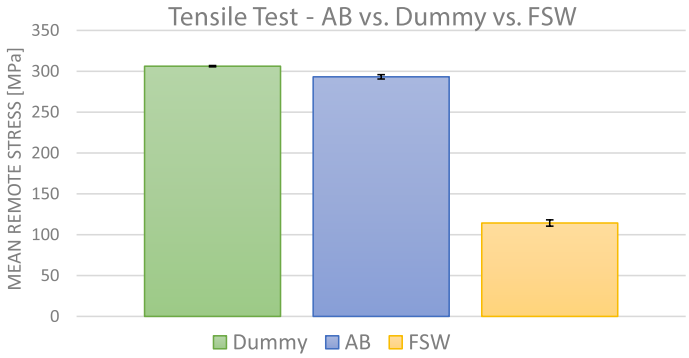

Figure 4.9: Dummy vs AB vs FSW joint strength.

the changes in the mechanical properties of the aluminium alloy due to the heat input are factors that lead to a poorer performance of the FSW SLJ.

If we assume that the effective width of the joint in the interface between the substrates is ≈ 10 mm the effective shear area is ≈ 250 mm^2 and the average shear stress is 25.30 MPa, that is not too far away of the AB SLJ shear stress.

The reduced scatter in maximum displacement and load between the specimens tested indicates that the FSW manufacturing process is under control.

The failure surface obtained in the tensile tests are shown in Figure 4.10.

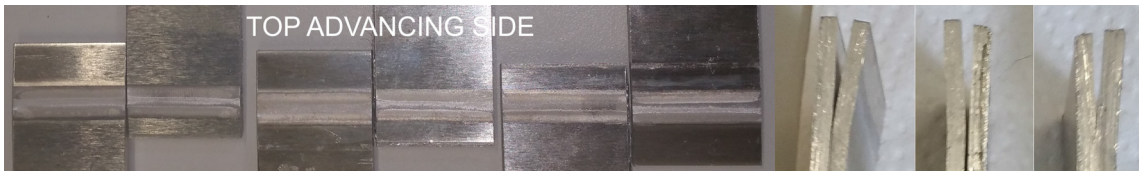

Figure 4.10: Left: FSW failure surface ; right: side view yielding of the specimens.

The failure occurred within the weld and not by the advancing side, this may indicate that the "hook" defect is of small dimensions.

Although the geometrical differences from the specimens used in the past work developed by our workteam, the usage of a downward force of 425 kg resulted in a significant increase in the strength of the FSW joint. In the past the 450 kg joint achieved an average static strength of 4558 N. The results obtained now were 25% higher.

4.2.1.4 Hybrid joint 425 kgf (Hyb-425-20)

Sixteen specimens of hybrid joints made with the Araldite® 420 A/B adhesive and 425 kgf of downward force were produced. The *Quasi*-static tests performed on this kind of joint had the same goal than in the other types: to define the joint strength and fatigue load levels. Also the main goal was to assess the viability of this hybridization process with such a small overlap length.

The Load vs Displacement curves obtained are shown in Figure 4.11.

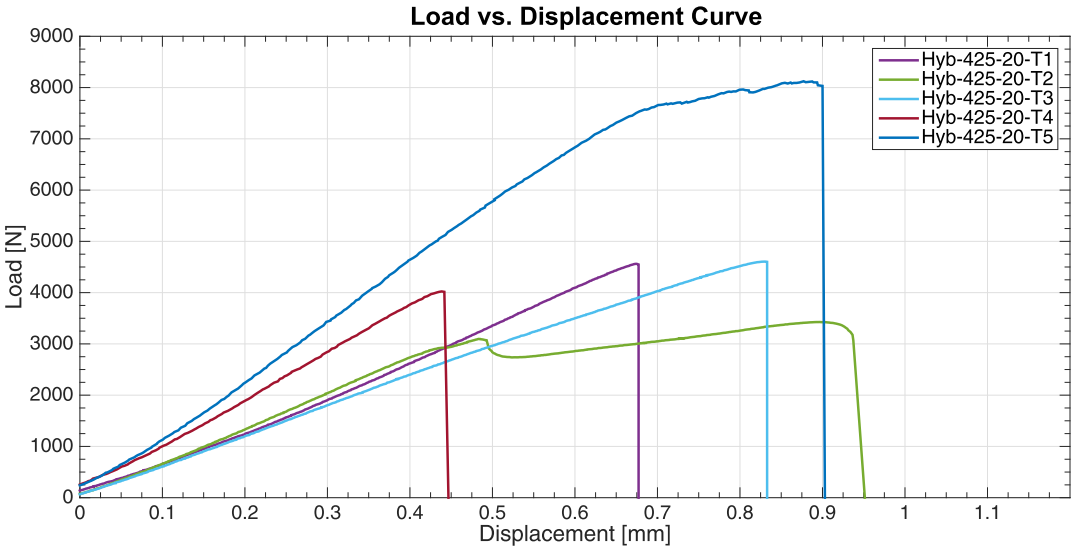

Figure 4.11: Load vs. Displacement curve of the Hybrid SLJ 425 kgf 20mm overlap specimens.

The five specimens tested were selected from different zones of the weld. Analysing the five experimental curves obtained it's possible to identify three different behaviours. The group of three specimens (T1,T3,T4) presented lower strength than FSW specimens tested with the same welding parameters, suggesting that the adhesive may be acting like a defect/contamination (due to inclusion of the adhesive in the welding line weakening the chemical linkage between the aluminium alloy).

A typical failure surface for this group of joint is shown in Figure 4.12.

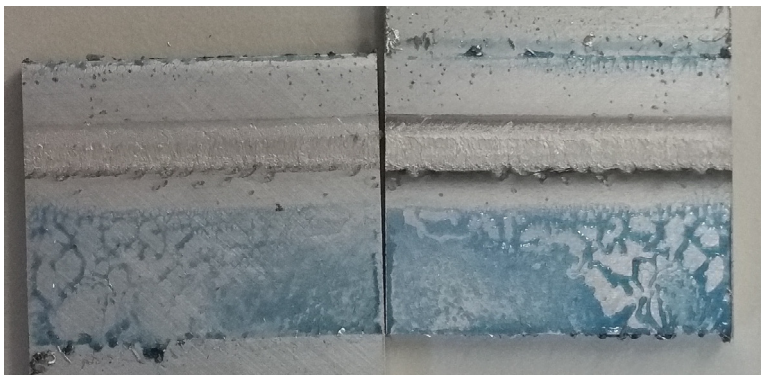

Figure 4.12: Representative failure surface of Hyb-425-T(1,3,4) specimens.

As it's possible to observe the adhesive layer presented has a strange light-blue colour different than the typical Araldite® 420 A/B colour. Also the thickness of the layer seems to be lower than the specified 0.2 mm. On the advancing side there's no solid evidence of presence of adhesive. The marks on the adhesive are similar to a flow done by capillary. There is obviously a manufacturing problem that is causing the adhesive to flow away. Also the welding line is de-centred.

The specimen T2 presents a Load vs Displacement curve that indicates an hybrid behaviour however with a strength lower than the FSW alone. The first force peak (displacement ≈ 0.49 mm) is due to the failure of the FSW welding being the rest of the load accommodated by the adhesive layer. The curve points the degradation of the welding performance in the presence of the adhesive.

The failure surface for the T2 specimen is shown in Figure 4.13.

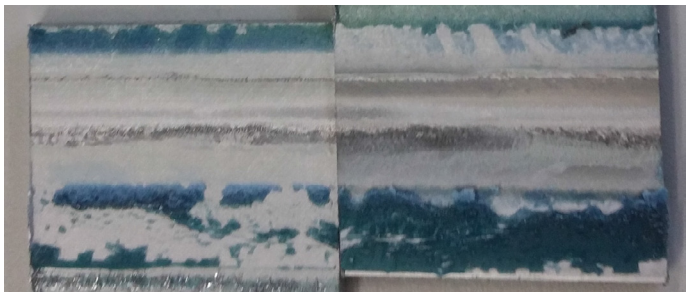

Figure 4.13: Surface of failure of specimens Hyb-425-T2

The welding line is de-centred with the overlap length. This is a clue that points to manufacturing deficiencies and uncontrolled variables, a limitation of the process with the available means of production, or a limitation of the concept for a reduced overlap as it is 20 mm.

The specimen T5 was the only 20 mm hybrid joint that performed better than FSW joints being the ultimate load achieved of 8123 N (σ_{remote} of 157.87 MPa or a $\tau_{AVG.}$ of 16.18 MPa) that is 54% of average strength of the adhesive joint and 1.38 times higher than the FSW joint.

The failure surface for the T5 specimen is shown in Figure 4.14.

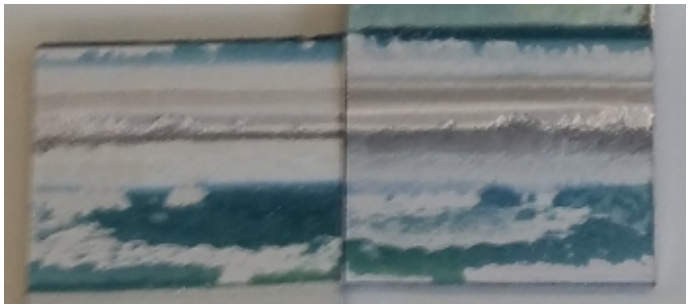

Figure 4.14: Surface of failure of specimens Hyb-425-T5

There was no visible yielding of the aluminium substrates, since the loads achieved were too low. In Table 4.4 a summary of the mechanical properties found is done. Standard deviation lead to the conclusion that the process presents huge inconsistencies in terms of load and displacement

Table 4.4: Summary of Hyb-425-2 SLJ with 20mm of overlap average mechanical properties obtained in the tensile test

Max. Load	**Max.** σ_{remote}	**Max.** $\tau_{AVG.}$	**Max. Disp.**	**Energy Ab.**
4198 ± 1838 N	95.96 ± 35.71 MPa	9.84 ± 3.66 MPa	0.766 ± 0.2 mm	2.23 ± 1.31 J

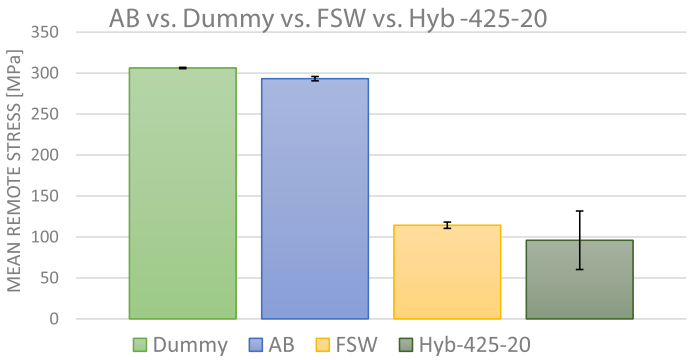

Figure 4.15: Dummy vs AB vs FSW vs Hyb-425-20 joint strength.

for this kind of joint. At this point, not a conclusive cause or justification has been found. The root of the problem reported can be a limitation inherent to the hybridization process or to the manufacturing process. For example, a malfunction of the FSW machine used to produce the joints can be the source of this behaviour (it's reported some leakages of the refrigerant liquid of the tool, and some random stoppages of the rotation movement during the weld manufacturing). More details about the possible causes will be presented in Section 4.2.2.2.

Hybrid joints with the same adhesive and an downward force of 450 kgf, that in the past resulted in better mechanical properties, were produced.

4.2.1.5 Hybrid joint 450 kgf (Hyb-450-20)

Eight specimens of hybrid joints made with 450 kgf of downward force were produced. The failure surface obtained is shown in the Figure 4.16. It's also possible to observe two distinct groups.

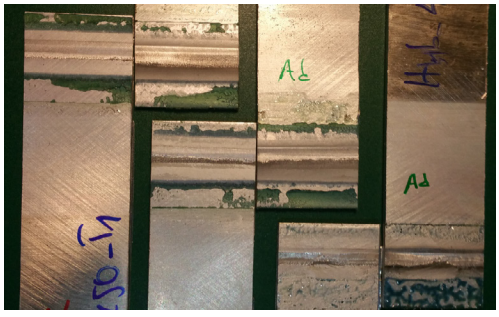

Figure 4.16: Failure surface of Hyb-450-20 specimen.

The Load vs Displacement curves obtained are shown in Figure 4.17.

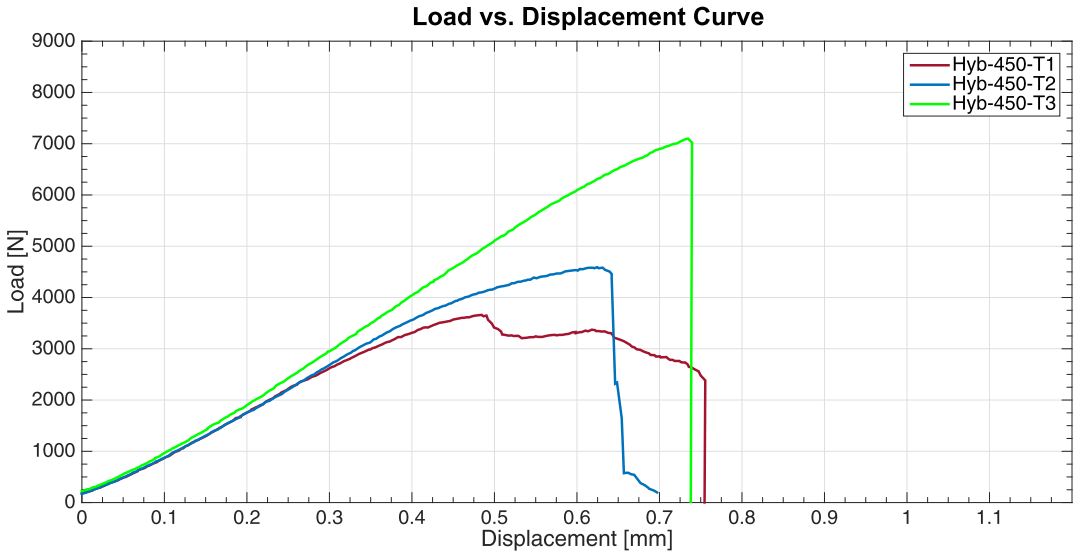

Figure 4.17: Load vs. Displacement curve of the Hybrid SLJ 450 kgf 20mm overlap specimens.

The same three different groups found in the Hyb-425-20 specimens were found in the 450 ones. The T1 specimen presented an hybrid behaviour however with a maximum load lower than the FSW alone.

The T2 specimen behaved like an FSW joint with a lower performance.

The T3 specimen presented a strength higher than the FSW alone being the ultimate load achieved of 7100 N (σ_{remote} of 141.99 MPa or a $\tau_{AVG.}$ of 14.55 MPa) what is 48% of average strength of the adhesive joint and 1.20 times higher than the FSW joint.

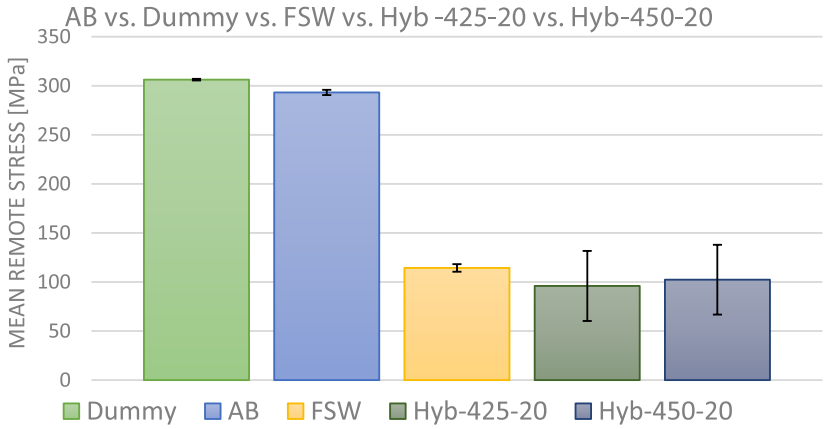

Figure 4.18: Dummy vs AB vs FSW vs Hyb-425-20 vs Hyb-450-20 joint strength.

The hypotheses established earlier about the possible causes for the scatter verified remain the same because between the two types of hybrid joints were not identified significant changes in the mechanical behaviour. (Figure 4.18).

Table 4.5 summarizes the results obtained in tensile tests.

Table 4.5: Summary of Hyb-450-20 SLJ average mechanical properties obtained in the tensile test

Max. Load	Max. σ_{remote}	Max. $\tau_{AVG.}$	Max. Disp.	Energy Ab.
5117 ± 1779 N	102.34 ± 35.57 MPa	10.49 ± 3.65 MPa	0.721 ± 0.05 mm	2.14 ± 0.53 J

4.2.1.6 Summary

A Load vs Displacement curve of the different joints tested are shown in Figure 4.19.

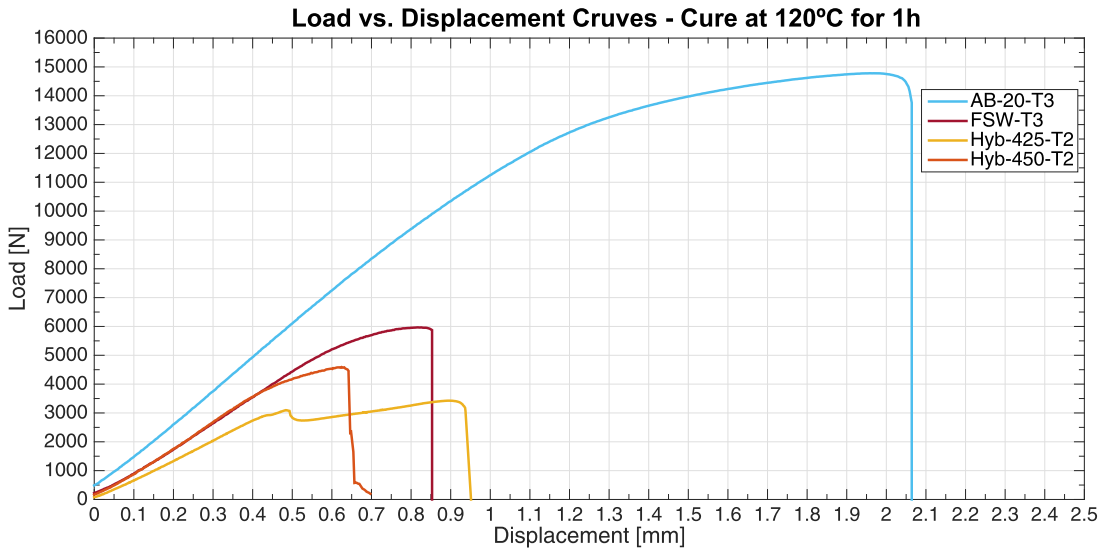

Figure 4.19: Load vs. Displacement curves of the joints studied with 20mm overlap.

As it may be observed in Figure 4.18 and 4.19 there is a huge gap in the joint strength between the adhesive single lap joint and the others (FSW and hybrid). The manufacturing process of the adhesive and FSW joints are under control. The hybrid joints present several inconsistencies that indicates that the manufacturing process is flawed.

Concerning the hybrid joints with 20 mm of overlap they were not studied in fatigue due to the inconsistency problems. The workteam decided to change the overlap from 20 to 40 mm in an attempt to understand if the problems identified were due to a concept limitation or a manufacturing problem.

4.2.2 40 mm overlap SLJ

Due to the bad performance and high scatter of the hybrid joints with the 20 mm overlap the overlap length was changed in order to assess if the root cause of the inconsistencies found were due to the machine (manufacturing process) or a limitation of the concept.

The only joints with 40 mm studied were the adhesive and the hybrid ones. The FSW and dummy joints due to time limitations were not studied.

Since the change in the downward force in the joints with 20 mm overlap resulted in no significant changes. The downward force that in the past work presented the best results (450 kgf) was chosen.

4.2.2.1 Araldite® 420 A/B adhesive SLJ (AB-40)

A typical Load vs. Displacement curve of the AB-40 specimen is shown in Figure 4.20.

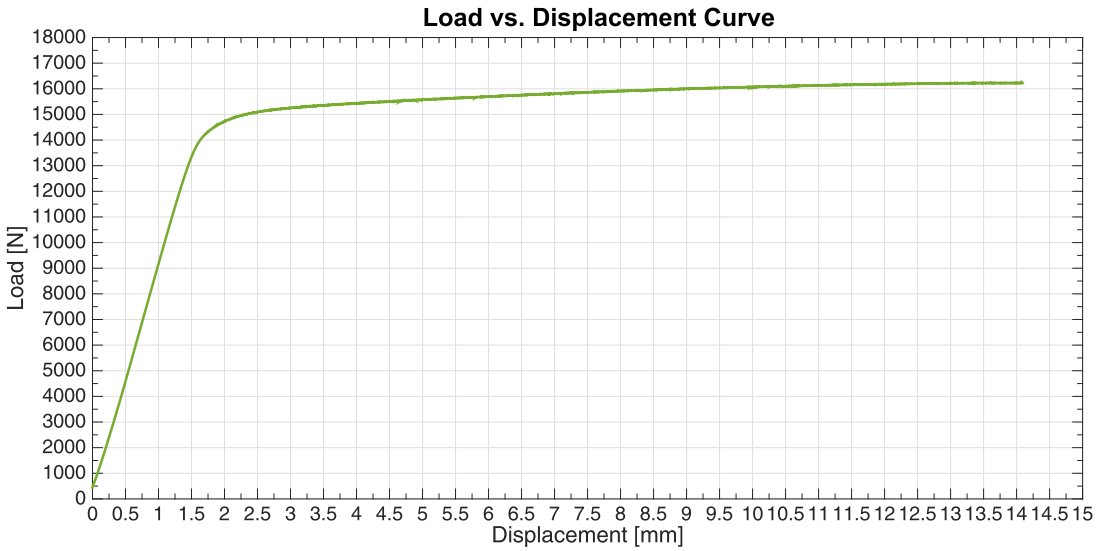

Figure 4.20: Typical Load vs. Displacement curve of the AB-40 specimens.

This overlap length leaded the joint to a failure in the adherend near the clamping location (Figure 4.21). This means that this overlap it is making the adherend the weakest part in the joint. Possibly there is a smaller overlap length that can achieve the same load levels since the joint strength is now governed by the adherend and not by the adhesive. The high displacement reached is due to the plastic deformation in the adherend.

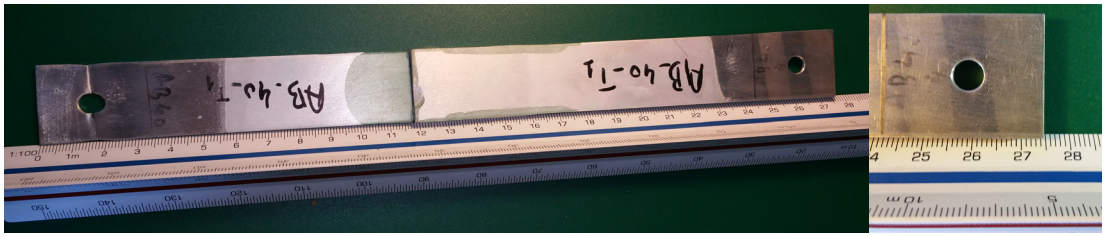

Figure 4.21: Failure on the AB-40 specimens.

It was notice a severe plastic deformation on the specimen as can be seen in Figure 4.21, the initial length was 260 mm and the final one was $\approx$ 274.5 mm.

The Table 4.6 summarizes the results obtained.

Table 4.6: Summary of AB-40 SLJ mechanical properties obtained in the tensile test

Max. Load	**Max.** σ_{remote}	**Max.** $\tau_{AVG.}$	**Max. Disp.**
16229 N	324.59 MPa	20.29 MPa	14.09 mm

The ultimate tensile stress achieved is in the range of the UTS of the base material, the joint reached the maximum strength possible with this materials.

4.2.2.2 Hybrid joint 450 kgf (Hyb-450-40)

The hybrid joints with an overlap of 40 mm were produced with the geometry presented in Figure 3.7. The specimens Hyb-450-40 were manufactured with the Araldite® 420 A/B adhesive (0.2 mm layer) and 450 kgf of downward force. All the manufacturing stages were maintained and fourteen specimens produced. The Load vs Displacement curves obtained are shown in Figure 4.22.

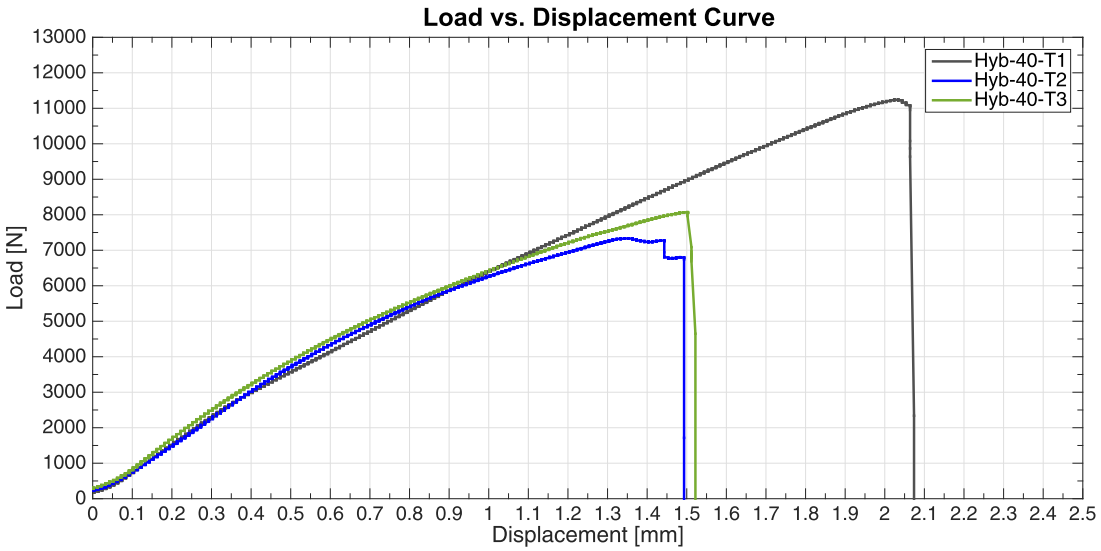

Figure 4.22: Load vs. Displacement curve of the Hybrid SLJ 450 kgf 40 mm overlap specimens.

The specimen Hyb-40-T1 presented the best performance, being the ultimate tensile remote stress equal to 223.55 MPa. This value is significantly lower than the average maximum remote stress of the adhesive joints. It is 23.75% lower than the adhesive joint with 20 mm of overlap and 31.12% lower than the adhesive joint with 40 mm. This specimen was located at the end of the hybrid plate from one of the two plates produced.

The failure surface of the Hyb-40-T1 specimen is show in the Figure 4.23.

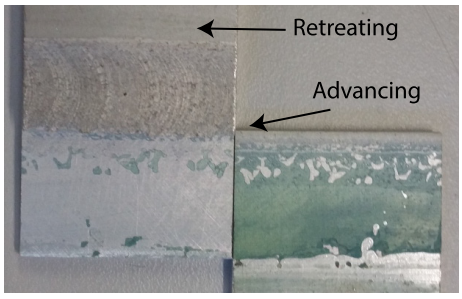

Figure 4.23: Failure surface of the Hyb-450-40-T1 specimen.

There is a visible difference of the failure surface when compared with the majority of the specimens with 20 mm of overlap. A continuous layer of adhesive can be observed. It suggests

that the increase in the overlap length allows, with more easily, the production of a hybrid joint where the adhesive layer can be properly loaded.

The specimen T2 was machined from the other plate produced in the same position of the specimen T1 (end of the welding). The specimen T5 belonged to the plate of the specimen T1 and was obtained from the middle. The two specimens presented similar mechanical behaviour being the maximum load sustained by both in the same range. The poorer performance of this two specimens allied with the inconsistency of the results obtained, when compared to the T1, points clearly to a problem during the manufacturing of the joint. The 40 mm of overlap length adopted is, theoretically, enough to produce consistent joints like the ones produced in the past with 60 mm overlap [75].

The Table 4.7 summarizes the results of the 3 specimens in the tensile tests.

Table 4.7: Summary of Hyb-450-40 SLJ (40mm of overlap) average mechanical properties obtained in the tensile test

Max. Load	**Max.** σ_{remote}	**Max.** $\tau_{AVG.}$	**Max. Disp.**	**Energy Ab.**
8886 ± 2076 N	176.87 ± 41.14 MPa	9.06 ± 2.11 MPa	1.696 ± 0.33 mm	9.17 ± 3.44 J

The failure surface of the specimen Hyb-failure-450-40-T2 revealed an abnormal adhesive layer, as can be seen in Figure 4.24.

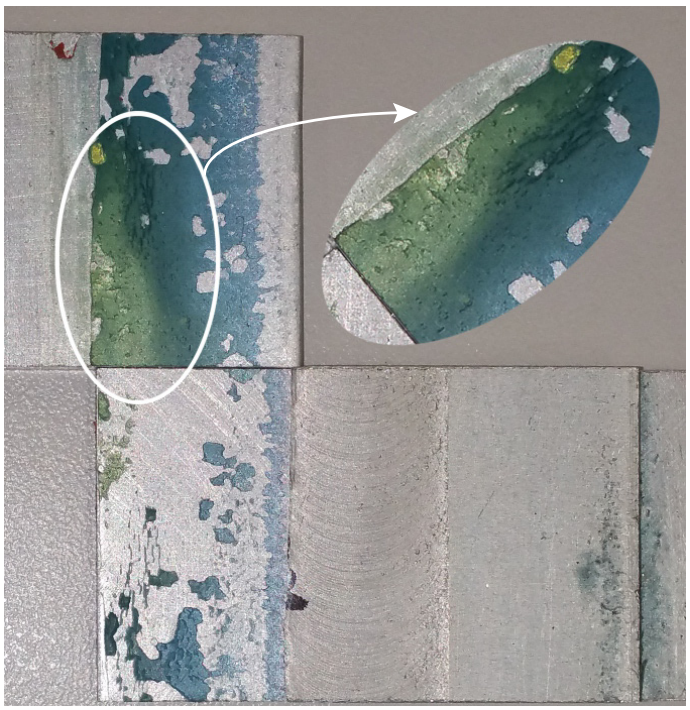

Figure 4.24: Failure surface of the Hyb-450-40-T2 specimen.

It's possible to observe three different areas within the adhesive layer. There is a region that presents a greenish tone, other area that is blueish and there is also a yellow dot. These differences

are due to some sort of contamination during the manufacturing of the hybrid joint. That contamination can be a possible cause to the unexpected lack of strength and scatter of the hybrid joints when compared to the adhesive ones (in the past work was found that the hybrid joint had similar strength than the adhesive joints). The failure mode seems to be mixed more closer to the adhesive failure than cohesive (It will be discussed in Section 4.4).

In order to assess what kind of contamination is happening with this kind of joints the specimens T1 and T2 were examined at CEMUP using the EDS technology. The goal was to observe any abnormality and try to track the root of them. The results of the analysis for the specimen T1 is shown in Figure 4.25.

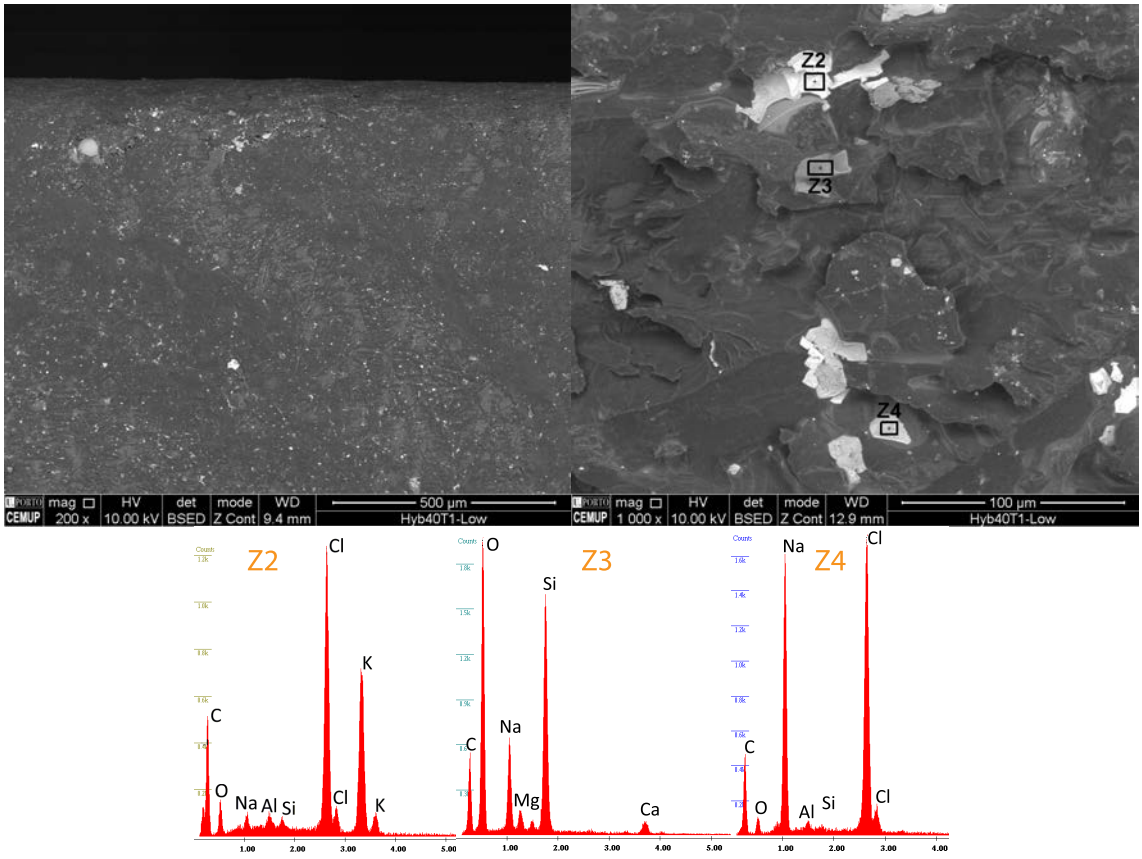

Figure 4.25: EDS analysis of the failure surface on Hyb-450-40-T1

As it may be seen there is a vast presence of contaminations within the adhesive layer. These kind of particles influence negatively the mechanical behaviour of the joint. The Energy-dispersive X-ray spectroscopy revealed particles containing chemical elements like the carbon, oxygen,sodium, aluminium, silica, chlorine, manganese, calcium and potassium.

The adhesive, being an aromatic polymer (epoxy), in this kind of analysis is identified by a big concentration of carbon and oxygen (more details about EDS analysis in the Section 4.4).

The particle identified in the image with the tag Z2 is mainly composed by potassium and chlorine. It can be Potassium chloride (KCl), that is a white crystal or crystalline powder. It can be found in fertilizers, in chemical feedstock, and it is used for the manufacture of potassium

hydroxide and potassium metal, in food processing, medicine and in the water or some de-ice liquids. From all this sources the most plausible is the water or some liquid used during the manufacturing process.

The Z3 area presents several chemical elements, that may indicate that is a multi-contamination zone. The *Na*, *Si* and *O* concentrations may point to a compound belonging to the Sodium silicate family ($Na_2(SiO_2)_nO$). They are used in drilling fluids and industrial oils as an additive. The other compound that can be present is the Calcium carbonate ($CaCO_3$), it is also used in oils, drilling liquids and in the water as a treatment.

In the Z4 zone it seems to be a grain of Sodium chloride ($NaCl$), the 1 : 1 ratio of sodium and chloride ions points to that compound. It can be present in the pipe water and in some sort of oils or similar fluids.

The specimen T2 presented also the same kind of contaminations, it was also analysed the two areas that presented different colours, the EDS result is shown in the Figure 4.26.

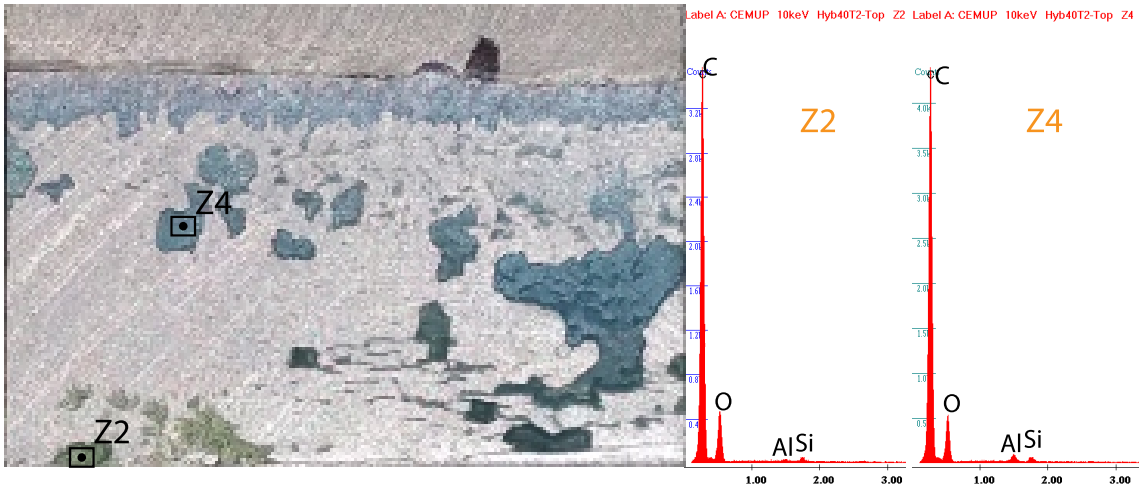

Figure 4.26: EDS analysis of the failure surface on Hyb-450-40-T2

As it's possible to see it was not found significant chemical difference between the two zones. However that does not necessarily mean that there is no contamination or differences in mechanical properties. The EDS technology is not sensitive to several elements like for example the nitrogen. If the contamination is an organic one that can be contributing to a higher concentration of carbon, that seems to be higher than the obtained in the adhesive joints. In the Section 4.4 this layer of adhesive will be compared to the one obtained in the adhesive joints.

All these types of contaminations degrades the adhesion and the chemical linkage within the adhesive what leads to a poorer mechanical performance. The manufacturing process was analysed in order to find possible causes for contaminations.

The machine used to perform the welding in the hybrid joint was found to be leaking oil and refrigerant liquid directly over the joint with high cadence. It was also reported that in several welding operations the machine stops the process unexpectedly. Figure 4.27 shows the refrigerant liquid leak mentioned.

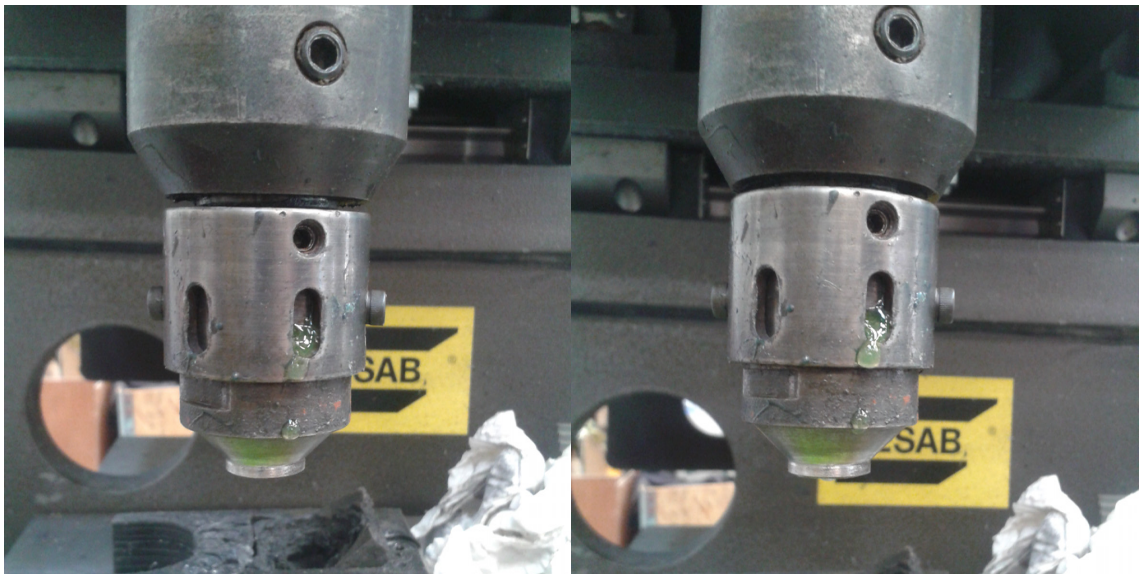

Figure 4.27: Refrigerant liquid leak.

This his a plausible source of the contaminations found in the EDS analysis.

In order to attempt to reduce the contaminations, the scatter and improve the mechanical performance of the joint were manufactured with the refrigeration system turned off. This results in higher temperatures in the tool and the heat input in the joint is also higher. To prevent an excessive heating compressed air was used to refrigerate the tool and the plates. The Load vs Displacement curves obtained are shown in Figure 4.28.

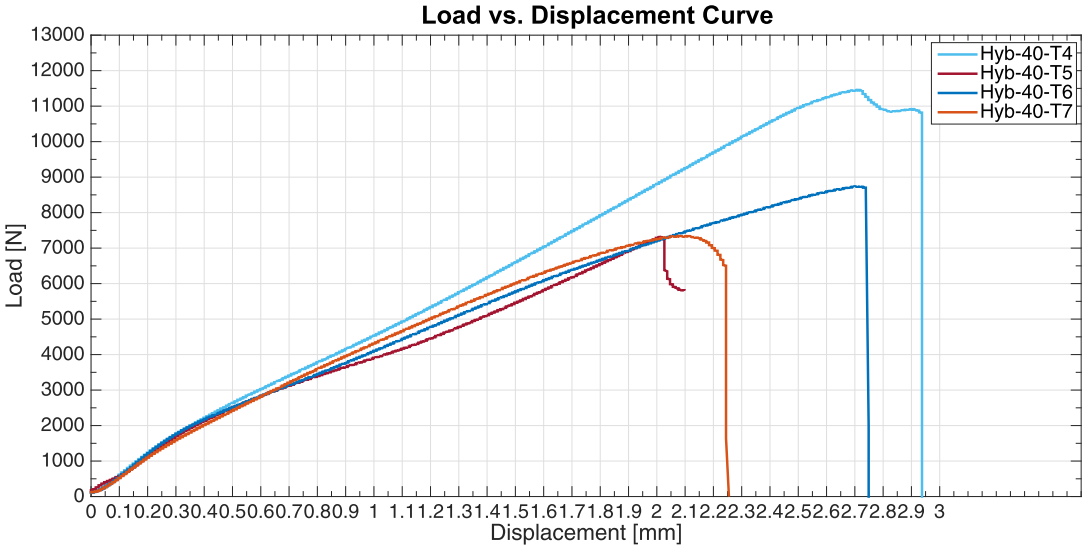

Figure 4.28: Load vs. Displacement curve of the Hybrid SLJ 450 kgf 40 mm overlap specimens produced with the refrigerant system turned off.

Once again there was a significant difference in the mechanical performance between the specimens tested not only in the maximum load as well as in the maximum displacement. In compari-

son with the previous joints (produced with the refrigerant system turned on) in terms of maximum load there was no significant differences, being the inconsistencies present in the two different kinds. In terms of displacement it seems to be a trend to have a higher maximum displacement in the last produced joints.

The Table 4.8 summarizes the results of the 4 specimens in the tensile tests.

Table 4.8: Summary of Hyb-450-40 SLJ (40mm of overlap) produced with the refrigerant system turned off average mechanical properties obtained in the tensile test.

Max. Load	**Max.** σ_{remote}	**Max.** $\tau_{AVG.}$	**Max. Disp.**	**Energy Ab.**
8718 ± 1942 N	174.37 ± 38.84 MPa	8.94 ± 1.99 MPa	2.50 ± 0.40 mm	12.89 ± 4.69 J

The Typical surfaces obtained in this hybrid joints is shown in the Figure 4.29.

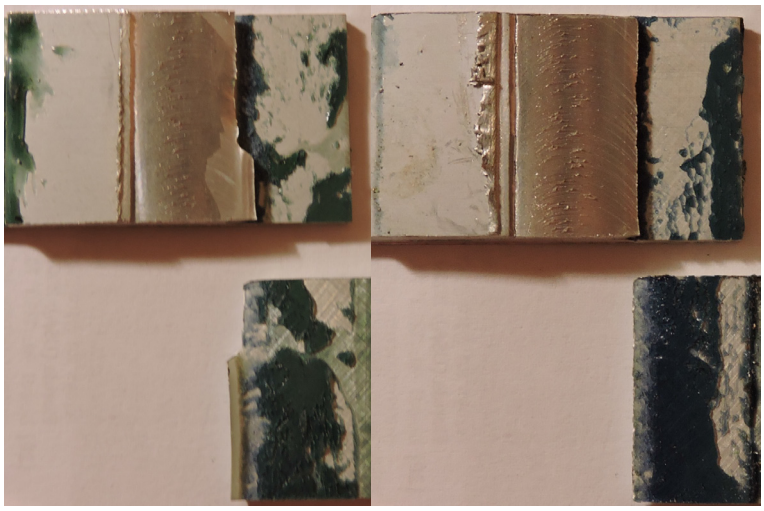

Figure 4.29: Typical failure surface of the Hybrid SLJ 450 kgf 40 mm overlap specimens produced with the refrigerant system turned off.

Even with the refrigerant system turned off there was leakage of refrigerant liquid, at much lower rates. On the other hand the usage of compressed air can be another source of contaminations because the air contains oil particles that lubricate the compressed air system.

The shoulder "pattern" in the joints produced with the refrigerant system turned off is deeper and presents some shavings and grooves (Figure 4.29). This can be attributed to the fact that heat input was larger. Being the machine force controlled, an higher heat input softens more the aluminium alloy resulting in a lower reaction force. In order to maintain the downward force specified, the machine plunges more the tool performing a deeper welding when compared with the first ones.

The adhesive layer is thicker than the obtained in the other joints. This may be due to some differences in the tightness of the clamping system.

The unexpected stoppages of the machine and the oil leakage point towards malfunction in several functions of the machine. This behaviour can be a result of lack of maintenance, that is overdue by a long period of time. The load cells (that measures and governs the force control

unity) and other components can be uncalibrated. There is also a severe damage of the base (table of the machine where the plates are supported) that can be seen in the Figure 4.30.

Figure 4.30: Groove at the table in the FSW machine.

This sort of long groove under the welding zone provides heterogeneous (irregular) mechanical support to the plates that are being welded. Since the machine works with force control, the irregularity induces the machine to respond to different reaction forces changing constantly the welding parameters (displacement). This can have a significant impact in the different performances of joints produced from the same plate.

The modular nature of the FSW tool can be another source of inconsistencies, since the parameters like the pin length are dictated by the tool assemble. It is difficult to achieve always a good assembly repeatability.

Other sources of contaminations can be mentioned like the environment where the joints are produced. The machine is located in a workshop that presents an high density of machines that work with a vast range of materials, making the air contaminated with liquids and solid particles like oil, metals, polymers and others. The clamping system used is mechanical and which may also lead to lower reproducibility of clamping conditions.

The Table 4.9 summarizes the tensile results of the 7 specimens tested.

Table 4.9: Summary of average mechanical properties obtained in the tensile test in the 7 specimens of the joint Hyb-450-40 SLJ (40mm of overlap).

Max. Load	**Max.** σ_{remote}	**Max.** $\tau_{AVG.}$	**Max. Disp.**	**Energy Ab.**
8790 ± 1824 N	175.44 ± 36.34 MPa	8.99 ± 1.86 MPa	2.16 ± 0.55 mm	11.30 ± 4.35 J

Due to the logistics and time limitations (production at IST, scarcity of materials, transportation and availability of testing machines) another change in the manufacturing process was introduced in the last week of the Master thesis project. A new cure cycle similar to the one used in the adhesive joints (1 hour at 120 °C) was applied in an attempt to reduce the scatter by reducing the time window for the contaminations diffusion and inclusion through the adhesive from the surrounding environment.

4.2.2.3 Hybrid joint 450 kgf cured at 120 °C (Hyb-450-40-cure)

The final joints were tested only under*quasi*-static conditions due to the time-frame mentioned previously.

The Load vs Displacement curve is shown in Figure 4.31.

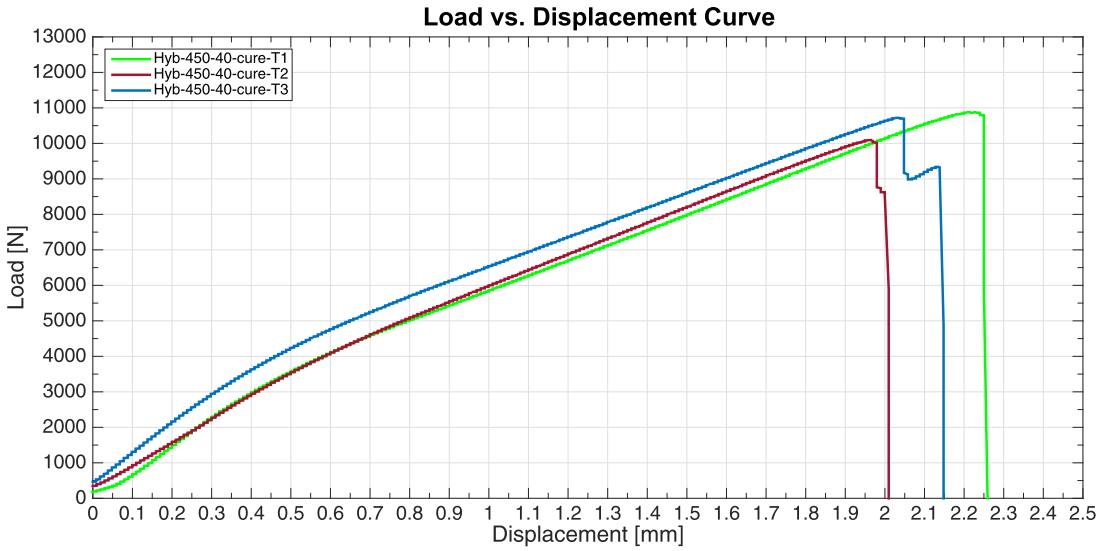

Figure 4.31: Load vs. Displacement curve of the Hybrid SLJ 450 kgf 40 mm overlap with cure cycle of 1h at 120 °C specimens.

Comparing with the other hybrid joints cured at room temperature there was a lower maximum load and displacement scatter. The average ultimate load and final displacement were also higher with the cure applied. This means that there was an improvement in the manufacturing process.

The Table 4.10 shows the average mechanical properties obtained with the introduction of the cure cycle.

Table 4.10: Summary of Hyb-450-40-cure SLJ average mechanical properties obtained in the tensile test

Max. Load	**Max.** σ_{remote}	**Max.** $\tau_{AVG.}$	**Max. Disp.**	**Energy Ab.**
10569 ± 415 N	211.38 ± 8.3 MPa	10.83 ± 0.43 MPa	2.243 ± 0.28 mm	13.2 ± 1.38 J

There was a significant reduction in the standard deviation values for all the properties presented in Table 4.10. Even so the joint strength is only 65.12%. It is an improvement when compared to the same joint without the cure cycle however there is still margin to improve mechanical performance.

The failure surface of this joint is shown in Figure 4.32.

The failure on the welding was on the advancing side being the failure in the adhesive, ate naked eye, mixed.

The mechanical properties obtained as well as the standard deviation shows that, despite the lower performance than what expected, the process is better controlled with the cure applied. It

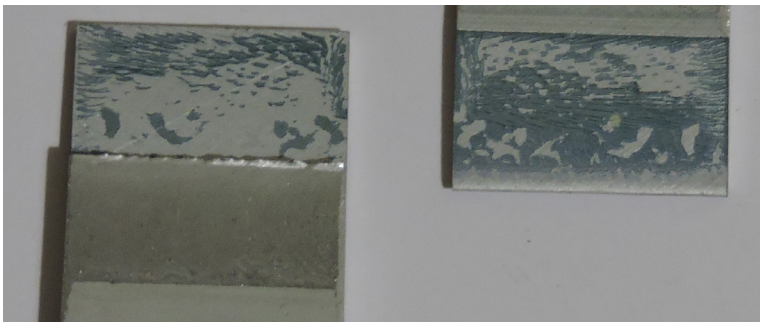

Figure 4.32: Failure surface of specimens Hyb-425-40-cure.

is a step in the right direction and there is room for improvement if the other causes of the poorer performance are eliminated. It would be helpful to analyse with EDS this type of joint as a future work.

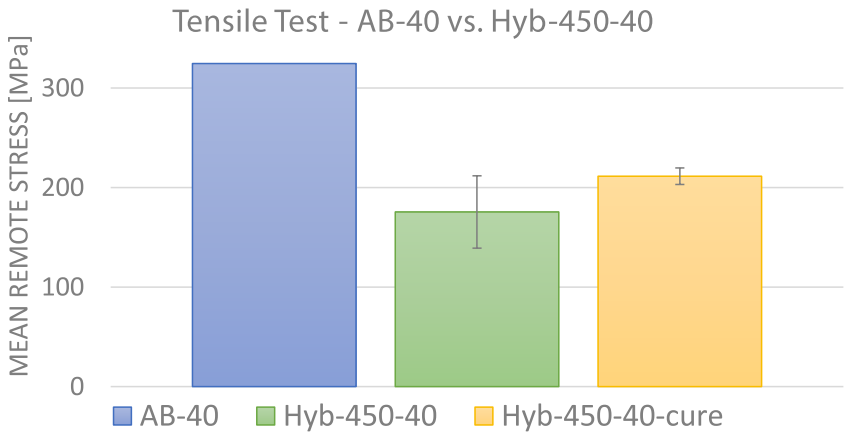

Figure 4.33: AB-40 vs Hyb-450-40 vs Hyb-450-40-cure joint strength.

Figure 4.33 shows clearly the improvement occurred with the cycle cure and the room for improvement when compared with the adhesive joint.

4.3 Fatigue

The fatigue tests performed allowed to characterize the behaviour under cyclic loads of the different types of joints. In order to benchmark the different joints, the S-N curves were obtained. The joints studied in fatigue were the dummy specimens with 20 mm of overlap, the adhesive joints (40 and 20 mm of overlap), the FSW joints (20 mm of overlap) and the hybrid joints with 40 mm of overlap with room temperature cure. The hybrid joints with the cure cycle of one hour at 120 °C were not assessed due to time and machine availability limitations.

The stoppage criteria or the infinite life criteria used was the two million cycles ($N = 2 \times 10^6$) in all joints studied.

In the Section 3.5 was presented four assumptions that need to be true in order to obtain a good S-N curve.

The first one was the linearity of relationship between the $\log S$ and $\log N$ and it can be easily tested by fitting a linear regression and analysing the r^2 value or the residuals. If there is some degree of uncertainty it's possible to fit a polynomial (typically a quadratic or cubic) in logS to the data and perform a ANOVA analysis to test whether the quadratic/cubic regression components are statistically significant.

The second assumption was that N is log-normally distributed. It can be tested by an "eyeball" assessment of whether a normal probability plot of the residuals of $\log N$ from the regression line of logS versus $\log N$ follows a linear trend.

The third one was to guarantee the homogeneity of standard deviation of $\log N$ with respect to S. This can be easily checked by simply examining a plot of the residuals from the linear regression vs $\log S$.

The last one was to assure the statistical independence of the test results. This is guaranteed by the nature of the tests. The result of a specimen does not depend on the result from the previous so the independence is secured.

As a term of comparison will be used the fatigue data of the base material AA 6082-T6 presented in the article [30].

Due to time limitations and scarcity of resources (limitations on the usage of the servo-hydraulic machines) the number of specimens tested were limited, however it was enough to benchmark with a good certainty level the FSW and adhesive joints. The Dummy specimens (not in the initial plan of the Master thesis) and the hybrid joints were not possible to complete the fatigue analysis with an high level of accuracy.

4.3.1 Dummy with 20 mm overlap DM-20

The goal of studying dummy specimen under fatigue was to assess the impact in the fatigue strength of the geometry of the single lap joint when compared to the bare material. Unfortunately due to machine time limitations only the higher levels of loads were performed with a single specimen per level. Even so it is presented the results of the tests performed.

The Table 4.12 shows the levels defined and the number of cycles obtained until the failure of the specimen.

Table 4.11: Load levels used in the fatigue tests on the dummy specimens with 20 mm of overlap and results.

Level	Fraction	σ_{remote}	$\tau_{AVG.}$	Number of Cycles
Static	100%	305.65 MPa	30.57 MPa	–
1	80%	244.52 MPa	24.45 MPa	1198
2	70%	213.96 MPa	21.40 MPa	1392
3	50%	152.83 MPa	15.28 MPa	3029
4	40%	122.26 MPa	12.23 MPa	7077
5	30%	91.70 MPa	9.17 MPa	96563

Figure 4.34 shows the results obtained and a curve fit. They are compared to the data of the bare aluminium AA 6082-T6.

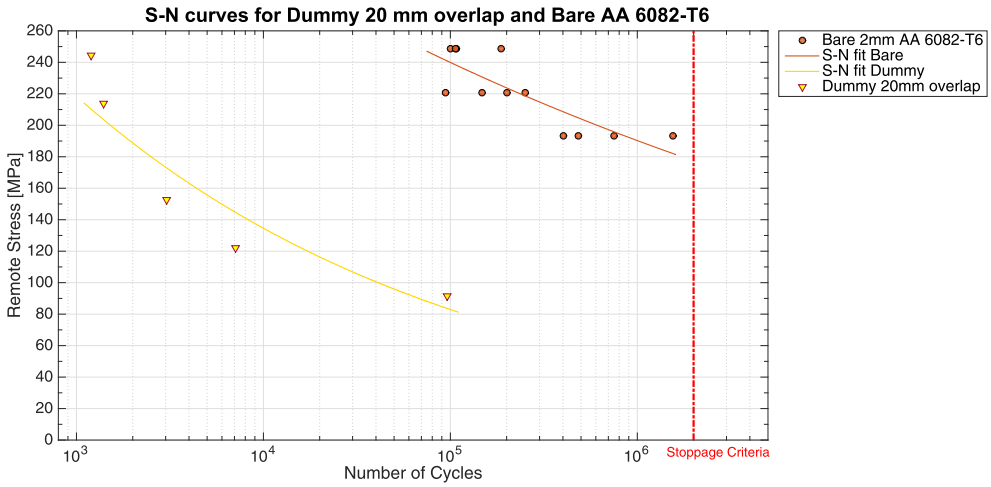

Figure 4.34: S-N curve for the dummy specimens and bare aluminium.

The fit curve equation found for the experimental data was:

$$S^{4.183240}N = 7.429624 \times 10^{12} \tag{4.1}$$

Despite the low number of specimens studied it's possible to claim that the geometry of the single lap joint degrades with a great impact the fatigue strength of the material. For the 10^5 number of cycles the fatigue strength of the dummy specimens is ≈ 92.00 MPa it is $\approx 38.33\%$ of the strength in the same conditions for the bare material (≈ 240.16 MPa). This reduction is due to the stress concentrations in the specimen geometry.

4.3.2 Adhesive joint with 20 mm overlap AB-20

In order to obtain the S-N curve for the adhesive joints with 20 mm of overlap fatigue tests for four different load levels were performed. The levels can be defined in terms of remote stress or

average shear stress. The two types of curves will be presented. The Table 4.12 shows the levels defined and the number of cycles obtained until the failure of the specimen.

Table 4.12: Load levels used in the fatigue tests on the adhesive joints with 20 mm of overlap and results.

Level	**Fraction**	σ_{remote}	$\tau_{AVG.}$	**Number of Cycles**			
Static	100%	293.20 MPa	29.18 MPa	**Spec. 1**	**Spec. 2**	**Spec. 3**	**Spec. 4**
1	60%	176.41 MPa	18.12 MPa	3198	3777	–	–
2	40%	117.61 MPa	12.10 MPa	35195	21545	–	–
3	26%	76.00 MPa	7.91 MPa	249236	185032	155731	223700
4	17%	49.98 MPa	5.13 MPa	1022089	1406927	1553150	–

The Minitab software, used in statistics, was used to analyse the fatigue data obtained. Figure 4.35 shows the fitted linear regression of the data with the scale in $\log N$ and $\log S$, being S the remote stress.

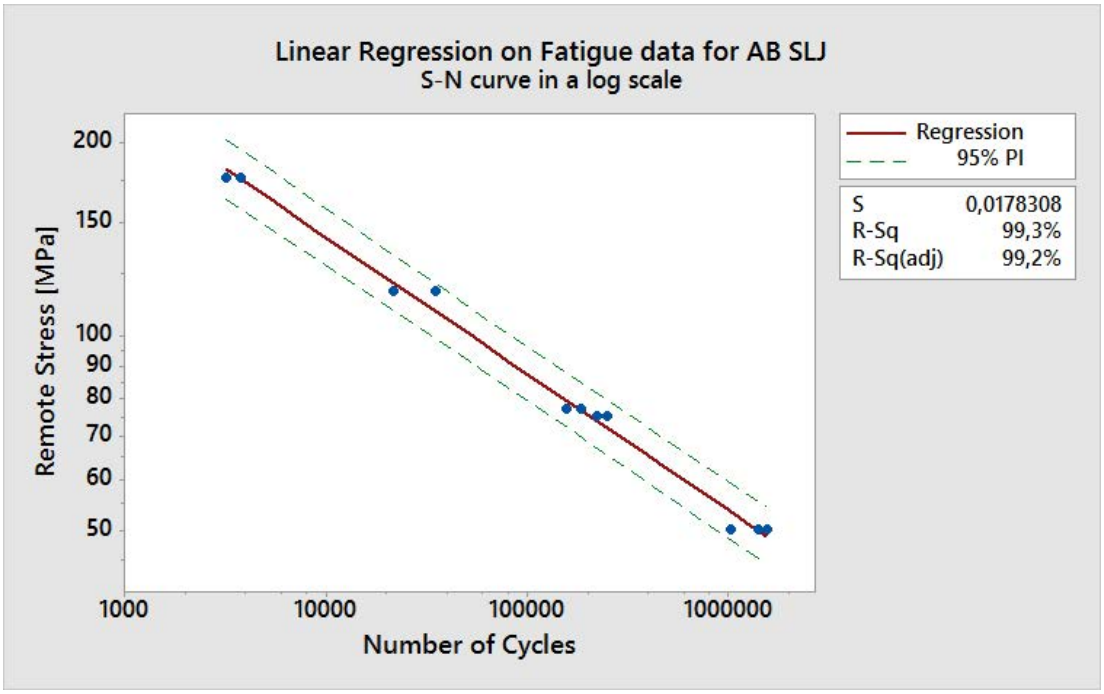

Figure 4.35: Linear regression of the fatigue data from AB-20 specimens.

The value of the Standard Error of the Regression (S) is measured in the units of the response variable ($\log S$) and represents the standard distance data values fall from the regression line, or the standard deviation of the residuals. For a given study, the better the equation predicts the response, the lower the value of S. The S value is low, which is an indicator of a Goodness-of-Fit.

The R-Sq (R-squared) is a statistical measure of how close the data are to the fitted regression line. The value of the R-Sq for this fit is 99.3%, attending to the number of the specimens studied this is a impressive value and proves the consistency of the results and consequently of the manufacturing process of the adhesive joints. The first assumption is validated.

The dashed green lines indicate the prediction interval curves (PI). They were obtained with a 95% level of confidence, that is the common value used [82]. The PI curves represent the range where a single new observation is likely to fall.

The second assumption (N is log-normally distributed) can be validated analysing the normal probability plot of the residuals of $\log N$, the Figure 4.36 shows that plot.

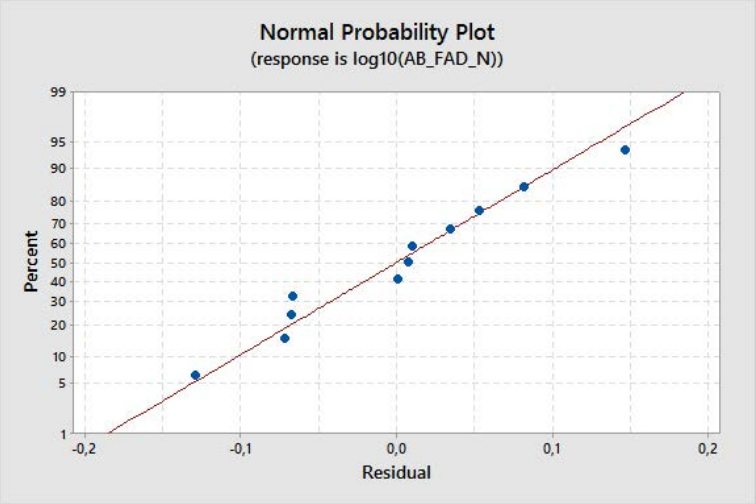

Figure 4.36: Normal probability plot of the residuals of $\log N$ in AB-20 specimens.

As it may be verified the normal probability plot of the residuals of $\log N$ from the regression line follows a linear trend. The second assumption for a good S-N curve is also checked.

The third assumption (homogeneity of standard deviation of $\log N$ with respect to S) is checked with a plot of the residuals vs the load levels, the dispersion is relatively low as can be seen in the Figure 4.37

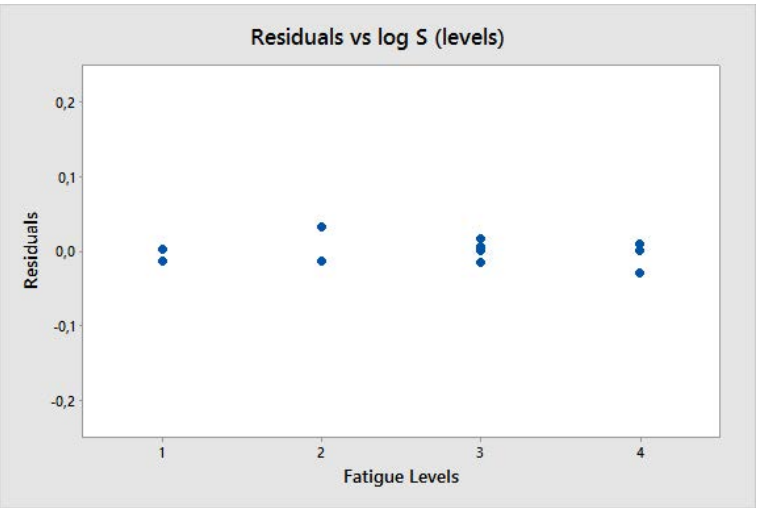

Figure 4.37: Plot of the residuals vs the load levels.

The fatigue data regarding adhesive joints with 20 mm overlap complied with the statistical tests defined by the IIW [82] with good indicators. The data will originate S-N curves with high

reliability to the benchmark goal, despite the limited number of specimens tested.

Using the linear regression represented in the Figure 4.35 is possible to obtain the Wöhler (S-N) curve that is governed by the *Basquin* law (high cycle fatigue). The fitted curve found was (remote stress in MPa):

$$\log S = 3.003735 - 0.212326 \log N \Leftrightarrow \tag{4.2}$$

$$\Leftrightarrow \log N = 14.083270 - 4.676859 \log S \Leftrightarrow \tag{4.3}$$

$$\Leftrightarrow S^{4.676859} N = 1.211352 \times 10^{14} \Leftrightarrow \tag{4.4}$$

$$\Leftrightarrow N = \frac{1.211352 \times 10^{14}}{S^{4.676859}} \Leftrightarrow \tag{4.5}$$

$$\Leftrightarrow S = \frac{1008.6372429}{N^{0.212326}} [MPa] \tag{4.6}$$

The power law equation (Eq. 4.7) that describes the S-N relationship, when plotted on a log-log scale, is defined by the *Basquin* slope (b) and any coordinate pair (N, S) on the S-N curve.

$$N_1 = N_2 \left(\frac{S1}{S2} \right)^{\frac{1}{b}} \tag{4.7}$$

Being the *Basquin* slope (b) for adhesive joints with 20 mm overlap equal to:

$$b = \frac{-(\log S_1 - \log S_2)}{\log N_2 - \log N_1} = 0.212326 \tag{4.8}$$

The S-N curve for the adhesive joint w/ 20 mm of overlap was compared to the S-N curve of a bare aluminium AA 6082-T6 plate, the Figure 4.38 shows both curves.

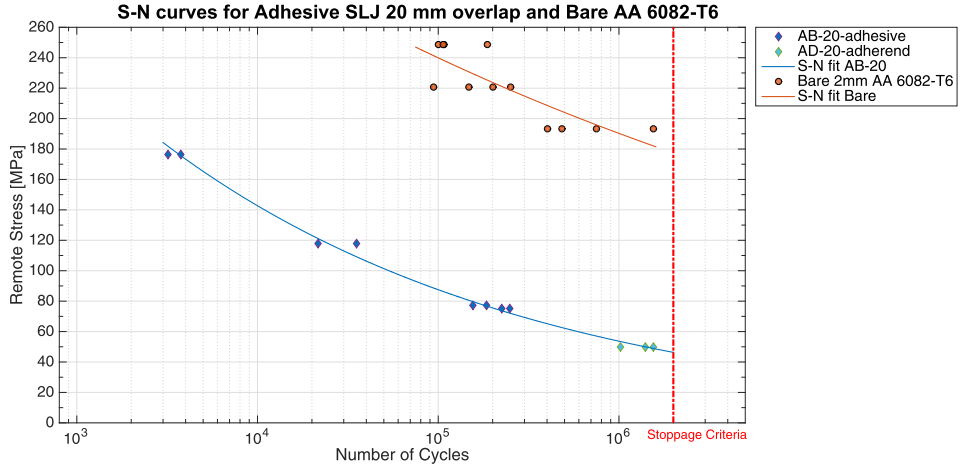

Figure 4.38: S-N curve for adhesive SLJ and bare aluminium.

The fatigue strength of the adhesive joint for the 10^5 number of cycles is ≈ 87.52 MPa and it represents $\approx 29.85\%$ of the static strength of the joint. The fatigue strength of the bare aluminium for the same number of cycles is ≈ 240.16 MPa. Comparing the two fatigue strengths the joint presents a significant reduction (63.53%). This reduction in strength of the adhesive single lap joint is normal and expected due to the geometry of the joint that induces complex efforts like shear and peel when compared to the bare material (The same trend was observed in the fatigue tests in the dummy specimens).

Two distinct failure mode groups were identified in the S-N curve of this joint. The three highest load levels resulted in a failure within the overlap (adhesive layer). The lower level of load studied resulted in a failure in the adherend. This indicates that the adhesive suffers more damage than the adherend for high stresses and presents less strength than the aluminium alloy, for lower stresses levels the opposite occurs. The goal of the dummy fatigue behaviour characterization was also try to assess if for the lower levels of loading a convergence in S-N curves (adhesive vs dummy) occurred. Since the data for the dummy specimens was scarce the analysis made next is based on a plausible assumption. If we assume that the fit found can be extrapolated, despite the statistical robustness being low, and considered valid until the stoppage criteria (two million cycles) it's possible to obtain a inferred curve that is shown in Figure 4.39.

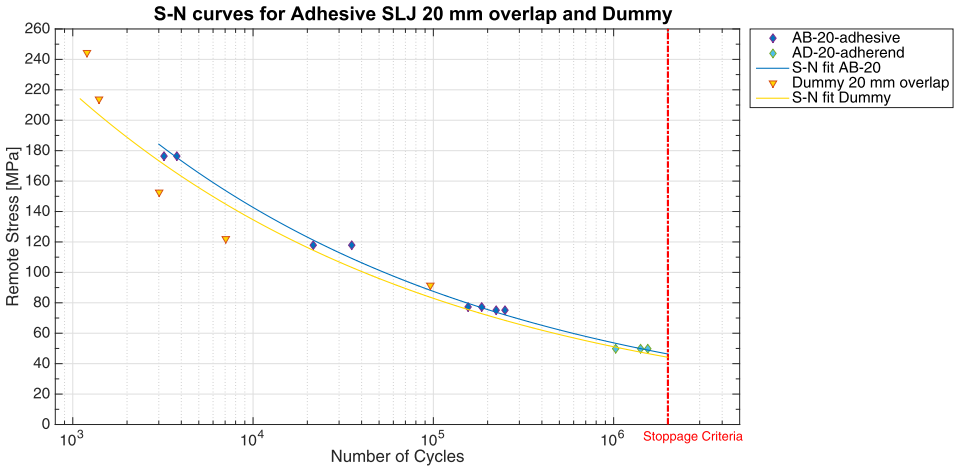

Figure 4.39: S-N curve for adhesive SLJ and extrapolation of fit in Dummy specimen.

The proximity of both curves, almost an overlapping, allied with the static results that proven that the adhesive joint performed similar (in terms of maximum stress) to the dummy specimen justifies the failure in the adherend for the lower levels of stress being the failure governed by the adherend material. The likeness of the two curves is a clear indicator that the adhesive joint is performing in the verge of the adherend strength for the given geometry under static and fatigue conditions.

It's important to refer that the failure mode when occurred in the adhesive layer was cohesive. This will be addressed in the Section 4.4. Figure 4.40 shows the typical failure surface.

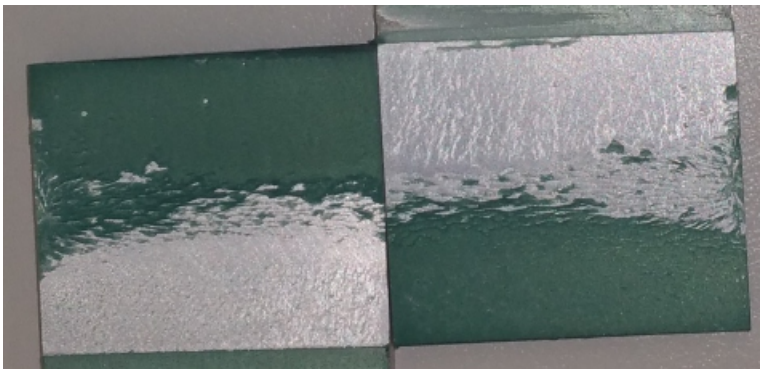

Figure 4.40: Typical failure surface of the AB-20 specimens under fatigue loads

The curves can be also presented in terms of average shear stress (τ [MPa]) vs the number of cycles being the fit expression:

$$\tau^{4.676859} N = 2.54924 \times 10^{9} \tag{4.9}$$

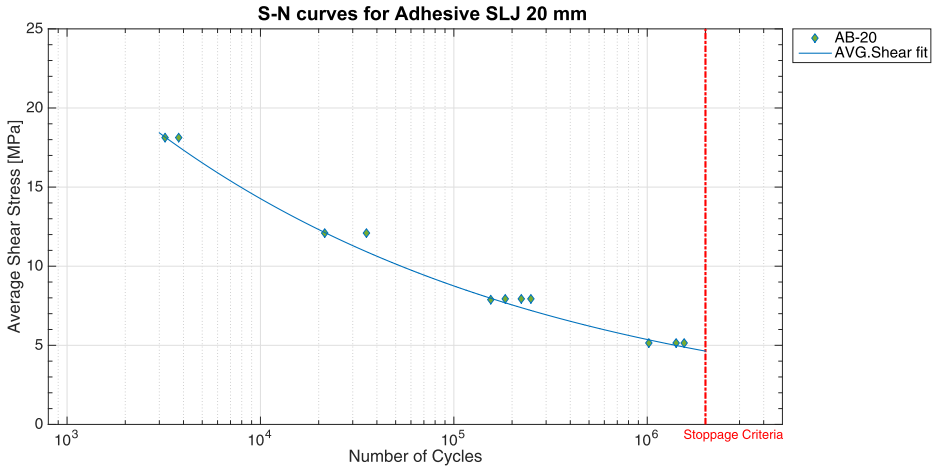

Figure 4.41: Average shear stress vs number of cycles AB SLJ curve.

4.3.3 FSW joint with 20 mm overlap FSW-20

In order to obtain a robust fit to the fatigue data several FSW specimens were tested. The overlap studied was the initial proposed (20 mm) and the fatigue tests were initiated before the inconsistencies found in the manufacturing process of the hybrid joints (20 and 40 mm of overlap). Tests for four different load levels were performed. The Table 4.13 shows the levels defined and the number of cycles obtained until the failure for each specimen.

The lower load levels were studied with more specimens due to the propensity to higher variations in low stress levels.

Table 4.13: Load levels used in the fatigue tests on the FSW joints with 20 mm of overlap and their results.

Level	**Fraction**	σ_{remote}	$\tau_{AVG.}$	**Number of Cycles**		
Static	100%	114.31 MPa	11.72 MPa	**Spec. 1**	**Spec. 2**	**Spec. 3**
1	60%	68.01 MPa	6.97 MPa	24029	22851	–
2	45%	50.44 MPa	5.23 MPa	43322	47787	–
3	33%	37.41 MPa	3.79 MPa	177808	158560	–
4	22%	24.94 MPa	2.56 MPa	1236742	1621806	1102467

The Minitab software was also used to treat the fatigue data and analyse if the assumptions for a good S-N curve were respected. Figure 4.42 shows the fitted linear regression of the data with the scale in $\log N$ and $\log S$, being S the remote stress in MPa.

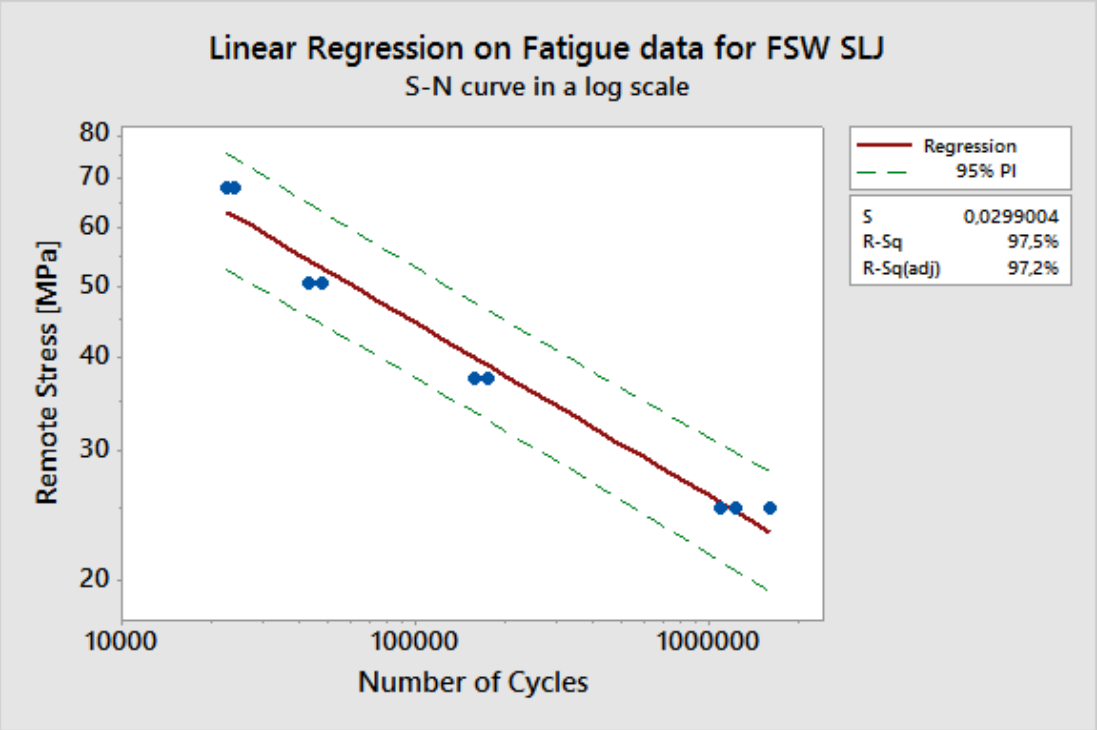

Figure 4.42: Linear regression of the fatigue data from FSW-20 specimens.

In Figure 4.42 is also represented the prediction interval curves (PI) with a 95% level of confidence.

The value of the Standard Error of the Regression (S) is 0.0299 and it's in the same order of magnitude than the value obtained for the AB-20 specimens (0.0178). This means that the standard distance data values fall close to the regression line. The R-Sq (R-squared) value for the FSW fit found was 97.5%. The value obtained is lower than the one for the AB-20 specimens however it's more than a satisfactory value. The two parameters assess the Goodness-of-Fit and help to check the first assumption (linear relationship between logS and logN). They may indicate that the manufacturing process is controlled for this type of joint, this is in line with the results

found in the static tests.

The second assumption (N is log-normally distributed) can be assessed analysing the normal probability plot of the residuals of $\log N$, the Figure 4.43 shows that plot.

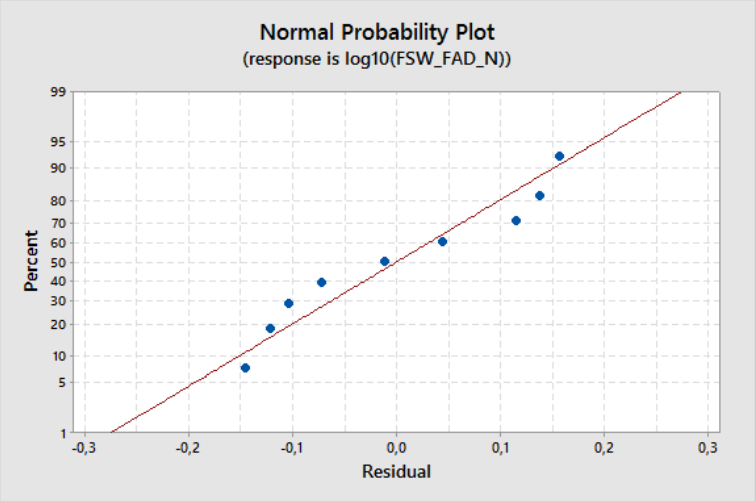

Figure 4.43: Normal probability plot of the residuals of $\log N$ in FSW-20 specimens.

It's possible to observe that the residual points follow a "s shape" trend although not highly pronounced. However, they can be satisfactorily approached by a linear regression. The second assumption is validated, however with less certainty than in the case of the AB-20 specimens.

The third assumption (homogeneity of standard deviation of $\log N$ with respect to S) is checked with a plot of the residuals vs the load levels, the dispersion within the load levels is relatively low as can be seen in the Figure 4.44

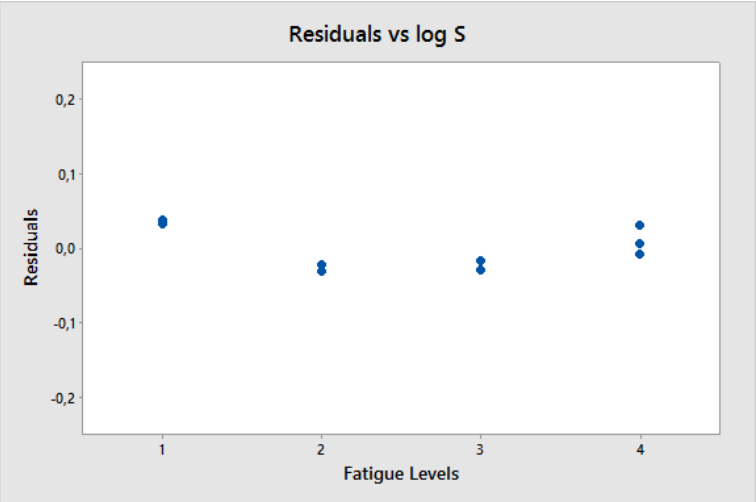

Figure 4.44: Plot of the residuals vs the load levels.

The three assumptions were checked with a satisfactory performance for the FSW joints. This data will originate S-N curves with a good reliability to the benchmark goal, despite the limited number of specimens tested.

The data gathered allowed to determine the S-N curve expression. Using the linear regression represented in the Figure 4.42 is possible to obtain the the equation of the *Basquin* law that governs the S-N curve. The equation is (remote stress in MPa):

$$\log S = 2.823202 - 0.234794 \log N \Leftrightarrow \tag{4.10}$$

$$\Leftrightarrow \log N = 11.856231 - 4.154149 \log S \Leftrightarrow \tag{4.11}$$

$$\Leftrightarrow S^{4.154149} N = 7.18767 \times 10^{11} \Leftrightarrow \tag{4.12}$$

$$\Leftrightarrow N = \frac{7.18767 \times 10^{11}}{S^{4.154149}} \Leftrightarrow \tag{4.13}$$

$$\Leftrightarrow S = \frac{665.583206}{N^{0.234794}} [MPa] \tag{4.14}$$

The *Basquin* slope that can be used in the equation 4.8 for the FSW single lap joint with a overlap of 20 mm is equal to 0.234794.

The S-N curve for this joint was compared to the S-N curve of a bare aluminium AA 6082-T6 plate and the adhesive SLJ with the 20 mm of overlap, the Figure 4.45 shows the three different curves.

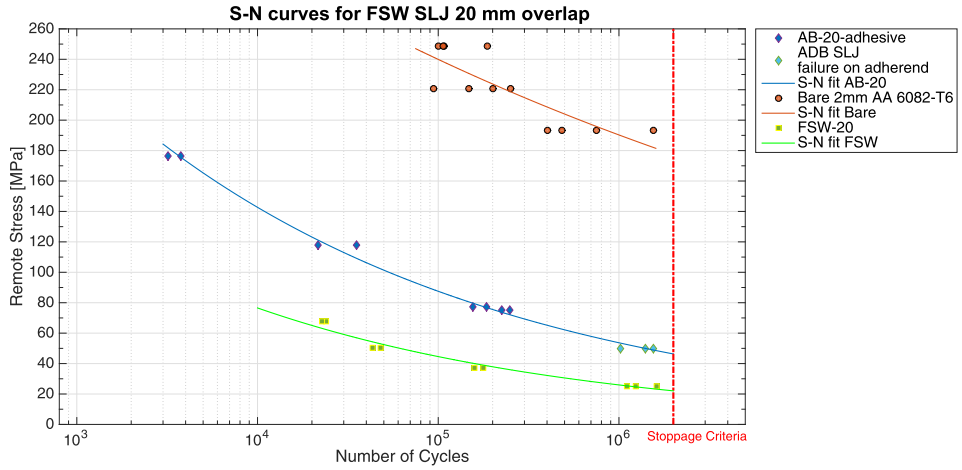

Figure 4.45: S-N curve for FSW joint compared to the AB-20 and bare aluminium curves.

As expected the FSW joints performed poorly under fatigue when compared to the adhesive joints with the same overlap, giving the hybrid joint an opportunity to improve the fatigue behaviour of the FSW only joint if manufacturing hurdles are overtaken. The fatigue strength of the friction stir welding single lap joint for 10^5 number of cycles is ≈ 44.59 MPa and it represents $\approx 39.01\%$ of the static strength of the joint. This is an higher fatigue/static strength ratio when compared to the AB-20 joint, however it's obtained to lower stress level.

The fatigue strength of the FSW SLJ when is compared to the bare aluminium for the same number of cycles represents only 18.57%. The same comparison can be done with the AB-20 joint, the fatigue strength of the FSW is 50.95% of the AB-20 one. This is a significant strength reduction, that was expected based on the static performance and reflects the difference in mechanical performance between the adhesive and the welding. However, the reduction in the strength was higher under static conditions (Section 4.2.1.3) than under fatigue when compared to the AB-20 joints. It's possible to plot (Figure 4.46) the fatigue strength ratio between the FSW-20 and AB-20 SL joints and verify that it follows a linear trend that decreases with the increase in the number of cycles and varies from 53.65% and 47.63%. This proves that in all the fatigue life of the FSW joint the reduction in strength is less severe than in the static conditions when compared with the adhesive joint. This remarkable fact can be explained by appealing to the known high sensibility of the adhesives to the strain rate that does not verifies in metals like the aluminium. The higher the strain rate the stiffer becomes the adhesive reducing the total capability to absorb energy. In the static tests the adhesive acts as a more ductile material than under fatigue testing (performed with an average frequency of 6Hz, that resulted in displacements of 0.2mm that correspond to a displacement rate of 1.2 mm/s compared to the velocity of the static tests that were performed at 0.00278 mm/s). This high velocity solicitation results in a more brittle behaviour by the adhesive and consequently for the adhesive joint (absorbing less energy than in the static test). The FSW joint is not much as sensitive to the strain rate being the ability to observe energy in static or fatigue tests almost the same. This may justify the difference in the strength reduction under static and fatigue conditions of the FSW joint when compared with the AB-20

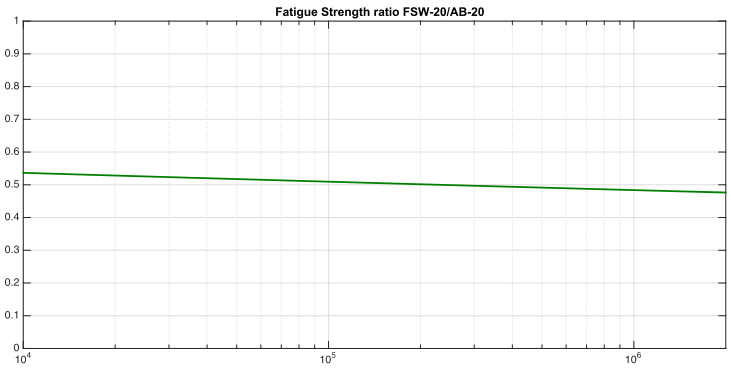

Figure 4.46: Fatigue Strength ratio FSW-20/AB-20

Two different modes of failure were obtained, for higher and for lower loads. For higher loads the crack started within TMAZ in other location different from the "hook defect" (will be seen in Section 4.4), for higher loads there was a fracture that came from a pre-crack similar to the "hook defect" (an effective sheet thickness reduction).

Figure 4.47: Fatigue failure surface of the FSW specimens.

The fatigue life curve can be also presented in terms of average shear stress (τ [MPa]), being the area of the overlap considered, vs the number of cycles being the fit expression:

$$\tau^{4.154149} N = 5.035957 \times 10^{7} \tag{4.15}$$

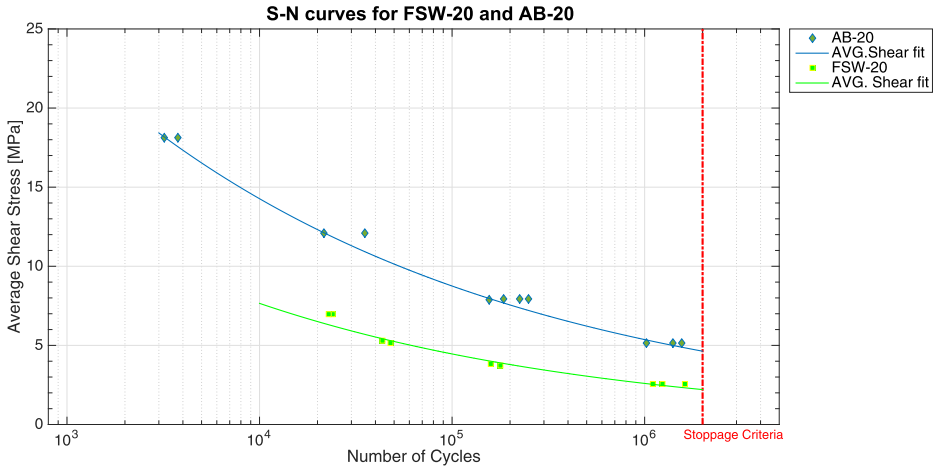

Figure 4.48: Average shear stress vs number of cycles for FSW-20 and AB-20 curves.

4.3.4 Adhesive joint with 40 mm overlap AB-40

For the adhesive joint with 40 mm of overlap only eight specimens were studied. That allowed to find only a trend that is sufficient for benchmarking purposes.

The Table 4.14 shows the levels defined and the number of cycles obtained until the failure for each specimen.

Figure 4.49 shows the fitted linear regression of the data with the scale in $\log N$ and $\log S$, being S the remote stress in MPa.

As expected due to the low number of specimens tested the fitness of the curve to the fatigue data was not the most accurate, as the S and R-Sq value confirm.

Table 4.14: Load levels used in the fatigue tests on the adhesive joints with 40 mm of overlap and their results.

Level	Fraction	σ_{remote}	$\tau_{AVG.}$	Number of Cycles	
Static	100%	324.59 MPa	10.83 MPa	**Spec. 1**	**Spec. 2**
1	72.71%	236.00 MPa	12.10 MPa	12592	19813
2	46.21%	150 MPa	7.88 MPa	21022	–
3	36.23%	117.6 MPa	6.03 MPa	193600	–
4	23.11%	75.00 MPa	3.94 MPa	338951	–
5	20.023%	65 MPa	3.33 MPa	819753	–
6	15.40%	50 MPa	2.56 MPa	2034162^{stoped}	–

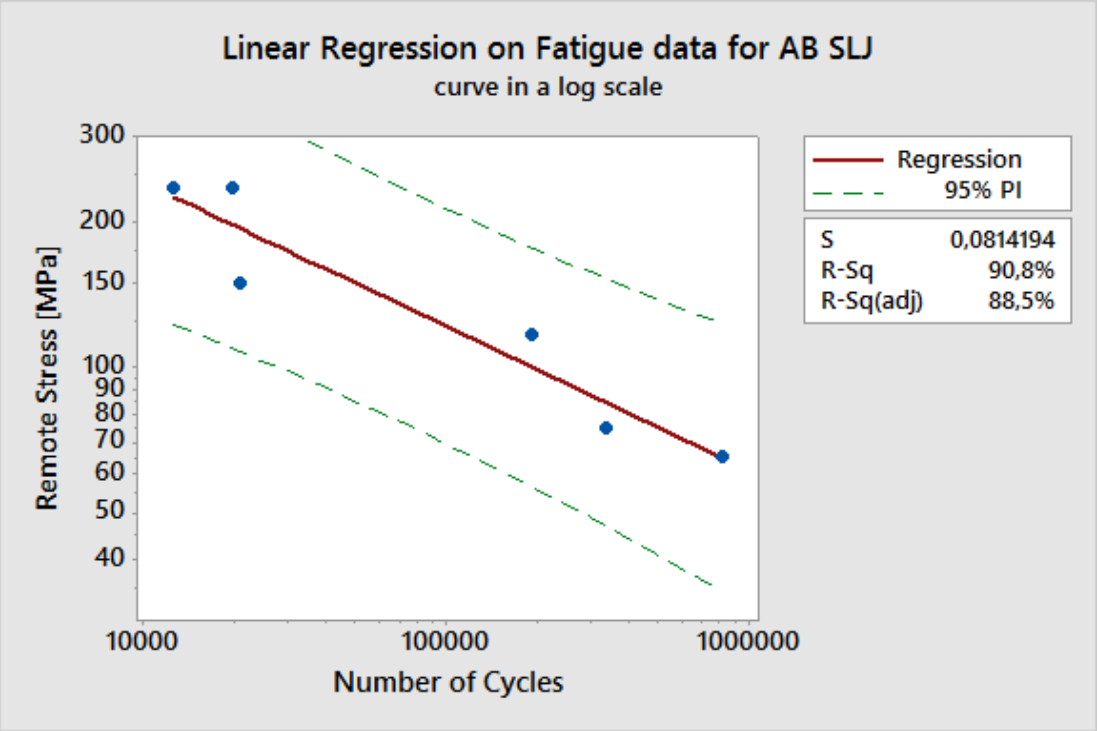

Figure 4.49: Linear regression of the fatigue data from AB-40 specimens.

The expressions of the curve that will be presented requires confirmation and are not representative of a proper S-N curve. Time and resources limitations did not allowed a deeper study on this kind of joint. The equations found were:

$$\log S = 3.583339 - 0.299477 \log N \Leftrightarrow \tag{4.16}$$

$$\Leftrightarrow \log N = 11.314604 - 3.031252 \log S \Leftrightarrow \tag{4.17}$$

$$\Leftrightarrow S^{3.031252} N = 2.063498 \times 10^{11} \Leftrightarrow \tag{4.18}$$

$$\Leftrightarrow N = \frac{2.063498 \times 10^{11}}{S^{3.031252}} \Leftrightarrow \tag{4.19}$$

$$\Leftrightarrow S = \frac{3831.238171}{N^{0.299477}} [MPa] \tag{4.20}$$

The "S-N" curve for the adhesive joint w/ 40 mm of overlap was compared to the S-N curve of a bare aluminium AA 6082-T6, the AB-20 and the FSW-20 specimens. Figure 4.50 shows the curves.

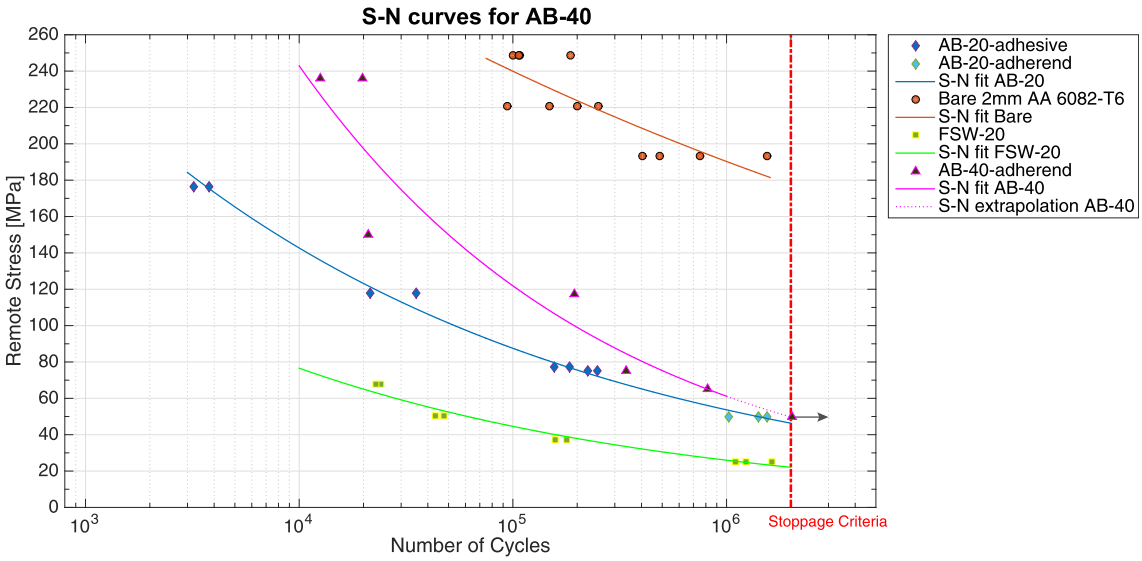

Figure 4.50: S-N curve for adhesive 40 mm overlap.

All the specimens failed in the aluminium adherend, meaning that the joint is stronger than the aluminium adherend. As it is possible to observe when the stress levels were lower the failure in the AB-20 specimens were in the adherend being the two curves (AB-20 and AB-40) nearly coincident. This validates that for the lower stress level, in the joint w/ 20 mm of overlap, the joint is actually stronger than the adherend being from that point on the fatigue life governed by the base material and stress concentrations inherent to the specimen configuration. The difference in fatigue strength and failure mode between the AB-40 and AB-20 for the other levels shows that the AB-40 specimen has an overlap that is enough to assure that the bonded area is always stronger than the adherend. This overlap lead to a maximum fatigue strength with the geometry and material chosen.

There was a specimen that reached the stoppage criteria. Having the test been interrupted without specimen failure. This specimen was not used to find the fitting of the curve.

The fatigue strength obtained for the AB-40 specimens at 10^5 number of cycles was found to be $\approx$ 121.57 MPa. This value is not representative of the real fatigue strength as it requires more tests to be accurately defined, however it's sufficient to benchmark and find the relative differences

for the other types of joint's studied. This fatigue strength obtained represents $\approx 37.45\%$ of the static strength of the joint.

The fatigue strength of the bare aluminium for the same number of cycles is ≈ 240.16 MPa, comparing the two fatigue strengths the joint shows a strength that is 63.53% of the base material strength. The curve obtained expressed in remote stress vs number of cycles can be shown in shear stress vs number of cycle. The fitted curve is now:

$$\tau^{3.031252} N = 2.348844 \times 10^{7} \tag{4.21}$$

It is possible to plot the curve and compare it with the specimens AB-20 and FSW-20 (Figure 4.51). However since the failure of the AB-40 specimens occurs in the adherend the joint strength will decrease due to an increase in the bonded area that is not followed by a significant increase in the fatigue strength (because it's limited by the adherend and not by the adhesive). This was expected even if we consider that the ultimate tensile shear stress in the static tests was already lower in the AB-40 specimens than in the AB-20. This plot would be interesting for overlaps that had failure in the adhesive.

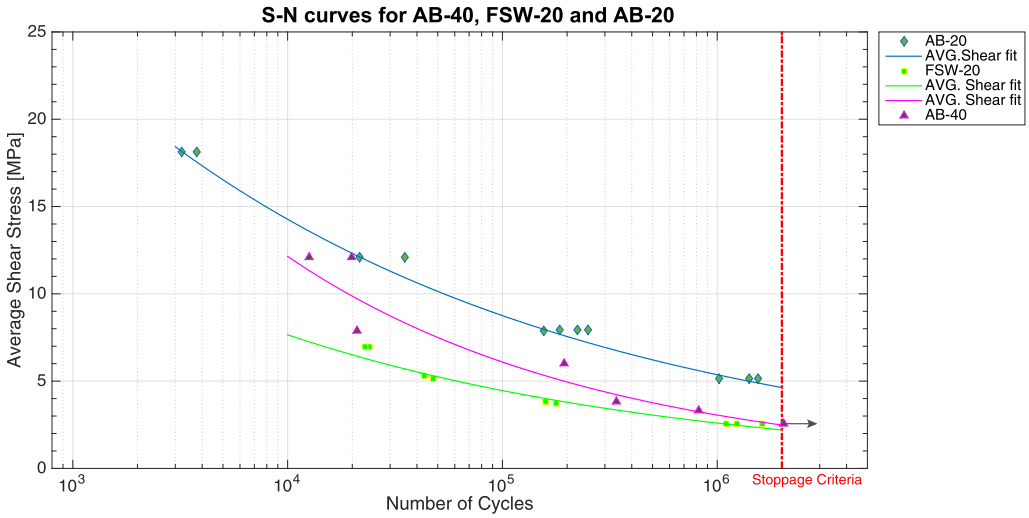

Figure 4.51: Average shear stress vs number of cycles for AB-40, FSW-20 and AB-20 curves.

This graph allows to conclude that the overlap of 40 mm is oversized for the adherend chosen and there is an optimum overlap length that can result in similar results for fatigue strength expressed in remote stress and an higher strength expressed in shear stress.

4.3.5 Hybrid joint with 40 mm overlap Hyb-40

Nine specimens under fatigue loads were tested, the Table 4.15 shows the levels tested and the number of cycles obtained until the failure for each specimen.

The specimens with the tag "stopped" reached the stoppage criteria of 2 million of cycles. The same inconsistent performance that was identified in the static conditions was as well verified

Table 4.15: Load levels used in the fatigue tests on the hybrid joints with 40 mm of overlap and their results.

Level	**Fraction**	σ_{remote}	$\tau_{AVG.}$	**Number of Cycles**			
Static	100%	175.44 MPa	8.99 MPa	**Spec. 1**	**Spec. 2**	**Spec. 3**	**Spec. 4**
1	50.00%	88.44 MPa	4.38 MPa	23269	–	–	–
2	40.00%	77.75 MPa	3.60 MPa	28518	46130	101795	280796
3	31.66%	55.54 MPa	2.84 MPa	Stopped	–	–	–
4	25.00%	44.22 MPa	2.24 MPa	41751	Stopped	–	–

under fatigue loads. The level 4 presented a large inconsistency. One specimen failed after 41751 cycles having another specimen under the same load conditions reached the stoppage criteria. The same heterogeneity can be found in the stress level 2 where two of the four specimens presented failures much earlier than the other two, being the number of cycles of a different order of magnitude. For that level the average number of cycles was 114310 and the standard deviation was even higher than the average, 115301.

The plot of the fatigue data obtained is shown in Figure 4.52 and it's compared to the AB-40 and FSW joints data.

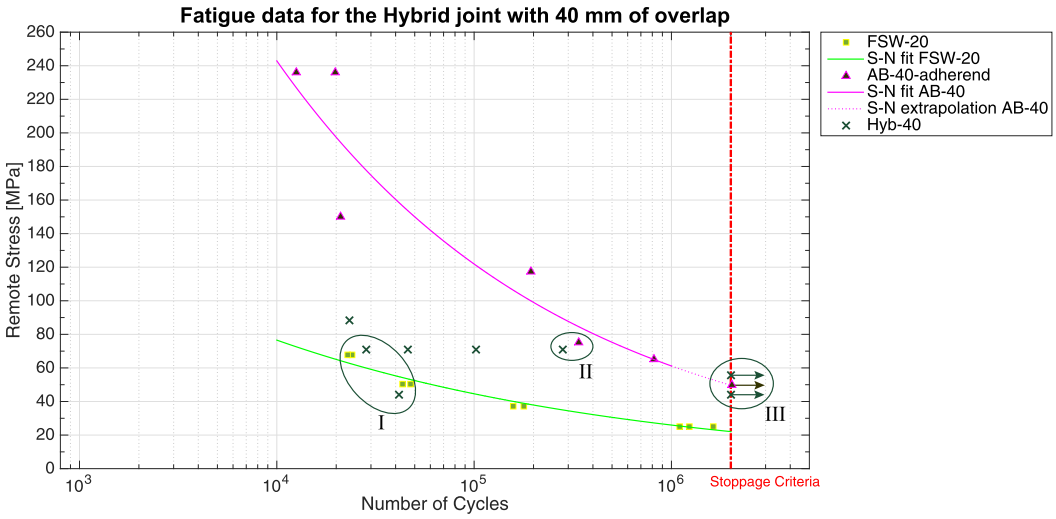

Figure 4.52: Fatigue data for the Hybrid joint with 40 mm of overlap.

The group I of points in the graph validate the claim done with the results of the static tests. The presence of the adhesive, when it does not bound well or carry any load by any other reason, acts like a defect in the welding being the mechanical behaviour of the hybrid joint close or worst than the FSW joint alone. The group II and III indicates that when the manufacturing process problem is less significant the behaviour under fatigue is closer to the adhesive joint.

It's relevant that the stoppage criteria for some specimens was reached in the same stress region than the adhesive joints (20 and 40 mm). It's a clear sign that the hybridization concept has potential to be applied with success as soon as the manufacturing problems are overcome.

The typical failure surface in the hybrid joint under fatigue is shown in the Figure 4.53.

Figure 4.53: Failure surface of the Hyb-450-40 specimens under fatigue fatigue loads.

4.3.6 Summary

The S-N curves were successfully obtained with a high level of certainty for the FSW and adhesive joints with 20 mm of overlap. For adhesive joint with 40mm of overlap a fit with a reasonable representativeness of the fatigue behaviour of the joint was obtained. The dummy data was insufficient to define a clear trend however it was enough to find that the differences from the dummy to the AB-20 specimens are not very significant.

The data gathered for the hybrid joints were influenced by the problems found in the manufacturing process and lead to inconclusive results in order to benchmark the fatigue behaviour of a well produced joint. However there were some results that seem to indicate that the concept for this overlap has potential.

The plot for all data of fatigue gathered is shown in Figure 4.54.

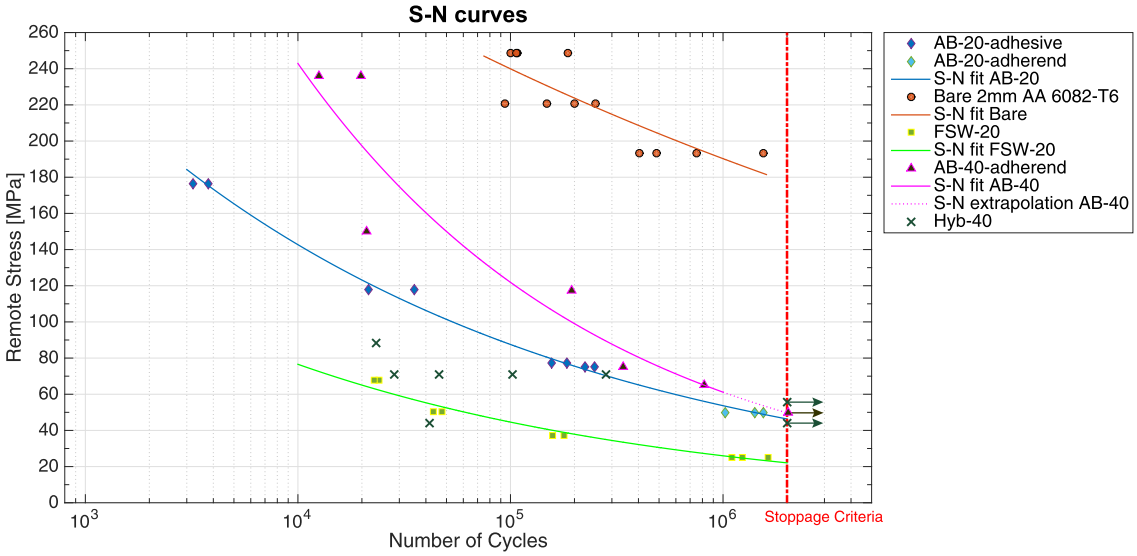

Figure 4.54: Fatigue data for the joints studied.

Figure 4.55 shows the fatigue strength at 10^5 number of cycles for the different joints studied.

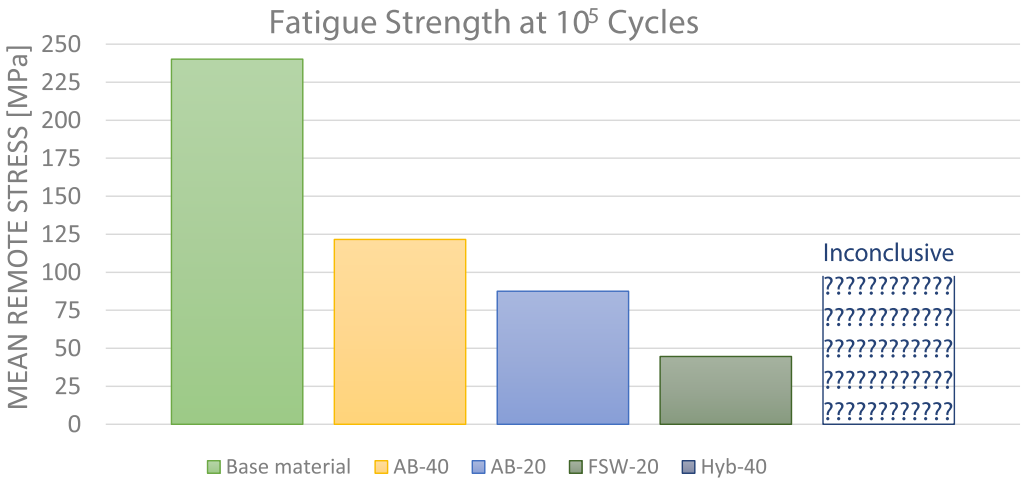

Figure 4.55: Fatigue strength for the joints studied at 10^5 cycles.

In the Table 4.16 is shown the coefficients found for the *Basquin* law that governs the S-N curves, being $S^m N = K_0$.

Table 4.16: Coefficients found for S-N curves

Joint	m	K_0
Dummy	4.183240	7.429624×10^{12}
AB-20	4.676859	1.211352×10^{14}
FSW-20	4.154149	7.18767×10^{11}
AB-40	3.031252	2.063498×10^{11}

4.4 EDS surface analysis

The results obtained in the EDS analysis are shown here, apart the contamination analysis of the hybrid joints done in Section 4.2.2.2.

4.4.1 Anodization surface

In order to assess if the PAA anodization process adopted by the author based on the ASTM 3933 standard produced the expected porous surface that enhance the adhesion between the adhesive and adherend. Figure 4.56 shows the anodization surface obtained.

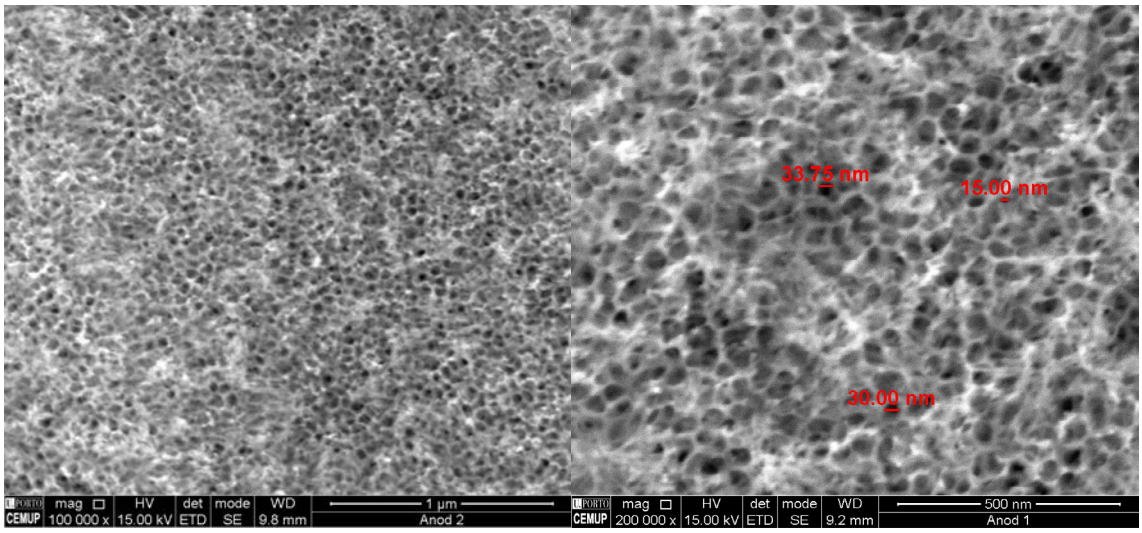

Figure 4.56: Anodized surface EDS analysis.

The anodized surface was obtained with great success and the diameters of the pores are close to the theoretical ones (Figure 2.33). This PAA anodization process was applied in the adhesive and hybrid joints. An enhanced adhesion due to the surface treatment is expected.

4.4.2 FSW failure surface analysis

A specimen from the load level 1 of the FSW joint that was submitted to fatigue loads was analysed. The failure occurred within the welding due to the high loads. There was severe plastic deformation on the weld nugget that lead to the failure of the specimen. The surface analysed was similar to the shown in the Figure 4.57.

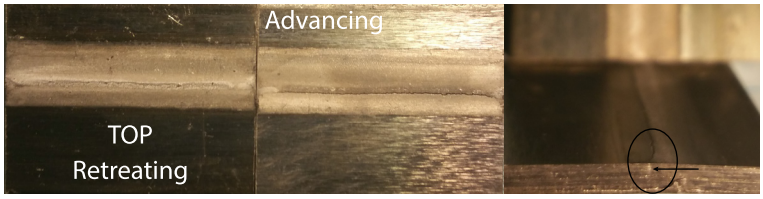

Figure 4.57: FSW surface analysed.

There was a formation of a crack in the bottom substrate on the retreating side. This crack is present in the majority of the specimens tested, and at lower loads lead to the joint failure (the crack grew through all of the substrate thickness, it's indicated with an arrow in the Figure 4.57). This indicates that the crack is a consistent effective sheet reduction (inherent to the process) with small dimensions that due to the configuration adopted (FSW joint produced in order to assure that in the top sheet the advancing side is in the loaded side, see Figure 2.16 a)) is under higher load than the hook defect in the advancing side. Figure 4.58 shows the magnified image of the failure surface.

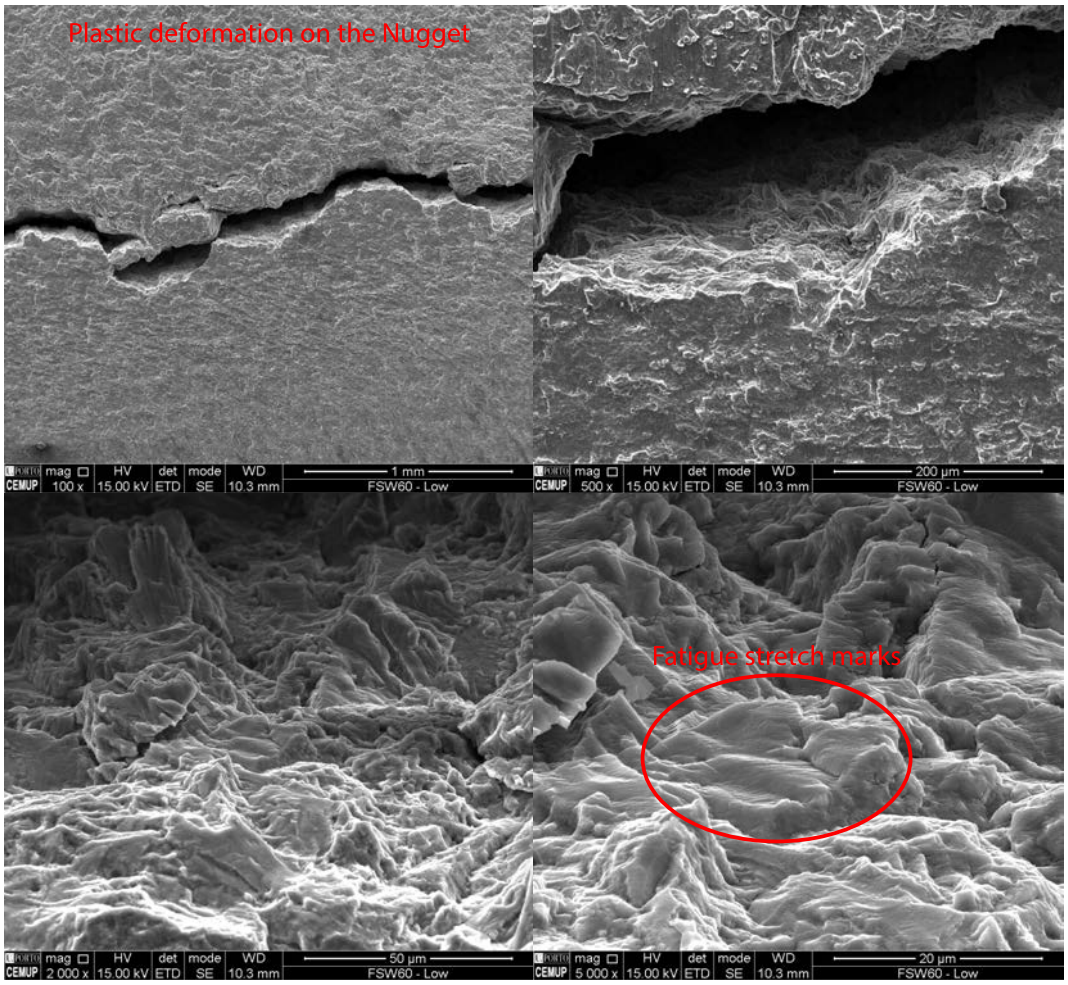

Figure 4.58: FSW surface analysed in EDS.

It is possible to notice a severe plastic deformation on the nugget zone where the failure occurred. The crack shown presents fatigue stretch marks identified near the crack edge, what indicates that it was a tiny pre-crack (defect).

4.4.3 Adhesive failure surface analysis

The specimen studied in EDS analysis was submitted to fatigue loading (load level 4) and the failure surface was presented in the Figure 4.40.

The mode of failure, at naked eye, seemed to be a mixed mode that tend more to a cohesive close to the interface. The EDS analysis was useful to clarify.

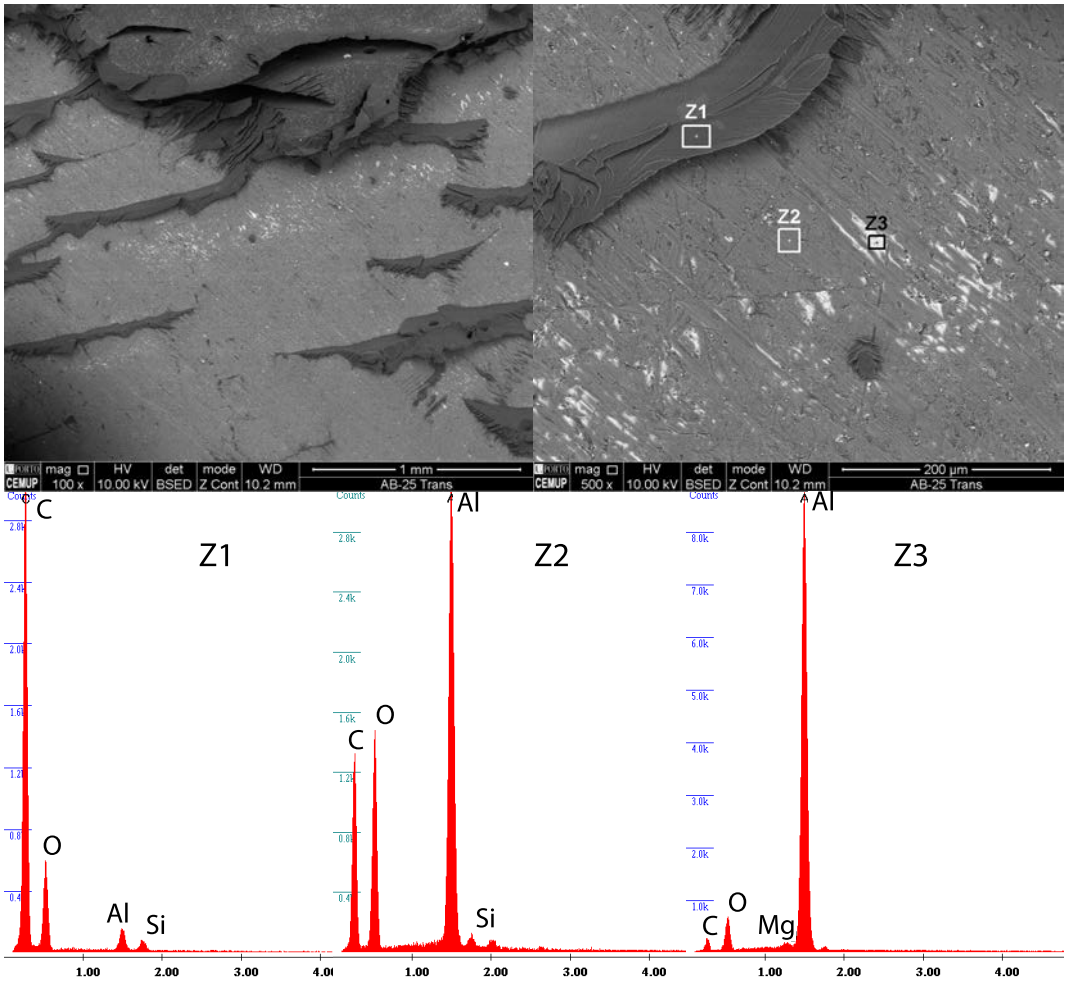

Figure 4.59: adhesive joint surface analysed in EDS.

The zone Z1 is clearly an adhesive zone. The spectrum of the adhesive in the EDS analysis is characterized by a strong peak in the Carbon content and a moderate one on the Oxygen. The remaining aluminium present in the spectrum is paired with a small fraction of the O and it's Al_2O_3 pulled out from the other adherend.

An adhesive layer is present in zone Z2 (due to the strong Carbon peak), anodization layer (Al_2O_3) and was also detected the aluminium adherend. Since the EDS analysis penetrates more than the thickness of the adhesive layer, on this zone the adherend was detected also. The carbon spectrum is a proof that the surface is covered by the adhesive, being the failure mode cohesive near to the interface.

The zone Z3 is clearly an adherend zone (a strong peak of aluminium) and there is a small trace of the anodization layer. This is interesting, it tells us that the anodization layer was pulled out from the adherend. Since the Figure 4.56 was demonstrated that the anodization was well

performed. This means that the peel efforts are stronger than the chemical linkage between the adherend and the anodization layer, meaning that we reached the full potential of the bond.

This pull out of the anodization layer is confirmed in the Figure 4.60.

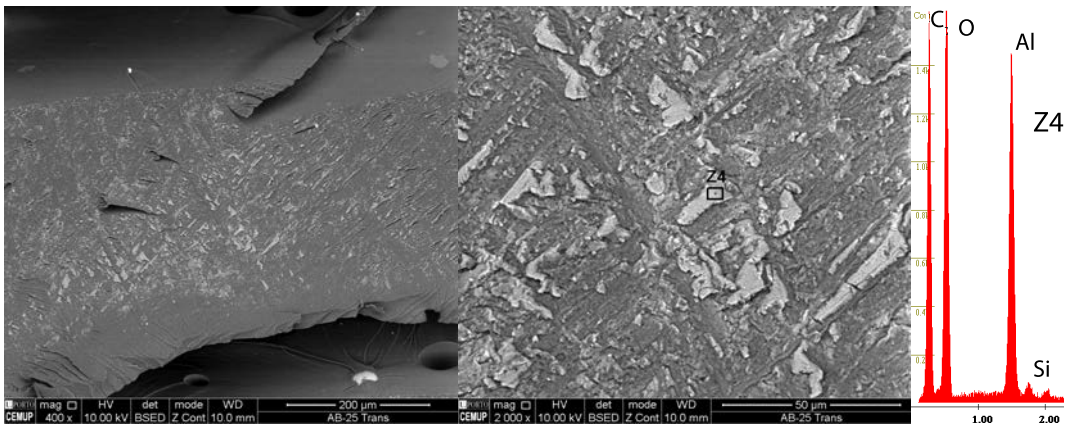

Figure 4.60: Adhesive joint surface analysed in EDS.

The EDS analysis shows that in the other face in Z4 zone there is adhesive and anodization layer (Al_2O_3) due to the higher concentration of Oxygen and aluminium. Meaning that the anodization layer was pulled out from the other side.

There was no signs of contaminations like the ones found in the hybrid joints. The manufacturing process lead to a strong bonding of the joint.

4.4.4 Hybrid joint failure surface analysis

Some results for the hybrid joint EDS analysis were already presented, at that point we concluded that the hybrid joint is highly contaminated, what may explain the poor mechanical performance and high scatter. The hybrid joint specimens analysed were submitted to tensile tests.

Figure 4.61 shows an area with a lower density of contaminations.

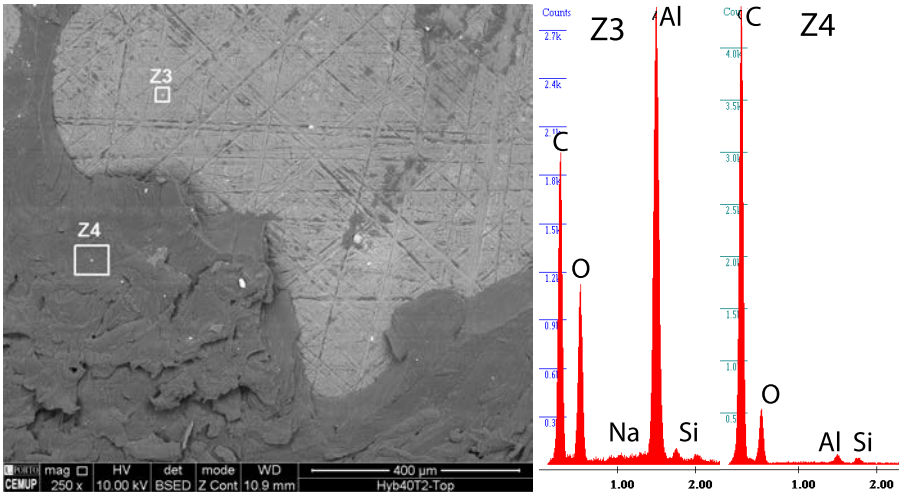

Figure 4.61: Hybrid joint surface analysed in EDS.

As it's possible to observe there is in the zone Z4 a robust adhesive layer and in the zone Z3 there is the presence of a thinner adhesive layer as well a small concentration of Na. This proves that the failure mode is cohesive near the interface in the areas that present less contaminations.

4.5 Dynamic analysis

The dynamic analysis performed allowed to obtain the frequency response function of each type of joint and the coherence function. Only the first three modes were studied and the maximum frequency achieved was ≈ 1100 Hz. Figure 4.62 shows the mode shapes for the first 3 modes for a beam under free-free boundary conditions (the same tested).

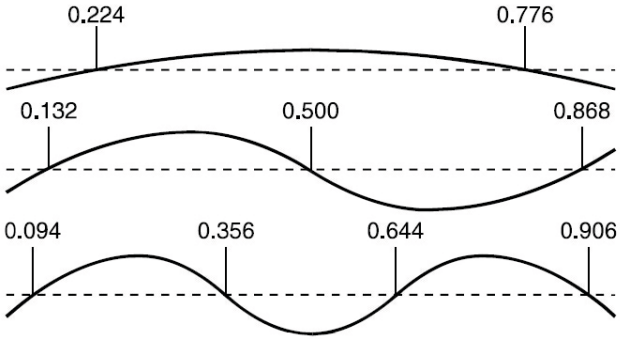

Figure 4.62: Mode shapes for the first 3 modes for a beam under free-free boundary conditions. [39]

In the following Subsections will be presented the FRF, coherence function and damping ratio (ξ) for each type of joint.

4.5.1 Friction stir welding SLJ with 20 mm of overlap

The typical FSW joint frequency response function obtained in one specimen is shown in the Figure 4.63. The resolution obtained in the measurements was 0.1563 Hz.

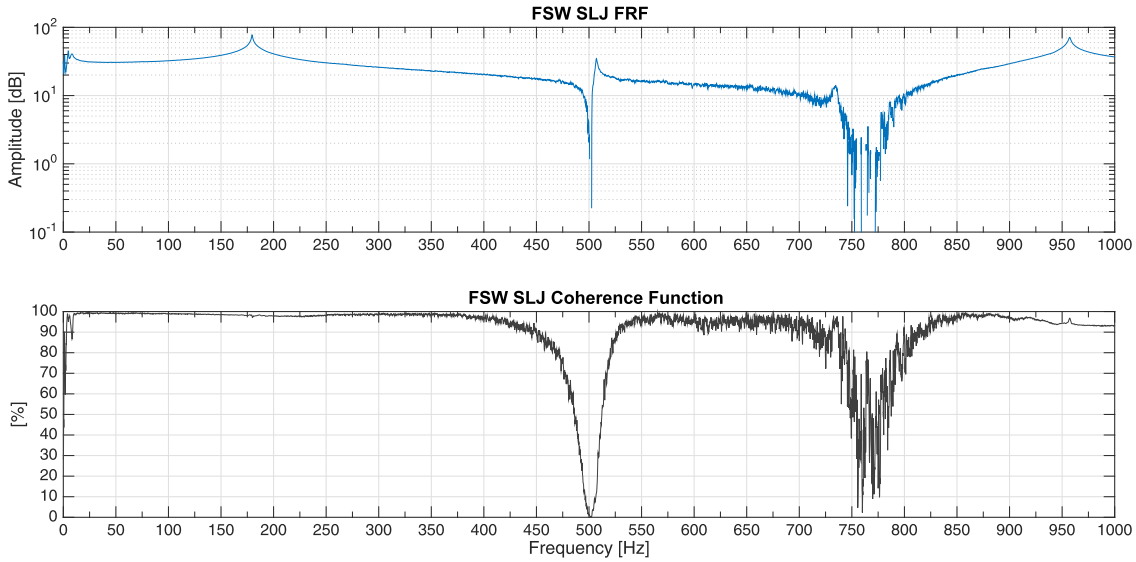

Figure 4.63: FRF and coherence function for the damping analysis in the FSW joint.

In the first zone of the FRF plot [0;20] Hz, the typical rigid body behaviour is present as was expected. The first natural frequency (first mode) found in the two specimens was equal to $\omega_{n1} = 178.91$ Hz. The coherence value for this measure was nearly 100%.

In the anti-resonances the coherence function drops drastically. This is a normal behaviour in this kind of analysis and it was verified. The second natural frequency found had a lower coherence value (because it was preceded by a strong anti-resonance) however in the two specimens tested the value was similar. The average value found was $\omega_{n2} = 505.94$ Hz.

Within the frequency range of [650;850] Hz the measurement was a bit inaccurate, however this had no influence in the damping analysis because in that frequency range there is no natural mode.

The third natural frequency found had an high coherence between the measurements and was equal to $\omega_{n3} = 956.09$ Hz.

This measurements allied to the equation 3.1 allowed to obtain the damping ratio (ξ) of the joint for each natural mode. The Table 4.17 shows the average ξ values found for the FSW joint for the first three natural modes.

Table 4.17: Average ξ values found for the FSW joint for the first three natural modes

Natural mode	**Damping ratio ξ**
1	0.177%
2	0.097%
3	0.079%

The FSW joint presents a very small damping ratio as expected by a joint of this type. There is no specific damping element in this system. The damping capability is mainly due to the base material. Being $\tan\delta = 2\xi$ and having in mind the value of the $\tan\delta$ presented in the Section 3.1.1 the value found is within the range of the aluminium damping.

4.5.2 Adhesive SLJ with 20 mm of overlap

The average frequency response function obtained in one specimen of the adhesive single lap joint with 20 mm of overlap is shown in the Figure 4.64. The resolution obtained in the measurements was 0.250 Hz. The dropping in the resolution was due to the need to go further in the frequency range to find the third natural mode that was higher than the previous 1000 Hz maximum.

The FRF obtained for the AB-20 joint was more accurate in all the frequency range that the one obtained for the FSW joint.

In the first zone of the FRF plot [0;10] Hz the rigid body behaviour was found. The first natural frequency (first mode) average value found in the two specimens was equal to $\omega_{n1} = 190.83$ Hz. The coherence value for this measure was nearly 100%.

The reduction in the coherence function was less severe in the anti-resonances range due to the lower anti-resonance. This leaded to a higher accuracy in the measurement of the second average natural frequency. The average value found was $\omega_{n2} = 504.25$ Hz.

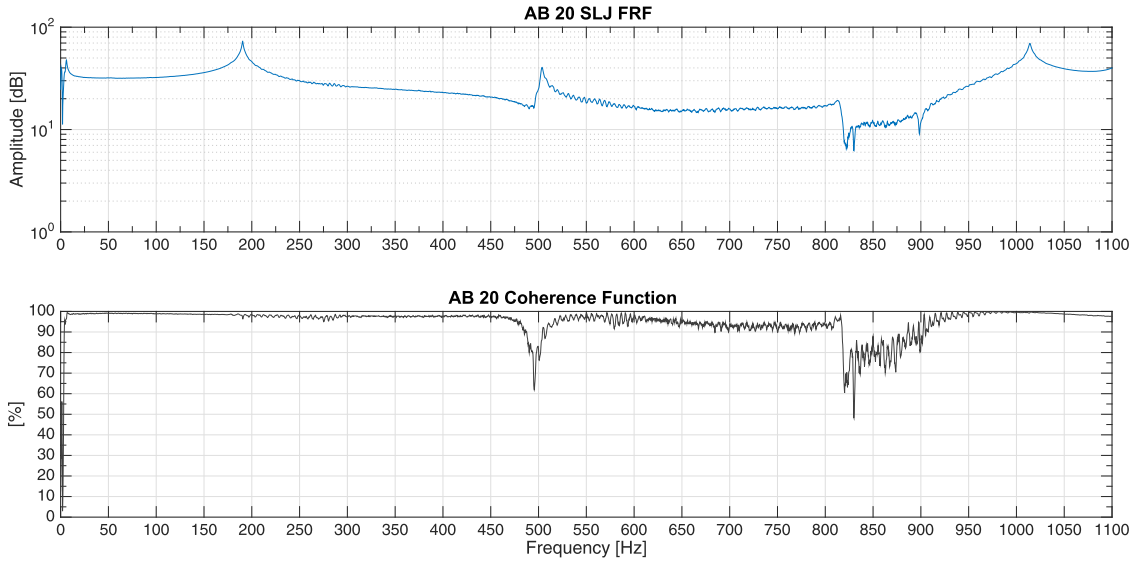

Figure 4.64: FRF and coherence function for the damping analysis in the AB-20 joint.

The third average natural frequency found had an high coherence between the measurements, nearly 100% and was equal to $\omega_{n3} = 1016.00$ Hz.

This measurements allied to the equation 3.1 allowed to obtain the damping ratio (ξ) of the joint for each natural mode. The Table 4.18 shows the average ξ values found for the AB-20 joint for the first three natural modes.

Table 4.18: Average ξ values found for the AB-20 joint for the first three natural modes.

Natural mode	**Damping ratio ξ**
1	0.222%
2	0.221%
3	0.086%

The shape of the natural mode is equal for this specimen and for the FSW one. As expected it was found that the adhesive joint is more damped than the FSW joint, however they are both very small damped. The biggest difference between the two types of joints is in the second natural mode. Attending to the shape of that mode, that presents a node in the middle of the specimen (joint), this makes sense because the joint is more solicited in that mode than in the others. The adhesive is more requested what allows to damp more, leading to a bigger difference in the damping ratio.

4.5.3 Adhesive SLJ with 40 mm of overlap

The average frequency response function obtained in one specimen of the adhesive single lap joint with 40 mm of overlap is shown in the Figure 4.65. The resolution obtained in the measurements was 0.1563 Hz.

The coherence function assures that the measurements were very consistent between them.

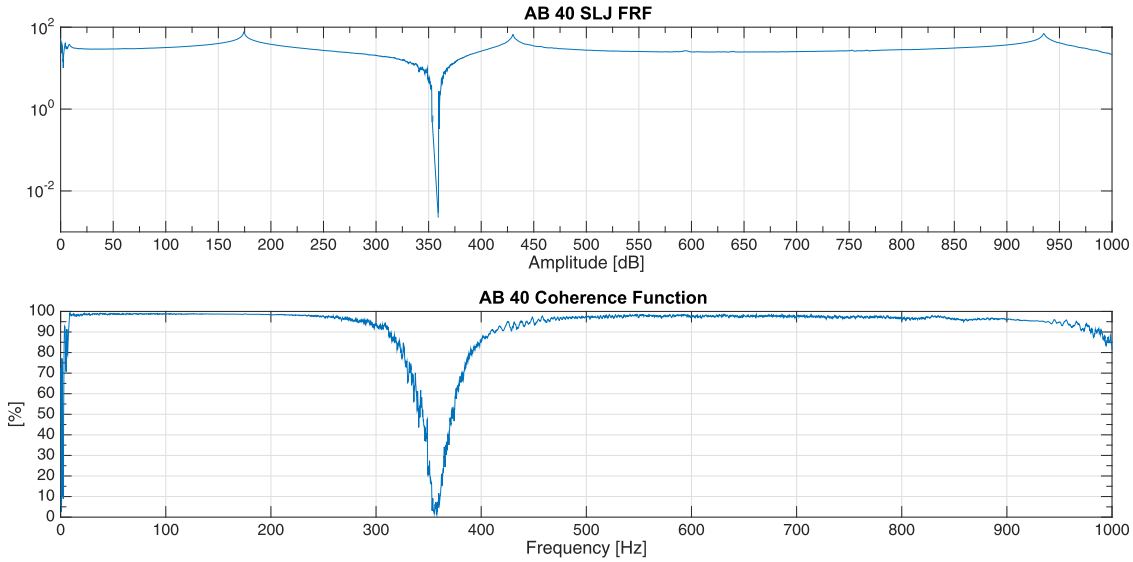

Figure 4.65: FRF and coherence function for the damping analysis in the AB-40 joint.

In the first zone of the FRF plot [0;15] Hz the rigid body behaviour was found. The first natural frequency (first mode) average value found in the two specimens was equal to $\omega_{n1} = 175.16$ Hz.

The second average natural frequency had the average value of $\omega_{n2} = 431.88$ Hz.

The third average natural frequency found had an high coherence between the measurements, nearly 100% and was equal to $\omega_{n3} = 937.89$ Hz.

This measurements allied to the equation 3.1 allowed to obtain the damping ratio (ξ) of the joint for each natural mode. The Table 4.19 shows the average ξ values found for the AB-40 joint for the first three natural modes.

Table 4.19: Average ξ values found for the AB-40 joint for the first three natural modes.

Natural mode	Damping ratio ξ
1	0.176%
2	0.083%
3	0.069%

Since 20 and 40 mm length specimens have different total lengths it is not possible to directly compare the damping ratio of these two specimens. The apparent reduction in the damping can be a misleading since the $\xi = c/2mw_n$ (being m the mass and c the damping). This joint will only be compared with the Hyb-40 specimen.

4.5.4 Hybrid SLJ with 40 mm of overlap

The average frequency response function obtained in one specimen of the hybrid single lap joint with 40 mm of overlap is shown in the Figure 4.66. The resolution obtained in the measurements was 0.1563 Hz.

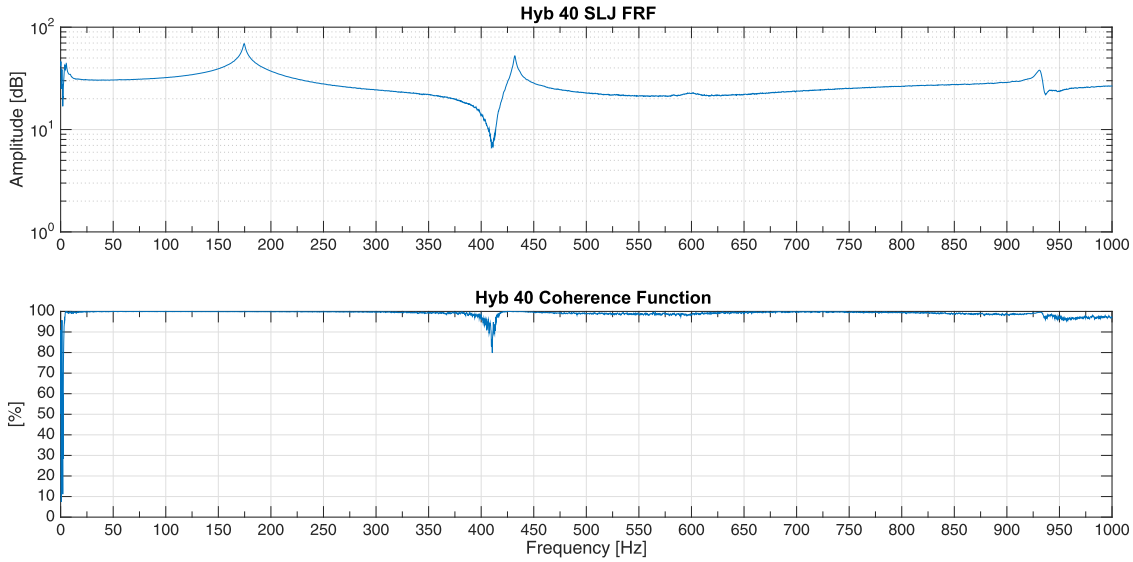

Figure 4.66: FRF and coherence function for the damping analysis in the Hyb-40 joint.

The coherence function obtained was excellent, the FRF analysis lead to an observation of lower amplitudes reached in these joints when compared to the AB-40 specimen. It may indicate a higher damping what is surprising (since, in theory the adhesive joint should have more damping due to the bigger area of effective adhesive layer).

The rigid body behaviour was also found in this kind of joint. The first natural frequency (first mode) average value obtained for the Hyb-40 specimen was $\omega_{n1} = 174.53$ Hz.

The second average natural frequency that resulted from the analysis performed was $\omega_{n2} = 431.87505$ Hz.

Lastly, the third average natural frequency found was equal to $\omega_{n3} = 931.25$ Hz.

This measurements allied to the equation 3.1 allowed to obtain the damping ratio (ξ) of the joint for each natural mode. The Table 4.19 shows the average ξ values found for the Hyb-40 joint for the first three natural modes.

Table 4.20: Average ξ values found for the Hyb-40 joint for the first three natural modes.

Natural mode	**Damping ratio ξ**
1	0.384%
2	0.181%
3	0.249%

Such a big difference in the damping ratio between the AB-40 and Hyb-40 specimens was unexpected. In the first natural mode there was an increase of 218% in the damping ratio. The natural frequency for the AB-40 specimen was 175.16 Hz and for the Hyb-40 was 174.53 Hz. They are very close, the mass is practically the same (40 g vs 41 g) and being $\xi = c/2m\omega_n$, the only way to have such a big increase in ξ is to have a similar increase in the damping (c). Since the adhesive is the same in both joints a plausible cause for that increase is the existence of some

voids in the adhesive layer that contain entrapped air. This entrapped air could be working as a "damping box" within the joint leading to higher damping when compared to a sound hybrid joint with no manufacturing defects.

The damping capabilities are correlated with the fatigue behaviour, so it was expected that the damping ratio was similar between the AB-40 and Hyb-40 joints. If a extrapolation is done the fatigue strength of the Hyb-40 joint needed to be much higher than the AB-40 and it isn't the case.

The known manufacturing problems found are the most likely cause for this unexpected result. The tests need to be redone after the manufacturing process is overcome as a future work.

4.5.5 Summary

The tests on the adhesive and hybrid joints with the 40 mm of overlap were inconclusive to assess the real damping capabilities of each type of joint due to the lack of trust in the perfection of the hybrid joint itself.

The tests were useful to find the differences between the damping capabilities between the FSW and adhesive joints. Figure 4.67 shows the balance graph comparing the damping ratios for the three natural modes.

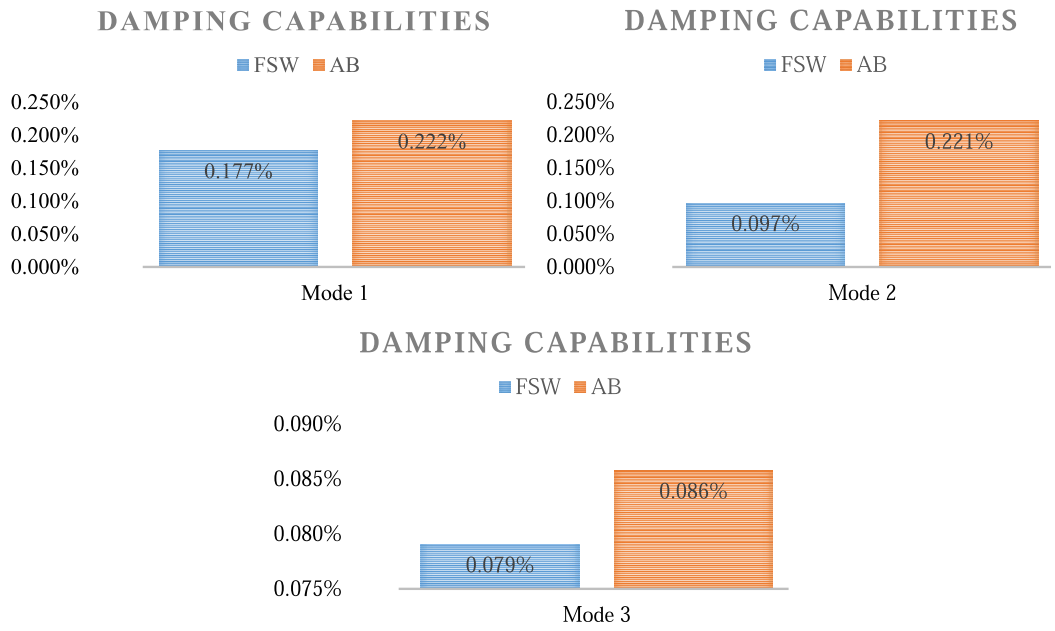

Figure 4.67: Comparison of the damping capabilities of FSW and AB SLJ.

The mode 2 is the more useful to assess the differences between the SLJ because the maximum displacements are within the bonding area.

Clearly in mode 2 there is a significant improvement from the FSW to the adhesive joint in the damping ratio of 228.60%. The trend found in the fatigue tests was also identified in the dynamic analysis being the adhesive joint the one that presented the better performance in fatigue and damping capability.

In the mode 1 and 3 there is no significant differences being the major contributor to the damping the base material.

Chapter 5

Numerical analysis

5.1 *Quasi*-static tests

A finite element analysis was performed using the numerical simulation program Abaqus® (Dassault Systèmes, Suresnes, France) to obtain the load-displacement curves and get a prediction of the failure load. FEM analyses for the FSW joint, adhesive joint 20mm of overlap and 40 mm were performed. The hybrid joint will not be addressed due to the manufacturing limitations that do not allowed the validation of the numerical model and comparison with the experimental results.

The experimental results showed that in the adhesive joints there is a severe plastic deformation in the aluminium adherends, so the plastic characterization was considered in the FEM model through the input of plastic properties in a tabular form that modules the plastic behaviour of the material. For the FSW joints the plastic work is the cause of the joint failure, so the plastic properties of the different zones of the weld were also taken into account. Those mechanical properties were obtained in the past by our workteam in tensile tests and using Digital Image Correlation (DIC) [30].

The rupture was not taken into account in order to simplify and reduce the processing time of the models.

In order to characterize the adhesive a cohesive triangular law was used, using quads damage for the traction separation. The elastic properties were also used (Young's and shear modulus).

The numerical models developed for the different kinds of joints consisted in a standard implicit model computed in a general/static analysis being the adherend and the adhesive created as a 2D deformable part. In the case of the FSW joint there were partitions for the different zones of the weld (the base material, the TMAZ, HAZ and nugget zones). In the adhesive ones there was a partition that was composed by cohesive elements with the length and thickness of the adhesive layer.

Boundary conditions mimicking the experimental tests were used (one end cantilevered and the other a set displacement along loading axis). For the adhesive joint the Scalar stiffness degradation (SDEG) was requested in field outputs in order to observe the crack propagation as a degra-

dation of the cohesive elements. In the FSW joint the PEEQ (Effective Plastic Strain - Scalar) was requested in order to assess the plastic deformation of the joint. It was also requested in the adhesive joint.

In the adhesive joint the mesh size used in the adherends and adhesive had a global size of 0.2 mm. Figure 5.1 shows the mesh used in this adhesive joint model.

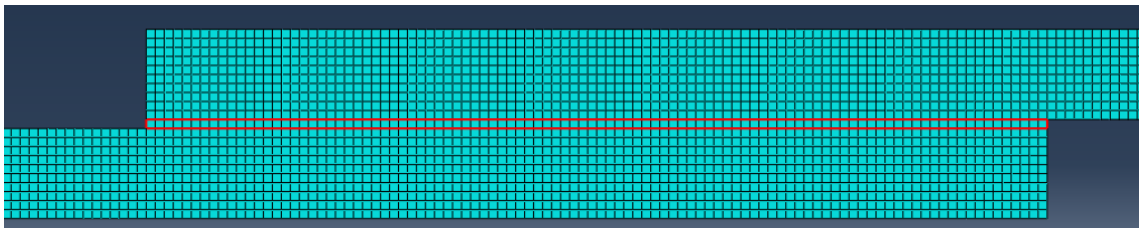

Figure 5.1: Mesh used in the AB-20 specimen static FEM analysis.

The element type for the cohesive zone was defined as a 4-node two-dimensional cohesive element (COH2D4). For the aluminium adherends the element type was a 4-node bilinear plane strain quadrilateral, reduced integration with hourglass control (CPE4R).

In the FSW joint the mesh size used had a global size of 0.2 mm. The assembly was composed by two parts that are the top and bottom substrates. In the areas surrounding the welding the material properties were distinctly modelled [30]. A small crack was placed in the advancing side to simulate the "hook defect". Figure 5.2 shows the assembly used.

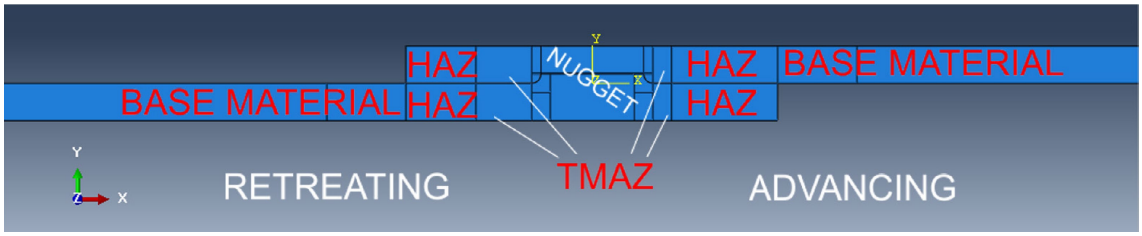

Figure 5.2: Assembly used in FEM simulation for the FSW-20 specimen.

The element type used was the CPS4R that is a 4-node bilinear plane stress quadrilateral, reduced integration, hourglass control.

The results found are shown next and compared with the experimental data.

5.1.1 AB-20 SLJ

The Load vs Displacement curve obtained for this joint in the FEM analysis and experimental is shown in the Figure5.3.

The FEM simulation resulted in a stiffer joint behaviour, this is a common feature of this kind of simulation since the rigidity of the testing machine is not taken into account. Also the triangular cohesive law is not the best way to characterize the adhesive, however it's the only standard way to do it in Abaqus.

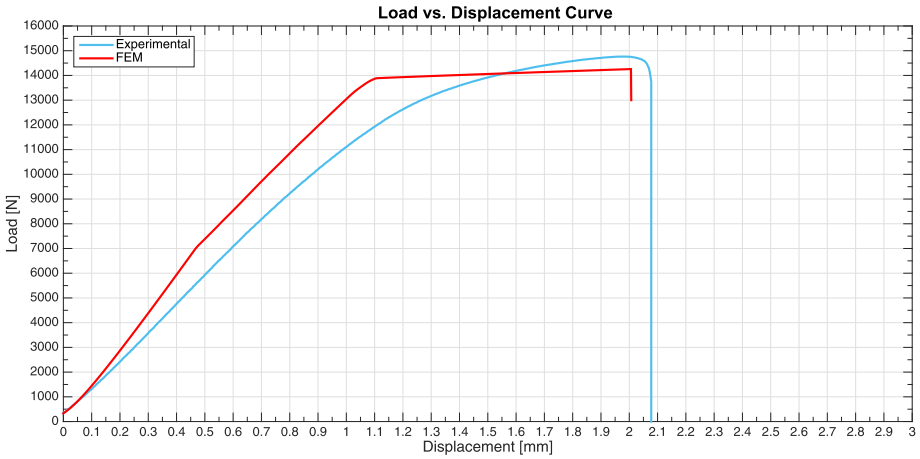

Figure 5.3: Numerical Load vs. Displacement curve of the AB-20 specimens.

The maximum load was fairly predicted. In the simulation however since the properties for the adhesive had changed with the cure cycle an are not yet fully characterized the input values resulted in a more ductile adhesive being the maximum achieved in the simulation lower.

The failure mode was also well predicted since the joint had failed in the experimental and simulation on the adhesive.

5.1.2 AB-40 SLJ

The Load vs Displacement curve obtained for the AB-40 joint in the FEM analysis and experimental is shown in the Figure5.4. In the experimental tests the failure occurred on the clamping gripes.

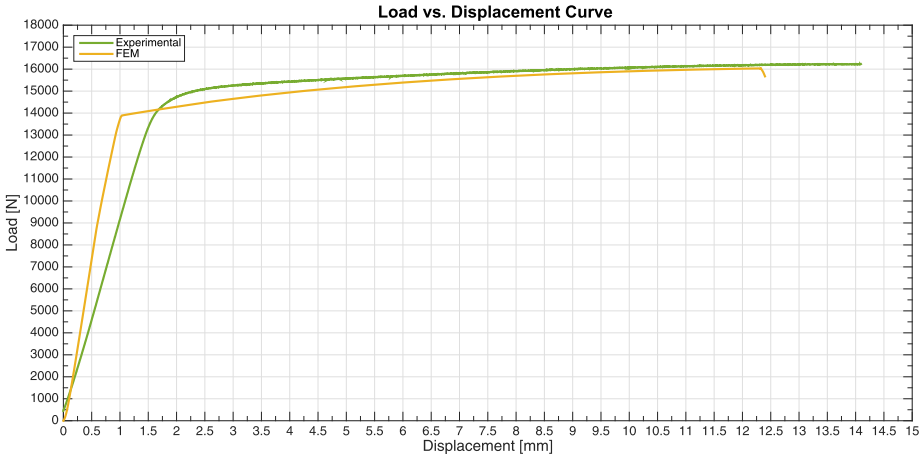

Figure 5.4: Numerical Load vs. Displacement curve of the AB-40 specimens.

Once again the FEM simulation is stiffer as expected. The maximum displacement is naturally lower in the FEM simulation. The most important feature of the this model is that the maximum

load was very accurately obtained. The failure mode obtained in the FEM simulation was also on the adherend close to the clamping system (Figure 5.5).

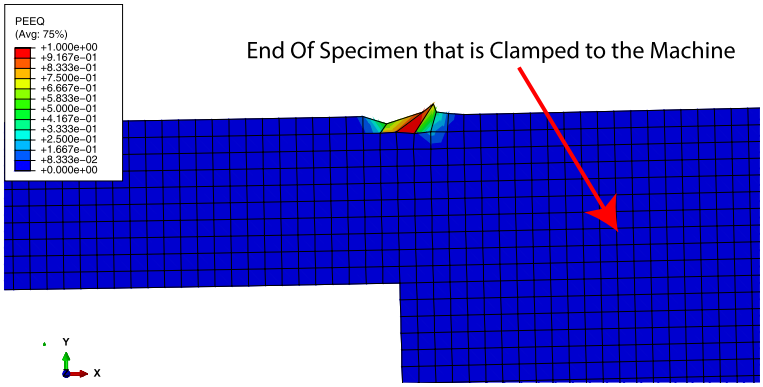

Figure 5.5: Failure mode obtained in FEM for AB-40.

5.1.3 FSW-20 SLJ

The Load vs Displacement curve obtained for the FSW-20 joint in the FEM analysis and experimental is shown in the Figure 5.6.

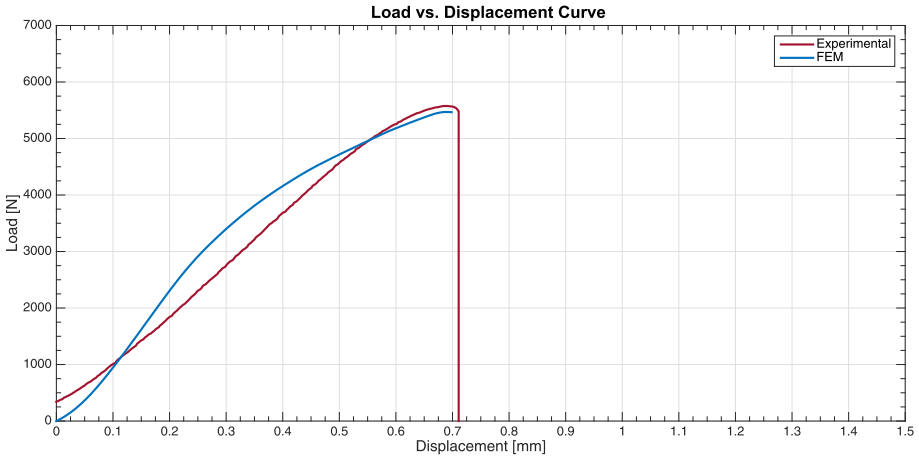

Figure 5.6: Numerical Load vs. Displacement curve of the FSW-20 specimens.

The maximum load was obtained with great accuracy, the difference in the shape of the FEM curve is due to the failure mode. In FEM the failure occured in the "hook defect", in the experimental tensile tests the failure was in the nugget. The plastic behaviour is different in the nugget.

5.2 Natural modes analysis

A finite element analysis was performed using the numerical simulation program Abaqus® (Dassault Systèmes, Suresnes, France) to obtain the first three natural modes with free free boundary conditions and to get a prediction on the natural frequencies for that modes.

The material properties defined for this analysis where the elastic and density of each material. The Table 5.1 presents the properties used.

Table 5.1: Material properties used in the numerical analysis.

Material	Density	Young's Modulus	Poisson's Ratio
Base aluminium AA6082-T6	2.7×10^{-9} ton/mm^3	70000 MPa	0.346
Araldite® 420 A/B	1.05×10^{-9} ton/mm^3	1850 MPa	0.395
AA6082-T6 HAZ Adv.	2.7×10^{-9} ton/mm^3	70000 MPa	0.330
AA6082-T6 HAZ Ret.	2.7×10^{-9} ton/mm^3	70000 MPa	0.330
AA6082-T6 TMAZ Adv.	2.7×10^{-9} ton/mm^3	69500 MPa	0.330
AA6082-T6 TMAZ Ret.	2.7×10^{-9} ton/mm^3	69500 MPa	0.330
AA6082-T6 Nugget	2.7×10^{-9} ton/mm^3	69000 MPa	0.330

The numerical model consisted on a Standard & Explicit analysis and the sections defined were solid, homogeneous. The boundary conditions were free-free. The Step used for all analysis were of the type Linear perturbation, Frequency.

5.2.1 AB-20 SLJ

In AB-20 joint the numerical model was defined as a 3D and deformable part. A seed with approximate global size of 0.5 was used and for the aluminium adherends and adhesive the element used was the C3D8R.

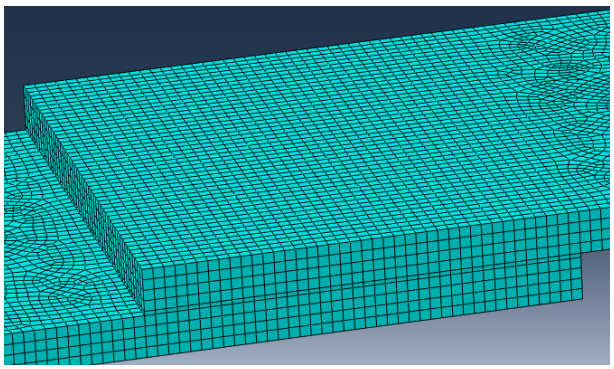

Figure 5.7: Mesh used in the AB-20 specimen analysis.

The natural modes found are shown in the Figure 5.8 and correspond to the expected ones.

As expected the first natural mode presents two nodes near the ends of the specimen. The overlap is only lightly loaded.

The second mode presents three nodes, two at the ends and one in the middle of the joint.

The third mode presents four nodes being the overlap between the two central nodes.

It was possible to find the natural frequencies for this three modes, the Table 5.2 shows the FEM and experimental results.

The results obtained were quite accurate. Being the most distant prediction for the $\omega_n FEM$ 96.1% of the experimental value.

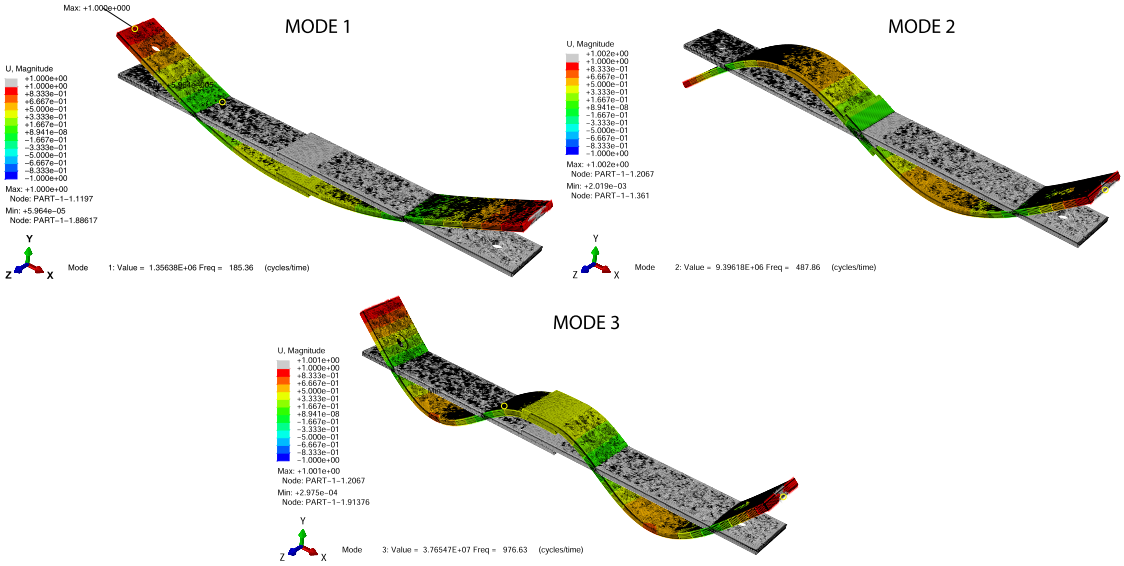

Figure 5.8: Modes obtained for the AB-20 pecimen on FEM analysis.

Table 5.2: Natural frequencies found in FEM vs Experimental for the AB-20 specimen.

Mode	ω_n **FEM**	ω_n **Experimental**
1	185.39 Hz	190.83 Hz
2	487.86 Hz	504.25 Hz
3	976.14 Hz	1016 Hz

5.2.2 AB-40 SLJ

In AB-40 joint the numerical model was defined as a 3D and deformable part. A seed with approximate global size of 0.5 was used and for the aluminium adherends and adhesive the element used was the C3D8R. The only difference for the previous model was the overlap length.

The natural modes found are shown in the Figure 5.9and correspond to the expected ones.

The general shape of the three modes are as expected. The curvature on the adhesive joint area seems to be more severe in the AB-20 joint than in the AB-40 what may result in lower damping capability of the AB-40 when compared to the AB-20.

It was possible to find the natural frequencies for this three modes, the Table 5.3 shows the FEM and experimental results.

Table 5.3: Natural frequencies found in FEM vs Experimental for the AB-40 specimen.

Mode	ω_n **FEM**	ω_n **Experimental**
1	170.43 Hz	175.16 Hz
2	416.09 Hz	431.88 Hz
3	899.10 Hz	937.89 Hz

Also, the results obtained were very accurate. The most distant prediction for $\omega_n FEM$ 96.1% the 95.9% of the experimental result.

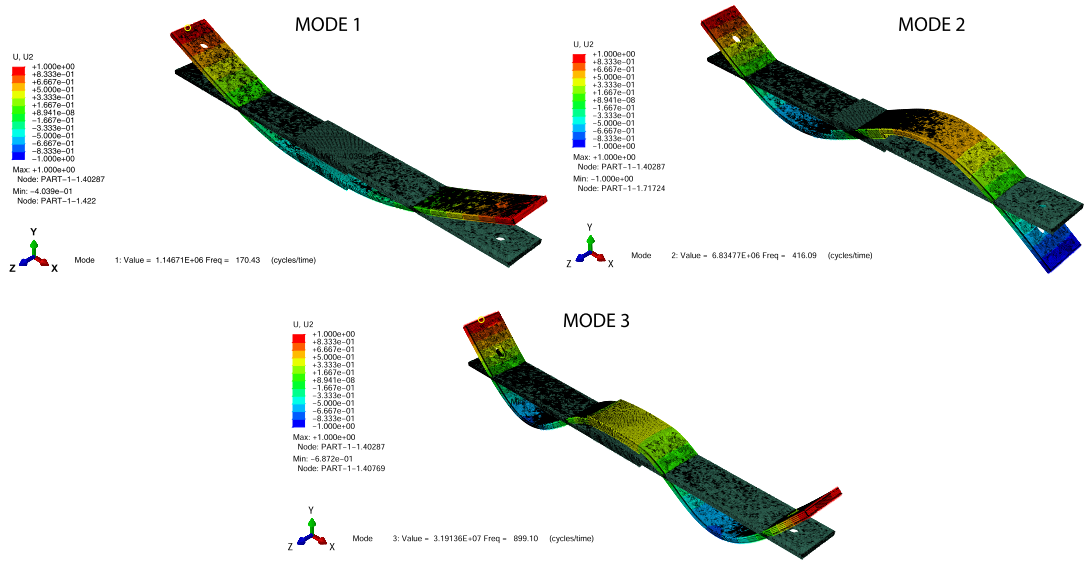

Figure 5.9: Modes obtained for the AB-40 specimen on FEM analysis.

5.2.3 FSW-20 SLJ

In this joint the numerical model consisted in two 2D planar and deformable parts. The parts had different partitions corresponding to the different zones (changes in the mechanical properties) created along the specimen due to the changes induced by the FSW manufacturing process. The properties used were presented in the Table 5.1. These properties were found by our work team in the past [22].

A seed with approximate global size of 0.1 was used. The element type used was the CPS4R for all partitions.

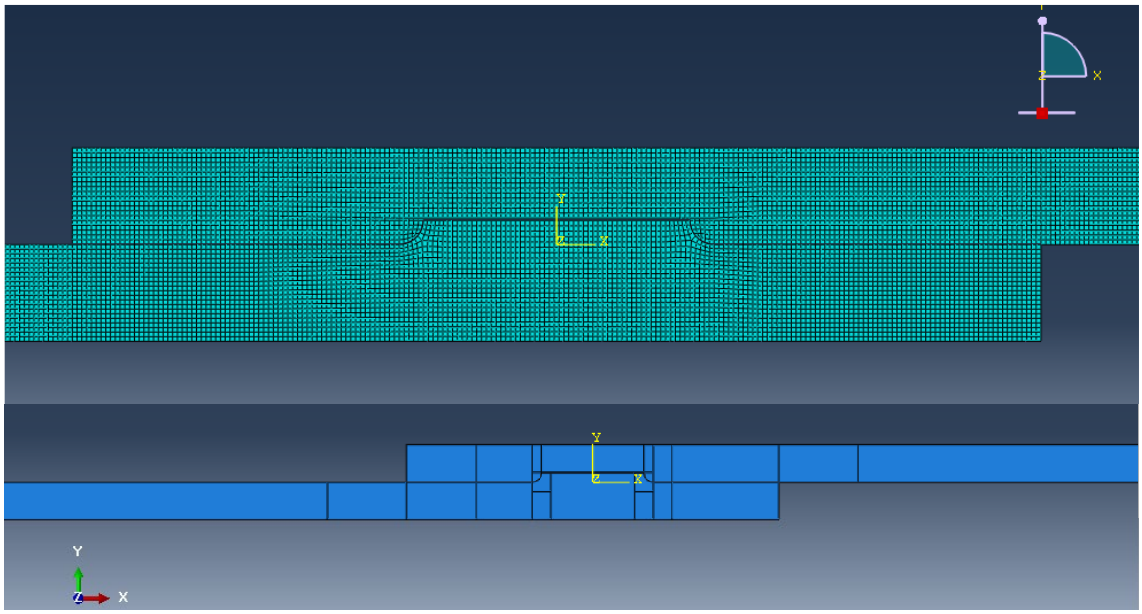

Figure 5.10: Mesh and partitions used in the FSW-20 specimen analysis.

The natural modes found were the same as the AB-20 specimens and are shown in the Figure 5.11.

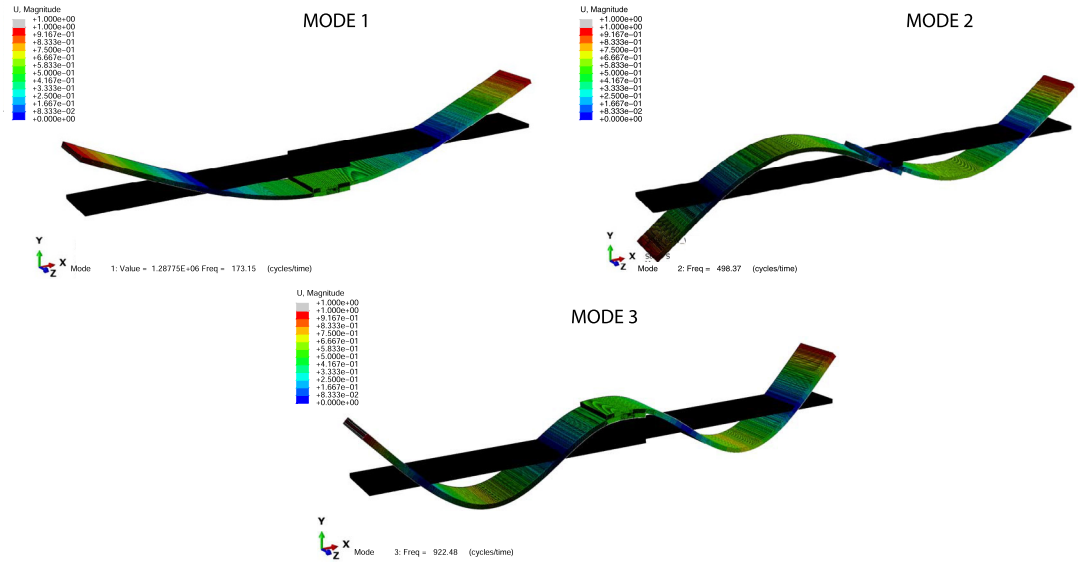

Figure 5.11: Modes obtained for the FSW specimen on FEM analysis.

The natural frequencies for the first three modes is shown in the Table 5.4 shows the FEM and experimental results.

Table 5.4: Natural frequencies found in FEM vs Experimental for the FSW specimen.

Mode	ω_n **FEM**	ω_n **Experimental**
1	173.15 Hz	178.91 Hz
2	498.37 Hz	505.94 Hz
3	922.48 Hz	956.09 Hz

The results obtained were quite accurate being the most distant prediction 96.5% of the experimental result.

5.2.4 Hyb-40 SLJ

In that joint the numerical model consisted in two 2D planar and deformable parts.

The parts correspondent to the adherends had different partitions corresponding to the different zones (changes in the mechanical properties) created along the specimen due to the changes induced by the FSW manufacturing process like the model of the FSW joint.

The adhesive layer was added to the FSW model and had a 0.2 mm thickness and a proper constraint to fix them together was used.

The global size of the mesh was 0.1 mm. Both adherends and adhesive were modelled with the CPS4R element type.

Figure 5.12 shows the model developed where is possible to see the adhesive layer and the welding joint.

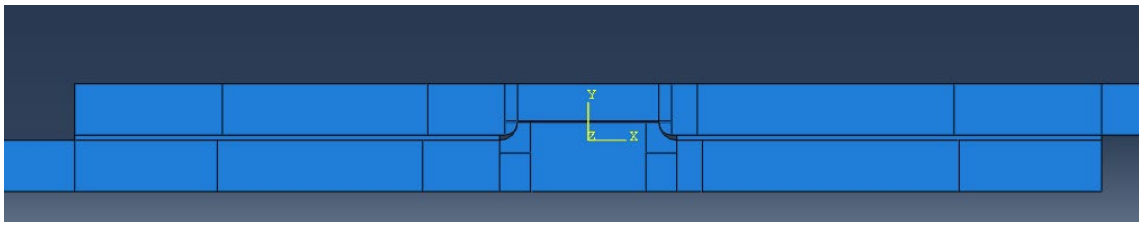

Figure 5.12: Joint model used in the FSW-20 specimen analysis.

The natural modes shape are shown in the Figure 5.13.

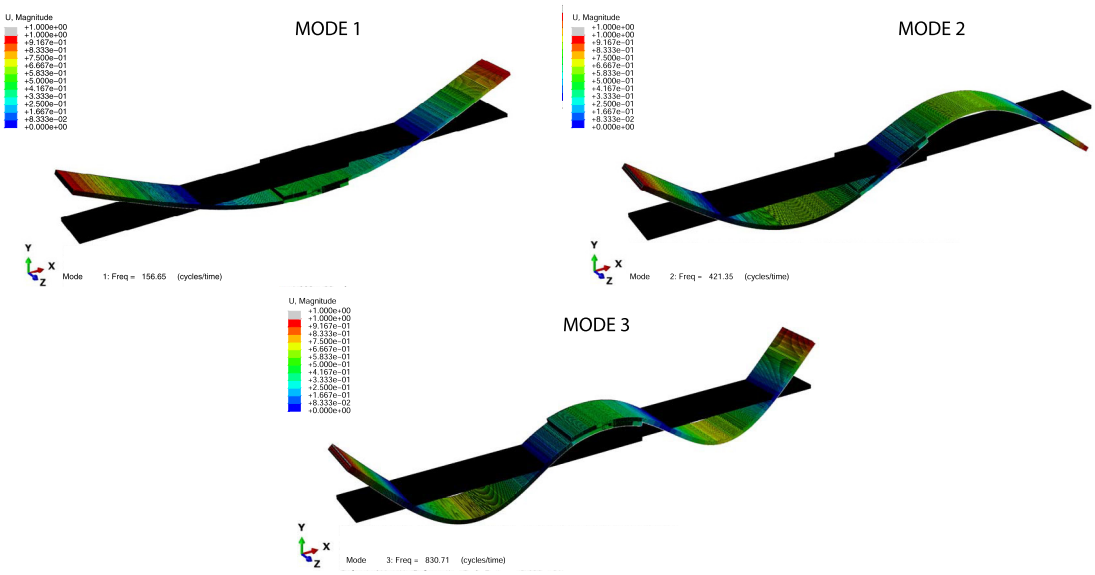

Figure 5.13: Modes obtained for the Hyb-40 specimen on FEM analysis.

The natural frequencies for the first three modes is shown in the Table 5.5 shows the FEM and experimental results.

Table 5.5: Natural frequencies found in FEM vs Experimental for the Hyb-40 specimen.

Mode	ω_n FEM	ω_n Experimental
1	156.65 Hz	174.53 Hz
2	421.35 Hz	431.88 Hz
3	830.71 Hz	931.25 Hz

The results found for the natural frequency in the hybrid specimens were accurate in the mode 2 and 3 and in the mode 1 there was a small level o accuracy (it was only 89.76% of the measured value).

5.2.5 Summary

It was possible to successfully obtain the first three natural modes and frequencies for the different kind of joints.

The values of the natural frequencies obtained with the FEM analysis are consistent and always lower than the experimental results. This fact may be explained attending that the FEM model does not include the suspension method (elastic cord), the induced mass by the accelerometer and the rigidity induced by the cable of the accelerometer.

Chapter 6

Conclusions and Future Work

6.1 Conclusions

The initial goals of this Master thesis were to study and benchmark the FSW, the adhesive and the FS Weldbonded joints under static and cyclic fatigue loadings. Beyond the original 20 mm overlap configuration other specimen configurations were also studied in order complete hypothesis and improve the results discussion, being the initial goals surpassed. The damping capabilities of each type of joint and EDS analysis on the failure surface were also performed. Numerical analysis in order to simulate the static strength and natural modes for each joint was done.

Regarding the static strength of each type of joint it was concluded that the adhesive joints performed better than all others. AB joint with 20 mm of overlap had an static strength efficiency of 96% compared to the dummy specimen. The cure cycle adopted in conjunction with the changes in the anodization process resulted in a better controlled manufacturing process for the adhesive joints. The FSW with 20 mm of overlap was not the worst performing joint, as expected, since the hybrid joints with 20 mm of overlap presented manufacturing problems that leaded to an average strength lower than all other joint types. The hybrid joints cured at room temperature with 40 mm of overlap also presented a mechanical performance lower than the expected, however they were stronger than the FSW-20 joint due to the bigger adhesive area. The scatter due to the manufacturing problems was attenuated by adopting a similar cure cycle used in the adhesive joints. However, the joint strength was not the expected and can be improved as soon as the problems are completely overcomed. On the adhesive SLJ the increase in the overlap did not lead to a significant increase in strength as the joint strength was limited by the aluminium substrate (plasticization and failure in the adherend).

The EDS analysis proved that there is a strong concentration of contaminations in the hybrid joints that came from the manufacturing process and the source is most likely the FSW machine which is requiring maintenance operations and is not in the best conditions. The anodization process adopted was proven to be effective. The same EDS analysis allowed to conclude that the failure mode in the adhesive joints where mainly cohesive near the interface.

The damping capabilities of the adhesive and FSW joints were successfully obtained, being

the damping capabilities of the adhesive joint significantly higher, following the trend found in the fatigue test results. The mode 2 was found to be the most useful to assess the damping capabilities. Regarding the hybrid joint the damping ratio obtained seemed to be very dependent on the manufacturing quality of the joints.

The numerical analysis allowed the accurate prediction of the adhesive and friction stir welded joint strength under static loads. The natural frequencies and modes were also obtained for all the specimens tested with very good accuracy.

Concerning fatigue it was possible to assess the different behaviour for each type of joint, except for the hybrid joints that presented high levels of scatter which lead to an inconclusive assessment. S-N curves with good reliability were obtained for the FSW and adhesive joints. For the dummy specimen it was possible to infer the performance, with less accuracy, and was found that the geometry of the SLJ configuration results in a severe decrease in the joint strength. The best performing joint was the adhesive with 40 mm of overlap followed by the adhesive joint with 20 mm of overlap. The FSW joint presented the worst performance under fatigue loadings. The hybrid joint showed signs that, if well manufactured, can present a fatigue strength closer to the adhesive joint. On the adhesive joints the increasing of the overlap length from 20 to 40 mm resulted in increased fatigue strength although mostly at higher load levels. At lower load levels the difference was almost negligible due to the nature of the failure.

6.2 Future Work

The FS weldbonding is an innovative manufacturing process, and can be further studied not only in the SLJ configuration as well as in T-joint configuration that can be useful in practical appliances. A Design of Experiments can be done regarding the several manufacture variables in order to find the optimized parameters for the FS Weldbonding process.

An EDS analysis on the hybrid joints produced with the cure cycle adopted should be done in order to understand if the presence of contamination remains the same or not. After the manufacturing difficulties being overcomed the hybrid joints should be produced again in order to benchmark under static and fatigue loadings in order to compare the results obtained in this Master thesis for the AB and FSW joints. It will allow to assess if the hybridization process is advantageous for industrial applications.

A cure cycle like the one adopted should be used in all hybrid and adhesive joints since it allowed to better control the manufacturing process what leads to lower scatter.

It would be very interesting to study and benchmark the static and fatigue behaviour of the different kind of joints when subjected to aging conditions. This can be done following standards like the ASTM D1183 - 03(2011)[86]. This kind of study has an high interest since the adhesive joints are very sensitive to ambient degradation. This study can exposed the real advantage of using FS Welding joint in real applications like in aeronautical structures.

References

[1] Directive 2009/33/ec - the promotion of clean and energy-efficient road transport vehicles.

[2] R.S. Mishra and Z.Y. Ma. Friction stir welding and processing. *Materials Science and Engineering: R: Reports*, 50(1–2):1 – 78, 2005. ISSN 0927-796X. doi: http://dx.doi.org/10.1016/j.mser.2005.07.001. URL http://www.sciencedirect.com/science/article/pii/S0927796X05000768.

[3] Sindo Kou. *Precipitation-Hardening Materials I: Aluminum Alloys*, pages 353–374. John Wiley & Sons, Inc., 2003. ISBN 9780471434023. doi: 10.1002/0471434027.ch15. URL http://dx.doi.org/10.1002/0471434027.ch15.

[4] D. Fersini and A. Pirondi. Analysis and modelling of fatigue failure of friction stir welded aluminum alloy single-lap joints. *Engineering Fracture Mechanics*, 75(3-4):790–803, feb 2008. doi: 10.1016/j.engfracmech.2007.04.013. URL http://dx.doi.org/10.1016/j.engfracmech.2007.04.013.

[5] L. Cederqvist and A. P. Reynolds. Factors affecting the properties of friction stir welded aluminum lap joints. *Welding Journal*, pages 281–287, 2001. URL http://www.americanweldingsociety.org/wj/supplement/Cederqvist12-01.pdf.

[6] R NANDAN, T DEBROY, and H BHADESHIA. Recent advances in friction-stir welding process, weldment structure and properties. *Progress in Materials Science*, 53(6):980–1023, aug 2008. doi: 10.1016/j.pmatsci.2008.05.001. URL http://dx.doi.org/10.1016/j.pmatsci.2008.05.001.

[7] X. Cao and M. Jahazi. Effect of tool rotational speed and probe length on lap joint quality of a friction stir welded magnesium alloy. *Materials & Design*, 32(1):1 – 11, 2011. ISSN 0261-3069. doi: http://dx.doi.org/10.1016/j.matdes.2010.06.048. URL http://www.sciencedirect.com/science/article/pii/S0261306910004346.

[8] D Lohwasser Z. Chen. *Friction Stir Welding*. Elsevier Science, 2009. URL http://www.ebook.de/de/product/22050157/friction_stir_welding.html.

[9] R.S. Mishra and M.W. Mahoney. *Friction Stir Welding and Processing*. ASM International, 2007. ISBN 9781615030972. URL https://books.google.pt/books?id=JW2l2L-UYS4C.

[10] Sérgio Manuel Oliveira Tavares. *Design and advanced manufacturing of aircraft structures using friction stir welding*. PhD thesis, Tese de Programa Doutoral. Líderes para Indústrias Tecnológicas. Universidade do Porto. Faculdade de Engenharia, 2011. URL http://hdl.handle.net/10216/63446.

[11] A. S. Hassan, T. S. Mahmoud, F. H. Mahmoud, and T. A. Khalifa. Friction stir welding of dissimilar a319 and a356 aluminium cast alloys. *Science and Technology of Welding and Joining*, 15(5):414–422, 2010. doi: 10.1179/136217110X12720264008358. URL http://www.tandfonline.com/doi/abs/10.1179/136217110X12720264008358.

[12] K. Krasnowski, C. Hamilton, and S. Dymek. Influence of the tool shape and weld configuration on microstructure and mechanical properties of the al 6082 alloy FSW joints. *Archives of Civil and Mechanical Engineering*, 15(1):133–141, jan 2015. doi: 10.1016/j.acme.2014.02.001. URL http://dx.doi.org/10.1016/j.acme.2014.02.001.

[13] Nuno Mendes, Pedro Neto, Altino Loureiro, and António Paulo Moreira. Machines and control systems for friction stir welding: A review. *Materials & Design*, 90:256 – 265, 2016. ISSN 0264-1275. doi: http://dx.doi.org/10.1016/j.matdes.2015.10.124. URL http://www.sciencedirect.com/science/article/pii/S0264127515307024.

[14] B.T. Gibson, D.H. Lammlein, T.J. Prater, W.R. Longhurst, C.D. Cox, M.C. Ballun, K.J. Dharmaraj, G.E. Cook, and A.M. Strauss. Friction stir welding: Process, automation, and control. *Journal of Manufacturing Processes*, 16(1):56 – 73, 2014. ISSN 1526-6125. doi: http://dx.doi.org/10.1016/j.jmapro.2013.04.002. URL http://www.sciencedirect.com/science/article/pii/S1526612513000601. Recent Developments in Welding Processes.

[15] Yoshihiro Kusuda. Honda develops robotized FSW technology to weld steel and aluminum and applied it to a mass-production vehicle. *Industrial Robot*, 40(3):208–212, apr 2013. doi: 10.1108/01439911311309889. URL http://dx.doi.org/10.1108/01439911311309889.

[16] W. TANG, X. GUO, J. C. McCLURE, L. E. MURR, and A. NUNES. Heat input and temperature distribution in friction stir welding. *Journal of Materials Processing & Manufacturing Science*, 7(2):163–172, oct 1998. doi: 10.1106/55tf-pf2g-jbh2-1q2b. URL http://dx.doi.org/10.1106/55tf-pf2g-jbh2-1q2b.

[17] M. Maeda, H. Liu, H. Fujii, and T. Shibayanagi. Temperature field in the vicinity of FSW-tool during friction stir welding of aluminium alloys. *Weld World*, 49(3-4):69–75, mar 2005. doi: 10.1007/bf03266478. URL http://dx.doi.org/10.1007/bf03266478.

[18] G. Buffa, G. Campanile, L. Fratini, and A. Prisco. Friction stir welding of lap joints: Influence of process parameters on the metallurgical and mechanical properties. *Materials Science and Engineering: A*, 519(1–2):19 – 26, 2009. ISSN 0921-5093. doi: http://dx.doi.

org/10.1016/j.msea.2009.04.046. URL http://www.sciencedirect.com/science/article/pii/S0921509309005255.

[19] B Heinz and B Skrotzki. Characterization of a friction-stir-welded aluminum alloy 6013. *METALLURGICAL AND MATERIALS TRANSACTIONS B-PROCESS METALLURGY AND MATERIALS PROCESSING SCIENCE*, 33(3):489–498, JUN 2002. ISSN 1073-5615. doi: {10.1007/s11663-002-0059-5}.

[20] K. Krasnowski. Fatigue and static properties of friction stir welded aluminium alloy 6082 lap joints using triflute-type and smooth tool. *Archives of Metallurgy and Materials*, 59 (1), jan 2014. doi: 10.2478/amm-2014-0025. URL http://dx.doi.org/10.2478/amm-2014-0025.

[21] L. Reis, V. Infante, M. de Freitas, F.F. Duarte, P.M.G. Moreira, and P.M.S.T. de Castro. Fatigue behaviour of aluminium lap joints produced by laser beam and friction stir welding. *Procedia Engineering*, 74:293 – 296, 2014. ISSN 1877-7058. doi: http://dx.doi.org/10.1016/j.proeng.2014.06.265. URL http://www.sciencedirect.com/science/article/pii/S1877705814008352. {XVII} International Colloquium on Mechanical Fatigue of Metals (ICMFM17).

[22] Daniel F. O. Braga Pedro M. G. P. Moreira Lucas da Silva Virginia Infante Jurgen Silvanus Marco Pacchione. Innovative structural connections for lightweight structural design. November 2015.

[23] Valentin Richter-Trummer, Pedro Miguel Guimarães Pires Moreira, João Ribeiro, and Paulo Manuel Salgado Tavares de Castro. The contour method for residual stress determination applied to an AA6082-t6 friction stir butt weld. *Materials Science Forum*, 681:177–181, mar 2011. doi: 10.4028/www.scientific.net/msf.681.177. URL http://dx.doi.org/10.4028/www.scientific.net/msf.681.177.

[24] M. Mahoney M. James. Proceedings of the first international symposium on friction stir welding. In *Thousand Oaks, CA, USA, June 14–16*, 1999.

[25] *Proceedings of the Third International Symposium on Friction Stir Welding*, number 27–28, Kobe, Japan, September 2001. C.D. Donne, E. Lima, J. Wegener, A. Pyzalla, T. Buslaps.

[26] M. Peel, A. Steuwer, M. Preuss, and P.J. Withers. Microstructure, mechanical properties and residual stresses as a function of welding speed in aluminium {AA5083} friction stir welds. *Acta Materialia*, 51(16):4791 – 4801, 2003. ISSN 1359-6454. doi: http://dx.doi.org/10.1016/S1359-6454(03)00319-7. URL http://www.sciencedirect.com/science/article/pii/S1359645403003197.

[27] Yutaka S. Sato, Hiroyuki Kokawa, Masatoshi Enomoto, Shigetoshi Jogan, and Takenori Hashimoto. Precipitation sequence in friction stir weld of 6063 aluminum during aging. *Metallurgical and Materials Transactions A*, 30(12):3125–3130. ISSN 1543-1940. doi: 10.1007/s11661-999-0223-5. URL http://dx.doi.org/10.1007/s11661-999-0223-5.

[28] M. W. Mahoney, C. G. Rhodes, J. G. Flintoff, W. H. Bingel, and R. A. Spurling. Properties of friction-stir-welded 7075 t651 aluminum. *Metallurgical and Materials Transactions A*, 29(7):1955–1964, 1998. ISSN 1543-1940. doi: 10.1007/s11661-998-0021-5. URL http://dx.doi.org/10.1007/s11661-998-0021-5.

[29] Mats Ericsson, Lai-Zhe Jin, and Rolf Sandström. Fatigue properties of friction stir overlap welds. *International Journal of Fatigue*, 29(1):57 – 68, 2007. ISSN 0142-1123. doi: http://dx.doi.org/10.1016/j.ijfatigue.2006.02.052. URL http://www.sciencedirect.com/science/article/pii/S0142112306001010.

[30] V. Infante, D.F.O. Braga, F. Duarte, P.M.G. Moreira, M. de Freitas, and P.M.S.T. de Castro. Study of the fatigue behaviour of dissimilar aluminium joints produced by friction stir welding. *International Journal of Fatigue*, 82, Part 2:310 – 316, 2016. ISSN 0142-1123. doi: http://dx.doi.org/10.1016/j.ijfatigue.2015.06.020. URL http://www.sciencedirect.com/science/article/pii/S0142112315002005. 10th Fatigue Damage of Structural Materials Conference.

[31] M Ericsson. Influence of welding speed on the fatigue of friction stir welds, and comparison with MIG and TIG. *International Journal of Fatigue*, 25(12):1379–1387, dec 2003. doi: 10.1016/s0142-1123(03)00059-8. URL http://dx.doi.org/10.1016/s0142-1123(03)00059-8.

[32] Gordon Kelly. Quasi-static strength and fatigue life of hybrid (bonded/bolted) composite single-lap joints. *Composite Structures*, 72(1):119–129, jan 2006. doi: 10.1016/j.compstruct.2004.11.002. URL http://dx.doi.org/10.1016/j.compstruct.2004.11.002.

[33] Mats Ericsson Rolf Sandström. Fatigue of fsw overlap joints in aluminium welded with different tool designs.

[34] E. Nicholas Kallee, S. and W. Thomas. Friction stir welding- invention, innovations and applications. *Journal of Light Metal Welding and Construction*, 2005.

[35] S. Inaniwa, Y. Kurabe, Y. Miyashita, and H. Hori. Application of friction stir welding for several plastic materials. In Hidetoshi Fujii, editor, *Proceedings of the 1st International Joint Symposium on Joining and Welding*, pages 137 – 142. Woodhead Publishing, 2013. ISBN 978-1-78242-163-4. doi: http://dx.doi.org/10.1533/978-1-78242-164-1.137. URL http://www.sciencedirect.com/science/article/pii/B9781782421634500213.

[36] M.K. Besharati-Givi and P. Asadi. *Advances in Friction-Stir Welding and Processing*. Woodhead Publishing Series in Welding and Other Joining Technologies. Elsevier Science, 2014. ISBN 9780857094551. URL https://books.google.pt/books?id=qZhzAwAAQBAJ.

[37] Bob Carter. Introduction to friction stir welding (fsw). In *NASA Glenn Research Center Advanced Metallics Branch*.

[38] Chapman A. J. Kinloch and Hall. *Adhesion and adhesives-science and technology*, volume 26. WILEY, 1988. doi: 10.1002/pol.1988.140260811.

[39] L.F.M. da Silva, A. Öchsner, and R.D. Adams. *Handbook of Adhesion Technology*. Handbook of Adhesion Technology. Springer Berlin Heidelberg, 2011. ISBN 9783642011689. URL https://books.google.pt/books?id=CsKoeKzXvl8C.

[40] Dow Automotive Systems. Structural bonding of lightweight cars. Technical report, Dow Automotive Systems, -.

[41] Edward M. Petrie. *Handbook of Adhesives and Sealants, Second Edition*. New York, Chicago, San Francisco, Lisbon, London, Madrid, Mexico City, Milan, New Delhi, San Juan, Seoul, Singapore, Sydney, Toronto, 2007.

[42] M.R. Ayatollahi and A. Akhavan-Safar. Failure load prediction of single lap adhesive joints based on a new linear elastic criterion. *Theoretical and Applied Fracture Mechanics*, 80, Part B:210 – 217, 2015. ISSN 0167-8442. doi: http://dx.doi.org/10.1016/j.tafmec.2015.07.013. URL http://www.sciencedirect.com/science/article/pii/S0167844214201340.

[43] Lucas F. M. da Silva. Aulas pap - adesivos. In *FEUP - Aulas*, 2015.

[44] O. Lunder, B. Olsen, and K. Nisancioglu. Pre-treatment of aa6060 aluminium alloy for adhesive bonding. *International Journal of Adhesion and Adhesives*, 22(2):143 – 150, 2002. ISSN 0143-7496. doi: http://dx.doi.org/10.1016/S0143-7496(01)00049-5. URL http://www.sciencedirect.com/science/article/pii/S0143749601000495.

[45] N. B. Ekwe D. F. Aloko. Anodization of aluminum. *International Journal of Scientific and Research Publications*, 3(3):380, March 2013.

[46] Astrid Bjorgum Fabrice Lapique John Walmsley Keith Redford. Anodising as pre-treatment for structural bonding. *International Journal of Adhesion and Adhesives*, 23(5):401 – 412, 2003. ISSN 0143-7496. doi: http://dx.doi.org/10.1016/S0143-7496(03)00071-X. URL http://www.sciencedirect.com/science/article/pii/S014374960300071X.

[47] R. A. Pethrick. Design and ageing of adhesives for structural adhesive bonding - a review. *Proceedings of the Institution of Mechanical Engineers, Part L: Journal of Materials: Design and Applications*, 229(5):349–379, feb 2014. doi: 10.1177/1464420714522981. URL http://dx.doi.org/10.1177/1464420714522981.

[48] Y. Zhang, R. D. Adams, and Lucas F. M. da Silva. Effects of curing cycle and thermal history on the glass transition temperature of adhesives. *The Journal of Adhesion*, 90(4): 327–345, 2014. doi: 10.1080/00218464.2013.795116. URL http://dx.doi.org/10.1080/00218464.2013.795116.

[49] R.D. Adams. *Adhesive Bonding: Science, Technology and Applications*. Woodhead Publishing Series in Welding and Other Joining Technologies. Elsevier Science, 2005. ISBN 9781845690755. URL https://books.google.pt/books?id=kq6jAgAAQBAJ.

[50] R. Budynas and K. Nisbett. *Shigley's Mechanical Engineering Design*. McGraw-Hill Education, 2010. ISBN 9780073529288. URL https://books.google.pt/books?id=eT1DPgAACAAJ.

[51] Lucas F.M. da Silva, Paulo J.C. das Neves, R.D. Adams, and J.K. Spelt. Analytical models of adhesively bonded joints—part i: Literature survey. *International Journal of Adhesion and Adhesives*, 29(3):319 – 330, 2009. ISSN 0143-7496. doi: http://dx.doi.org/10.1016/j.ijadhadh.2008.06.005. URL http://www.sciencedirect.com/science/article/pii/S0143749608000730.

[52] Lucas F.M. da Silva, Paulo J.C. das Neves, R.D. Adams, A. Wang, and J.K. Spelt. Analytical models of adhesively bonded joints—part ii: Comparative study. *International Journal of Adhesion and Adhesives*, 29(3):331 – 341, 2009. ISSN 0143-7496. doi: http://dx.doi.org/10.1016/j.ijadhadh.2008.06.007. URL http://www.sciencedirect.com/science/article/pii/S0143749608000742.

[53] M. Goland and E.Reissner. The stresses in cemented lap joints. *J. Appl. Mech*, 1944.

[54] D. Feldman. Structural adhesive joints in engineering, by r.d. adams and w.c. wake, elsevier applied science, london and new york, 1984, 309 pp. *Journal of Polymer Science: Polymer Letters Edition*, 23(11):601–601, 1985. ISSN 1543-0472. doi: 10.1002/pol.1985.130231111. URL http://dx.doi.org/10.1002/pol.1985.130231111.

[55] Fabrizio Moroni and Alessandro Pirondi. Technology of rivet: Adhesive joints. In *Advanced Structured Materials*, pages 79–108. Springer Science Business Media, 2010. doi: 10.1007/8611_2010_37. URL http://dx.doi.org/10.1007/8611_2010_37.

[56] M.F. Kanninen and C.H. Popelar. *Advanced Fracture Mechanics*. Oxford engineering science series. Oxford University Press, 1985. ISBN 9780195035322. URL https://books.google.pt/books?id=Wb8-W_DBdrEC.

[57] M.W. Rushforth, P. Bowen, E. McAlpine, X. Zhou, and G.E. Thompson. The effect of surface pretreatment and moisture on the fatigue performance of adhesively-bonded aluminium. *Journal of Materials Processing Technology*, 153-154:359–365, nov 2004. doi: 10.1016/j.jmatprotec.2004.04.319. URL http://dx.doi.org/10.1016/j.jmatprotec.2004.04.319.

[58] M.-L. Abel, A.N.N. Adams, A.J. Kinloch, S.J. Shaw, and J.F. Watts. The effects of surface pretreatment on the cyclic-fatigue characteristics of bonded aluminium-alloy joints. *International Journal of Adhesion and Adhesives*, 26(1-2):50–61, feb 2006. doi: 10.1016/j.ijadhadh.2004.12.004. URL http://dx.doi.org/10.1016/j.ijadhadh.2004.12.004.

[59] A.M. Pereira, J.M. Ferreira, F.V. Antunes, and P.J. Bártolo. Study on the fatigue strength of {AA} 6082-t6 adhesive lap joints. *International Journal of Adhesion and Adhesives*, 29(6):633 – 638, 2009. ISSN 0143-7496. doi: http://dx.doi.org/10.1016/j.ijadhadh.2009.02.009. URL http://www.sciencedirect.com/science/article/pii/S0143749609000268. Special Issue on Durability of Adhesive Joints.

[60] F. Moroni, A. Pirondi, and F. Kleiner. Experimental analysis and comparison of the strength of simple and hybrid structural joints. *International Journal of Adhesion and Adhesives*, 30 (5):367–379, jul 2010. doi: 10.1016/j.ijadhadh.2010.01.005. URL http://dx.doi.org/10.1016/j.ijadhadh.2010.01.005.

[61] I-Car. Aluminum/steel construction of the bmw 5 series. Technical report, I-Car, 2003.

[62] T. Sadowski, M. Kneć, and P. Golewski. Experimental investigations and numerical modelling of steel adhesive joints reinforced by rivets. *International Journal of Adhesion and Adhesives*, 30(5):338–346, jul 2010. doi: 10.1016/j.ijadhadh.2009.11.004. URL http://dx.doi.org/10.1016/j.ijadhadh.2009.11.004.

[63] T. Sadowski, P. Golewski, and E. Zarzeka-Raczkowska. Damage and failure processes of hybrid joints: Adhesive bonded aluminium plates reinforced by rivets. *Computational Materials Science*, 50(4):1256–1262, feb 2011. doi: 10.1016/j.commatsci.2010.06.022. URL http://dx.doi.org/10.1016/j.commatsci.2010.06.022.

[64] Jan R. Weitzenböck and Dag McGeorge. Science and technology of bolt-adhesive joints. In *Advanced Structured Materials*, pages 177–199. Springer Science Business Media, 2011. doi: 10.1007/8611_2011_54. URL http://dx.doi.org/10.1007/8611_2011_54.

[65] Gordon Kelly. Load transfer in hybrid (bonded/bolted) composite single-lap joints. *Composite Structures*, 69(1):35–43, jun 2005. doi: 10.1016/j.compstruct.2004.04.016. URL http://dx.doi.org/10.1016/j.compstruct.2004.04.016.

[66] Saied M. H. Darwish. Science of weld: Adhesive joints. In *Advanced Structured Materials*, pages 1–36. Springer Science Business Media, 2010. doi: 10.1007/8611_2010_35. URL http://dx.doi.org/10.1007/8611_2010_35.

[67] A.M. Pereira, J.A.M. Ferreira, F.V. Antunes, and P.J. Bártolo. Assessment of the fatigue life of aluminium spot-welded and weld-bonded joints. *Journal of Adhesion Science and Technology*, 28(14-15):1432–1450, 2014. doi: 10.1080/01694243.2012.698107. URL http://dx.doi.org/10.1080/01694243.2012.698107.

[68] Holger Gaul and Gert Weber. Technology of weld-adhesive joints. In *Advanced Structured Materials*, pages 37–77. Springer Science Business Media, 2011. doi: 10.1007/8611_2010_47. URL http://dx.doi.org/10.1007/8611_2010_47.

[69] Liming Liu and Daxin Ren. A novel weld-bonding hybrid process for joining mg alloy and al alloy. *Materials & Design*, 32(7):3730 – 3735, 2011. ISSN 0261-3069. doi: http://dx.doi.org/10.1016/j.matdes.2011.03.050. URL http://www.sciencedirect.com/science/article/pii/S0261306911002251.

[70] Tsung-Yu Pan Armando Joaquin Daniel E. Wilkosz Larry Reatherford John M. Nicholson Zhili Feng Michael L. Santella. Spot friction welding for sheet aluminum joining.

[71] S.H. Chowdhury, D.L. Chen, S.D. Bhole, X. Cao, and P. Wanjara. Lap shear strength and fatigue behavior of friction stir spot welded dissimilar magnesium-to-aluminum joints with adhesive. *Materials Science and Engineering: A*, 562:53 – 60, 2013. ISSN 0921-5093. doi: http://dx.doi.org/10.1016/j.msea.2012.11.039. URL http://www.sciencedirect.com/science/article/pii/S0921509312015912.

[72] L.-M. Liu, H.-Y. Wang, and Z.-D. Zhang. The analysis of laser weld bonding of al alloy to mg alloy. *Scripta Materialia*, 56(6):473–476, mar 2007. doi: 10.1016/j.scriptamat.2006.11.034. URL http://dx.doi.org/10.1016/j.scriptamat.2006.11.034.

[73] H.Y. Wang and L.M. Liu. Analysis of the influence of adhesives in laser weld bonded joints. *International Journal of Adhesion and Adhesives*, 52:77 – 81, 2014. ISSN 0143-7496. doi: http://dx.doi.org/10.1016/j.ijadhadh.2014.04.005. URL http://www.sciencedirect.com/science/article/pii/S0143749614000943.

[74] Liming Liu, Daxin Ren, and Yongfei Li. Static mechanics analyses of different laser weld bonding structures in joining {AZ61} mg alloy. *International Journal of Adhesion and Adhesives*, 31(7):660 – 665, 2011. ISSN 0143-7496. doi: http://dx.doi.org/10.1016/j.ijadhadh.2011.06.009. URL http://www.sciencedirect.com/science/article/pii/S0143749611000790.

[75] Luís Miguel Campos de Sousa. Hybrid friction stir bonding. Master's thesis, Faculdade de Engenharia da Universidade do Porto, 2015.

[76] Daniel F.O. Braga, L.M.C. de Sousa, V. Infante, Lucas F.M. da Silva, and P.M.G.P. Moreira. Aluminum friction stir weldbonding. *Procedia Engineering*, 114:223 – 231, 2015. ISSN 1877-7058. doi: http://dx.doi.org/10.1016/j.proeng.

2015.08.062. URL http://www.sciencedirect.com/science/article/pii/S1877705815017014. {ICSI} 2015 The 1st International Conference on Structural Integrity Funchal, Madeira, Portugal 1st to 4th September, 2015.

[77] D.F.O. Braga, L.M.C. De Sousa, V. Infante, L.F.M. Da Silva, and P.M.G.P. Moreira. Aluminium friction-stir weld-bonded joints. *Journal of Adhesion*, 92 (7-9):665–678, 2016. doi: 10.1080/00218464.2015.1085860. URL https://www.scopus.com/inward/record.uri?eid=2-s2.0-84962449225&partnerID=40&md5=31d43af39253b2bf376170f760a27929.

[78] Joseph C. Benedyk. International temper designation systems for wrought aluminum alloys: Part ii – thermally treated (t temper) aluminum alloys. *LIGHT METAL AGE*, 2010.

[79] Granta Design Limited. Ces edupack 2015. *CES*, 2015.

[80] P. Davies, L. Sohier, J.-Y. Cognard, A. Bourmaud, D. Choqueuse, E. Rinnert, and R. Créac'hcadec. Influence of adhesive bond line thickness on joint strength. *International Journal of Adhesion and Adhesives*, 29(7):724 – 736, 2009. ISSN 0143-7496. doi: http://dx.doi.org/10.1016/j.ijadhadh.2009.03.002. URL http://www.sciencedirect.com/science/article/pii/S0143749609000402.

[81] R.J.C. Carbas, L.F.M. da Silva, and G.W. Critchlow. Adhesively bonded functionally graded joints by induction heating. *International Journal of Adhesion and Adhesives*, 48:110 – 118, 2014. ISSN 0143-7496. doi: http://dx.doi.org/10.1016/j.ijadhadh.2013.09.045. URL http://www.sciencedirect.com/science/article/pii/S0143749613001838.

[82] INTERNATIONAL INSTITUTE OF WELDING, editor. *BEST PRACTICE GUIDE ON STATISTICAL ANALYSIS OF FATIGUE DATA*, FEBRUARY 2003.

[83] H. Saunders. Book reviews : SHOCK AND VIBRATION HANDBOOK (2nd edition) c.m. harris and c.e. crede - editors McGraw-hill book company, new york (1976). *The Shock and Vibration Digest*, 10(1):34–34, jan 1978. doi: 10.1177/058310247801000107. URL http://dx.doi.org/10.1177/058310247801000107.

[84] *The Fundamentals of Modal Testing*, 2000.

[85] Baisheng Wu. A correction of the half-power bandwidth method for estimating damping. *Archive of Applied Mechanics*, 85(2):315–320, aug 2014. doi: 10.1007/s00419-014-0908-0. URL http://dx.doi.org/10.1007/s00419-014-0908-0.

[86] Practices for resistance of adhesives to cyclic laboratory aging conditions. URL http://dx.doi.org/10.1520/d1183-03r11.